UNIVERSIDAD POLITÉCNICA DE MADRID
Escuela Técnica Superior de Ingenieros Industriales

Engineering Design Methodology for Robot-Based Non-Planar Additive Manufacturing (RbNPAM)

D O C T O R A L T H E S I S

Submitted for the degree of Doctor by:

Adrián López Arrabal

Bachelor's degree in Industrial Engineering Technologies
Master's degree in Industrial Engineering

Madrid, 2025

UNIVERSIDAD POLITÉCNICA DE MADRID
Escuela Técnica Superior de Ingenieros Industriales

Doctoral Degree in Mechanical Engineering

Engineering Design Methodology for Robot-Based Non-Planar Additive Manufacturing (RbNPAM)

D O C T O R A L T H E S I S

Submitted for the degree of Doctor by:

Adrián López Arrabal

Bachelor's degree in Industrial Engineering Technologies
Master's degree in Industrial Engineering

Under the supervision of:
Dr. Andrés Díaz Lantada

Madrid, 2025

Title: Engineering Design Methodology for Robot-Based Non-Planar Additive Manufacturing (RbNPAM)

Author: Adrián López Arrabal

Doctoral Programme: Mechanical Engineering

Thesis Supervision:

Dr. Andrés Díaz Lantada, Full Professor, Ph.D. in Mechanical Engineering, Mechanical Engineering Department, ETSI Industriales, Universidad Politécnica de Madrid.

External Reviewers:

Thesis Defense Committee:

Thesis Defense Date:

This thesis has been partially supported by:

BIOMET4D: *Smart 4D biodegradable metallic shape-shifting implants for dynamic tissue restoration*, European Union's Horizon Research and Innovation. No.101047008.

CYBERCELL: *Sistema de producción ciberfísico para la planificación inteligente de células de fabricación.* Plan Estatal project No.PID2021-124838OB-I00.

Predicción automatizada del comportamiento dinámico de un brazo robot para corrección de trayectorias en la realización de tareas de alta precisión, and *Calibración de posicionamiento absoluta de un robot por reconocimiento de patrones geométricos mediante algoritmos de resolución del problema de máximo clique.* E.T.S.I. Industriales, Primeros Proyectos call: ETSIIUPM24-PU02, and ETSII-UPM24-PM02.

"The soul is a compact of mind-masses combined in a most intimate and manifold manner. It grows constantly by accession of mind-masses, and upon these depend its development. [...] Every entering mind-mass excites all related mind-masses and this excitation is the more powerful the more insignificant the diversity of their inner states."

- Bernhard Riemann

A Álvaro Guzmán Bautista,

gracias por eneseñarme que no existen retos complejos en la ciencia, sino carencias de conocimiento en Topología aplicada.

Espero seguir muchos años a tu lado en la busqueda de la variedad de Riemann en la que merezca la pena transformar la Universidad que nos ha tocado vivir.

Institutional acknowledgement

I would like to express my gratitude to all the institutions and projects that made the completion of this doctoral thesis possible:

I would like to express my sincere gratitude to the Universidad Politécnica de Madrid (UPM) and, in particular, to the Escuela Técnica Superior de Ingenieros Industriales de Madrid (ETSII) for the financial and material support provided for the completion of this work.

In particular, I would like to thank the Departamento de Ingeniería Mecánica (DIMEC) for their efforts, and the División de Ingeniería de Máquinas (DIM) for their involvement, the resources and facilities provided, as well as their administrative and financial support for the project. I would like to thank the Laboratorio de Tecnologías Mecánicas - Ingeniaría de Procesos de Fabricación (IPF) for the resources provided for the completion of this work.

I would like to thank the ETSII for granting two projects of the *"Primeros Proyectos"* call for this research: *Predicción automatizada del comportamiento dinámico de un brazo robot para corrección de trayectorias en la realización de tareas de alta precisión (ETSII-UPM24-PU02)*, and *Calibración de posicionamiento absoluta de un robot por reconocimiento de patrones geométricos mediante algoritmos de resolución del problema de máximo clique (ETSII-UPM24-PM02).*

I would like to thank European project No.101047008: *BIOMET4D: Smart 4D biodegradable metallic shape-shifting implants for dynamic tissue restoration,* European Union's Horizon Research and Innovation Programme, for funding part of the research for this work.

I would like to thank Plan Estatal project No.PID2021-124838OB-I00: *CYBERCELL: Sistema de producción ciberfísico para la planificación inteligente de células de fabricación,* for funding part of the research for this work.

Agradecimientos Personales

Son muchas las personas que han hecho que estos cuatro años de camino interminable hayan dado su fruto. Es probable que en unas pocas palabras no sea capaz de reflejar la estima que os tengo y el apoyo incondicional que habéis sido para mí todo este tiempo.

Quiero empezar agradeciéndole a Andrés su labor de Director de Tesis, una tesis que ha sido una carrera de obstáculos en la que los avatares de la vida decidieron que, lo que comenzó siendo descarga corona de plasma atmosférico, acabase siendo fabricación aditiva no plana. Y en la que te quiero agradecer especialmente el día que me dijiste que, si quería empezar en la Universidad, no iba a pasar nada por dejar un tema atrás y empezar con otro nuevo. Gracias a esa decisión hoy probablemente sea de los pocos afortunados que tiene la opción de dedicar su vida a lo que verdaderamente le apasiona.

El segundo pilar sin el que esto no se sostiene es Álvaro, te tengo que agradecer muchas cosas pero sin duda la capacidad de hacer que lo imposible sea matemáticamente viable es una de ellas. Te agradezco también el ecosistema de trabajo que hemos conseguido generar y, en lo personal, que hayas estado conmigo en todo momento. Es una verdadera fortuna tener tu apoyo y confío ciegamente en que voy a seguir teniéndolo hasta el día que nos jubilemos. Porque si algo te pido, es que en 2060 estemos en Benidorm jugando al mus en un viaje del Imserso. Recordémonos mutuamente, cuando llegue el momento, que cualquier éxito actual será en vano si acabamos destruyéndolo por miedo a dejarnos enseñar por los que, ya hoy, vienen por detrás pisando fuerte.

Me gustaría agradecer a la División de Ingeniería de Máquinas el apoyo al proyecto, económico y de gestión. Además, me gustaría agradeceros el apoyo personal que todos habéis demostrado: Javier, Kike, Paco, Soqui, Javi, Gonzalo, José Luis, Juanma, Andrés, Adri y Pedro. Sois una familia increíble con la que da gusto trabajar cada día.

José Luis, quiero agradecerte en particular cada vez que has estado para hablar conmigo en los momentos más difíciles de estos tres años. Eres para mí un ejemplo de humildad, y un referente del tipo de persona que quiero ser cuando llegue a tu edad. Sigue tirándote con la bici por la montaña, buceando en cuevas o haciéndote DJ... sigue siendo feliz y contagiando a los demás de lo que eres.

Soqui, sé que todavía no soy tu favorito, está la competencia muy fuerte esta temporada, pero prometo seguir trabajando para serlo. Gracias por sacar dinero de debajo de las piedras para que siga haciendo mis locuras mentales. Prometo no entregar postviajes fuera de plazo. Y gracias por las charlas que nos permitimos de vez en cuando, no son muy Montessori, pero da gusto aprender de la vida contigo.

Kike, gracias por confiar en mí. Sé que hoy no estaría en la Universidad sin tu apoyo y que, lo que nos han enseñado los últimos dos años, vale la pena por tener claro el futuro increíble que nos queda por vivir juntos. Y gracias por seguir confiando, estoy muy contento de poder compartir esta nueva etapa siendo compis de despacho, aunque te mudes al de José Luis...

Javier, te lo digo muy poco pero te admiro mucho, desde que fuiste mi profe te he ido

conociendo más y me sorprendes a mejor cada día. Especialmente me alegra mucho tu última etapa, te veo muy feliz y sé que estás haciendo lo correcto. Gracias por preocuparte por mí y por todo el chocolate que, realmente, era muy necesario para acabar esta tesis.

Juanma, gracias por ayudarme con todo lo que ha estado de tu mano. Espero que nos queden muchas reuniones para debatir si los modelos de vibraciones tienen o no sentido, aunque son duras, salgo de ellas con la cabeza llena de conocimiento.

Paco, me gustaría agradecerte todo el apoyo que me has dado durante estos años. Creo que eres un ejemplo de templanza, sabes estar en todo momento y es algo que quiero seguir aprendiendo de ti. Gracias por seguirme el rollo con las locuras de docencia que se me ocurren porque sin ti se me pira la olla bastante, por liarnos a todos para ir a los carnavales o engancharnos a la escalada. Eres de esas personas que sabe construir equipo y cuidarlo, por eso yo te quiero en el mío.

Javi, no sé si ponerte en agradecimientos de la DIM o de la familia, porque en estos años te has convertido en un apoyo imprescindible en mi vida. Tenemos el don de saber cuándo nos hacemos falta, sea una mudanza, una obra, montar un mueble, cambiar unos frenos, llevarnos en coche a por otro coche que dejamos aparcado lejos de casa, tomarnos una cerveza hablando de lo mal que se nos da gestionar la vida, o salsear, que nunca está de más. Gracias por enseñarme que no es buen plan ir dos personas en un bicimad por la calle Serrano y que no pasa nada por interactuar con bebés aunque no me gusten. No hay toxicidad que separe nuestra pasión por la mecánica, pero no más caballitos en la M-30 por favor y gracias.

Pedro, gracias por todas las impresiones de última hora que te han tenido mareado, sin ellas hubiese sido imposible acabar esto. Además, quiero agradecer que me ayudases con el ordenador y el problema de la clave bitlocker que casi me deja sin tesis a medio escribir. Has sido una gran ayuda.

Gonzalo, el safety guy de la DIM, jajaja gracias por todos los buenos momentos que nos estás dando, por preocuparte de nuestra seguridad y porque creo que en poco tiempo te has convertido en uno más del equipo. Gracias por contribuir al buen rollo y al salseo del curro.

Adri, aunque seas la última incorporación, llevo ya muchos años siguiendo tu trayectoria y sé que va a ser increíble. Estoy muy contento de que hayas entrado en el equipo; sin duda tenemos muchas temporadas interesantes por delante de las que espero aprendamos mucho juntos.

Afortunadamente, si algo me han enseñado los 8 años que llevo involucrado en la División de Ingeniería de Máquinas, es que el éxito de una unidad docente se mide en la calidad humana de las personas que deciden unirse al grupo y colaborar en él. En este caso, no me puedo olvidar de la "sala de becarios:" Sonia, William, Rodri, Carlos, Pepe y Álex, gracias por mantener vivo este espíritu y no dejar que decaiga.

Sonia, nuestra amistad nació con el comienzo de una tesis doctoral y casi llegamos al final de ésta con un 2% de la estabilidad mental que teníamos al principio. Gracias por compartir esta batalla diaria conmigo y porque vamos a estar juntos en el proceso de recuperación de

la estabilidad mental. Gracias por los momentos de risas, las discusiones, los debates y las tonterías de siempre. Estoy seguro de que empezamos una nueva etapa cerrando las tesis en la que quiero estar a tu lado.

William, quiero agradecerle todo el trabajo y el apoyo en casos de estudio y en los desarrollos del Biomet. Ha tenido sus momentos duros pero estoy seguro de que la recompensa cuando celebremos el final de las tesis va a hacer que merezca la pena. Gracias también por descubrirnos el Limanta, best cevichito ever.

El trabajo que hacemos en la Universidad tiene como último fin impactar en los estudiantes y, en ese sentido, creo que he tenido mucha suerte en contar con los mejores como alumnos de Trabajo de Fin de Titulación: Mario , Alejandro , Amparo , Laura , Iñaki, Pedro, David, Andrés, Víctor, Adri, Victoria, Samu, Rubén, Pepe, Jorge y Charo. Hayáis hecho algo que tenga que ver con esta Tesis o no, habéis sido parte de mi camino de aprendizaje como docente y estoy muy orgulloso de veros seguir con vuestros proyectos personales.

Laura, estoy muy orgulloso de ti, aguantaste mi etapa de mayor inseguridad con los modelos de vibraciones del robot y elegiste confiar. Creo que has llegado al sitio donde mereces y no es ni la décima parte de donde puedes llegar si te lo propones. Gracias por confiar, eres para mí la mejor prueba de que la vocación por enseñar da sus frutos. Solo te deseo que la vida te cuide tanto como cuidas tú a los demás.

Pedro, empezamos mal pero remontamos fuerte, me río mucho cada vez que leo el primer correo que me mandaste. Creo que en la vida hace mucha falta gente como tú. Gracias por montarme el passion project de mis sueños, a los dos nos hacía falta aprender de desmontar motores de moto (pero no se lo digas a Javi). Gracias por involucrarte con nosotros tanto, creo que vamos tarde para compensarte la cantidad de veces que nos ayudas en el Laboratorio. Aunque tú probablemente no te des cuenta del cambio que has dado en estos dos años, me siento muy orgulloso del punch de confianza en ti mismo con los estudios. También gracias porque más de una chapa de PVs te has comido cuando estaba tristón y has sabido estar ahí siempre.

David, vas a llegar muy lejos porque tienes una calidad de trabajo increíble. Creo que he aprendido más de hacer las cosas bien yo de ti que tú de mi y me siento muy agradecido de ello. Espero que te lleves contigo la capacidad de tener paciencia con algunas personas, que ya has visto que tiene sus frutos. Pero no pierdas el David rebelde, de vez en cuando no viene mal sacarlo!

Amparo, creo que te mereces un enorme reconocimiento porque tu trabajo es, sin duda, la primera piedra de esta Tesis. Gracias por creer en las locuras que Álvaro y yo planteamos y, sobre todo, por ser para nosotros un apoyo en un momento muy complicado. No tengo duda de que vas a llegar muy alto.

La mejor parte de la vocación docente es la motivación que recibes cuando un alumno confía en ti su formación. Ese momento en el que dejas de impartir formación reglada y pasas a aprender conjuntamente con ellos sobre sus inquietudes. Quería agradeceros a todos aquellos partícipes de esta motivación: Edu, Óscar, Pedro, Laura, Charo y Chema por parte de los

lubricólogos; Alba, Alicia, Laura y Lara por dar las mejores prácticas de TMM; y Ángel, David, Pedro y Laura por ser el apoyo de tantos proyectos.

Finalmente, me gustaría agradecer a aquellas personas que, a lo largo de este camino, han dedicado su tiempo a apoyarme en lo personal o profesional: Jon, Andrea, Mónica, Álex, Daysi, Rami y Rodolfo. Gracias por escuchar ideas, elaborar críticas constructivas y formar parte de este proceso de mejora.

Fuera del ámbito laboral, ha sido de gran importancia construir una red sana donde no se hable de Ingeniería en la que poder evadirme de la Tesis. Tengo mucho que agradecer a toda esa red:

Mamá, si hay alguien a quien le debo todo en la vida, eres tú. Gracias por estar en los momentos buenos y en los malos, por darme unos valores de los que sentirme orgulloso y por demostrarme cada día que se puede seguir trabajando en vivir mejor con uno mismo y con los demás. Gracias por ser la persona en la que poder sentirme reflejado y la que poder aspirar a ser. Por enseñarme a caerme y levantarme, a gestionar los problemas y no guardármelos, a valorar el tiempo de calidad con los demás y a muchas otras cosas que me dan para otra tesis doctoral. Puedo decir con mucha certeza que, si he llegado hasta donde estoy hoy, es gracias a ti.

Jesús, gracias por ser mi compañero en todo este proceso, por aprenderte nombres de gente que no has visto en tu vida para comprender por lo que estaba pasando, por esforzarte en entender movidas ingenieriles y, sobre todo, por nunca dejarme solo con esto. Te agradezco infinitamente todas las horas que hemos echado hablando, tus consejos, la ayuda incondicional en todo momento. Gracias por seguir construyendo incluso en los momentos más difíciles, estoy muy orgulloso de ti y del presente que compartimos juntos, pero cada día con más ganas de vivir el futuro que tenemos pendiente. Sé que vas a conseguir todo lo que se te ponga por delante, y voy a estar en lo bueno y en lo malo para que no te sientas solo. Gracias por compartir conmigo tu forma de ver el mundo y por haber encontrado conmigo una forma común de verlo y compartirlo. Me hace muy feliz y te quiero mucho.

A mi tía Trini y a mi primo Javi, me gustaría agradecerles el estar pendientes y preocuparse por mí durante todo este tiempo. Gracias por estar siempre ahí y por poder seguir celebrando juntos los logros de la familia.

A mis amigos me gustaría agradecerles muchas cosas, a lo largo de mi vida han construido la persona que soy y, aunque algunos son ingenieros y he dicho que no se hablaba de ingeniería en este apartado, tenemos en común que sabemos juntarnos y no hablar de ingeniería y eso, os hace especiales.

A mi grupo de la Uni (los de clase de la uni no los del trabajo) os quiero agradecer seguir juntos, creo que hemos conseguido una red de cuidados muy bonita y querernos cada uno como somos: Jorge, Martiña, Marina, Carlos, Víctor, Marta y Almu. Además, me pone contento vernos hacernos mayores, lograr nuestros objetivos y seguir siendo nosotros mismos.

A mi grupo de ESTIEM, nos vemos poco pero cada vez que nos vemos es como si nos

hubiésemos visto hace 2 días. Me enseñásteis que las amistades de calidad trascienden fronteras, y que nos seguiremos viendo todas las cenas de Navidad que hagan falta. Os estoy muy agradecido.

Me gustaría agradecer en particular a dos personas que admiro profundamente y que para mí han sido un referente de calidad humana, trabajo en equipo y humildad. Os echo mucho de menos en la Universidad, pero sabéis que me vais a tener siempre como amigo.

Mar, cada vez que pienso en ti solo puedo sentirme orgulloso de cómo has salido adelante siempre. Eres un ejemplo de compañera que dice las cosas y que pelea y eso te hace una persona increíble. Has llegado donde te mereces porque están construyendo todavía el siguiente escalón para que subas. Te echo un poquito de menos por Madrid, pero sé que es porque estás revolucionando Tarragona. Gracias por enseñarme tanto, desde el TFM hasta trabajar en Cedrión, hasta la Tesis. Este camino no habría sido recorrido sin estar tú en él.

Miguel, gracias por empezar esto con Álvaro y conmigo. Cada reunión hablando del potencial que tenía sabes que ha sido brutal para que ganemos confianza y hayamos llegado hoy a conseguirlo. Y gracias en lo personal a todo el apoyo, las mentorías y reflexiones con no saber qué hacer con nuestra vida. Los caminos a veces se tuercen pero las personas con la sensibilidad y el buen corazón con la que tú te mueves, acaban encontrando el suyo. Cuenta conmigo para ello.

Finalmente, me gustaría agradecer a la universidad pública la oportunidad que he tenido de formarme durante 13 años de mi vida en diferentes aspectos de la ingeniería. Y lo quiero agradecer porque soy muy consciente del tesoro que tenemos y del esfuerzo colectivo que cuesta construirlo. No me habría podido permitir llegar hasta aquí sin ella.

Fruto de esta reflexión, me gustaría agradecer al personal de la Universidad Politécnica de Madrid, y en particular de la E.T.S.I. Industriales, la gestión de este y tantos otros proyectos. Muchos ni nos conocemos en persona, solo nos mandamos correos con facturas y justificantes, y otros, sin embargo, nos vemos día a día en conserjería, cafetería, servicio de limpieza o mantenimiento. Pero todos juntos contribuimos a que la rueda gire y todo funcione. Muchas gracias.

Y a quienes me acompañáis en el camino y sois motivo para seguir luchando, muchas gracias de corazón.

Abstract

Robot-Based Non-Planar Additive Manufacturing (RbNPAM) explores advancements in integrating robotics with additive manufacturing, focusing on the development and application of non-planar layer stacking methodologies. This work aims to address the limitations of traditional planar Additive Manufacturing (AM) processes, such as poor surface quality, dependence on support materials, and constrained design flexibility, by enabling material deposition along curved paths. Additionally, the development of this additive manufacturing method brings forth the need to devise new mechanical design techniques capable of generating geometries that meet the specific requirements of this manufacturing approach. By combining non-planar methodologies with multi-axis robotic systems, the research expands the possibilities of AM in producing structurally optimized and geometrically complex parts.

The primary goal of the thesis is to advance the field of Robot-Based Non-Planar Additive Manufacturing by enhancing parametric slicing techniques, developing robotic systems for non-planar manufacturing, and demonstrating industrial applications. The research introduces novel slicing algorithms tailored to non-planar geometries, which align deposition paths with the curvature of the build surface. This objective involves the slicing process and infill strategy between two homeomorphic workspaces interconnected through a bijective transformation. Through this transformation, planar slicing performed in one of the subspaces is converted into curved trajectories of high geometric complexity when the transformation is reversed.

To demonstrate the practical viability of this methodology, a robotic cell prototype was designed and built, integrating advanced controllers, adaptable extrusion systems, and thermally stable build platforms. The prototype was validated through extensive testing, ensuring precision in trajectory execution and repeatability in non-planar manufacturing tasks. The system proved capable of maintaining stable layer alignment, even under challenging operational conditions.

The second objective of the thesis is the development of a design for additive manufacturing methodology, specifically non-planar, to establish a workflow capable of producing parts suitable for fabrication using the robotic cell. To achieve this, a comprehensive library of origami devices is created, designed for 4D printing, which change shape after being printed on curved layers in response to the stimulus of a variation in one of their components. This case study not only enables the development of the design methodology but also demonstrates the wide range of possibilities that can be integrated into the non-planar additive manufacturing cell.

The thesis also presents several case studies showcasing the potential of Robot-Based Non-Planar Additive Manufacturing across diverse industrial applications. For example, coronary stents were fabricated using non-planar deposition to achieve improved mechanical properties and precision. Origami-inspired robotic grippers were created by leveraging multi-material capabilities to integrate soft and rigid components seamlessly. An application is developed for texture mapping on complex surfaces using the custom-developed slicer. Additionally, forming dies optimized for mechanical performance were produced using customized slicing strategies, demonstrating the feasibility of non-planar techniques for industrial tooling. These examples

highlight the ability of Robot-Based Non-Planar Additive Manufacturing to manufacture complex, high-performance components with reduced material waste and minimized post-processing.

The main conclusions of the thesis results indicate that a solid slicing methodology has been developed that simplifies the task of generating complex trajectories for robotic additive manufacturing. Furthermore, the industrial implementation of this methodology has been successfully validated, and the material deposition error has been modeled through experiments. These experiments validate the downscaling of current systems that do not allow for robotic additive manufacturing at small scales.

The thesis highlights the industrial applications of Robot-Based Non-Planar Additive Manufacturing, particularly in the production of high-precision components for industries such as aerospace, healthcare, and automotive. It emphasizes the need for automation in the design and slicing processes to enhance efficiency and broaden the adoption of this technology. By demonstrating Robot-Based Non-Planar Additive Manufacturing's ability to improve design flexibility and manufacturing performance, this work paves the way for future advancements. It calls for continued innovation in robotic systems, material science, and computational tools to further expand the capabilities of non-planar additive manufacturing and make it viable for a wide range of industrial applications.

Resumen

La Fabricación Aditiva Robótica No Plana (FA-Rb-NP) explora los avances en la integración de la robótica con la fabricación aditiva, enfocándose en el desarrollo y la aplicación de metodologías de apilamiento de capas no planas. Este trabajo tiene como objetivo abordar las limitaciones de los procesos tradicionales de fabricación aditiva plana, tales como la baja calidad superficial, la dependencia de materiales de soporte y la flexibilidad de diseño limitada, al permitir la deposición de material a lo largo de trayectorias curvas. Además, el desarrollo de este método de fabricación aditiva plantea la necesidad de idear nuevas técnicas de diseño mecánico capaces de generar geometrías que cumplan con los requisitos específicos de este enfoque de fabricación. Al combinar metodologías no planas con sistemas robóticos de múltiples ejes, la investigación amplía las posibilidades de la fabricación aditiva en la producción de piezas estructuralmente optimizadas y geométricamente complejas.

El objetivo principal de la tesis es avanzar en el campo de la FA-Rb-NP mediante la mejora de las técnicas de laminado paramétrico, el desarrollo de sistemas robóticos para fabricación no planar y la demostración de aplicaciones industriales. La investigación introduce nuevos algoritmos de laminado adaptados a geometrías no planas, que alinean las trayectorias de deposición con la curvatura de la superficie de construcción. Este objetivo involucra el proceso de laminado y la estrategia de relleno entre dos espacios de trabajo homeomórficos interconectados mediante una transformación biyectiva. A través de esta transformación, el laminado plano realizado en uno de los subespacios se convierte en trayectorias curvas de alta complejidad geométrica cuando se invierte la transformación.

Para demostrar la viabilidad práctica de esta metodología, se diseñó y construyó un prototipo de célula robótica, integrando controladores avanzados, sistemas de extrusión adaptables y plataformas de construcción térmicamente estables. El prototipo fue validado a través de pruebas exhaustivas, asegurando la precisión en la ejecución de trayectorias y la repetibilidad en las tareas de fabricación no planar. El sistema demostró ser capaz de mantener una alineación estable de las capas, incluso bajo condiciones operativas complejas.

El segundo objetivo de la tesis es el desarrollo de una metodología de diseño para fabricación aditiva, específicamente no planar, para establecer un flujo de trabajo capaz de producir piezas adecuadas para su fabricación utilizando la célula robótica. Para lograr esto, se creó una biblioteca completa de dispositivos origami, diseñados para impresión 4D, que cambian de forma después de ser impresos en capas curvas en respuesta al estímulo de una variación en uno de sus componentes. Este caso de estudio no solo permite el desarrollo de la metodología de diseño, sino que también demuestra la amplia gama de posibilidades que pueden integrarse en la célula de fabricación aditiva no plana.

La tesis también presenta varios estudios de caso que muestran el potencial de la Fabricación Aditiva No Planar Basada en Robots en diversas aplicaciones industriales. Por ejemplo, se fabricaron stents coronarios utilizando deposición no plana para lograr propiedades mecánicas mejoradas y mayor precisión. Se crearon garfios robóticos inspirados en origami aprovechando las capacidades multimateriales para integrar componentes rígidos y blandos de manera perfecta. Se desarrolló una aplicación para el mapeo de texturas en superficies complejas

utilizando el slicer desarrollado por nosotros. Además, se produjeron matrices de conformado optimizadas para el rendimiento mecánico mediante estrategias de laminado personalizadas, demostrando la viabilidad de las técnicas no planas para herramientas industriales. Estos ejemplos resaltan la capacidad de la Fabricación Aditiva No Planar Basada en Robots para fabricar componentes complejos y de alto rendimiento con reducción de desperdicios de material y minimización de postprocesos.

Las principales conclusiones de los resultados de la tesis indican que se ha desarrollado una metodología de laminado sólida que simplifica la tarea de generar trayectorias complejas para la fabricación aditiva robótica. Además, se ha validado con éxito la implementación industrial de esta metodología y se ha modelado el error de deposición de material a través de ensayos. Estos ensayos validan la reducción de escala de los sistemas actuales que no permiten trabajar con fabricación aditiva robótica a pequeña escala.

La tesis resalta las aplicaciones industriales de la Fabricación Aditiva No Planar Basada en Robots, particularmente en la producción de componentes de alta precisión para industrias como la aeroespacial, la salud y la automotriz. Se enfatiza la necesidad de automatizar los procesos de diseño y laminado para mejorar la eficiencia y ampliar la adopción de esta tecnología. Al demostrar la capacidad de la Fabricación Aditiva No Planar Basada en Robots para mejorar la flexibilidad de diseño y el rendimiento de fabricación, este trabajo abre el camino para futuros avances. Hace un llamado a la innovación continua en sistemas robóticos, ciencia de materiales y herramientas computacionales para expandir aún más las capacidades de la fabricación aditiva no planar y hacerla viable para una amplia gama de aplicaciones industriales.

Table of Contents

Institutional Acknowledgement v
Agradecimientos personales vii
Abstract xiii
Resumen xv
List of Figures xix
List of Tables xxx
Abbreviations xxxii
Nomenclature xxxiv

1 Introduction and objectives **1**
1.1 Background 1
1.2 Motivation, objectives and structure of the PhD Thesis 6
1.2.1 Motivation of the PhD Thesis 6
1.2.2 Objectives of the PhD Thesis 7
1.2.3 Structure of the PhD Thesis 8

2 State of the art **9**
2.1 Additive manufacturing technologies 9
2.1.1 Extrusion processes in additive manufacturing 15
2.2 Non-planar additive manufacturing technologies 17
2.2.1 Multiple degrees of freedom additive manufacturing machines 19
2.2.2 Geometry representation on multi-axis additive manufacturing 21
2.2.3 Non-planar slicing algorithms 24
2.3 Design for additive manufacturing 27
2.3.1 Methodologies and tools 28
Multimaterial additive manufacturing 28
4-dimensional additive manufacturing 31
Built orientation optimization 34

3 Theoretical Framework **37**
3.1 Mathematical basis 37
3.1.1 Topology 37
3.1.2 Differential geometry 40
3.1.3 Computational geometry 41
3.2 Robotics 44

3.2.1 Robot space representation . . . 44
3.2.2 Rigid-body motion: Screw Theory . . . 47
Rotations matrices . . . 47
Homogeneous transformation matrices . . . 48
Screw axis definition . . . 50
3.2.3 Robot kinematics . . . 51
Forward kinematics . . . 51
Inverse kinematics . . . 53
3.2.4 Trajectories and paths . . . 55

4 Materials **59**
4.1 Laboratory equipment . . . 59
4.2 Software . . . 63
4.3 Materials . . . 66

5 Axisymmetric non-planar slicing and path planning strategies for robot-based additive manufacturing **69**
5.1 Methodology for Slicing Solids using Parametric Non-Planar Axisymmetric Layers . . . 70
5.1.1 Part design and optimal layer shape selection . . . 70
5.1.2 Definition of the isomorphism . . . 71
Build platform geometry definition through parametric curves . . . 72
Necessary conditions for a curve to be used as build platform . . . 72
Isomorphism definition . . . 72
Inverse transformation: $(L, \theta, H)_{\{e\}} \rightarrow (x, y, z)_{\{b\}}$ . . . 74
Direct transformation: $(x, y, z)_{\{b\}} \rightarrow (L, \theta, H)_{\{e\}}$ . . . 75
5.2 Slicing and infill strategies on non-planar surfaces . . . 76
5.2.1 Slicing algorithm in $\{e\}$ . . . 76
5.2.2 Infill procedure: functionalities and specific NPAM features . . . 79
Layer wall generation . . . 79
Infill density . . . 80
Infill direction . . . 84
Traveling trajectory design . . . 85
5.2.3 Output trajectories: robot implementation . . . 86
5.3 Construction of an industrial robot-based NPAM cell prototype . . . 87
5.4 Results and discussion . . . 90
5.4.1 Robot-based NPAM slicer . . . 90
5.4.2 Robotic Non-Planar Additive Manufacturing cell prototype . . . 93
Build platform prototype construction . . . 97
Extrusion-callibration head prototype construction . . . 100

6 Slicing space: key enabler for improved Design for Non-Planar Additive Manufacturing **105**
6.1 Methodology . . . 106
6.1.1 Using the Slicing space as design space overview . . . 106

6.1.2 Origami structures for skin expansion . . . 107
6.1.3 Design of the origami pattern library . . . 108
6.1.4 Design for non planar additive manufacturing . . . 119
6.1.5 Non planar slicing process for DfNPAM actuators . . . 121
6.2 Results and Discussion . . . 123
6.2.1 Planar resting state origami actuators library . . . 123
6.2.2 Non-planar resting state origami actuators library . . . 133

7 Applications of Robot-Based Non-Planar Additive Manufacturing 141
7.1 Coronary stents . . . 141
7.1.1 Case Study description . . . 143
Build platform definition in $\{b\}$ . . . 143
Trajectory generation in $\{e\}$ . . . 145
Built platform definition preparation . . . 147
7.1.2 Results and discussion . . . 147
7.2 Design of an origami-type robotic gripper . . . 150
7.2.1 Case study description . . . 150
$\{b\}$ as a functionality-oriented Design Space . . . 152
RBNPAM trajectory generation . . . 153
7.2.2 Results and discussion . . . 153
7.3 Texture mapping . . . 156
7.3.1 Case study description . . . 156
7.3.2 Results and discussion . . . 159
NPAM trajectory generation . . . 161
Chemical etching trajectory generation . . . 162
7.4 Additive manufactured forming die performance optimization . . . 165
7.4.1 Case study description . . . 165
7.4.2 Results and discussion . . . 170

8 Conclusions and future research proposals 177
8.1 Main achievements of the PhD Thesis . . . 177
8.2 Conclusions on advances in Robot-based Non-planar Additive Manufacturing 179
8.3 Conclusions on advances in Design for Non-planar Additive Manufacturing . 181
8.4 Future research proposals . . . 183
8.5 Environmental, social, and economic impact of the PhD Thesis . . . 188
8.6 Summary of the scientific-technological contribution of the PhD Thesis . . . 190
Articles in scientific journals . . . 190
Publications in proceedings of scientific conferences . . . 190
Final degree theses supervised . . . 190
Research projects . . . 191
8.7 Educational contribution of the PhD Thesis . . . 192

References 193

Annex A: Slicer validations through simple geometries 209

List of Figures

1.1 Industrial Robot-based AM Machines manufactured by Meltio, CEAD and CARACOL[25][26][27]. 2
1.2 Conceptual map of the development areas of RbNPAM technology. 5

2.1 Additive manufacturing technologies. a) Material Extrusion. b) Material Jetting. c) Direct Energy Deposition. d) Binder Jetting. e) Vat Photopolymerization. f) Powder Bed Fusion. g) Sheet Lamination. 10
2.2 Logarithmic-scale correlation map between printing speed s and maximum deposition accuracy in the most unfavorable direction r for the seven families of additive manufacturing. Table 2.1 serves as a guide for understanding the diagram. 12
2.3 Trend map of additive manufacturing technology development classified by levels of detail and research depth. 14
2.4 Thermal analysis of a full size car chasis MEX process for parameter optimization. a) AM machine. b) Built part. c) Experimental setup. d) Thermal image taking on the building process [113]. 16
2.5 Experiments carried out to prove the mechanical properties enhancement obtained by building curved lattices using non-planar layers. a) Test specimens. b) Manufacturing process on a 3-axis AM machine c) Tensile test. REF: Enrique Cuan-Urquizo et al. 17
2.6 Manufacturing process of cylindrical lattices using non-planar layers. a) Npn-planar trajectory generation. b) Manufacturing process on a 5-axis AM machine c) Final result [125]. 19
2.7 Additive Manufacturing machine configurations with more than five degrees of freedom: a) A fixed build platform paired with a movable extruder. b) A rotatable build platform combined with a movable extruder. c) A stationary extruder with a movable build platform. d) Both the extruder and the build platform are movable[127]. 20
2.8 Examples of multi-plane strategies to reduce support material on NPAM machines. a) Planar layers on different planes. b) Non-planar layers on different planes [131]. 21
2.9 Geometry representation formats used in Additive Manufacturing Processes [140, 141, 142, 143, 144]. a) Boundary Representation. b) Tessellated Model. c) NURBS. d) Voxel Representation. e) Point Cloud. f) Function Representation. 23

2.10 Planar printing compared to Non-planar Curvislicer part result form [14]. . . 25
2.11 Slicer workflow based on offsetted surfaces: a) 3D visualization displaying a subset of the layers. b) 3D visualization of all layers required to construct the part. c) 3D representation of the slicing surface (highlighted in cyan) extending beyond the 3D model, where no intersection occurs, marking the termination of the slicing process. d) 3D visualization of all layers necessary for constructing the UA model [153]. 26
2.12 Design for additive manufacturing process of an automotive knuckle: Simulation and final result. a) 3D design b) Outcome design from the topology optimization process. c) Outcome design from the generative design process [167]. 28
2.13 Miao et al. Design and material composition of temporomandibular joint implants [175]: a) The mandible with artificial cartilage after implantation. b) Comparison of initial and modified designs of TMJ implants and artificial cartilage. c) A finite element analysis model incorporating 10 additional material layers as artificial cartilage. d) Material property distributions within the artificial cartilage, including hard, hard-soft transitions, and functionally graded designs. e) Experimental setup for analysis and testing. 30
2.14 4d printed design with dinamic reversible mechanicm of activation [180]. a) Schematic functioning diagram. b) Experimental results. 32
2.15 Response to magnetic stimulus of various actuators used in soft robotics [185]: a) Biomimetic butterfly. b) Miura Ori pattern. c) Cross pattern. d) Ring. . . 34
2.16 Testing to validate the improvement in mechanical strength of parts using Non-Planar Additive Manufacturing (NPAM) technology: a) Geometry selected for testing. b) Experimental setup. c) Non-planar fabrication on a 5-degree-of-freedom machine. d) Comparative results showing the performance of PLA and LCP parts produced with planar techniques versus LCP parts manufactured non-planarly [187]. 35

3.1 a) S^2 topological space defined by two angular coordinates corresponding to the latitude and longitude of the point: $[-180°, 180°) \times [-90°, 90°]$. b) T^2 topological space defined by two angular coordinates: $[0°, 360°) \times [0°, 360°)$. . 38
3.2 Topological definition of the four workspaces defined referred to its orthonormal base. $\{s\}$: World space referred to the robot base, $\{j\}$: Joint space, $\{b\}$: World space referred to the robot's end-effector, and $\{e\}$: Slicing space. 39
3.3 Cubic B-spline representation with control polygon defined by points: $P_0 = (0, 0)$, $P_1 = (1, 2)$, $P_2 = (3, 3)$, and $P_3 = (4, 1)$. Bernstein polynomials associated to a cubic B-spline definition. 42
3.4 a) Spline concatenation with C^0 continuity. b) Spline concatenation with C^1 continuity. c) Spline concatenation with C^2 continuity. 43
3.5 Convex hull and alpha shape polygons associated to the 2D point set S. . . . 44
3.6 Robot frames definition, Global space frame, $\{s\}$; end-effector frame, $\{b\}$; and link associated frames $\{1, 2, ..., n\}$. Joint identification: $j_{1,2,...,n}$. Joint position coordinate $\theta_{1,2,...,n}$ 45
3.7 A) Planar 2R robot workspace referred to $\{s\}$ in light blue. B) Planar 3R robot workspace referred to $\{s\}$ in light blue. 46

3.8 Representation of $\{s\}$, $\{a\}$, and $\{b\}$ frames with the same origin in o. . . . 47
3.9 Representation of $\{a'\}$, and $\{a''\}$ as the result of pre-multiplying and post-multiplying the rotation operation $\mathbf{Rot}(\hat{x}, 90)$ with $\mathbf{R}_{sa}$. 48
3.10 Relative position and orientation of frames $\{s\}$, $\{a\}$, and $\{b\}$ 49
3.11 Graphical result of pre-multiplying and post-multiplying the displacement operator $\mathbf{T}(\mathbf{Rot}(\hat{y}, 90°), (1, 0, 0)^T)$ and the relative position matrix $\mathbf{T}_{sb}$. . . . 50
3.12 Graphical representation of a Screw axis. 51
3.13 Reference frames for $3R$ plane robot. The lengths of links 1 and 2 are respectively L_1, and L_2. Frames $\{s\}$ and $\{1\}$ have the same origin but are shown separately for clarity. 52
3.14 Comparison between a straight-line path defined in Joint space $\{j\}$ and World space $\{s\}$. 56
3.15 Example of straight-line path interpolation from nine given waypoints. The green line shows the objective path while the dash black straight-lines its interpolation from the given waypoints. Note that waypoints in $\{s\}$ are defined in both position and orientation. 57

4.1 UR10 CB3 collaborative robot. 60
4.2 SICK laser distance sensor OD5 - 30W05. 62
4.3 Mitutoyo Crysta-Plus M544. 63
4.4 BIQU H2V2S extruder. 64

5.1 Schematic diagram of the methodology presented. 70
5.2 a) Diagram of a helical spring under a compression load, b) typical cross-section stress diagram of a compressed helical spring, c) conventional 3 axis AM slicing of a helical spring, d) optimal NPAM slicing for a helical spring, e) a cylindrical helical spring sliced following cylindrical layers and f) an hourglass-shaped helical spring sliced following hourglass-shaped layers. Figures e) and f) depict the springs in cross-section to appreciate the deposition of the layers. 71
5.3 Schematic representation of the trajectory generation workflow. Of note, the STL model and the build platform shape are required as inputs for the algorithm, resulting in the 6 DoF pose list trajectory to be executed by the robotized station. 71
5.4 a) Example of a base piecewise-defined parametric curve fulfilling all mathematical conditions. b) Example of a G^2 base piecewise-defined parametric curve with cusps. For both examples, left-hand side diagrams represent the base curve in solid red line, its control polygon in dashed red line and its curvature comb in blue. The center diagrams represent the build platform (yellow) when the based curve is used as the generatrix for the surface of revolution. Lastly, the right-hand side diagrams represent in cyan shade the areas of printable locations for a cross section of the build platform. 73
5.5 Schematic representation of an isomorphism between Task space $\{b\}$ and slicing $\{e\}$ coordinate systems given an arbitrary revolved curve $\mathbf{\Gamma}(u)$ (solid blue) as a build platform (yellow). 74

5.6 Schematic representation of the isomorphism, depicting the transformation of coordinates between the Task coordinate system $\{b\}$ (left-hand diagram) and the slicing coordinate system $\{e\}$ (right-hand diagram). 75

5.7 Examples of a complete transformation of a set of points in $\{e\}$ given a base curve $\mathbf{\Gamma}$. a) Straight line base curve $\mathbf{\Gamma}$, b) Barrel-shaped base curve $\mathbf{\Gamma}$. 77

5.8 a) Non-filtered STL part model after the isomorphism onto $\{e\}$. b) Slicing of non-filtered STL part model. c) Filtered STL part model after the isomorphism. d) Slicing of filtered STL part model. The yellow shaded rectangles indicate the regions where the inherited Cartesian STL connectivity matrix creates faces wrapping around the θ axis and slicing errors. 78

5.9 Helical spring coil converted to $\{e\}$ sliced by a plane λ built parallel to $L\theta$-plane. 78

5.10 Helical spring coil layer in $\{e\}$ standard double wall along its entire perimeter. 80

5.11 Axysimmetric cylinder layer in $\{e\}$ seam wall on $\theta = 0$ and $\theta = 2\pi$. 80

5.12 Axysimmetric cylinder layer in $\{e\}$ seam wall based on layer superposition in the vicinity of $\theta = 0$. a) shows the even layers layout, $n \in \mathbb{Z}^+$. b) shows the odd layers layout, $n \in \mathbb{Z}_{\geq 0}$. 81

5.13 a) Cylinder laminated by cylindrical layers. b) Parameter definition of the layers viewed from the $x_b y_b$-plane. c) $d\theta$ definition for two pairs of equidistant points in each layer λ_1 and λ_2. 81

5.14 Surface curvature and deformation along the L and θ directions. a) Curvature κ_L along the build plate. b) Curvature κ_θ along the build plate. c) Linear deformation [%] along the L-direction. d) Linear deformation [%] along the θ-direction. 83

5.15 Methodology for filling layer contours in a specified direction $\mathbf{n}$ on a helical coil layer: a) inward offset of the contour; b) definition of lines with an assigned density along the specified direction $\mathbf{n}$; c) identification of intersections between the inner contour and the generated lines; d) trajectory definition. The yellow line represents the first iteration of contour filling, the green line indicates the second iteration, and the red line denotes a travel displacement between the two trajectories. 85

5.16 Schematic representation of the transformation operations to locate the part under the extrusion nozzle. 87

5.17 Steps for the implementation of the theoretical basis in a robotized station. With respect to (w.r.t.). 88

5.18 Representation of RFs defined in the robotized station. 89

5.19 Planarly printed case studies. a) Cylindrical spring case, build platform control polygon and resulting test artifact, b) Hourglass shaped spring, build platform control polygon and resulting test artifact. The case studies were manufactured using poly(lactic acid) (PLA), specifically, Ultrafuse PLA from BASF. 90

5.20 Instrumented robotized station utilized for testing. 91

5.21 Slicer workflow. 92

5.22 Trajectory generation for a cylindrical spring coil. a) STL file and print bed in World space referred to $\{b\}$. b) STL file converted to Slicing space referred to $\{e\}$. c) laminated solid in $\{e\}$ with its defined trajectories: $\mathcal{X}_{\{e\}}$. d) laminated solid in $\{b\}$ with its defined trajectories: $\mathbf{X}_{\{b\}}$. Normal vectors in black represents the extruder orientation. 93
5.23 Trajectory generation for an Hourglass-shapped spring coil. a) STL file and print bed in World space referred to $\{b\}$. b) STL file converted to Slicing space referred to $\{e\}$. c) laminated solid in $\{e\}$ with its defined trajectories: $\mathcal{X}_{\{e\}}$. d) laminated solid in $\{b\}$ with its defined trajectories: $\mathbf{X}_{\{b\}}$. Normal vectors in black represents the extruder orientation. 94
5.24 a) Planarly generated trajectories of the cylindrical case study in the slicing coordinate system $\{e\}$, first layer. b) Planarly generated trajectories of the hourglass-shaped case study in the slicing coordinate system $\{e\}$, first layer. c) Parametric 6 DoF pose list in $\{bp\}$, first layer. d) Parametric 6 DoF pose list in Cartesian coordinate system $\{bp\}$, first layer. For this case study, only the first 3000 points were represented for diagram clarity. 95
5.25 Measured distance between $\{TCP\}$ and $\{ext\}$ along trajectory execution. a) cylindrical spring case, b) hourglass-shaped case. 96
5.26 Repeatability in the trajectory execution: a) Cylindrical spring case. b) Hourglass-shaped case. 96
5.27 Robot-based NPAM built platform final design. a) Model. b) Manufactured prototype. 98
5.28 COMSOL Multiphysics thermal analysis under working condition. Axial cross section. 98
5.29 a) Built platform thermal operation conditions test setup. b) Temperature results under operating conditions in different build platform areas. 99
5.30 CAD model of the extrusion head designed with two extruders, calibration laser, and protective structure. 102
5.31 Final design of the robot-based non-planar additive manufacturing cell. . . . 102
5.32 Final assembly of the robot-based non-planar additive manufacturing cell consisting of: robot manipulator from Universal Robots UR10, movable build platform mounted on the robot's TCP, and fixed extrusion head anchored to the workbench. 103

6.1 Verification of bijective areas for three curve cases with both positive and negative curvature. a) C^2 continuity. b) C^1 continuity. c) C^0 Continuity . . 106
6.2 Proposed fold design for the origami patterns. a) Fold zone 1. b) Fold zone 2. c) Fold zone 3. 109
6.3 Proposed methodology for transitioning from origami patterns to basic design geometry. a) Base origami pattern. b) Folding zone definition. c) Facet adjustment. 110
6.4 a) Yoshimura pattern definition. b) Yoshimura tesselation. 111
6.5 a) Kresling pattern definition. b) Helicoidal Kresling tesselation. c) Inverted Kresling tesselation. 113
6.6 a) Accordion fan pattern definition. b) Accordion fan tesselation. 113

6.7 a) Miura-ori pattern definition. b) Miura-ori tesselation. 114
6.8 Square twist pattern definition. 115
6.9 Simulation process followed to understand the behavior under stresses in each of the designed folding zones. Folding zone 2. a) Test specimen design. b) Test specimen meshing and material properties assignation. c) Fixed support with free rotation on the upper right vertex. d) Forced displacement on the $x-$axis direction on the lower left vertex. 118
6.10 Specimens tested for activation through degradation in an aquatic environment. a) Folding zone 1. b) Folding zone 2. c) Folding zone 3. d) Origami pattern built up using folding zone 1 joints. 119
6.11 Generation of workspace from deformation modeled by simulation. a) deformation curvature. b) build platform and design space in $\{e\}$. 120
6.12 Bijection check of the designed part on the selected build platform. 121
6.13 Design process. a) Original part in $\{b\}$. b) build platform used to define $\{e\}$. c) Deformed and located part to fit in $\{e\}$. d) Final design result in $\{b\}$ . . . 122
6.14 Slicing operations when parts have been already designed for NPAM. 122
6.15 Yoshimura pattern design and fabrication results. a) Folding zone 1. b) Folding zone 2.1. c) Folding zone 3. d) Manufactured Yoshimura pattern with folding zone 1. 124
6.16 Kresling pattern design and fabrication results. a) Folding zone 1. b) Folding zone 2.1. c) Folding zone 3. d) Manufactured Kresling pattern with folding zone 1. 124
6.17 Accordion fan pattern design and fabrication results. a) Folding zone 1. b) Folding zone 2.1. c) Folding zone 3. d) Manufactured Accordion Fan pattern with folding zone 1. 125
6.18 Miura-ori pattern design and fabrication results. a) Folding zone 1. b) Folding zone 2.1. c) Folding zone 3. d) Manufactured Miura-ori pattern with folding zone 1. 125
6.19 Square Twist pattern design and fabrication results. a) Folding zone 1. b) Folding zone 2.1. c) Folding zone 3. d) Manufactured Square Twist pattern with folding zone 1. 126
6.20 FEM analysis of folding zone 1 with $27mm$ length.a)Equivalent stress. b) Equivalent elastic strain. c) Maximum principal elastic strain. 127
6.21 FEM analysis of folding zone 2.1 with $24mm$ length.a)Equivalent stress. b) Equivalent elastic strain. c) Maximum principal elastic strain. 129
6.22 FEM analysis of folding zone 2.2 with $21mm$ length.a)Equivalent stress. b) Equivalent elastic strain. c) Maximum principal elastic strain. 130
6.23 FEM analysis of folding zone 2.3 with $27mm$ length.a)Equivalent stress. b) Equivalent elastic strain. c) Maximum principal elastic strain. 132
6.24 Design process of Folding Zone 1 with double curvature. a) Original part in $\{b\}$. b) Build platform used to define $\{e\}$. c) Deformed and located part to fit in $\{e\}$. d) Final design result in $\{b\}$ 133
6.25 Design process of Folding Zone 2 with single curvature. a) Original part in $\{b\}$. b) Build platform used to define $\{e\}$. c) Deformed and located part to fit in $\{e\}$. d) Final design result in $\{b\}$ 134

6.26 Design process of Folding Zone 2 with double curvature. a) Original part in $\{b\}$. b) Build platform used to define $\{e\}$. c) Deformed and located part to fit in $\{e\}$. d) Final design result in $\{b\}$ 135
6.27 Design process of Folding Zone 2 with axis misalignment. a) Original part in $\{b\}$. b) Build platform used to define $\{e\}$. c) Deformed and located part to fit in $\{e\}$. d) Final design result in $\{b\}$ 136
6.28 Design process of an Accordion Fan on a conical build platform. a) Original part in $\{b\}$. b) Build platform used to define $\{e\}$. c) Deformed and located part to fit in $\{e\}$. d) Final design result in $\{b\}$ 137
6.29 Design process of an Accordion Fan on a spring-shaped bed. a) Original part in $\{b\}$. b) Build platform used to define $\{e\}$. c) Deformed and located part to fit in $\{e\}$. d) Final design result in $\{b\}$ 137
6.30 Design process of a Yoshimura pattern on a Hollow-shaped build platform. a) Original part in $\{b\}$. b) Build platform used to define $\{e\}$. c) Deformed and located part to fit in $\{e\}$. d) Final design result in $\{b\}$ 138
6.31 Design process of a Kresling pattern on a Cylindrical-shaped build platform. a) Original part in $\{b\}$. b) Build platform used to define $\{e\}$. c) Deformed and located part to fit in $\{e\}$. d) Final design result in $\{b\}$ 139
6.32 Design process of a Square Twist pattern on a Spherical-shaped build platform. a) Original part in $\{b\}$. b) Build platform used to define $\{e\}$. c) Deformed and located part to fit in $\{e\}$. d) Final design result in $\{b\}$ 139
6.33 Design process of a Miura Ori pattern on a Spherical-shaped build platform. a) Original part in $\{b\}$. b) Build platform used to define $\{e\}$. c) Deformed and located part to fit in $\{e\}$. d) Final design result in $\{b\}$ 140
6.34 DfNPAM patterns presented on their built platform. a) Square Twist on spherical build platform. b) Miura Ori on spherical build platform. c) Miura Ori on double curvature build platform. d) Kresling on a cylindrical platform. 140

7.1 s) Stent's $\{model\}$ reference system with the Z axis as the axis of symmetry. b) Revolution build plate control polygon referred to the xz-plane. 143
7.2 Printable area associated to the proposed build plate defines as the green surface. 145
7.3 Complete build plate and slicing surfaces representation for the defined generatrix. 145
7.4 Complete slicing process. The points and connectivity matrices defined in the STL geometry in $\{b\}$ are transformed to $\{e\}$. Once transformed the new geomtry is sliced. The generated trajectories are then transformed into $\{b\}$ obtaining the final toolpath (both points and tool orientation). 146
7.5 Manufacturing set up consisting of built platform, PVA support and stent. THe model has been adapted to be printed on the real built platform in Figure 5.27. 147
7.6 Stent's robot based NPAM trajectories defined in $\{e\}$. Slicing surface normal vectors on each waypoint shown in blue. For clarity, only the first layer has been represented. 148
7.7 Examples of different grids applied to the stent shape and build platform proposed in this case study. 148

7.8 a) PVA Support defined in Figure 7.5 transformed to $\{e\}$. b) Plane trajectories defined by the slicer in $\{e\}$. 149
7.9 Left-hand side: design workflow for multi-material RBNPAM soft robotics grippers. Right-hand side: selected parameters for the present case study. . . 151
7.10 Example of the Yoshimura origami design proposed for the present case study. On the top side, CAD design and in-house manufactured prototype by multi-material MEX. On the bottom side, a detail of the interlocking between the stiff material (poly-(lactic acid), in black) and the compliant material (thermoplastic polyurethane 95A, in red). 151
7.11 a) CAD model of the compliant mechanism based on a Yoshimura-based origami pattern. b) Model after θ-scaling. c) Model positioned in $\{s\}$ with $L_{centroid} = L_{curve}/2$. 153
7.12 Representation of the build platform (in yellow shade), with the Cartesian part located on it. The red shaded areas indicate the unreachable areas, in this case, with a multiplicity of homomorphisms greater than 1, whereas the blue-striped areas show the reachable region. 154
7.13 Cartesian models located on their build platforms. a) Cylinder case. b) Double curvature case. c) Hollow case. 155
7.14 Detail of cross-section of planar toolpaths made by Ultimaker Cura. Shell trajectories in red, infill (100%) trajectories in orange. 155
7.15 RBNPAM trajectory (red line) for the double curvature case (build platform in yellow). Only the first 250000 points are represented for clarity. 156
7.16 Shark-skin texture geometry used in the execution of the case study. 158
7.17 Bijection evaluation in the proposed curved design spaces. a) Positive curvature surface. b) Negative curvature. c) Combined curvature surface. Red areas represent non-bijective regions of the space transformation. 158
7.18 Texture mapped in the outter side of four different surfaces: a) Cyllinder, b) Positive curvature surface, c) Negative curvature surface, and d) combined curvature surface. 160
7.19 Texture mapped in the inner side of a cylindrical build platform. 161
7.20 The trajectory generation and transformation process prior to final surface mapping. a) planar trajectories in Carthesian space designed by Cura. b) Non scaled planar trajectories in the slicing space $\{e\}$. c) Scaled planar trajectories in the slicing space $\{e\}$ according to its final platform transformation. 162
7.21 Final trajectories displayed on the Carthesian space referred to the robot's TCP, $\{b\}$. a) Cyllinder, b) Positive curvature surface, c) Negative curvature surface, and d) combined curvature surface. 163
7.22 Point homogeneous distribution for shark fin texture chemical etching on a convex surface. a) Initial seed in $\{e\}$, b) Final distribution in $\{e\}$, c) Initial seed in $\{b\}$, and d) Final distribution in $\{b\}$. 164
7.23 Chemical etching generated trajectory to generate shark.fin textures on a convex surface. 165
7.24 Sheet metal forming validation. Cylindrical shape formed using a Tough PLA matrix using 0.5$[mm]$ thicknes AW1050 aluminum sheet. 166
7.25 Sheet metal forming part design. 167

7.26 Tooling used in the deep-drawing process of the target part. 168

7.27 Load distribution over the volume of the studied component. Shear stress on the deep-drawing surface is shown in red, and radial compression of the component is shown in orange. 169

7.28 Layer distribution on component 3. a) Planar additive manufacturing. b) Non-Planar additive manufacturing. 170

7.29 Result of the lamination of component 3. a) STL part positioned relative to its print bed. b) STL part transformed into the slicing space $\{e\}$. c) Laminated solid with trajectories generated in $\{e\}$. d) Printing trajectories in the world space $\{b\}$. 171

7.30 Detail of the lamination result for the first four layers of component 3. Odd-numbered layers are shown with infill oriented in the direction favorable for resisting surface shear stress, while even-numbered layers form concentric rings to support the compressive forces on the component. 172

7.31 Determination of the bijectivity area of the transformation associated with the base curve proposed for the case study development. The non-bijective region is highlighted in red. 173

7.32 Placement of component 3 on the curved build platform for non-planar additive manufacturing. The robot grasping side and the removal direction are shown. 174

8.1 Geodesically equidistant points in curved surfaces as base of TPMS in NPAM future implementation. Convex build platform. 184

8.2 Geodesically equidistant points in curved surfaces as base of TPMS in NPAM future implementation. Double curvature build platform. 184

8.3 Cylindrical sector transformed into a space defined by a non-planar, non-axisymmetric base surface. 185

8.4 Optimization process for the racing car knuckle build platform. The layers are constructed by offsetting the build platform and aligned with the principal stresses in the material's preferred direction of anisotropy for the specific load case. 186

8.5 Automated identification of non-bijective regions through offset curve intersections. 187

6 Trajectory generation for half of a cylinder using cylindrical layers. a) STL file and print bed in World space referred to $\{b\}$. b) STL file converted to Slicing space referred to $\{e\}$. c) laminated solid in $\{e\}$ with its defined trajectories: $\mathcal{X}_{\{e\}}$. d) laminated solid in $\{b\}$ with its defined trajectories: $\mathbf{X}_{\{b\}}$. Normal vectors in black represents the extruder orientation. 209

7 First four layers of the half cylinder on a cylindrical build plate case. Layers 1 and 2 with 100% infill built on perpendicular directions and layers 3 and 4 with 20% infill also built in perpendicular directions. 210

8 Trajectory generation for a cylinder using cylindrical layers. a) STL file and print bed in World space referred to $\{b\}$. b) STL file converted to Slicing space referred to $\{e\}$. c) laminated solid in $\{e\}$ with its defined trajectories: $\mathcal{X}_{\{e\}}$. d) laminated solid in $\{b\}$ with its defined trajectories: $\mathbf{X}_{\{b\}}$. Normal vectors in black represents the extruder orientation. 211
9 Trajectory generation for a truncated cone using conical layers. a) STL file and print bed in World space referred to $\{b\}$. b) STL file converted to Slicing space referred to $\{e\}$. c) laminated solid in $\{e\}$ with its defined trajectories: $\mathcal{X}_{\{e\}}$. d) laminated solid in $\{b\}$ with its defined trajectories: $\mathbf{X}_{\{b\}}$. Normal vectors in black represents the extruder orientation. 212
10 Trajectory generation for half hourglass shaped model sliced with a hourglass-shape layers. a) STL file and print bed in World space referred to $\{b\}$. b) STL file converted to Slicing space referred to $\{e\}$. c) laminated solid in $\{e\}$ with its defined trajectories: $\mathcal{X}_{\{e\}}$. d) laminated solid in $\{b\}$ with its defined trajectories: $\mathbf{X}_{\{b\}}$. Normal vectors in black represents the extruder orientation. 213
11 Trajectory generation for a cube model sliced with a hourglass-shape layers. a) STL file and print bed in World space referred to $\{b\}$. b) STL file converted to Slicing space referred to $\{e\}$. c) laminated solid in $\{e\}$ with its defined trajectories: $\mathcal{X}_{\{e\}}$. d) laminated solid in $\{b\}$ with its defined trajectories: $\mathbf{X}_{\{b\}}$. Normal vectors in black represents the extruder orientation. 214

List of Tables

2.1 Summary table of nomenclature and references for the generation of the comparative diagram of printing speed and accuracy for the seven existing families of additive manufacturing. 11

4.1 Specifications of the UR10 CB3 collaborative robot, including geometrical parameters [197]. 61
4.2 Specifications of the BIQU H2V2S Extruder [200]. 62

5.1 Flatness tolerance results for the manufactured part faces referred as shown in Figure 5.27.Values of 12 points dataset and 4 repetitions on each plane. . . . 100
5.2 Perpendicularity tolerance between contiguous faces. Results for the manufactured part faces referred as shown in Figure 5.27.Values of 12 points dataset and 4 repetitions on each plane. 100
5.3 Paralelism between faces of the external and internal cubes. Results for the manufactured part faces referred as shown in Figure 5.27.Values of 12 points dataset and 4 repetitions on each plane. 100

6.1 Design space definition in $\{e\}$ for curved fold zones design. 120
6.3 Simulation results for the three evaluated lengths of folding zone 1: applied force up to the yield of PVA, maximum principal stress, equivalent elastic strain, and maximum principal strain 127
6.4 Simulation results for the three evaluated lengths of folding zone 2.1: applied force up to the yield of PVA, maximum principal stress, equivalent elastic strain, and maximum principal strain 128
6.5 Simulation results for the three evaluated lengths of folding zone 2.2: applied force up to the yield of PETG, maximum principal stress, equivalent elastic strain, and maximum principal strain 130
6.6 Simulation results for the three evaluated lengths of folding zone 2.3: applied force up to the yield of PETG, maximum principal stress, equivalent elastic strain, and maximum principal strain 131

7.1 Parametric build platform's generatrix curve, Γ, defined in the xz-plane . . . 144
7.2 Definition of composite Bézier splines for build platforms 152

Abbreviations

2PP Two-Photon Polymerization

3-FFF More than 3 Degrees of Freedom Fused Filament Fabrication machines

ABS Acrylonitrile Butadiene Styrene

AM Additive Manufacturing

BJ Binder jetting

CAD Computer Aided Design

CEX Contour Crafting Extrusion

CF-PLA Carbon-fiber-reinforced PLA

DED Direct Energy Deposition

DfAM Design for Additive Manufacturing

DFFF Drone based Fused Filament Fabrication

DfNPAM Design for Non-Planar Additive Manufacturing

DLP Digital Light Processing

DMD Direct Metal Deposition

DMLS Direct metal Laser Sintering

DoF Degrees of Freedom

EBM Electron Beam Melting

FEA Finit Element Analysis

FFF Fused Filament Fabrication

(H) Helical joint

LF-FFF Large Format Fused Filament Fabrication

LMD Laser Metal Deposition

LOM Sheet Lamination

MEX Material Extrusion

MFFF Micro scale Fused Filament Fabrication

MJ Material Jetting

NPAM Non-Planar Additive Manufacturing

(P) Prismatic joint

PBF Powder Bed Fusion

PETG Glycol-Modified Polyethylene Terephthalate

PHP Vat Photopolymerization

PJ Polyjet

PLA Poly(lactic acid)

PLC Programmable Logic Controller

PoE Power of Exponential formula

PVA Polyvinyl Alcohol

(R) Revolute joint

RBNPAM Robot-Based Non-Planar Additive Manufacturing

RF Reference Frame

(S) Spherical joint

SLA Stereolithography

SLM Selective Laser Melting

SLS Selective Laser Sintering

SMP Shape memory Polymer

STL Stereolithography format

TCP Tool Center Point

TCP/IP Transmission Control Protocol/Internet Protocol

TPU Thermoplastic Polyurethane

UTS Ultimate Tensile Strength

WAAM Wire Arc Additive Manufacturing

Nomenclature

α Alpha shape definition parameter.

$\mathbf{\Gamma}$ Parametric notation of the generatrix curve. Could be find as a function of parameters t o u.

ϵ Maximum allowed error while solving the inverse kinematics problem.

$\mathbf{\Theta}$ Joint position vector of a robotic manipulator.

$\mathbf{\Theta}_H$ Joint position vector of a robotic manipulator at its *Home* position.

κ Curvature.

λ Slicing plane.

ρ Radius of curvature.

∇ Gradient operator.

∇^2 Second order Gradient operator.

$\mathbf{B}(t)$ Bezier curve as function of parameter t.

$b_{i,n}(t)$ Bernstein polynomials of grade n as function of parameter t.

$\mathcal{B}(\omega, v)$ Screw Axis defining a rotation ω together with translation v along its axis referred to $\{b\}$.

c_i i-constraint.

e Existing error between the calculated position and the target position while solving the inverse kinematics problem.

$\mathbf{e}_\theta$ Unit vector along the z-axis.

$\mathbf{e}_H$ Unit vector normal to the generatrix curve.

$\mathbf{e}_L$ Unit vector tangent to the generatrix curve.

H Height in the normal direction to the generatrix curve at each point.

$\{i\}$ Notation for a generic frame i where a Topological Space is referred.

j_i i-joint.

$\mathbf{J}$ Jacobian matrix of the robotic manipulator.

L Length of a curve.

$L(u)$ Distance from the curve's origin to the point defined by the parameter u along the curve.

m Degrees of freedom of a topological space.

$\mathbf{M}$ Homogeneous Transformation matrix of $\{b\}$ with respect to $\{s\}$ at the robot's *Home* position.

$\mathbf{n}$ Vector that defines the layer infill orientation on the $L\theta$-plane.

$\mathbf{p}_{ij}$ Position vector of the frame j with respect of frame i.

$\mathbf{P}_0, \mathbf{P}_1, \ldots, \mathbf{P}_n$ Control polygon points of a B-spline.

R Radius of curvature of a build platform on the xy-plane direction.

$\mathbf{R}_{ij}$ Orientation of the frame j with respect to i.

$\mathbf{Rot}(\hat{\omega}, \theta)$ Rotation operator. Used to rotate an angle θ along the $\hat{\omega}$ axis.

$\mathcal{S}(\omega, v)$ Screw axis defining a rotation ω together with translation v along its axis referred to $\{s\}$.

$\mathbf{T}_{ij}$ Homogeneous Transformation matrix of the frame j with respect to i.

$\mathbf{X}(t)$ Homogeneous Transformation matrix of the frame $\{b\}$ with respect to $\{s\}$ along time.

$\mathbf{X}_{\{b\}}$ Slicer output trajectories with respect to $\{b\}$.

$\mathbf{X}_d$ Target Homogeneous Transformation matrix of the frame $\{b\}$ with respect to $\{s\}$.

$\mathcal{X}_{\{e\}}$ Slicer output trajectories with respect to $\{e\}$.

Chapter 1

Introduction and objectives

1.1 Background

Additive Manufacturing (AM) is reshaping traditional industries, offering enhanced customization, efficiency, and sustainability. By 2024, its market value is projected to surpass $15.8 billion, reflecting its transformative potential [1][2]. In the aerospace sector, AM enables the production of lightweight, high-performance components, such as intricate engine parts, while reducing waste by up to 90% [3]. Similarly, the healthcare industry leverages AM for bespoke implants and prosthetics, achieving patient-specific solutions that reduce surgery preparation times [4][5]. The automotive sector benefits from AM through rapid prototyping and the creation of complex tooling, cutting development timelines and facilitating design innovations[6][7].

AM's applications extend to the energy sector, where intricate heat exchangers and turbine components are fabricated with increased efficiency. AM allows for improved thermal performance and shorter lead times, reducing the environmental impact of energy production processes. In the maritime industry [8], Wire Arc Additive Manufacturing (WAAM) techniques fabricate large-scale ship components, such as propellers, improving production flexibility and reducing the need for extensive inventories [9]. Furthermore, the consumer electronics industry benefits from AM in designing complex geometries for housings, heat sinks, and functional prototypes, reducing assembly times while enabling greater product personalization [10][11][12].

Following the rapid growth and adoption of conventional additive manufacturing techniques—characterized by the stacking of planar material layers in a fixed direction—new approaches have emerged aiming to enhance the versatility of this conformal manufacturing method. Non-Planar Additive Manufacturing (NPAM) offers significant advantages over traditional layer-by-layer AM processes by addressing key limitations of planar printing[13]. It involves the deposition of non-planar material layers, either uniformly or adaptively. One notable benefit is the improved surface finish of parts. By enabling material deposition along curved surfaces or orientations that align with the part's contours, NPAM reduces or even eliminates the stair-step effects inherent to planar methods, thereby minimizing the need for

post-processing[14]. Additionally, NPAM significantly reduces the use of support material, making the process more sustainable and cost-efficient[15].

Furthermore, NPAM has opened new avenues for structural optimization of manufactured parts by accommodating anisotropy in material properties. However, while promising, this approach has faced considerable limitations in fully leveraging its potential for advanced structural optimization.

The integration of robotics into AM has enabled NPAM, overcoming limitations of traditional layer-by-layer deposition[16]. Robot-Based NPAM (RbNPAM) employs multi-axis robots to deposit material onto curved or freeform surfaces, enhancing part strength by eliminating layer delamination[17][18]. Industries increasingly explore RbNPAM to manufacture components with tailored mechanical properties, such as multi-functional prosthetics and aerospace structures with optimized aerodynamic profiles[19][20][21]. Nevertheless, synchronization between robotic arms, extrusion systems, and slicing software poses technical challenges, necessitating further research[22][23].

RbNPAM expands the creative possibilities for complex geometries. It allows for the fabrication of features like overhangs, freeform surfaces, and variable-thickness structures without requiring extensive support material. This capability reduces material waste, production time, and costs while facilitating the creation of custom designs for applications in medical implants and architectural components[24]. Additionally, the ability to print directly on existing curved parts makes NPAM ideal for repair operations, or pre-manufactured parts coatings.

Figure 1.1: Industrial Robot-based AM Machines manufactured by Meltio, CEAD and CARACOL[25][26][27].

Several machines have been designed to enable NPAM, utilizing robotic or traditional AM technologies. Robotic systems such as multi-axis robotic arms have been adapted for non-planar deposition, offering flexibility in material placement and orientation. These systems, often equipped with extruders for polymers or lasers for metal-based processes, enable the

precise deposition of material on curved surfaces. Figure 1.1 showcases examples of large-scale machines currently available on the market.

Designing and operating NPAM machines presents several technical challenges, primarily due to the complexity of controlling multi-axis robotic systems and ensuring material deposition on freeform geometries[28]. The first challenge is related to the mechanical limitations of existing robotic arms, which need to achieve high precision across multiple axes while maintaining consistency in the layer deposition[29][30][31]. Achieving this level of precision requires sophisticated control algorithms and high-performance hardware capable of continuously adjusting the machine's movements in real time, as well as ensuring stable material extrusion or deposition under varying orientations. Additionally, the development of specialized print heads or extruders for non-planar printing must overcome issues related to nozzle orientation and material flow consistency when printing on curved surfaces, particularly at angles that are difficult for traditional Material Extrusion (MEX) or Direct Energy Deposition (DED) machines to manage[32].

Another significant challenge lies in the design of optimal printing trajectories for these complex geometries. Traditional slicing algorithms, which assume planar layer-by-layer deposition, need to be adapted or replaced to handle the curvature of non-planar surfaces[23]. Path planning algorithms must account for intricate geometric shapes, material behavior under different conditions, and the robot's dynamic capabilities to prevent errors such as over-extrusion, gaps, or misalignment. Moreover, the need to automate trajectory generation while ensuring high-quality prints without excessive computational cost or time is crucial[33]. Advanced machine learning and computational design tools are often employed to optimize the slicing strategy for non-planar geometries, but these solutions are still in development and require further validation across different industries[34].

In addition to these technical obstacles, the integration of robotic systems with traditional AM machines poses a challenge in terms of synchronization. Ensuring seamless operation between the robotic arm's kinematics and the material deposition system requires sophisticated software solutions that manage multiple feedback loops, real-time adjustments, and error correction[35]. Furthermore, quality control for non-planar prints remains a hurdle, as defects may not be immediately visible and may require additional layers of post-processing inspection and testing to ensure the printed components meet industry standards[36].

From a materials perspective, the development of high-performance AM-compatible materials such as functionally graded polymers and hybrid composites broadens RbNPAM's potential. For example, the introduction of carbon-fiber-reinforced polymers in automotive applications improves stiffness and reduces weight[37]. RbNPAM introduces significant advantages for designing materials with internal anisotropy, which is critical in various engineering applications. One of the most notable advantages is the ability to tailor material properties within a single part, enabling the creation of parts with gradients in strength, stiffness, and other mechanical properties, thus optimizing their performance[38]. Unlike traditional manufacturing methods, RbNPAM allows the deposition of material layers with specific orientations, making it possible to design structures with customized anisotropic properties, where the material's behavior can be controlled depending on the applied load directions[39][40].

As a result of the evolution of additive manufacturing technologies and the materials utilized in these processes, Design for Additive Manufacturing (DfAM) emerges as a pivotal methodology[41]. It encompasses methodologies and tools aimed at optimizing the design process to leverage the unique advantages of AM, such as geometric freedom, material efficiency, and the ability to produce complex internal structures[42]. Research in DfAM has demonstrated its capacity to optimize mechanical properties, integrate multi-functional features, and reduce material waste by eliminating the constraints of subtractive manufacturing. Several studies have provided frameworks for applying DfAM principles across diverse domains, emphasizing the importance of topology optimization, lattice structure integration, and direct digital manufacturing pathways.

Building on these foundations, Design for Non-Planar Additive Manufacturing (DfNPAM) extends DfAM principles into the realm of non-planar deposition, addressing the limitations of traditional layer-by-layer processes. Non-planar AM introduces significant opportunities for improving surface quality, reducing stair-step artifacts, and aligning deposition paths with stress trajectories to enhance structural performance. Recent studies highlight the potential of DfNPAM to enable adaptive material deposition on curved or irregular geometries, allowing for better utilization of anisotropic material properties[43]. DfNPAM also leverages advanced computational tools to model complex deformation behaviors, ensuring geometric and mechanical accuracy in parts fabricated on non-planar platforms. This adaptation not only expands the design space but also promotes sustainable practices by minimizing support material and post-processing requirements, as validated by experimental studies on robot-based non-planar systems.

Through the integration of these principles, DfNPAM has proven itself to be a transformative approach for applications requiring high precision and adaptability, such as 4D printing, embedded sensing systems, and customized biomedical devices[44][45]. Its continuous evolution is driven by interdisciplinary advancements in computational geometry, robotics, and material science, paving the way for more efficient and versatile manufacturing solutions[44][46][47].

However, there remains a critical need for the development of small-scale RbNPAM technologies to broaden their applicability in manufacturing smaller components, ranging from high-value-added parts to everyday industrial and consumer items. Current solutions, due to their precision limitations, are primarily suitable for working with large-scale components. Furthermore, the automation of the design and slicing processes for these parts is essential to enable their industrial scalability and streamline their adoption across various sectors.

Figure 1.2 presents a global roadmap outlining the key development areas required to scale down the product size in RbNPAM technology. These include the advancement of design methodologies adapted to non-planar additive manufacturing, the slicing of non-planar solids, and the development of machinery capable of executing the process. Each of these aspects culminates in the validation of the integrated functionality of all three processes.

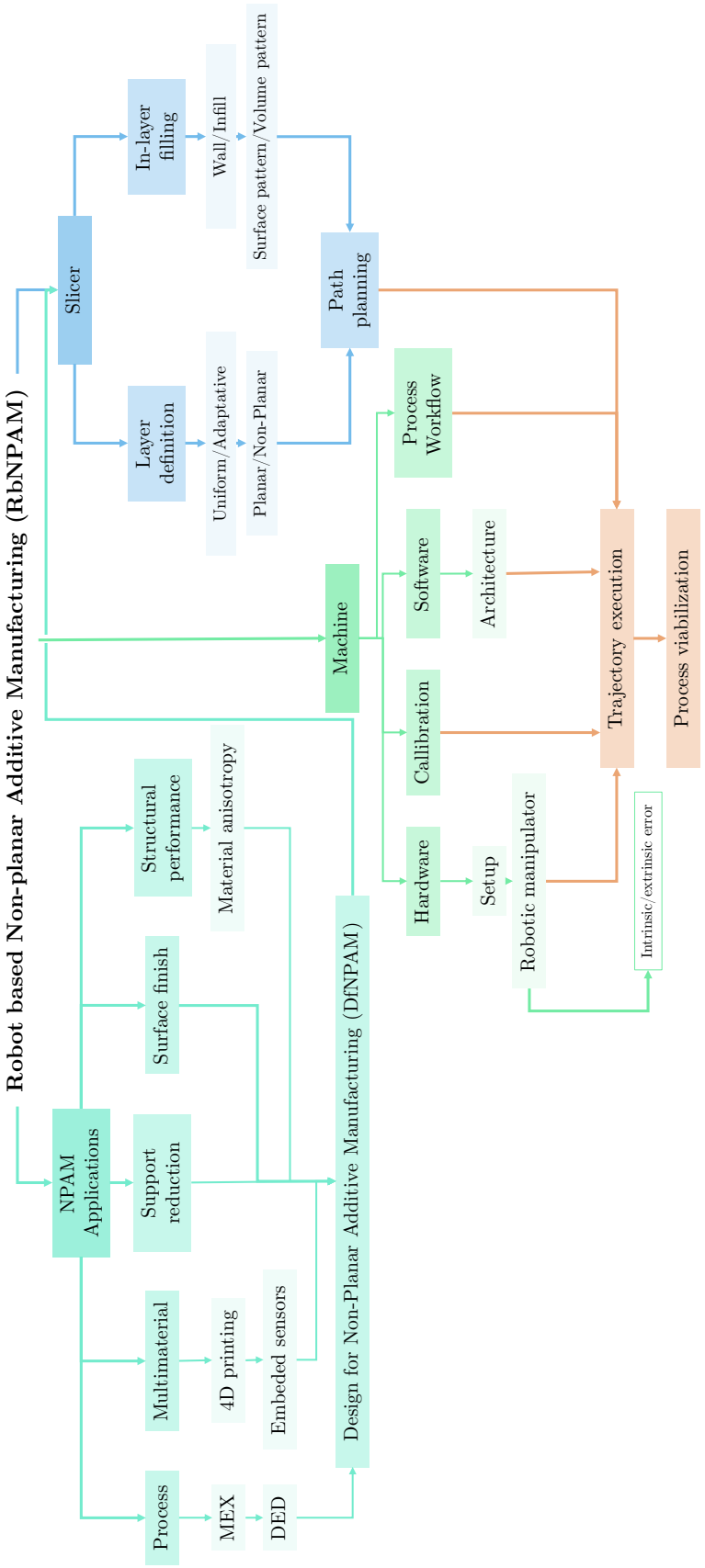

Figure 1.2: Conceptual map of the development areas of RbNPAM technology.

1.2 Motivation, objectives and structure of the PhD Thesis

1.2.1 Motivation of the PhD Thesis

Following a contextualization of the working environment in which this doctoral thesis was developed, its motivation is outlined: the advancement of Robot-based Non-Planar Additive Manufacturing technology. This innovation aims to equip users with tools for Design for Non-Planar Additive Manufacturing and enable their implementation within a validated robotic cell integrated with its custom slicer. This emerging technology arises from the need to develop 4D-printed devices capable of responding to degradation stimuli for the design of biodegradable implants. This effort is embedded within the BIOMET4D project: *Smart 4D Biodegradable Metallic Shape-Shifting Implants for Dynamic Tissue Restoration.*

Within the project, the design of degradation-driven devices is proposed for the treatment of craniosynostosis and as skin expanders that, being biodegradable, eliminate the need for a second surgical intervention to remove them. To address this requirement, the development of origami patterns capable of fulfilling these functions was pursued. In this approach, the patterns are 4D-printed, deformed, and, as they degrade, gradually adopt their final expanded shape, corresponding to the original printed geometry.

In both case studies, it becomes evident that the final required shape is volumetric rather than planar. This necessitates the ability to print these actuators so that their resting state corresponds to their curved configuration. Achieving this behavior requires the development of a tailored design and fabrication methodology for the specific case study.

Therefore, given the complexity of the project underlying this thesis, it is essential not only to design the non-planar actuators using 4D printing technology but also to develop the design methodology itself, as well as to conceptualize and validate their fabrication using RbNPAM technologies.

To conceptualize and validate the robotic additive manufacturing cell, support was provided by the CYBERCELL project: *Cyber-Physical Production System for Intelligent Manufacturing Cell Planning.* This project encompasses all tasks related to the construction of the cell, including the bed, extruder, calibration system, and control computer. It also covers the execution of trajectories by the robotic arm, as well as the measurement and control of errors in trajectory generation.

Finally, considering the complex development required for the integration of all systems, this thesis is motivated by the pursuit of additional applications linked to the developed technology within the industrial environment. These applications aim to leverage the advancements of this research in areas such as mechanical design, material internal structure, and the construction of geometries that are unachievable using conventional additive manufacturing techniques.

1.2.2 Objectives of the PhD Thesis

Considering the background of non-planar additive manufacturing executed through the use of robotic manipulators, as well as the mechanical design challenge of actuators for 4D printing stimulated by degradation with a non-planar resting state, the hypothesis of this thesis is that it is possible to develop a mechanical design methodology that automates the processing of geometries and their robotic non-planar additive manufacturing, enabling it to harness the advantages offered over traditional additive manufacturing methods.

Consequently, the main objective of this thesis is the development of a mechanical design methodology for non-planar additive manufacturing that can be implemented through a non-planar slicer in a robotic additive manufacturing cell. This methodology must automate the workflow for the development of industrial applications that leverage the advantages associated with this manufacturing method and validate its functionality.

The main objective can be further subdivided into three parts:

1. Creation of a parametric slicing methodology capable of working with non-planar layers in an automated manner.
2. Manufacture and implementation of a non-planar additive manufacturing robotic cell capable of executing the trajectories generated by the parametric slicer with a validated minimum precision.
3. Application of the developed technology to the manufacturing of non-planar resting state 4D-printed actuators stimulated by degradation. Exploration of its usage other industrial applications.

Finally, the objectives can be further subdivided into smaller tasks that contribute to the overall goal.

- Development of a topological space for addressing the non-planar lamination of a solid into parametric layers.
- Automation of trajectory generation within this workspace and definition of their properties.
- Generation of trajectory output. Development of the robotic cell setup.
- Calibration of the robotic cell.
- Kinematic programming of the trajectories generated by the slicer.
- Measurement of trajectory generation errors.
- Development of a flat library for validating 4D printing in degradation-driven origami mechanisms.
- Mechanical design methodology for transitioning mechanisms from the flat resting state to the non-planar resting state based on topological spaces.
- Exploration and development of new industrial applications for the methodology.

1.2.3 Structure of the PhD Thesis

The doctoral thesis is structured into seven chapters:

Chapter 1 provides an introduction to the project, outlining the initial hypotheses that will be validated throughout the course of the thesis. Additionally, it covers the motivation behind the development of the thesis and the objectives set for its completion.

Chapter 2 reviews the state of the art on robotic additive manufacturing, existing slicing methodologies, and design approaches applied to additive manufacturing, as well as the interrelation between these three topics.

Chapter 3 covers the mathematical foundations and robotics principles necessary for a proper understanding of the methodology. It also establishes the terminology and notation that will be used throughout the thesis.

Chapter 4 descrives the technical description of the materials used to achieve the objectives established in the development of the doctoral thesis.

Chapter 5 details the non-planar solid lamination methodology and layer infill strategies, along with their implementation in a non-planar additive manufacturing robotic cell. The outcomes of this chapter include the non-planar lamination slicer and the robotic cell, as well as the validation of trajectory generation.

Chapter 6 highlights the contributions of the proposed methodology to the field of Design for Additive Manufacturing. It shows how the defined Slicing Space serves as a design environment for both solid models and lamination layers, facilitating the optimization of geometry and fabrication processes. The key outcomes of this chapter include a library of origami-based devices designed for 4D printing, which are actuated by degradation stimuli applied to components of the device.

Chapter 7 presents a total of four industrial applications involving high-value-added components created through non-planar additive manufacturing, utilizing the methodologies developed in Chapters 5 and 6.

It is important to note that Chapters 5, 6, and 7 each contain their own results. This structure has been implemented to enhance the readability of the thesis, as the findings from each chapter influence the methodology presented in the subsequent chapter.

Finally, **Chapter 8** summarizes the main contributions of the thesis within the areas of study and presents the conclusions drawn from the work. Additionally, it outlines potential future research directions and includes the scientific output derived from the thesis.

Chapter 2

State of the art

2.1 Additive manufacturing technologies

Additive Manufacturing (AM) technologies, encompassing a range of processes from material extrusion to vat photopolymerization, have demonstrated transformative impacts across diverse industries. These processes, classified under ISO/ASTM standards [48], are not only tailored to specific materials and applications but also continually evolving to address emerging challenges in manufacturing and design. Figure 2.1 shows an overview of the seven identified AM technologies.

Material extrusion (MEX) involves depositing molten thermoplastics such as acrylonitrile butadiene styrene (ABS) or polylactic acid (PLA) through a heated nozzle. While it remains a cost-effective solution for prototyping, MEX is hindered by limitations in mechanical strength and layer adhesion. Innovations such as incorporating continuous fiber-reinforcement [49] and optimizing process parameters [50] are actively pursued to mitigate these issues.

Material jetting (MJ), a high-resolution AM technique, mimics inkjet printing by depositing droplets of photopolymers or wax. Some authors underscores its capability in producing multi-material parts with exceptional surface quality [51, 52]. Nevertheless, its high operational costs and slower production rates compared to other AM methods remain constraints that necessitate further optimization.

Directed Energy Deposition (DED) integrates material feeding and energy application to create parts layer-by-layer. Previous studies detail its versatility in multi-material fabrication and repair applications [53]. However, maintaining uniform microstructures and managing thermal gradients across layers remain critical challenges for this technology [54].

Binder jetting (BJ) employs liquid binders to consolidate powder particles, offering scalability and flexibility in materials such as metals and ceramics. Ziaee and Crane [55], provide comprehensive insights into the chemical bonding mechanisms and post-processing techniques critical for achieving desired part properties. Its ability to produce lightweight components with complex geometries makes it particularly attractive for the automotive and tooling industries.

Vat photopolymerization (PHP), dominated by Stereolithography (SLA) and Digital Light Processing (DLP), leverages photopolymer resins to create high-resolution parts. Innovations in bio-compatible and functional resins, [56, 57, 58], are driving its application in medical devices and dental implants. Despite these advances, the brittleness of cured resins and the need for post-processing are persistent hurdles.

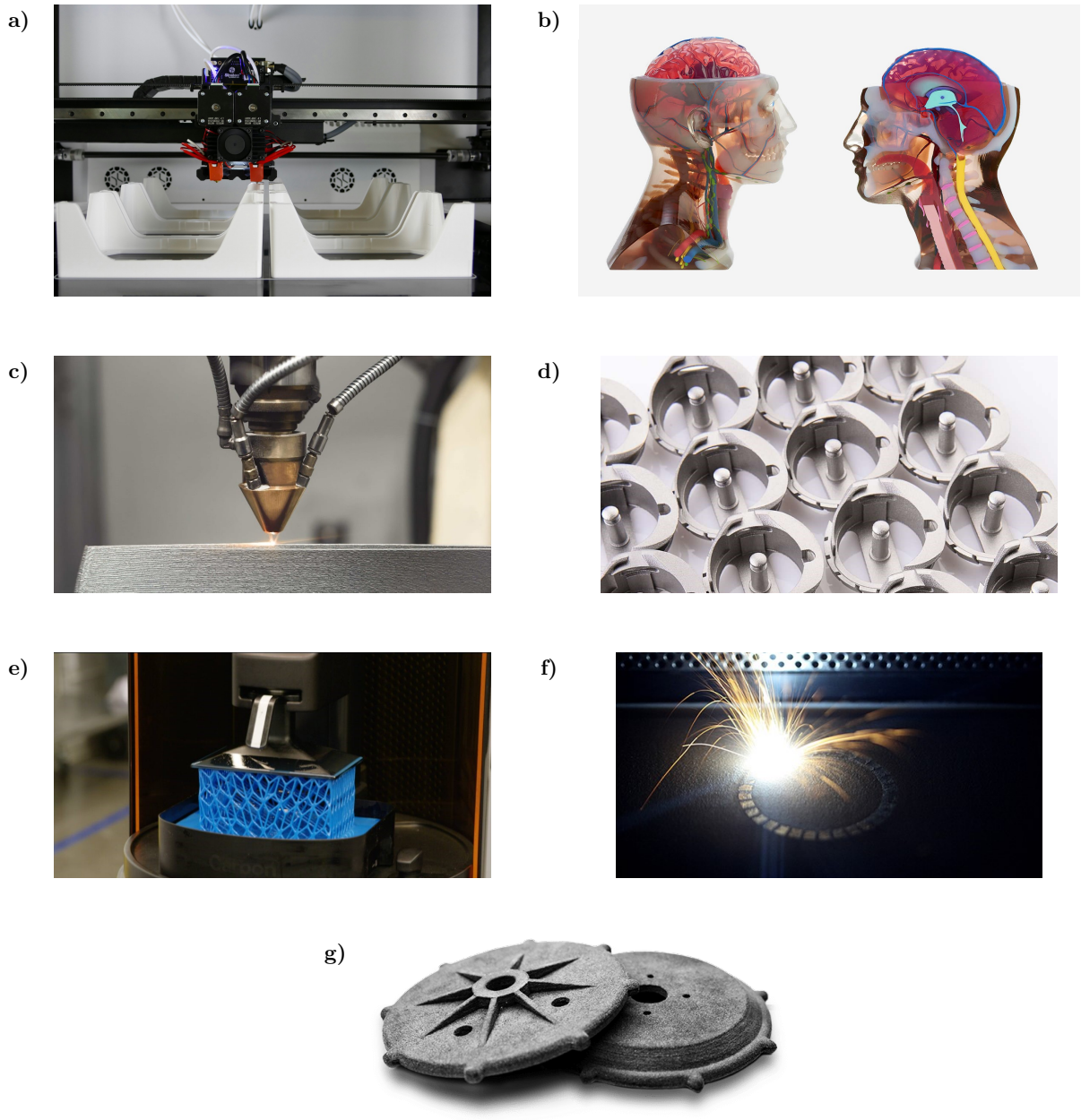

Figure 2.1: Additive manufacturing technologies. a) Material Extrusion. b) Material Jetting. c) Direct Energy Deposition. d) Binder Jetting. e) Vat Photopolymerization. f) Powder Bed Fusion. g) Sheet Lamination.

Powder Bed Fusion (PBF) technologies, are renowned for their high precision in fabricating metal and ceramic parts. Key studies highlight advances in process monitoring and defect

control, which mitigates porosity and ensures component integrity [59]. However, thermal stress and residual stress remain pressing challenges that demand enhanced simulation tools and material-specific approaches [60].

Sheet lamination (LOM), a lesser-utilized AM method, stacks and bonds sheets of material to form parts. While it offers cost advantages for producing large, simple geometries, its mechanical properties and resolution are inferior to other AM processes. Current research is focused on enhancing bonding mechanisms and exploring hybrid applications with subtractive manufacturing [61].

To better understand the added value of the results of this work, it is advisable to develop a diagram of additive manufacturing technologies that classifies them based on their current limitations in printing speed (s) and maximum deposition accuracy in the most unfavorable direction (r). Figure 2.2 presents this classification for the seven families of additive manufacturing.

AM Technology	Acronym	References
Material Extrusion	**MEX**	**[62, 63]**
Fused Filament Fabrication	FFF	[64]
Large Format FFF	LF-FFF	[65]
Drone based FFF	DFFF	[66, 67]
More than 3 DoF FFF machines	3-FFF	[68, 69]
Micro scale FFF machines	MFFF	[70]
Contour crafting extrusion	CEX	[71, 72]
Material Jetting	**MJ**	**[73, 51]**
Polyjet	PJ	[74]
Direct Energy Deposition	**DED**	**[75]**
Laser Metal Deposition	LMD	[76]
Direct Metal Deposition	DMD	[77]
Binder Jetting	**BJ**	**[78]**
Vat photopolymerization	**PHP**	**[79]**
Stereolithography	SLA	[80]
Digital Light Processing	DLP	[80]
Two-Photon Polymerization	2PP	[81]
Powder Bed Fusion	**PBF**	**[82]**
Direct Metal Laser Sintering	DMLS	[83]
Electron Beam Melting	EBM	[84]
Selective Laser Sintering	SLS	[85]
Sheet Lamination	**LOM**	**[86]**

Table 2.1: Summary table of nomenclature and references for the generation of the comparative diagram of printing speed and accuracy for the seven existing families of additive manufacturing.

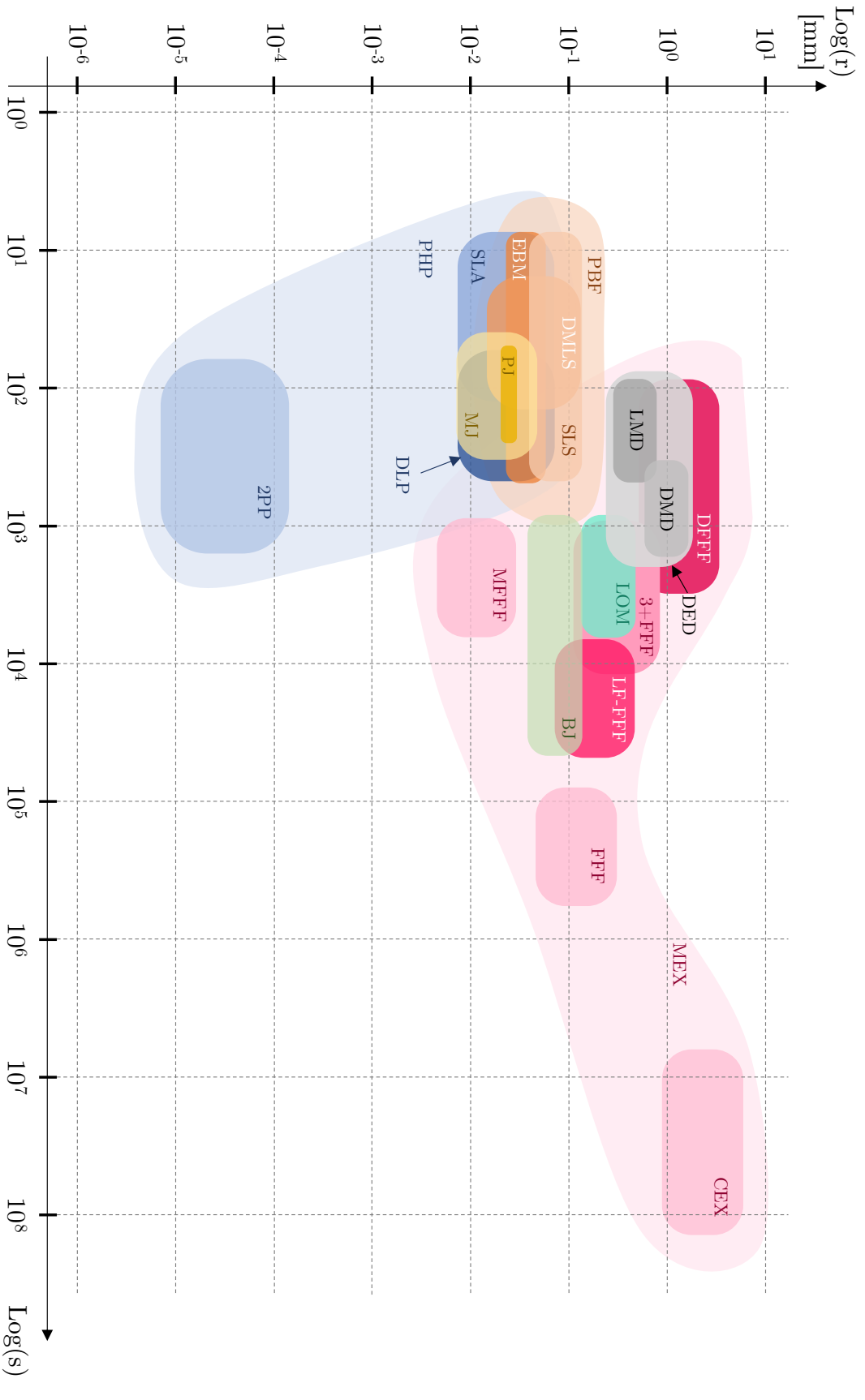

Figure 2.2: Logarithmic-scale correlation map between printing speed s and maximum deposition accuracy in the most unfavorable direction r for the seven families of additive manufacturing. Table 2.1 serves as a guide for understanding the diagram.

Recent advancements highlight transformative trends in AM technologies. Integration with artificial intelligence (AI) for process optimization, defect detection, and real-time control is gaining traction. AI-driven systems are enabling adaptive manufacturing environments that improve quality and reduce waste. These AI-enhanced solutions facilitate predictive maintenance and optimize material usage, streamlining production processes and reducing costs [87, 88].

Hybrid manufacturing, which combines additive and subtractive techniques, is emerging as a paradigm for achieving high-precision parts with complex geometries. This approach leverages the design flexibility of AM and the finishing capabilities of traditional machining to produce components with superior surface finishes and dimensional accuracy [89]. The integration of hybrid methods with robotic systems enhances automation and adaptability, enabling precise toolpath generation and synchronized multi-axis operations for complex geometries [90, 91].

Non-planar additive manufacturing technologies are revolutionizing traditional layer-based fabrication by introducing curved-layer paths, which enhance mechanical properties and aesthetic quality. These advancements address limitations such as the staircase effect and poor interlayer adhesion, common in conventional planar AM [92]. NPAM is especially relevant for producing components with organic shapes and stress-aligned geometries. The implementation of multi-axis robotic arms has been pivotal in NPAM, enabling the automation of non-planar toolpaths and facilitating the transition of this technology toward industrialization[93].

Multi-material and functionally graded materials are expanding the design envelope of AM. These innovations enable the fabrication of parts with tailored properties, such as varying stiffness or thermal conductivity, essential for aerospace and biomedical applications. Techniques to optimize inter-material bonding and minimize mismatched thermal expansion are critical areas of focus[94]. The combination of NPAM and multi-material systems further enhances the structural and functional performance of manufactured parts[95].

4D printing, an emerging evolution of additive manufacturing, integrates the dimension of time to create dynamic, self-transforming structures. This process involves the use of stimuli-responsive materials, such as shape-memory polymers, hydrogels, or metallic alloys, that change their properties or configurations in response to environmental triggers such as temperature, humidity, or magnetic fields [96]. Previous research highlights the potential of 4D printing in applications like biomedical devices, where self-deploying implants or tissue scaffolds adapt to their surroundings post-production [97, 98]. Additionally, 4D printing is being explored for aerospace and robotics, where structures can self-adjust to varying operational conditions. By incorporating programmable material behavior into AM, 4D printing expands the functional scope of manufactured parts, enabling adaptability and enhancing performance across industries [99].

Two-photon polymerization represents a breakthrough in microscale additive manufacturing, utilizing femtosecond lasers to achieve sub-diffraction-limited precision. By confining polymerization to localized volumes, two-photon polymerization enables the creation of highly intricate 3D structures. This technology has transformative potential in fields like biomedical engineering, photonics, and microfluidics, making it a pivotal advancement for precision AM at microscopic scales [100, 101].

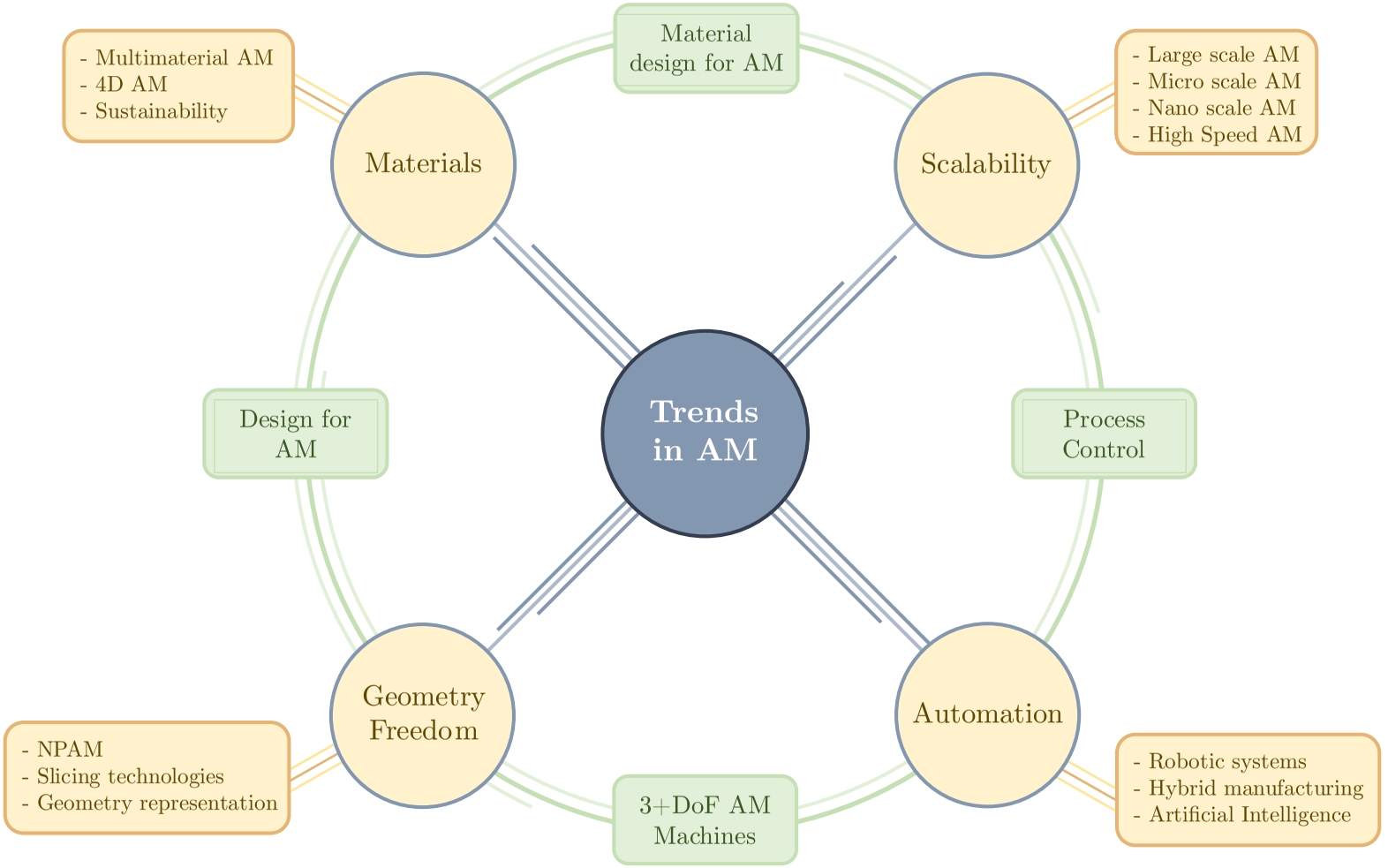

Figure 2.3: Trend map of additive manufacturing technology development classified by levels of detail and research depth.

The automation of AM processes through robotic systems is accelerating the industrialization of these technologies. Robotic arms equipped with advanced sensors and AI-driven controllers enable high-speed deposition and adaptive adjustments during production [102, 103]. This automation reduces human intervention, improves repeatability, and ensures consistent quality in large-scale manufacturing environments. Robotics integration also facilitates in-line inspection and real-time error correction, enhancing efficiency across the production chain [104].

Sustainability is becoming a cornerstone of AM research, with efforts to recycle waste materials, reduce energy consumption, and utilize bio-based feedstocks [105]. For instance, studies on plant-based polymers for material extrusion are exploring biodegradable alternatives to conventional thermoplastics [106].

Lastly, advances in high-speed, large-scale AM systems are pushing the boundaries of what can be achieved in industrial manufacturing. From construction-scale 3D printing with concrete to the rapid production of aerospace components, the scalability of AM technologies is transforming industries and challenging traditional manufacturing paradigms [107, 108, 109]. NPAM further supports this scalability by enabling the creation of structures that conform to intricate design constraints, without compromising on speed or quality. The conceptual map of the relationship between all the mentioned trends in AM is shown in Figure 2.3.

2.1.1 Extrusion processes in additive manufacturing

Material Extrusion is a cornerstone technology in additive manufacturing, recognized for its versatility and accessibility. The MEX process begins with a digital 3D model, which is sliced into layers and converted into machine-readable instructions [110]. During the printing process, the feedstock material—typically in the form of filaments, rods, or pellets—is fed into an extrusion head, where it is heated to a semi-solid state. The material is then deposited layer by layer onto a build platform as the extrusion head moves along predefined paths. Each layer solidifies upon cooling, and successive layers bond to form the final part. This sequential workflow allows for precise control over geometry, material distribution, and even multi-material printing. Variants of MEX, such as large-format printing or bioprinting, extend its applications into specialized fields like construction and healthcare.

MEX involves extruding feedstock material in a semi-solid state, which solidifies upon deposition. This versatile process accommodates various feedstock forms, including filaments, rods, and pellets, and diverse materials such as plastics, concrete, ceramics, and metals [111]. Applications range from aerospace components to customized medical devices. Large-format MEX, with build volumes exceeding $1m^3$, demonstrates the process's scalability for industrial applications [112].

Despite its advantages, including cost efficiency and simplicity, MEX faces challenges in ensuring consistent quality due to process-specific defects like warping, underfill, and geometric deviations. Process monitoring is critical to addressing these issues and advancing MEX's industrial adoption. Some monitoring techniques used to control Am MEX processes have been studied in the literature:

Vision technologies, particularly 2D and 3D imaging, dominate process monitoring due to their ability to capture geometric and surface features. 2D Vision: Liu et al. employed digital microscopes mounted on extrusion heads to detect underfill and overfill defects, achieving layer quality enhancement through proportional-integral-derivative (PID) control. 3D Vision: Holzmond and Li developed a stereoscopic imaging system to inspect layer geometries against CAD models, enabling defect detection for complex parts [113, 114].

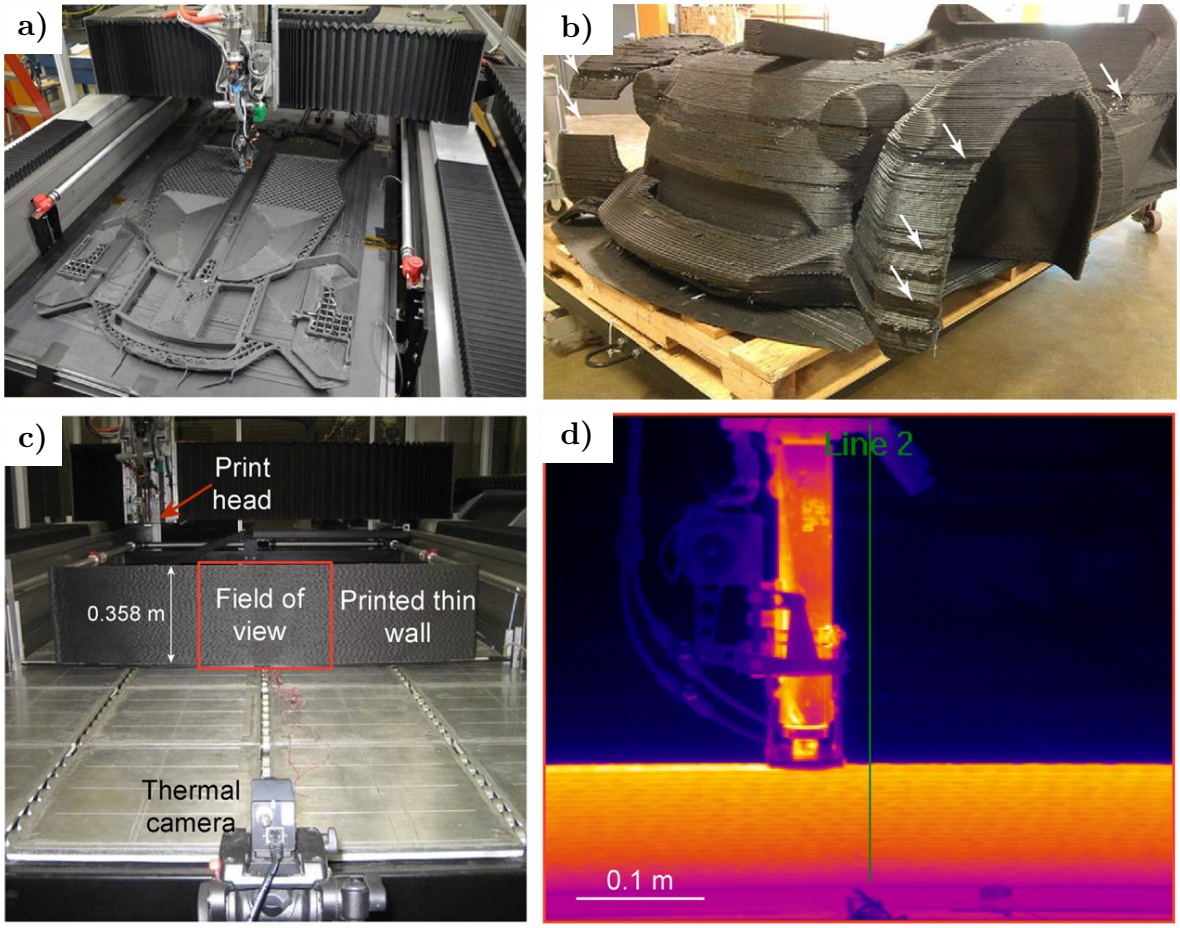

Figure 2.4: Thermal analysis of a full size car chasis MEX process for parameter optimization. a) AM machine. b) Built part. c) Experimental setup. d) Thermal image taking on the building process [113].

Thermal monitoring ensures proper material melting and deposition. Thermal cameras are used to predict tensile strength based on bead bonding temperatures. These studies demonstrated temperature-based layer initiation in large-format MEX, preventing structural collapse during rapid printing. Figure 2.4 illustrates that thermal control is used to ensure that the final part meets the minimum required specifications.

Accelerometers are used to measure vibrations that can indicate mechanical or process issues.Some authors utilized vibration data to detect nozzle clogging conditions, correlating amplitude changes with extrusion performance [115].

Sound-based monitoring captures process anomalies. Applied hidden semi-Markov models

were used to classify extrusion head conditions, achieving over 90% classification accuracy[116].

Force sensors and load cells measure extrusion dynamics. Some authors investigated piston-based extrusion forces for ceramic and polymer pastes, correlating variations with material flow [117].

Combining multiple sensor technologies enhances monitoring comprehensiveness. Integrated systems combining thermal, acoustic, and visual data have achieved high defect detection accuracy, laying the groundwork for closed-loop control.

2.2 Non-planar additive manufacturing technologies

Non-planar additive manufacturing (NPAM) introduces transformative capabilities that address key limitations of traditional planar additive manufacturing techniques. Among all the aforementioned additive manufacturing methodologies, non-planar additive manufacturing becomes particularly relevant in the further development of two techniques: material extrusion and direct energy deposition [118]. By leveraging curved layers, NPAM enhances structural integrity, aesthetic quality, and production efficiency. This approach mitigates issues like the staircase effect, improves mechanical properties, and offers new possibilities for complex geometries and functional designs. Recent studies, [119], demostrated the enhancement of curved lattices mechancical properties when they are manufactured using non planar layers. Figure 2.5 shows the experimental setup used for testing non-planar lattices built on a 3-axis AM machine.

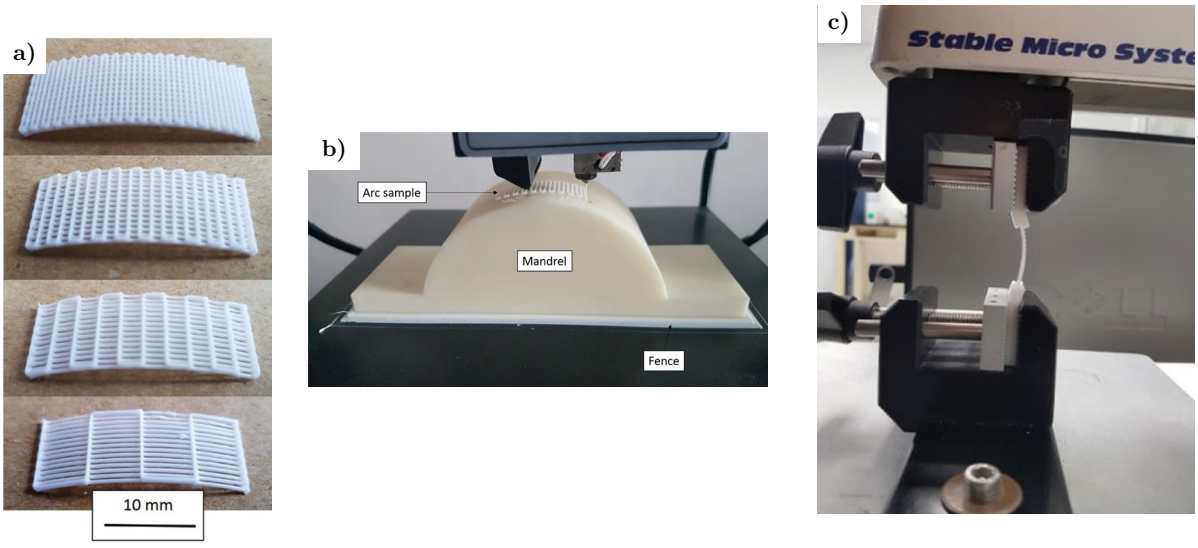

Figure 2.5: Experiments carried out to prove the mechanical properties enhancement obtained by building curved lattices using non-planar layers. a) Test specimens. b) Manufacturing process on a 3-axis AM machine c) Tensile test. REF: Enrique Cuan-Urquizo et al.

A fundamental limitation of conventional MEX AM technologies is the staircase effect, which arises due to the stacking of flat layers when printing curved geometries. This leads to poor surface finish and inaccuracies in complex shapes. By using curved layers, NPAM

effectively eliminates this problem, producing smoother surfaces and more precise geometries. Furthermore, the reduction in material usage and manufacturing time, attributed to the minimized need for support structures, aligns NPAM with sustainable manufacturing practices [15, 33].

The technological advancements in NPAM require significant modifications to conventional machines. Traditional three-axis printers, which operate in Cartesian coordinates, are limited in their ability to handle non-planar trajectories. Recent studies, [120, 121], demonstrate the incorporation of additional degrees of freedom (DOF) into printing systems. Multi-axis machines, such as 5-axis CNC systems and 6-axis robotic arms, enable the nozzle to dynamically adapt its orientation to the curvature of layers, achieving superior geometric accuracy and reducing material wastage.

The adoption of multi-axis systems also brings challenges in slicing and path planning. Unlike planar additive manufacturing, which generates layers through flat slicing, NPAM demands algorithms capable of defining three-dimensional trajectories. Techniques such as geodesic slicing [33], and parametric path generation[122], allow the creation of smooth and continuous paths that align with the mechanical requirements of the printed part. These advancements also reduce sharp corners in the printing trajectory, ensuring a seamless deposition process.

The mechanical performance of NPAM parts significantly outperforms that of planarly printed components. For instance some studies reveal that curved-layered parts exhibit higher flexural strength and improved fracture resistance. The alignment of rasters along curved paths reduces interlayer voids and enhances adhesion, contributing to improved load-bearing capacity [123]. Moreover,other authors proved that the number of inner curved layers has a minimal impact on mechanical performance, provided that porosity is minimized [124].

Applications of NPAM extend to advanced fields such as the fabrication of lattice metamaterials and shell structures. Non-planar lattice structures demonstrate the potential for creating lightweight and mechanically efficient components. These lattice geometries, when parametrically conformed to curved surfaces, provide significant advantages in aerospace, biomedical implants, and automotive engineering [119]. Additionally, experiments on cylindrical lattices show that Non-planar MEX parts exhibit 47% higher compression strength compared to planar-layered counterparts, underscoring the structural benefits of non-planar manufacturing. Figure 2.6 shows the manufacturing process of these cylindrical lattices [125].

Despite its potential, NPAM faces several challenges. The complexity of slicing algorithms and the high cost of multi-axis systems limit its accessibility. Furthermore, computational models must account for the dynamic interaction between nozzle orientation, material flow, and surface curvature to achieve precise deposition. Some researchers emphasize the need for advanced kinematic models and collision-free toolpath planning to address these challenges effectively.

The integration of NPAM into existing manufacturing workflows also requires interdisciplinary approaches. Combining adaptive slicing with hybrid manufacturing systems could bridge the gap between additive and subtractive techniques. This approach not only optimizes production but also ensures dimensional accuracy and surface quality in highly complex geometries.

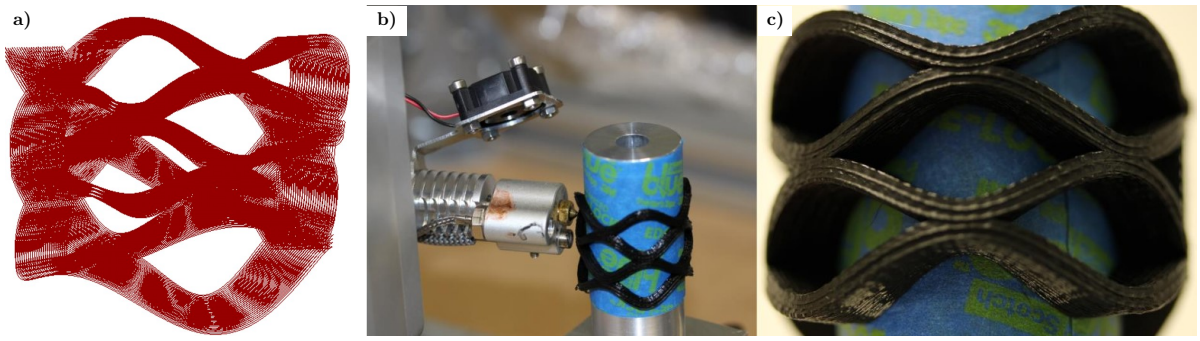

Figure 2.6: Manufacturing process of cylindrical lattices using non-planar layers. a) Npn-planar trajectory generation. b) Manufacturing process on a 5-axis AM machine c) Final result [125].

NPAM represents a revolutionary advancement in additive manufacturing, addressing the limitations of planar FFF while unlocking new possibilities for complex geometries and functional parts. Through advancements in multi-axis machine configurations, innovative slicing algorithms, and enhanced mechanical properties, NPAM positions itself as a pivotal technology in modern engineering and design. However, its widespread adoption will depend on the development of cost-effective solutions, user-friendly software, and further exploration of its applications in diverse industries. Continued research and collaboration across disciplines are essential to fully harness the potential of this transformative manufacturing paradigm.

2.2.1 Multiple degrees of freedom additive manufacturing machines

Multi-axis additive manufacturing (AM) represents a significant evolution from conventional 3-axis systems, addressing long-standing challenges such as anisotropic mechanical properties, the staircase effect, and limitations in geometry and scalability. By introducing additional degrees of freedom, multi-axis AM enables dynamic control over tool orientation and path planning, thus expanding the design space and functional capabilities of 3D-printed parts[92].

Conventional 3-axis AM systems construct parts layer by layer along the Z-axis, resulting in planar slicing and fixed-direction filling. While this approach simplifies the manufacturing process, it introduces several limitations. For instance, the staircase effect on curved surfaces compromises surface quality and dimensional accuracy, and the anisotropic mechanical properties of printed parts reduce their load-bearing capacities. Efforts such as adaptive slicing algorithms have mitigated these issues but fail to eliminate them entirely [126].

Multi-axis AM addresses these problems by leveraging redundant degrees of freedom to dynamically adjust the construction orientation during fabrication. This capability eliminates the need for extensive support structures, improves interlayer bonding, and allows for the production of complex geometries with high mechanical integrity. Figure 2.7 illustrates the most common setups for AM machines with more than five degrees of freedom. Among these configurations, setup on Figure 2.7.c ensures that the material flow is consistently aligned with the direction of gravity, minimizing potential complications. While the complexity of fabricated parts significantly increases with the number of system degrees of freedom, excessive

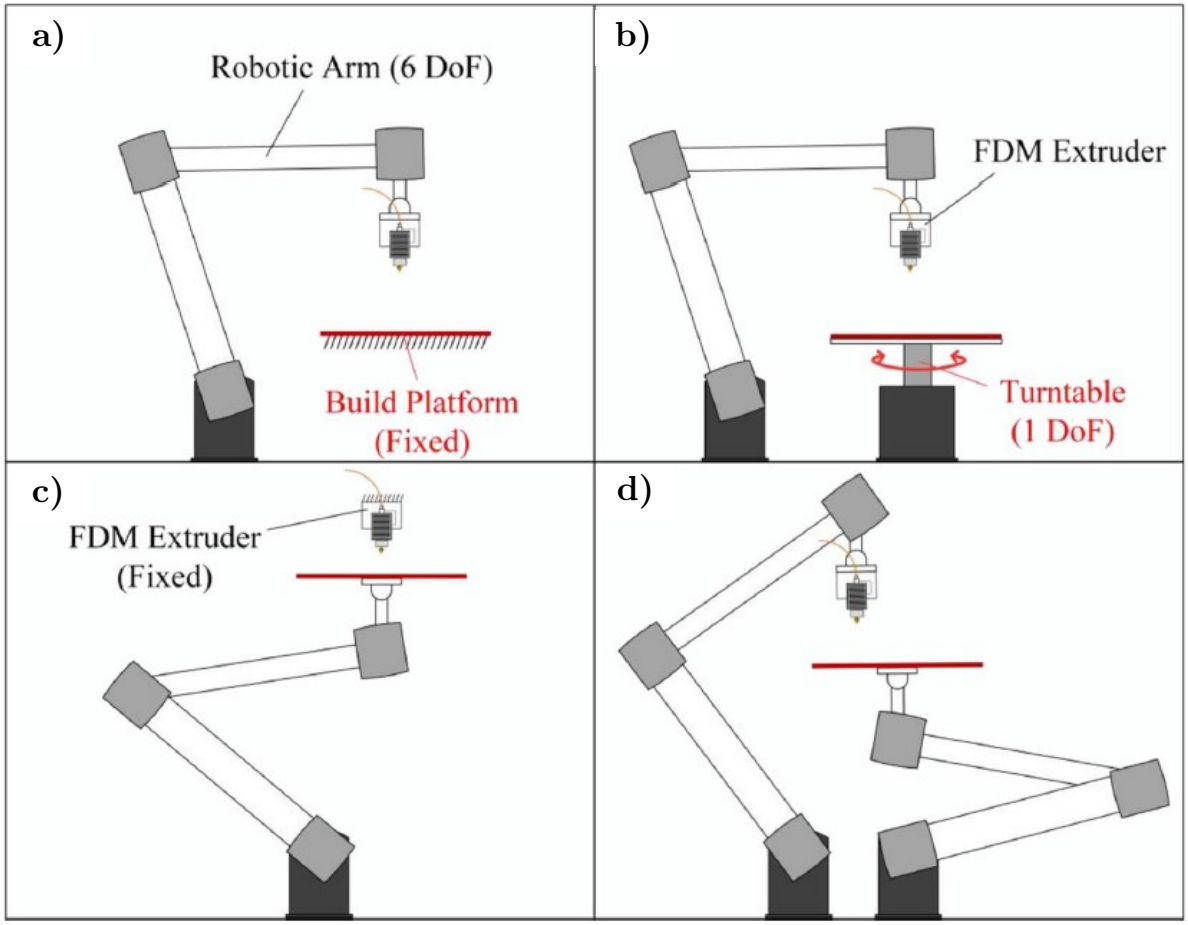

Figure 2.7: Additive Manufacturing machine configurations with more than five degrees of freedom: a) A fixed build platform paired with a movable extruder. b) A rotatable build platform combined with a movable extruder. c) A stationary extruder with a movable build platform. d) Both the extruder and the build platform are movable[127].

degrees of freedom can lead to a loss of stiffness and precision, potentially rendering the technology unsuitable for certain applications.

One of the core advancements in multi-axis AM lies in layering strategies. Beyond traditional planar layers, multi-axis systems utilize curved and mixed-layer approaches to improve part performance. Curved layers, constructed along a part's geometric contours, eliminate the staircase effect and optimize surface finishes [128]. Mixed-layer strategies combine planar and curved layers to balance manufacturing speed and part quality. Recent studies demonstrated a hybrid slicing method that achieved up to a 1.8-fold increase in production efficiency while maintaining high-resolution features on critical surfaces [129].

Non-supporting manufacturing is a particularly impactful capability of multi-axis AM. By dynamically altering build orientations, multi-axis systems can fabricate overhanging structures without the need for support materials. Figure 2.8 illustrates the two approaches to multi-plane operations in additive manufacturing using machines with more than three degrees of freedom. These approaches combine both planar and non-planar layering techniques. In

[130], a skeleton-based slicing method able to perform non-supporting fabrication of multi-branch structures on a 5-axis machine was introduced. This approach significantly reduces post-processing time and material costs while maintaining part integrity.

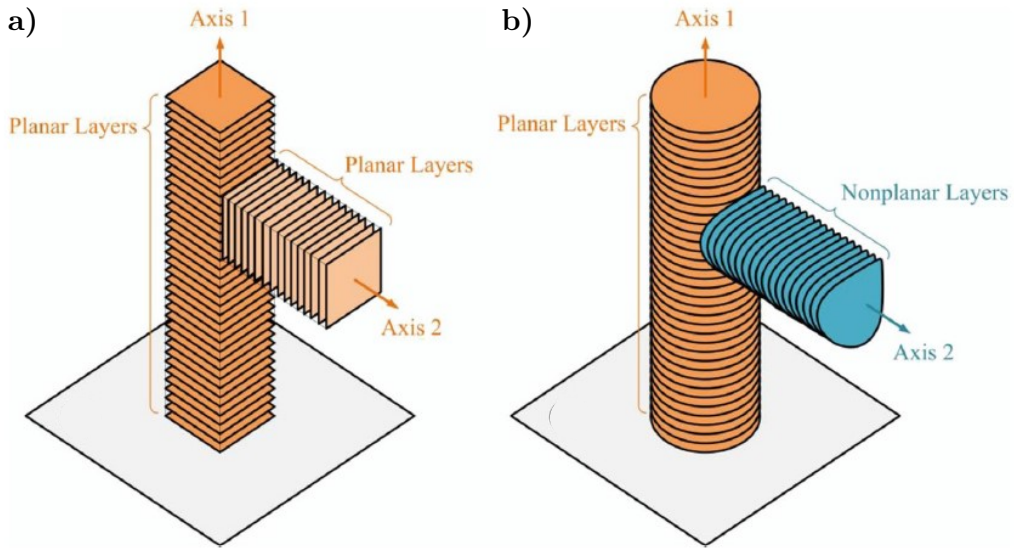

Figure 2.8: Examples of multi-plane strategies to reduce support material on NPAM machines. a) Planar layers on different planes. b) Non-planar layers on different planes [131].

Despite its advantages, multi-axis AM faces challenges related to computational complexity and hardware integration. Advanced CAM algorithms are required to generate collision-free toolpaths that account for machine kinematics and part geometry. Additionally, the high cost and complexity of multi-axis systems pose barriers to adoption. Research efforts are focused on developing cost-effective robotic platforms and user-friendly software to democratize this technology.

2.2.2 Geometry representation on multi-axis additive manufacturing

Geometry representation plays a crucial role in additive manufacturing, particularly in multi-axis additive manufacturing, where multiaxial deposition and complex geometries are achievable [23]. The following review discusses various representation methods, their applications, and notable works conducted in the field. Figure 2.9 explains the 6 geometry representation methods described in the text.

Boundary Representation defines a solid by its boundary, composed of interconnected faces, edges, and vertices. This method is commonly used in mechanical CAD systems like Solidworks and CATIA due to its precision and efficient data handling.

The study in [132] highlights Boundary Representation's effectiveness in mechanical designs, highlighting its compatibility with tools for topology optimization. Its application in workflows

that optimize material distribution and enhance the strength-to-weight ratio of designs have been also studied [133]. Although Boundary Representation is precise, its limited compatibility with simulation software presents challenges when integrating advanced manufacturing processes [134].

Tessellated models approximate surfaces using polygons, typically triangles, to ensure compatibility with slicing and AM software. This method facilitates the conversion of CAD models into printable formats.

The main objective of the recent studies is improving tessellation algorithms to reduce surface errors, using approaches like the marching cubes algorithm to prepare topology-optimized models for AM. In [135], the authors investigated the use of tessellated surfaces for WAAM (Wire and Arc Additive Manufacturing), discussing challenges in maintaining geometric fidelity during slicing.

Non-Uniform Rational B-Splines (NURBS) provide a flexible and smooth representation of curves and surfaces, enabling the creation of complex geometries [136, 137].

Previous studies demonstrated how NURBS enable the generation of organic and aerodynamic shapes with parametric control [133]. This adaptability makes it ideal for AM applications requiring intricate surface designs. Additional research have been done on NURBS-based workflows in hybrid manufacturing, emphasizing its ability to improve surface quality through post-processing integration [89].

Voxel representation divides objects into discrete 3D grids, making it suitable for representing internal properties and processing irregular geometries.

Voxelization techniques have been applied to RBAM, leveraging octree-based structures to improve computational efficiency during volume decomposition [138]. Similarly, voxel-based approaches were explored for collision-free tool-path generation, which are particularly useful in multiaxial deposition [139].

Point clouds represent geometries as collections of discrete 3D points, often derived from scanning or reverse engineering processes.

The necessity of converting point clouds into formats like tessellated or parametric models was discussed to make them suitable for AM. In this line, further research was done in the field of converting point clouds in hybrid manufacturing workflows, showcasing their application in reconstructing damaged components using robotic systems [89].

Function Representation implicitly describes geometry through mathematical functions, enabling the seamless creation of complex topologies.

Previous studies developed algorithms to directly slice Function Representation geometries without intermediate conversions, facilitating efficient tool-path generation for intricate shapes [145]. Other researchers highlighted Function Representation's potential for representing lattice structures and graded materials, emphasizing its suitability for AM applications requiring material variation and density control [146].

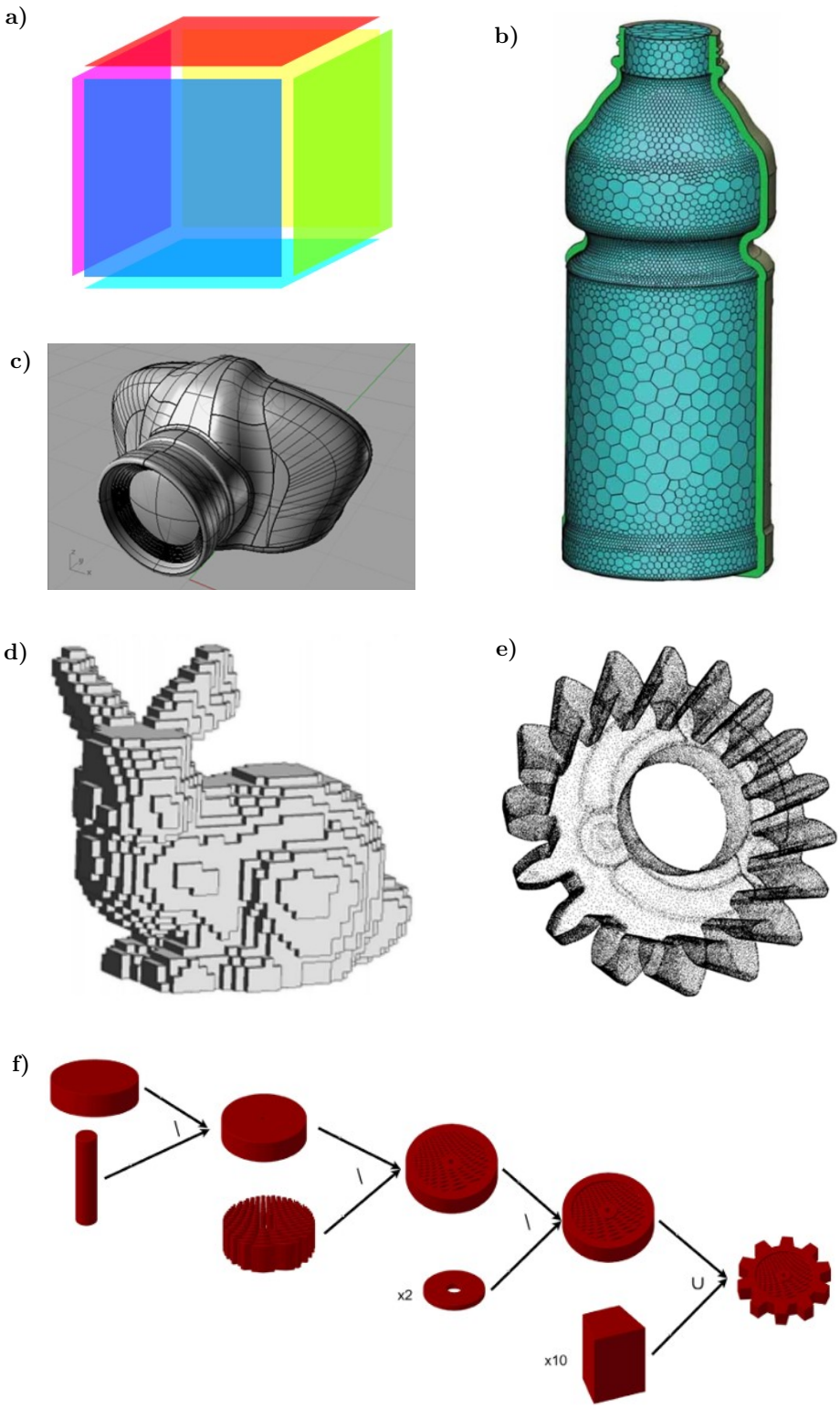

Figure 2.9: Geometry representation formats used in Additive Manufacturing Processes [140, 141, 142, 143, 144]. a) Boundary Representation. b) Tessellated Model. c) NURBS. d) Voxel Representation. e) Point Cloud. f) Function Representation.

2.2.3 Non-planar slicing algorithms

Fused deposition modeling (FDM) relies heavily on slicing algorithms to transform 3D models into layers for manufacturing. These algorithms are crucial in improving surface quality, build time, mechanical properties, and eliminating support structures. As discussed in [127], slicing methodologies are categorized into planar and non-planar approaches, each addressing specific challenges and trade-offs in additive manufacturing (AM).

Planar slicing remains the foundation of most FDM technologies due to its simplicity and computational efficiency. Hull's introduction of stereolithography in 1984 laid the groundwork for this method, which involves generating flat, parallel slices of the model [147]. From that invention, the first non planar slicing models focused on adaptive planar slicing, which adjusts layer thickness to enhance surface quality and reduce build time [148]. Years later, this methodology was extended by incorporating NURBS-based contours and optimizing zigzag toolpaths for greater accuracy and efficiency [149]. However, planar slicing often suffers from the staircase effect, where surface smoothness is compromised due to layer-by-layer deposition [150].

Non-planar slicing algorithms enable the generation of layers that follow curved geometries, requiring advanced computational approaches and sometimes additional hardware capabilities. Unlike planar slicing, which confines layers to flat planes, non-planar methods define toolpaths along curved surfaces, resulting in unique geometric configurations. Here, I detail the mechanisms and computational strategies behind the most significant non-planar slicing methods.

Soome studies implemented a semi-nonplanar slicing approach for conventional Cartesian 3D printers by modifying the top layers to follow curved toolpaths while keeping lower layers planar [16]. Their algorithm in Slic3r generates these curved paths by assessing potential collisions between the toolhead and the model, ensuring that the deposition can occur without interference. The integration of this method into existing software made it accessible but limited the curvature complexity due to hardware constraints.

A convex optimization approach to curve layers for better surface conformity was proposed in [14]. This method employs variable layer thicknesses ranging from 0.04 to 0.3$[mm]$, enabling smoother transitions between adjacent layers. The optimization procedure iteratively adjusts the curvature of layers to minimize discrepancies between the toolpath and the desired geometry, ensuring precise adherence to the model's shape. Figure 2.10 shows the result of this research.

Curved layer FDM (CLFDM) was introduced in [150], leveraging surface offsetting techniques to generate slicing surfaces. Their method computes overlapping beads and offsets the surface outward to generate toolpaths for each layer. While their algorithm effectively eliminates gaps between adjacent layers, the process requires intricate control of the extrusion gap, which they simulated without practical implementation.

A helical slicing method for thin-shell geometries was designed in [151], aiming to create a continuous toolpath along cylindrical or shell-like features. The algorithm calculates toolpaths by interpolating between successive planar slices while maintaining a smooth transition along

Figure 2.10: Planar printing compared to Non-planar Curvislicer part result form [14].

the curve. This interpolation ensures that the extrusion head moves seamlessly between layers without abrupt direction changes, avoiding defects like seam lines.

In their subsequent work, [152], a spherical slicing approach to address challenges in printing spherical features. This method begins with planar slicing to create a spherical base substrate. Subsequent layers are sliced along concentric spherical shells, calculated based on the model's geometry and scaled offsets. This algorithm provides uniform coverage of spherical surfaces while maintaining alignment between the toolpath and the spherical curvature.

A curved-layer slicing algorithm that integrates variable layer thickness was developed in [124]. This approach begins by offsetting the original surface using normalized signed distance fields to generate accurate slicing surfaces. The algorithm then calculates deposition paths for these surfaces, ensuring smooth transitions between varying thicknesses within a layer. The method is particularly effective for complex shell-like geometries, although its computational requirements are significant.

A novel toolpath generation technique based on volume decomposition was proposed in [43]. The algorithm segments a 3D model into convex regions using a combination of volume-to-surface and surface-to-contour transformations. Curved toolpaths are then derived from these regions, optimizing for collision avoidance and maintaining support stability. Their process is designed to work with robotic systems, leveraging their flexibility for collision-free movements.

Recent studies explored printing on arbitrary freeform substrates using offsetting approaches to align the model's geometry with the underlying support surface [153]. Their algorithm calculates intersections between the freeform substrate and the model to generate a base structure, which is then built upon with curved layers. This method adapts to irregular surfaces, ensuring that the deposited material conforms accurately to the substrate. The slicer's workflow is shown in Figure 2.11.

Finally, two non-planar slicing techniques were introduced in [154]: decomposition-based

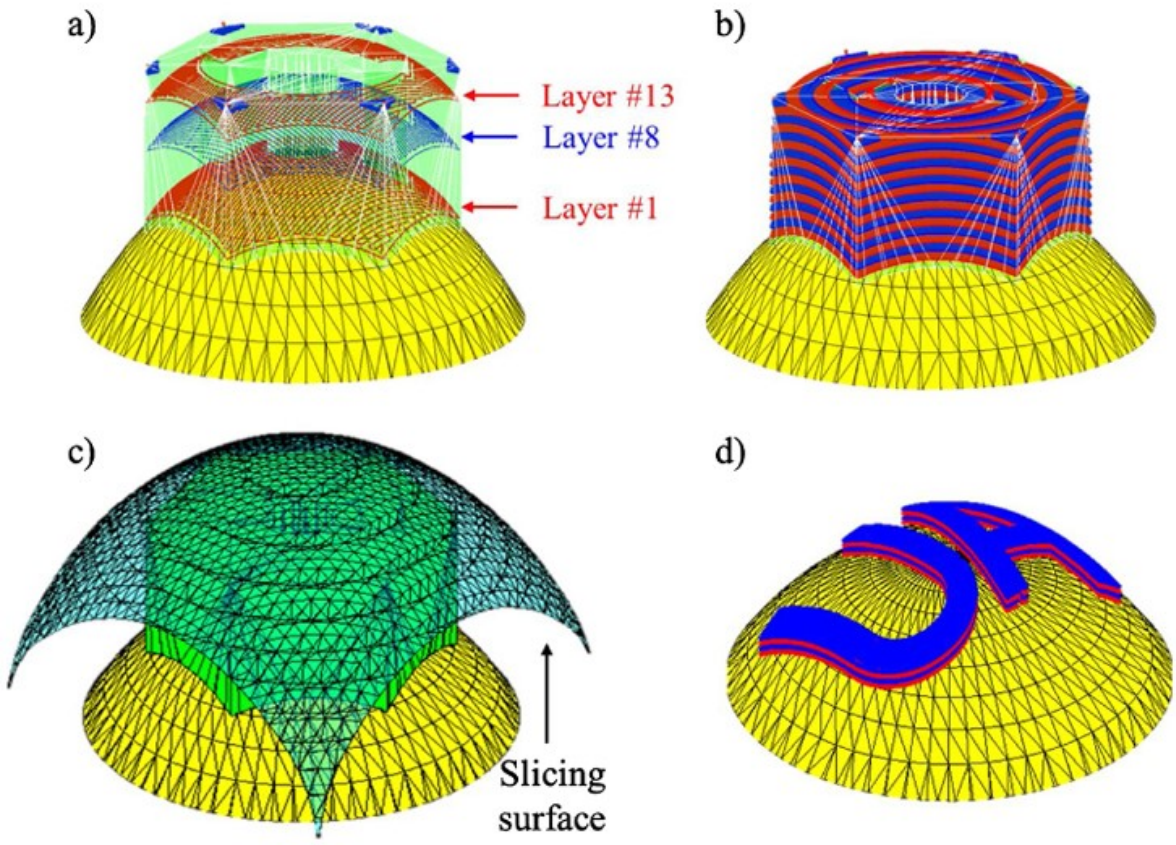

Figure 2.11: Slicer workflow based on offsetted surfaces: a) 3D visualization displaying a subset of the layers. b) 3D visualization of all layers required to construct the part. c) 3D representation of the slicing surface (highlighted in cyan) extending beyond the 3D model, where no intersection occurs, marking the termination of the slicing process. d) 3D visualization of all layers necessary for constructing the UA model [153].

curved surface slicing and transformation-based cylinder slicing. The former involves segmenting a STEP file into sub-volumes defined by concave loops, generating curved slicing surfaces from these sub-volumes, and calculating five-axis toolpaths. The latter focuses on cylinder-shaped models, flattening the geometry into a plane for planar slicing and then re-transforming the layers back to cylindrical coordinates. This dual approach ensures compatibility with different geometric configurations.

Each algorithm relies on specific geometric transformations, optimization procedures, and toolpath calculations to generate curved layers that align with the intended design. However, by focusing on computational techniques, these approaches push the boundaries of what can be achieved in FDM.

2.3 Design for additive manufacturing

The evolution of additive manufacturing (AM) technologies over the past decades has established Design for Additive Manufacturing (DfAM) as a critical field focused on optimizing designs to exploit AM's unique capabilities. This review outlines the historical progression, key methodologies, tools, and significant research contributions in DfAM.

The concept of DfAM emerged in the mid-2000s as a specialized adaptation of traditional Design for Manufacturing (DFM). It was driven by the need to overcome limitations in conventional design principles and align with AM's novel approaches. Early research by Hopkinson and Dickens, [155], introduced the concept of rapid manufacturing (RM), emphasizing cost reduction and efficiency for end-use products rather than prototypes. Hague et al. explored the transformative potential of RM, detailing design freedom and material opportunities [156]. Gibson et al. published the first article explicitly focused on DfAM, redefining DFM principles for AM-specific applications [157].

Design guidelines and principles provide foundational knowledge for integrating DfAM practices into AM workflows. Yang and Zhao proposed general design guidelines to leverage AM's benefits, such as using freeform designs, integrating features, and optimizing part strength and weight [158]. This ideas have been proved in several applications by reducing material usage and printing costs through optimized overhangs and hollow structures [159].

Lattice structures enable lightweight, high-strength designs by incorporating geometrically optimized patterns. Previous research developed uniform and graded porous lattices for automotive crash safety, improving energy dissipation during impacts [160]. Other authors replicated human bone architectures in AM titanium lattices, enhancing medical implants [161].

Optimal build orientation minimizes support structures, improves mechanical properties, and reduces costs. Researchers introduced a graphical tool for computational build orientation optimization, significantly enhancing producibility and surface finish [162]. This concept was also employed surrogate-based optimization to improve structural robustness by 90% [163].

Part consolidation reduces assembly requirements and enhances structural integrity. The study developed in [164], explored strategies to consolidate multiple parts into single geometries, minimizing assembly time and cost. Furthermore, in [165], the authors created a DfAM framework enabling lightweight design through part consolidation.

Generative design integrates AI algorithms to create optimized geometries based on predefined goals. A Generative-DfAM framework for designing safer and lighter automotive components, combining GD and AM was proposed in [166]. In other studies, Generative Design was used to develop aerodynamic and strong knuckle for automotive applications [167]. Figure 2.12 shows the result from the Generative Design optimization process.

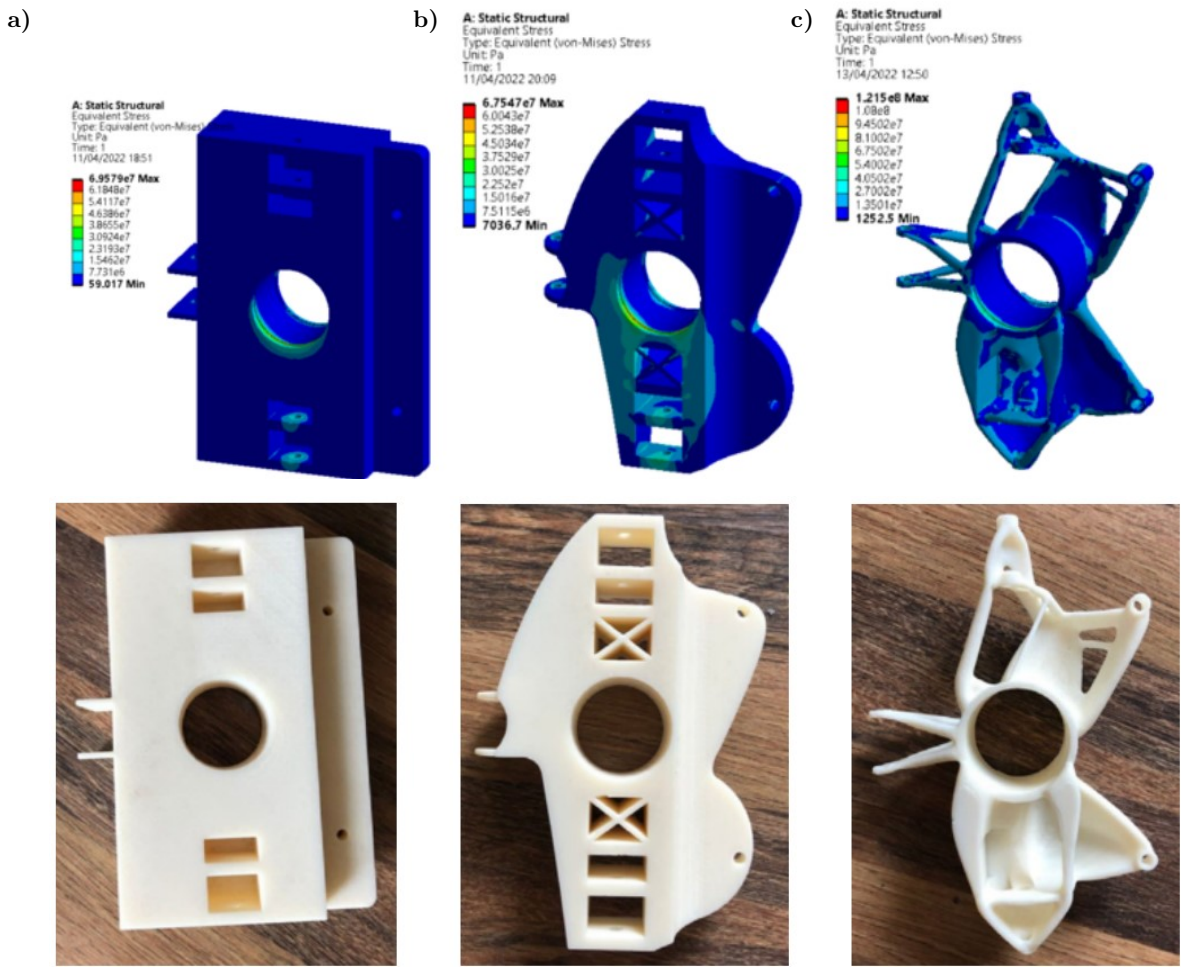

Figure 2.12: Design for additive manufacturing process of an automotive knuckle: Simulation and final result. a) 3D design b) Outcome design from the topology optimization process. c) Outcome design from the generative design process [167].

2.3.1 Methodologies and tools

Multimaterial additive manufacturing

Material Extrusion Additive Manufacturing has gained prominence as a cost-effective and flexible technology for fabricating multi-material polymer composites, specifically laminated composite structures. These structures combine various polymers with distinct mechanical and functional properties, enabling applications in industries such as aerospace, biomedical, automotive, and emerging fields like soft robotics. The growing interest in multi-material-based laminated structures arises from their ability to integrate materials with contrasting characteristics, like stiffness and flexibility, into a single functional component, allowing for tailored designs that meet unique performance criteria [168, 169].

MEX AM technologies utilize heated nozzles to extrude polymers and composite materials layer by layer. Commonly used materials include polylactic acid (PLA), acrylonitrile butadiene styrene (ABS), thermoplastic polyurethane (TPU), and polyethylene terephthalate glycol

(PETG). Studies highlight how combinations of these materials create laminated composite structures with enhanced mechanical performance, such as increased tensile strength and stiffness-to-weight ratios [170]. Moreover, bio-inspired designs, such as those mimicking tendon-to-bone transitions, further enhance performance by optimizing material interfaces.

The applications of multi-material MEX AM extend beyond conventional industries into transformative domains like soft robotics. Soft robotic systems rely on compliant, lightweight, and adaptive materials to mimic biological movements and achieve high degrees of flexibility. Laminated composites created using TPU and similar elastomers provide the necessary softness and durability, while rigid polymers such as PLA contribute structural integrity. This combination allows soft robotic actuators and grippers to operate effectively across various environments, including underwater and hazardous conditions. Studies have also demonstrated the integration of stimuli-responsive materials for creating self-actuating soft robotic components, enabling adaptive performance based on environmental cues [171].

Research has explored various configurations of bi-material laminated structures.Alternating layers of ABS and carbon-fiber-reinforced PLA (CF-PLA) achieved high interfacial bonding strength and improved impact resistance under optimized process parameters, such as layer thickness and infill density [172]. Such configurations are particularly promising for aerospace and automotive applications, where lightweight yet durable components are critical. In robotics, these configurations are leveraged to create protective casings, lightweight frameworks, and vibration-dampening layers for mechanical stability.

Tri-material laminated structures, which incorporate three distinct materials in layered configurations, offer additional design flexibility. Some studies optimize the fabrication of tri-material laminated composite structures comprising PLA, PETG, and ABS, achieving a balance between tensile strength and energy absorption. These advancements emphasize the role of multi-material systems in meeting stringent industrial requirements, including thermal insulation and impact resistance. Additionally, industries such as consumer electronics are beginning to utilize these materials for creating multifunctional components with integrated conductive, insulative, and structural layers [173].

Mechanical properties such as tensile strength, flexural modulus, and impact resistance are heavily influenced by process parameters, including nozzle temperature, printing speed, and layer thickness. Bi-material interfaces between PETG and TPU were studied, concluding that increased nozzle temperatures and optimized raster patterns significantly improved interfacial bonding and energy absorption capacity [174]. Advanced modeling techniques, such as Design of Experiments and machine learning algorithms, are increasingly employed to refine these parameters and predict optimal configurations. In soft robotics, these insights inform the development of actuators and sensors that require precise tuning of material interfaces for responsive behavior.

The integration of bio-inspired interfaces in multi-material laminated composite structures mimics natural structures, such as bone-tendon attachments, enhancing load transfer and crack resistance. Figure 2.13 illustrates the design, manufacturing, and testing process of a temporomandibular joint using multi-material 3D printing. Studies on metamaterial structures, including auxetic and lattice-based designs, reveal their potential in applications

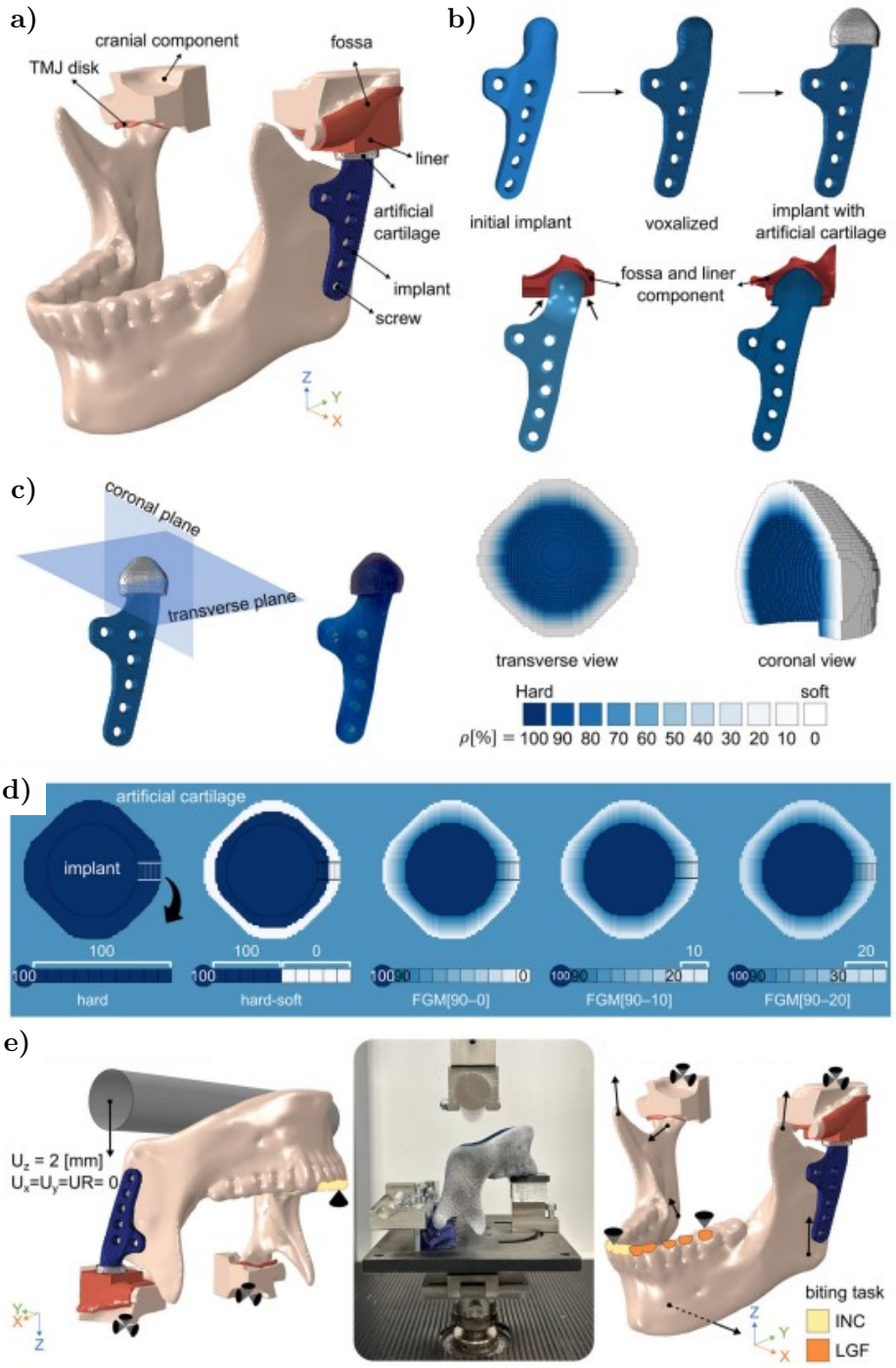

Figure 2.13: Miao et al. Design and material composition of temporomandibular joint implants [175]: a) The mandible with artificial cartilage after implantation. b) Comparison of initial and modified designs of TMJ implants and artificial cartilage. c) A finite element analysis model incorporating 10 additional material layers as artificial cartilage. d) Material property distributions within the artificial cartilage, including hard, hard-soft transitions, and functionally graded designs. e) Experimental setup for analysis and testing.

requiring high energy absorption, such as protective gear and automotive crash components. Similarly, soft robotic systems benefit from bio-inspired designs that enable adaptable and compliant interactions with delicate objects, expanding their use in healthcare and precision assembly tasks [175].

While multi-material MEX AM has shown great promise, challenges remain in achieving consistent interfacial bonding and addressing delamination under load. The high anisotropy of printed parts and the complexity of nozzle calibration in multi-material systems are ongoing hurdles. Advanced multi-nozzle systems and hybrid techniques integrating additive and subtractive methods are being explored to mitigate these issues. Future research should also focus on integrating AI-driven process monitoring and real-time error correction to improve reliability and scalability. Additionally, the development of multi-axis robotic arms capable of managing complex geometries offers a pathway to overcome these challenges in industrial-scale production.

Emerging trends in multi-material MEX AM include the development of functionally graded materials, bio-inspired designs, and AI-enhanced fabrication processes. Functionally graded materials enable the creation of components with spatially varying properties, essential for biomedical and aerospace applications. In soft robotics, graded materials allow the creation of actuators with smooth transitions between rigid and flexible regions, enhancing functionality and resilience. Bio-inspired interfaces optimize load distribution and damage tolerance, offering novel solutions to engineering challenges. These advancements collectively position multi-material MEX AM as a cornerstone of future manufacturing technologies across diverse industries [176].

4-dimensional additive manufacturing

4D printing, an extension of additive manufacturing, introduces time as a dynamic dimension to 3D-printed objects, enabling transformations in response to external stimuli. Skylar Tibbits first introduced the term in 2013, describing it as the capability of printed objects to autonomously change shape, properties, or functions when exposed to factors like temperature, light, or humidity [177]. This innovative concept has since gained traction due to its potential in creating adaptive, self-actuating designs that extend the utility of static 3D-printed structures. Among its applications, combining multi-material printing with non-planar layer strategies offers a groundbreaking approach to overcoming existing challenges and expanding its industrial relevance [178]

The integration of multi-material capabilities in 4D printing has facilitated the production of complex structures with distinct mechanical, thermal, or chemical properties. Material extrusion enables the combination of materials such as shape-memory polymers (SMPs), hydrogels, and thermoplastic elastomers to fabricate components with tailored functionalities. For instance, hydrogels and SMPs are frequently utilized for their biocompatibility and responsiveness to stimuli such as temperature or pH, making them ideal for applications in biomedical devices and soft robotics [179]. When combined, these materials allow the creation of actuators, sensors, and drug delivery systems that exhibit programmable, stimulus-driven behaviors.

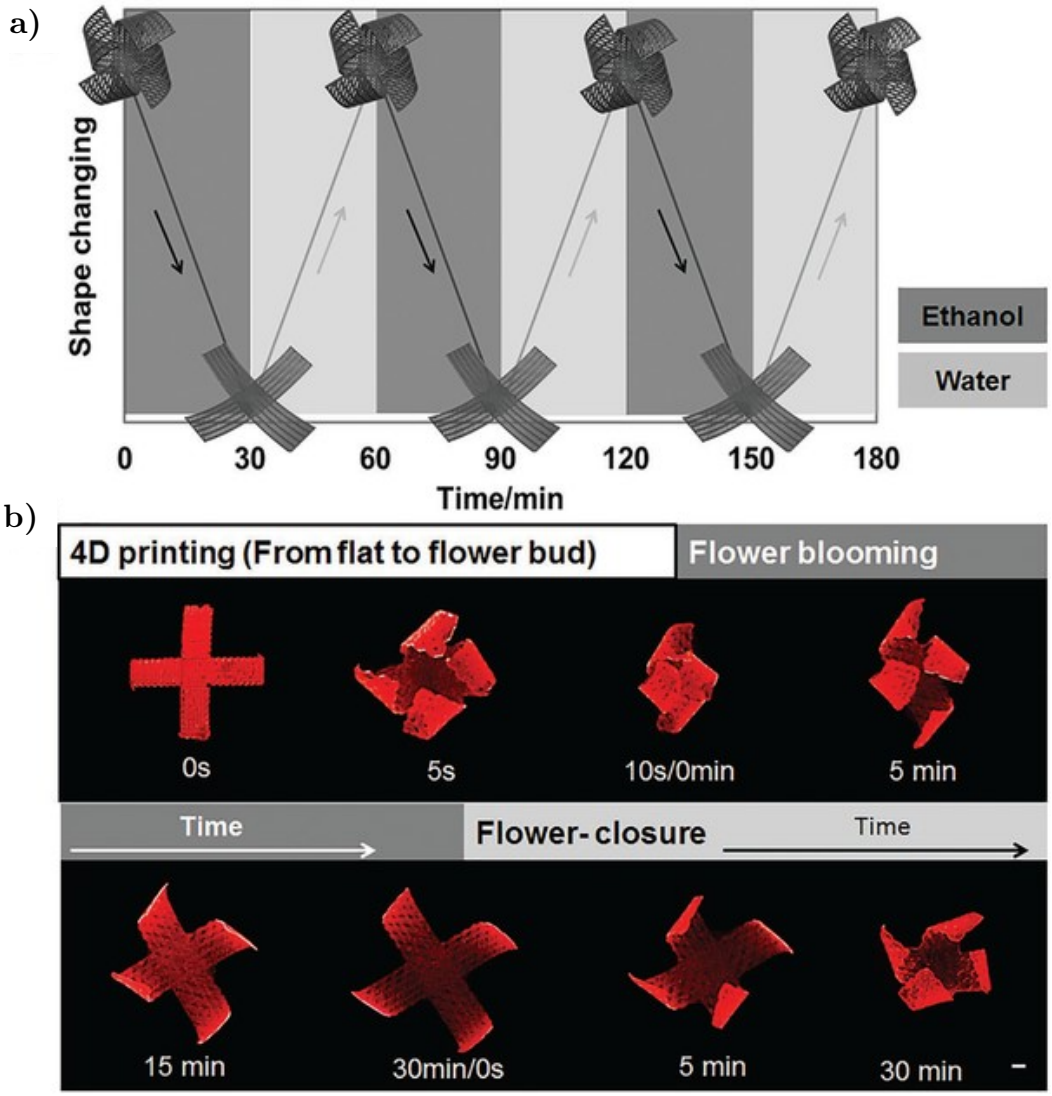

Figure 2.14: 4d printed design with dinamic reversible mechanicm of activation [180]. a) Schematic functioning diagram. b) Experimental results.

Non-planar layer techniques complement multi-material printing by improving the mechanical performance and functionality of 4D-printed parts. Traditional planar methods often result in anisotropic properties and interlayer weaknesses. Non-planar strategies, implemented through multi-axis robotic systems, address these issues by depositing materials along curved paths that align with the stresses and deformations the part will encounter. This method significantly enhances flexural strength, interlayer adhesion, and overall durability, particularly in applications like aerospace components and adaptive building facades [181, 182].

Soft robotics stands as a key area of development for 4D printing with multi-material and non-planar layers. By mimicking the compliant nature of biological systems, actuators and grippers produced using these methods achieve complex motions such as bending, twisting, and grasping. SMPs and elastomers are frequently used in combination, with SMPs providing the memory capability and elastomers offering flexibility. Non-planar layers further enhance the structural

resilience of these robotic components, enabling them to operate in constrained or hazardous environments. This synergy has proven particularly useful for medical robotics, underwater exploration, and advanced manufacturing processes. Figure 2.14 presents experimental results of 4D-printed devices activated by immersion in different liquids. The device opens when submerged in water and closes when immersed in ethanol [180].

In addition to soft robotics, the integration of bio-inspired and functionally graded designs highlights the versatility of 4D printing. These designs mimic natural interfaces, such as tendons transitioning to bone, by creating structures with gradual changes in material properties. Multi-material capabilities ensure these gradients are seamlessly integrated, while non-planar techniques optimize the structural performance. Applications range from orthopedic implants that adapt to biomechanical loads to aerospace parts that combine lightweight properties with high strength, effectively reducing material usage and improving efficiency [183].

Stimuli-responsive architectures remain a central focus in 4D printing research. Combining multi-material layers with non-planar geometries enables efficient and predictable responses to environmental triggers. Temperature-responsive SMPs combined with hydrogels have shown significant potential for applications such as smart textiles, adaptive airfoils, and deployable satellite components. These applications benefit from non-planar deposition paths, which ensure uniform deformation and robust structural integrity under complex stimuli [184]. Figure 2.15 illustrates the response of various 4D-printed actuators to a magnetic field used as a stimulus, both in simulations and experiments. It showcases the complex transformations that can be achieved with this technology [185].

Future trends in 4D printing include the adoption of artificial intelligence (AI) for process optimization, particularly in industrial-scale applications. AI algorithms are being developed to model and simulate the behavior of stimuli-responsive materials under various conditions, enabling predictive design and reducing the need for iterative prototyping. For instance, AI-driven systems are being explored to create adaptive automotive components that can modify their aerodynamic profiles in real-time, enhancing fuel efficiency [186].

Industrially, the use of multi-material 4D printing combined with non-planar techniques is gaining traction in sectors like aerospace and construction. In aerospace, adaptive wing structures that respond to flight conditions are being developed to improve performance and reduce energy consumption. Similarly, in the construction industry, deployable structures that autonomously adjust to environmental conditions are being fabricated using scalable 4D printing processes. These innovations leverage non-planar and multi-material strategies to produce robust, efficient solutions that meet the stringent demands of industrial applications [178].

The integration of 4D printing with multi-material processes and non-planar fabrication highlights its transformative potential in manufacturing. To overcome the mechanical limitations of polymers, the incorporation of metals with shape-memory or degradation-responsive properties introduces new possibilities, enhancing structural performance and expanding the range of applications. Combined with advancements in materials science, robotics, and AI-driven process optimization, these innovations position 4D printing to redefine design

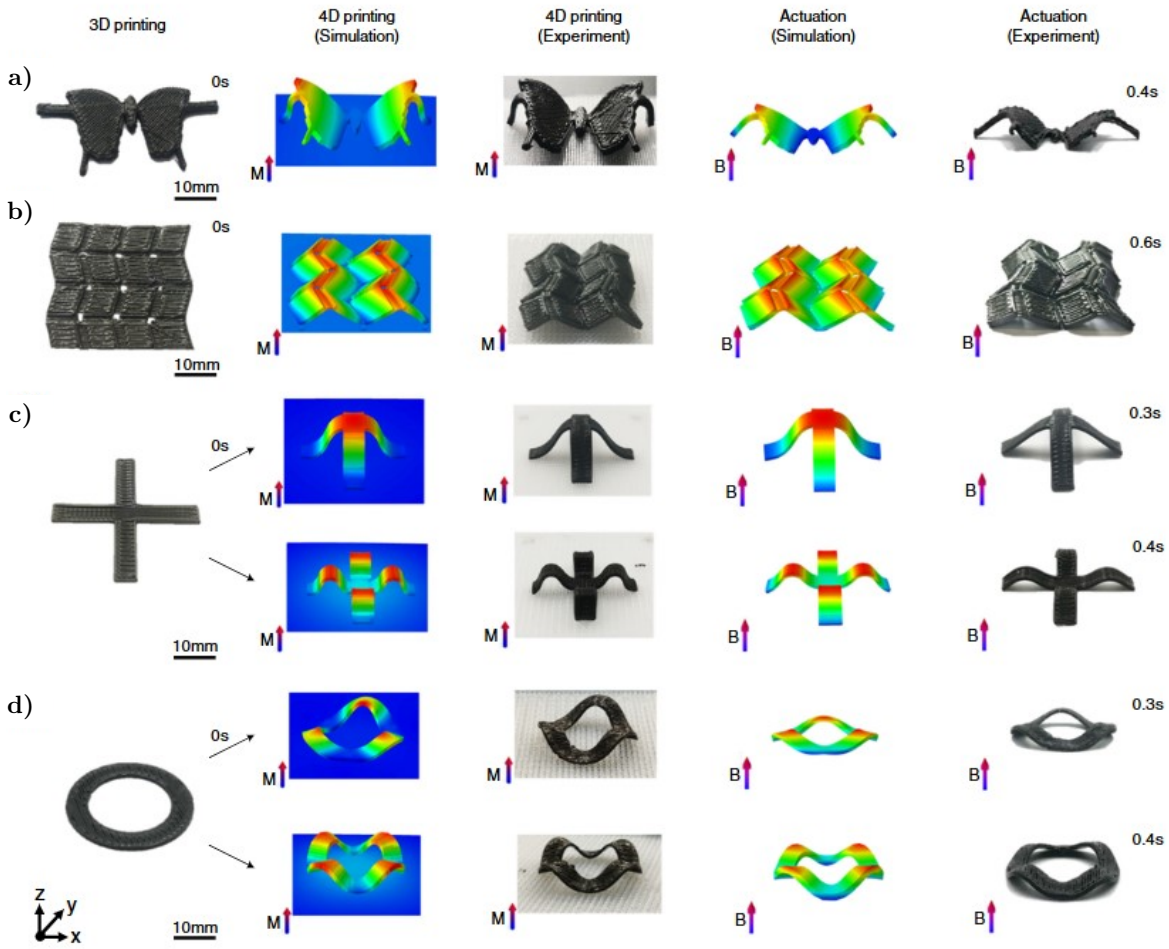

Figure 2.15: Response to magnetic stimulus of various actuators used in soft robotics [185]: a) Biomimetic butterfly. b) Miura Ori pattern. c) Cross pattern. d) Ring.

and production paradigms, driving the development of smarter, more resilient, and adaptive industrial ecosystems.

Built orientation optimization

The inherent process of additive manufacturing introduces material anisotropy, where properties such as mechanical strength, thermal conductivity, and electrical resistance vary with build orientation. This anisotropy poses challenges for structural and functional applications, particularly in components exposed to multi-axial stresses. Integrating anisotropy considerations into DfAM and exploring emerging techniques, such as non-planar layers, can mitigate these effects by aligning material properties with stress tensors, thus enhancing performance. Figure 2.16 illustrates the analysis process conducted to compare the mechanical property enhancements between two materials printed with planar and non-planar layers. The results highlight a significant improvement achieved by aligning the principal stress directions with the material's axis of greatest mechanical strength [187].

Material anisotropy is most pronounced in Fused Deposition Modeling (FDM), where weak

inter-layer adhesion and air voids compromise mechanical properties in directions perpendicular to the build plane. For example, in [188], a 27% reduction in compressive modulus was observed in the Z-direction of polylactic acid (PLA) parts compared to the longitudinal direction. Similar behavior has been reported for Selective Laser Sintering (SLS), where a 16% difference in tensile strength for polyamide 12 based on build orientation [162]. Although Digital Light Processing (DLP) and Stereolithography (SLA) exhibit lower mechanical anisotropy due to their stronger layer bonding, challenges remain in aligning properties with design requirements. A 5% anisotropy in DLP resin parts was highlighted when measured in transverse versus longitudinal orientations [189].

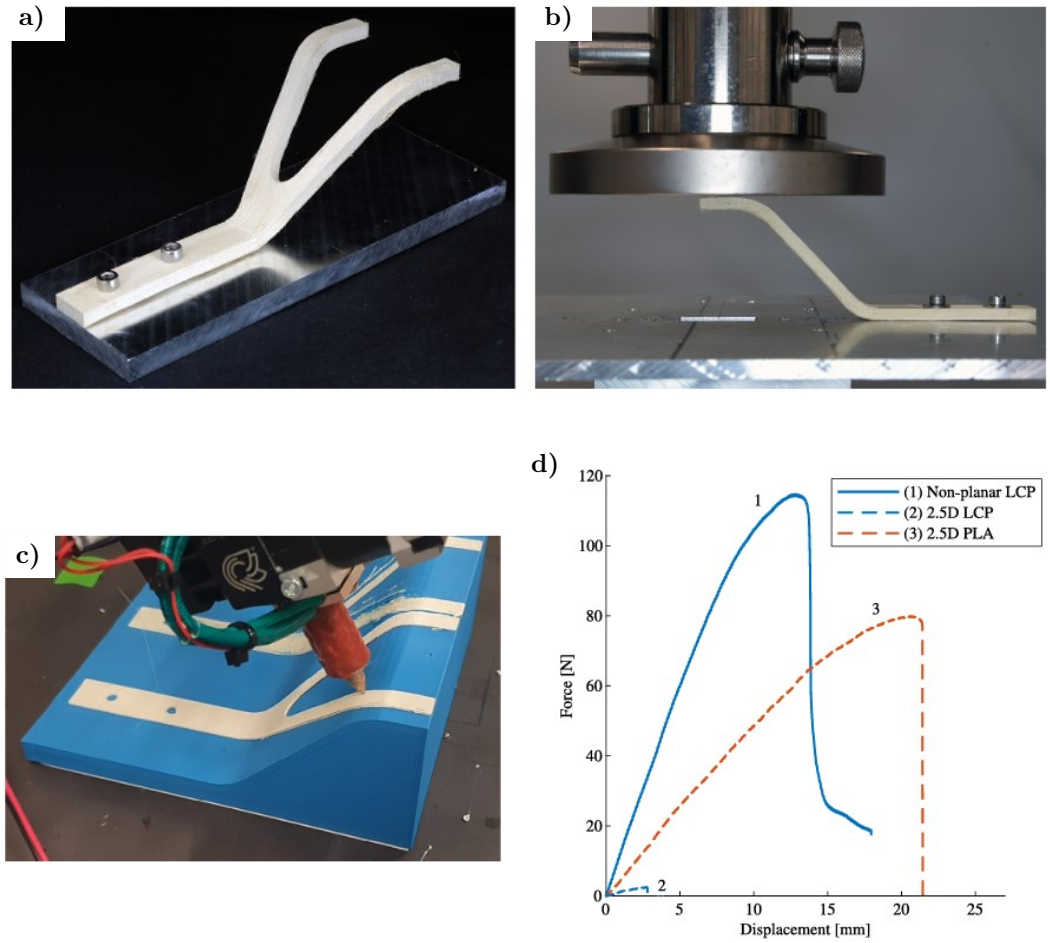

Figure 2.16: Testing to validate the improvement in mechanical strength of parts using Non-Planar Additive Manufacturing (NPAM) technology: a) Geometry selected for testing. b) Experimental setup. c) Non-planar fabrication on a 5-degree-of-freedom machine. d) Comparative results showing the performance of PLA and LCP parts produced with planar techniques versus LCP parts manufactured non-planarly [187].

Thermal and electrical anisotropies also significantly impact the functional behavior of additively manufactured polymers. Recent studies demonstrated substantial drops in thermal conductivity for ABS/Graphite composites when measured transversely, attributing this to filler alignment along deposition paths [190]. Similarly, a 32% variation in electrical resistance

in PBT/CNT composites was reported based on raster orientation [191]. These anisotropies can limit heat dissipation and electrical efficiency in components, underscoring the need for anisotropy-aware design.

Non-planar layer strategies represent a promising approach to mitigate anisotropy by aligning layers with stress tensors. Unlike traditional planar slicing, non-planar layering follows the contours of the design, improving inter-layer bonding and distributing stress more uniformly across the part. This method enhances the mechanical integrity of components under complex loading conditions, aligning material properties with the principal directions of stress. For instance, parts designed with non-planar layers exhibit improved fracture resistance as cracks propagate along pre-aligned paths rather than exploiting weak inter-layer bonds [192].

Mitigating anisotropy through DfAM requires a multi-faceted approach. Optimizing process parameters such as raster angle, layer thickness, and build orientation has shown promise in improving material performance. Alternating raster angles disrupt crack propagation, while thinner layers reduce void sizes and improve adhesion. Material innovations, including the incorporation of high-performance fillers like carbon fibers or additives like triallyl isocyanurate, have demonstrated significant improvements in layer bonding. These strategies, combined with non-planar layering techniques, not only reduce anisotropy but also unlock new possibilities for achieving isotropic or tailored properties in 3D-printed components.

Chapter 3

Theoretical Framework

3.1 Mathematical basis

This theoretical framework aims to develop the fundamental and essential concepts necessary for a proper understanding of the doctoral thesis. It has been based on the knowledge collected on the following books: [193, 194, 195, 196]. Additionally, it establishes the standard nomenclature that will be used.

3.1.1 Topology

The key topological concept around which the development of this thesis is structured is the homeomorphism of two topological spaces. Two topological spaces are considered homeomorphic if there exists a bijective, continuous function that maps one space to the other that has an inverse function.

A topological space is a set of elements, which we will call points, that are organized according to a specific topology. For a more geometric definition, this work will use topological spaces composed of a set of points to which distances are assigned, positioning them relative to one another. In other words, we will use metric topological spaces.

Let us define X and Y as two metric topological spaces. They are said to be homeomorphic if there exists a function $f : X \to Y$ that satisfies the following conditions:

- **Bijectivity:** The function f defines, for each element (point) in X, a unique point in Y (one-to-one).
- **Continuity:** The function f is continuous. For every open set in Y is an open set in X.
- **Continuous inverse:** f^{-1} is also continuous.

An isomorphism is a structure-preserving transformation between two structures of the same type. For topological spaces the term "isomorphism" is replaced by "homeomorphism" and in metric spaces, the term "isomorphism" is replaced by "transformation." It is important to highlight the significance of an isometry, which is defined as a transformation between

two metric spaces that preserves the distances between the elements (points) of the space. Reflection, rotation or translation are some commonly used isometric transformations on the Euclidean space.

While Euclidean space is the most well-known metric space, more complex metric spaces can be defined, which will be used throughout the thesis. These spaces arise from the combination of simple topological elements:

- **Line** ($\mathbb{R}^1$): which defines a position based on a lineal coordinate.
- **Plane** ($\mathbb{R}^2$): which defines a position based on two lineal coordinates.
- **Circumference** (S^1): which defines a position based on an angular coordinate.
- **Sphere** (S^2): which defines a position based on two angular coordinates.

One of the most commonly used topological elements for modeling the Joint space of a robotic manipulator is the Torus. This element allow us modelling revolute joints by their angular position. It is composed of two independent circumferences, allowing the entire surface to be mapped using two angular coordinates that vary between 0 and $2\pi[rad]$: ($T^2 = S^1 \times S^1$). It differs from the sphere, (S^2), in that both coordinates are independent, with each combination of angles reaching a unique point in the toroidal space. In contrast, on the sphere, multiple different combinations of angles can correspond to the same point as shown in Figure 3.1.

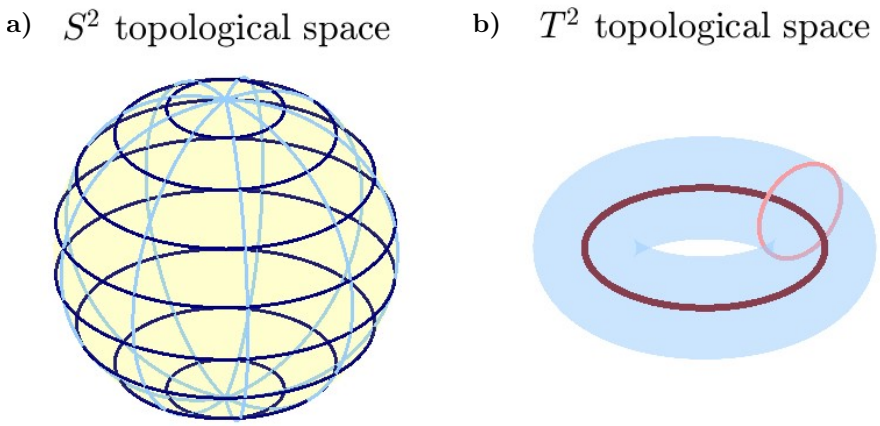

Figure 3.1: a) S^2 topological space defined by two angular coordinates corresponding to the latitude and longitude of the point: $[-180°, 180°) \times [-90°, 90°]$. b) T^2 topological space defined by two angular coordinates: $[0°, 360°) \times [0°, 360°)$.

Applying this same idea, Joint spaces of robotic manipulators can be modeled in a straightforward manner. For example, a robotic manipulator with six revolute joints ($6R$) can be modeled as a six-dimensional toroidal space: $T^6 = S^1 \times S^1 \times S^1 \times S^1 \times S^1 \times S^1$ Similarly, a manipulator with 2 revolute joints and 1 prismatic joint ($2RP$) has a Joint space in the form of a 3-dimensional space where the two revolute joints are represented by two angular coordinates, and the prismatic joint is represented by a linear coordinate: $S^1 \times S^1 \times \mathbb{R}^1 = T^2 \times \mathbb{R}^1$.

The position of a rigid body in Euclidean space can also be modeled using topological objects. This position is determined a point in a three-dimensional space, a point on a two-dimensional

sphere, and a point on a circle: $\mathbb{R}^3 \times S^2 \times S^1$.

Once the metric spaces in which this thesis will operate have been defined, it is necessary to reference them to a span. This refers to a coordinate origin that serves as a reference point for establishing the relative positions between the various elements present in the space. In two-dimensional spaces, two linearly independent vectors span a plane, and in three dimensions, three linearly independent vectors span a space. This concept can be generalized to n dimensions, where n linearly independent vectors span an n-dimensional space.

This concept, known as an orthogonal basis in Euclidean space, can be generalized to n dimensions in what is referred to as a Hilbert space. A Hilbert space is a generalization of Euclidean space to n dimensions. Moreover, if the basis vectors of the defined Hilbert space have a norm of one, this basis is known as an orthonormal basis.

Therefore, throughout the thesis, the workspaces related to the position of a rigid body in Euclidean space (World space) and the position of the joints of a 6 DoF robot (Joint space) will be modeled as two 6-dimensional Hilbert metric spaces with the previously described topologies. These spaces will be referenced to the orthonormal bases $\{s\}$ and $\{j\}$, which will be explained in subsequent chapters. Additionally, the World space will have a second 6-dimensional orthonormal reference frame associated with the end-effector of the robotic manipulator, denoted as $\{b\}$.

Finally, a non-isometric homeomorphic transformation will be applied to the Hilbert space referenced to $\{b\}$, generating the Slicing space, which is referenced to the orthonormal base $\{e\}$. This base serves as the reference for the lamination of solids in non-planar layers. Figure 3.2 represents schematically all the defined spaces and base frames with its relative transformations.

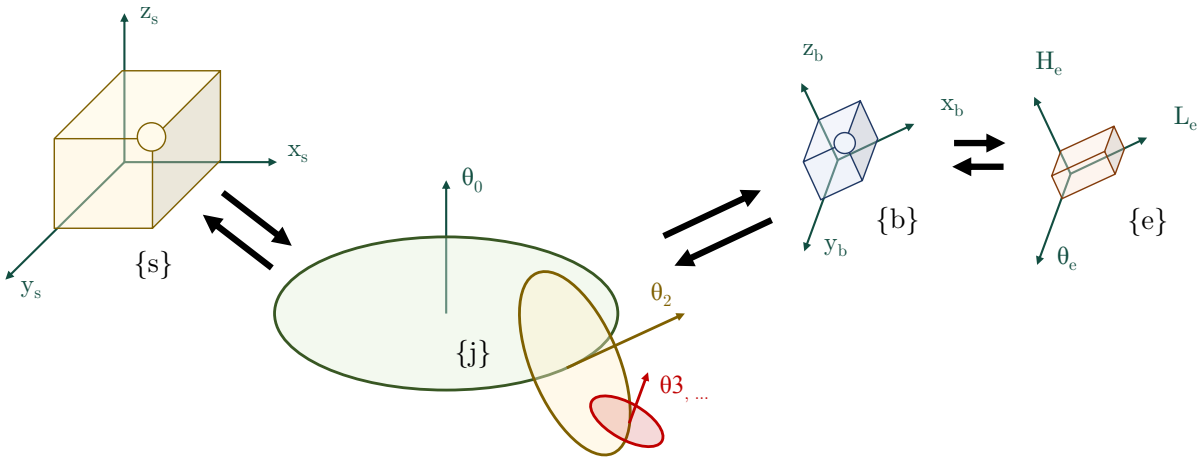

Figure 3.2: Topological definition of the four workspaces defined referred to its orthonormal base. $\{s\}$: World space referred to the robot base, $\{j\}$: Joint space, $\{b\}$: World space referred to the robot's end-effector, and $\{e\}$: Slicing space.

3.1.2 Differential geometry

Once the working spaces in which we will operate have been established, it is necessary to define a series of theoretical concepts from differential geometry that will allow us to move between the different spaces. This definition is particularly important for relating spaces $\{b\}$ and $\{e\}$.

The first relevant definition in this section is the concept of a parametric curve. To represent a curve $\mathbf{\Gamma}(u)$ parametrically in a plane or space, a variable called a parameter is defined in an interval of real numbers. Each coordinate of a point on the curve is a function dependent on the parameter. In this case, we will focus on parametric curves defined in the zx-plane: $\mathbf{\Gamma}(u) = (x(u), z(u))$. The most important properties of these curves are defined as follows:

Continuity: A curve is continuous over an interval $u \in [a, b]$ if the generating functions, $x(u)$ and $z(u)$ of that curve are continuous over that interval. This property ensures that as the parameter u changes, the position of the point $\mathbf{\Gamma}(u)$ in space changes continuously, without discontinuities.

Differentiability: A parametric curve is differentiable over an interval $u \in [a, b]$ if the functions $x(t)$, and $y(t)$ are differentiable over the interval. This means that for every $u_0 \in [a, b]$, the derivatives $x'(u_0)$, and $y'(u_0)$ exist.

According to these two properties, three types of continuity are defined:

- C^0: Curves meet at the same point at their junction.
- C^1: The tangent vectors of the two segments are equal in both magnitude and direction, meaning they share the same first parametric derivatives.
- C^2: The curves have the same second parametric derivatives at their point of connection.

Tangent vector: For any point in the parametric curve, $\mathbf{\Gamma}(u_0)$, the tangent vector $\mathbf{T}(u)$ is defined as in 3.1. This vector represents the curves local direction. Often, the tangent vector is normalized to obtain a unit vector with a length of 1 as shown in 3.2.

$$\mathbf{T}(u) = \nabla\mathbf{\Gamma}(u) = \left(\frac{\partial x(u)}{\partial u}, \frac{\partial z(u)}{\partial u}\right) \tag{3.1}$$

$$\frac{\mathbf{T}(u)}{||\mathbf{T}(u)||} = \frac{\nabla\mathbf{\Gamma}(u)}{||\nabla\mathbf{\Gamma}(u)||} \tag{3.2}$$

Curvature: At a given point in $\mathbf{\Gamma}(u)$, curvature ,κ, is the property that measures how the direction of the curve changes at that point. Mathematically, it is defined replacing equations 3.1 and 3.3 in 3.4. The higher the curvature at a point u_0, the smaller the radius of curvature ρ at that point, since $\rho(u_0) = 1/\kappa(u_0)$.

$$\nabla^2\mathbf{\Gamma}(u) = \left(\frac{d^2x(u)}{du^2}, \frac{d^2z(u)}{du^2}\right) \tag{3.3}$$

$$\kappa(u) = \frac{||\nabla\mathbf{\Gamma}(u) \times \nabla^2\mathbf{\Gamma}(u)||}{||\nabla\mathbf{\Gamma}(u)||^3} \tag{3.4}$$

Arc length: Given an interval $u \in [a, b]$ over which the curve $\mathbf{\Gamma}(u)$ is defined, the length of the curve segment between those two points in $\mathbf{\Gamma}(u)$ can be mathematically calculated as expressed in 3.5.

$$L = \int_{u(a)}^{u(b)} ||\nabla\mathbf{\Gamma}(u)||\, du \tag{3.5}$$

3.1.3 Computational geometry

Once the geometric properties of a parametric curve necessary for subsequent geometric developments have been defined, we proceed to explain how to computationally operate with curves of this nature. The requirements of this work necessitate the ability to approximate curves of an unknown mathematical form to parametric curves in order to obtain the previously described parameters. To achieve this, cubic B-spline representation has been selected.

B-splines have been chosen for modeling parametric curves due to their flexibility in approximating curves. Firstly, B-splines are concatenable and, through their definition, allow us to ensure the desired type of continuity (C^0, C^1, or C^2) at the joining point. Additionally, they are locally modifiable, meaning that to readjust a specific area of the curve, it is sufficient to modify the control points in that region while leaving the rest unchanged. Finally, if more detail is needed in a particular area, it is easy to incorporate additional control points there.

Mathematically, a Bézier curve is defined by a set of control points $\mathbf{P}_0, \mathbf{P}_1, \ldots, \mathbf{P}_n$. The number of control points determines the degree of the curve. For instance, if there are $n+1$ control points, the curve is of degree n. Any bezier curve $\mathbf{B}(t)$ can be define as 3.6, where $b_{i,n}(t)$ are the Bernstein polynomials given by 3.7, with $t \in [0, 1]$ and being $\binom{n}{i}$ the binomial coefficient.

$$\mathbf{B}(t) = \sum_{i=0}^{n} b_{i,n}(t)\mathbf{P}_i \tag{3.6}$$

$$b_{i,n}(t) = \binom{n}{i} t^i (1-t)^{n-1}, \qquad i = 0, 1, \ldots, n \tag{3.7}$$

The content of this work has been carried out using cubic B-splines. In this case, $n = 3$, meaning that 4 control points are required for the definition of the curve. Figure 3.3 shows the definition of a cubic B-spline curve based on its control points, as well as the resulting Bernstein polynomials applied in this context. The polygon created by connecting the control points with lines, beginning with P_0 and ending with P_n, is referred to as the control polygon. The convex hull of the control polygon encompasses the Bézier curve.

Some of the most interesting properties of Bézier splines are:

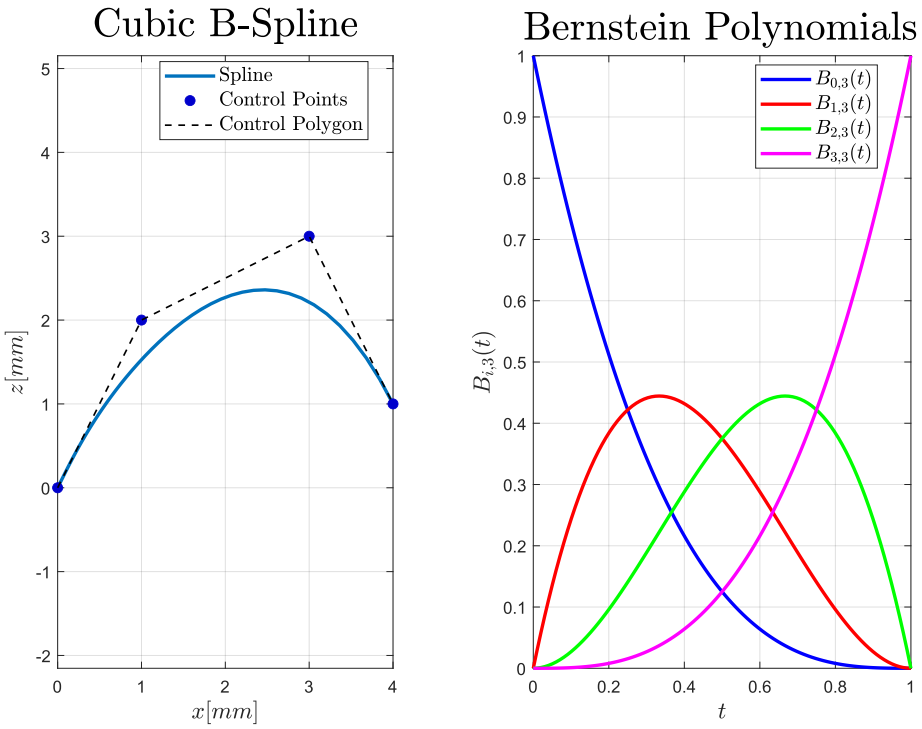

Figure 3.3: Cubic B-spline representation with control polygon defined by points: $P_0 = (0, 0)$, $P_1 = (1, 2)$, $P_2 = (3, 3)$, and $P_3 = (4, 1)$. Bernstein polynomials associated to a cubic B-spline definition.

- The curve is a straight line if and only if all the control points are collinear.
- The beginning and end of the curve are tangent to the first and last segments of the Bézier polygon, respectively.
- a curve can be divided at any point into two subcurves, or into any number of subcurves, each of which is also a Bézier curve.
- A Bézier curve of order greater than two can self-intersect or exhibit a cusp depending on the specific selection of control points.

Bézier curves can be connected based on the described properties to form more complex curves. This feature is particularly interesting and warrants further theoretical exploration. When two Bézier curves share either an initial or final control point, we can assert that they generate a larger B-spline that satisfies the C^0 continuity criterion. This new B-spline will be defined for $t \in [0, 2]$. In this way, as many curves as needed in the application can be concatenated.

If the continuity condition needs to be increased to a higher order, there will be a C^1 continuity condition as long as the points $\mathbf{P}_{n-1}$, $\mathbf{P}_n$, and $\mathbf{P}_{n+1}$, are collinear. Being $\mathbf{P}_n$ the shared control point of both connected B-splines.

Furthermore, if C^2 continuity is required, it must be added to the previous two conditions

that the distances between $\mathbf{P}_{n-1}$ and $\mathbf{P}_n$, as well as between $\mathbf{P}_n$ and $\mathbf{P}_{n+1}$, must be equal. Figure 3.4 illustrates the three possible types of continuity when concatenating two B-splines.

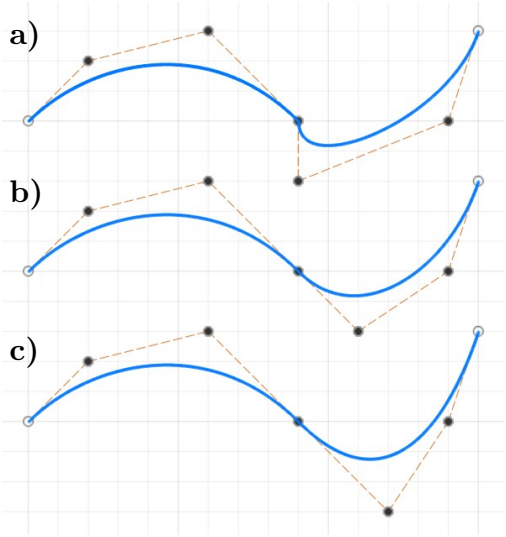

Figure 3.4: a) Spline concatenation with C^0 continuity. b) Spline concatenation with C^1 continuity. c) Spline concatenation with C^2 continuity.

The second computational geometry concept necessary for this work is the convex hull of a set of points in the plane. A convex hull of a set of points is defined as the smallest convex polygon that can contain all the points of the set either inside or on its boundary. It can be visualized as the shape formed by stretching a rubber band around the outermost points in the set.

The convex hull of a set of points has the following properties:

- **Convexity:** Any segment between two points of the polygon remains inside it.
- **Uniqueness:** Given a set of points, its convex hull is unique.
- **Minimality:** It is the polygon with the fewest possible sides that can contain all the points.

In general, generating a convex hull of a set of points in our application is often not sufficient. It becomes necessary to look for mathematical tools that allow us to define the contour of these sets with greater precision. One of the most widely used tools is the alpha-shape.

Alpha-shapes extend the concept of convex hulls by enabling the generation of more precise and tighter boundaries around a set of points, taking into account the local point density and spatial arrangement. By adjusting the parameter α, the level of detail in the resulting contour can be controlled, allowing for the capture of finer geometric features within the point set. This tool even allows for the modeling of contours with internal holes.

Figure 3.5 illustrates the disparity in precision achieved by both the convex hull and alpha-shape polygons, as generated from the same point set S.

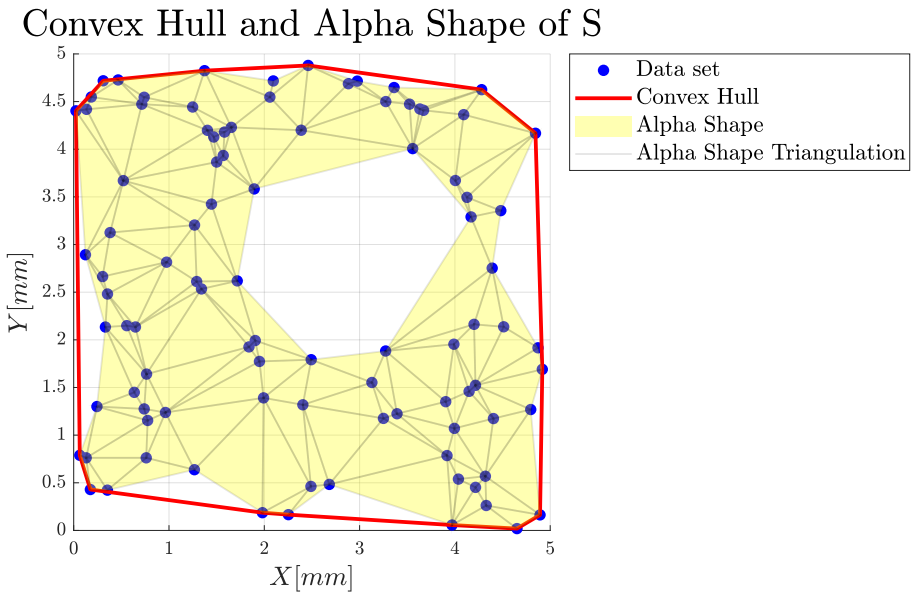

Figure 3.5: Convex hull and alpha shape polygons associated to the 2D point set S.

3.2 Robotics

This section aims to materialize the connection between the previously described mathematical concepts and robotics through the multibody theory developed via screw axis and Lie algebra. This perspective greatly facilitates kinematic calculations, trajectory generation, and the relative positioning of bodies in space.

3.2.1 Robot space representation

At the mechanical engineering level, we define a robot as a set of links that act as rigid solids. Each of them is connected to another through an articulation, which can be of various types: revolute joint (R), prismatic joint (P), helical joint (H), spherical joint (S), etc. The joints are operated by a series of actuators, which can be of different kinds. These actuators are governed by a controller. Finally, the tool carried by the robot to perform the commanded task is called end-effector.

The Degrees of Freedom (DoF) of a robotic manipulator are defined as the number of independent coordinates required to define the position and orientation of the entire system. The DoF depend on the constraints imposed on the joints connecting each link. Each rigid solid of the mechanism can move in space with six freedoms, $m = 6$, three rotations, and three translations. Each joint, $j_{1,2,\dots,n}$, adds a set of constraints c_i to the body freedoms. Therefore, by setting N as the total number of links in the manipulator, including the ground link, the DoF of the robotic manipulator can be determined using Grübler's Equation (3.8).

$$DoF = m(N-1) - \sum_{j_1}^{j_n} c_i \tag{3.8}$$

We consider an open-chain mechanism or serial mechanisms to be ones that connects only one of its links to the ground. On the other hand, we consider a closed-chain mechanisms to be ones that has multiple links connected to the ground. The robotic manipulators used in this work will always be serial mechanisms with revolute joints.

In order to carry out the robot motion calculations it is necessary to define a local coordinate system associated with each link. Of all these coordinate systems, two stand out: the system associated with the ground: $\{s\}$ frame, and the system associated with the end-effector: $\{b\}$ frame. Usually, the end-effector frame matches the frame known as Tool Center Point $\{TCP\}$. This frame refers the exact location where the end-effector is attached to the robot. See Figure 3.6.

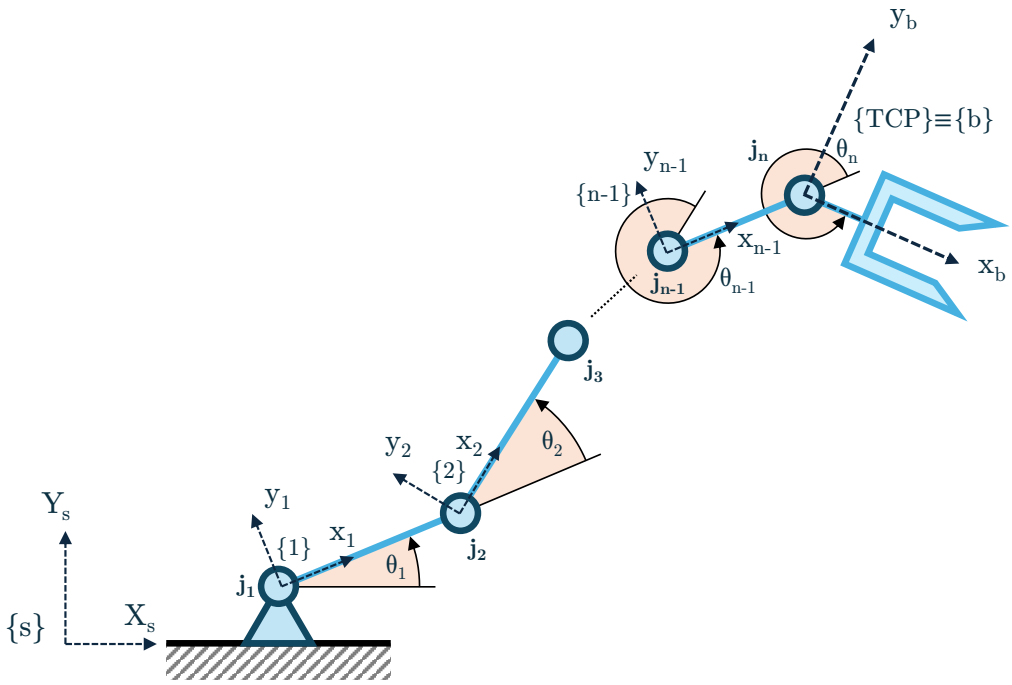

Figure 3.6: Robot frames definition, Global space frame, $\{s\}$; end-effector frame, $\{b\}$; and link associated frames $\{1, 2, ..., n\}$. Joint identification: $j_{1,2,...,n}$. Joint position coordinate $\theta_{1,2,...,n}$

Figure 3.6, also defines the joint position coordinates $\theta_{1,2,...,n}$. These coordinates can be angular or linear, and a single joint may have more than one coordinate if its position is defined by two or more DoF. The global position of the robot is represented as $\mathbf{\Theta}$ and the manipulator's home position, or zero position, is therefore defined as $\mathbf{\Theta}_H$ as shown in Equation 3.9.

$$\mathbf{\Theta} = \begin{bmatrix} \theta_1 \\ \theta_2 \\ \vdots \\ \theta_n \end{bmatrix} \qquad \mathbf{\Theta}_H = \begin{bmatrix} 0 \\ 0 \\ \vdots \\ 0 \end{bmatrix} \tag{3.9}$$

A robotic manipulator works between two different spaces known as the World space and the

Joint space. To understand them, a topological representation of both spaces in which the robot operates must be established.

The World space is a Carthesian space which defines the position and orientation of a body using six coordinates, with any object described by three linear coordinates in $\mathbb{R}^3$ and three angular coordinates: one on the surface of a two-dimensional sphere S^2 and another on a one-dimensional circle S^1. It gives a total Carthesian space of $\mathbb{R}^3 \times S^2 \times S^1$. These coordinates can be referenced to any of the frames mentioned in Figure 3.6, and the relationship between the coordinates in each frame can be calculated.

The Joint space is determined by the type of joints connecting the robot's links; in this work, all joints are revolute. Topologically, the Cartesian space of a 2R robot, which has two revolute joints in a plane, can be represented as $S^1 \times S^1 = T^2$. Here, T^2 describes the surface of a torus in three-dimensional space using two angular coordinates. Extending this to an nR robot, its Cartesian space can be defined as T^n, representing the surface of a torus in an $n+1$-dimensional space. The Joint Space is typically associated with the frame $\{j\}$, where the origin of the coordinates corresponds to the robot's home position.

The connection between the two spaces, World space and Joint space, is established through the robot's kinematics. The transformation from World space to Joint Space is referred to as forward kinematics, while the reverse operation is known as inverse kinematics.

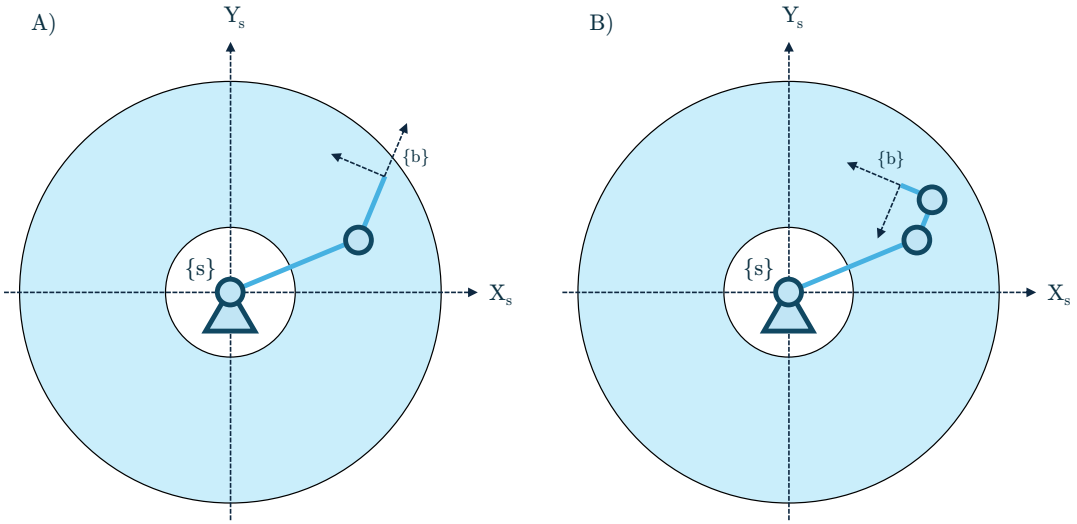

Figure 3.7: A) Planar 2R robot workspace referred to $\{s\}$ in light blue. B) Planar 3R robot workspace referred to $\{s\}$ in light blue.

Finally, it is necessary to define the boundaries of the robot's workspace. The workspace is defined as the set of points relative to $\{s\}$ that the robot can reach. The task space is defined as the set of points relative to $\{s\}$ that the robot can reach in any direction to perform the commanded task. All points in the task space belong to the workspace, but not every point in the workspace is suitable for performing every task. Figure 3.7 illustrates how adding a third revolute joint can expand the robot's task space without altering its workspace.

3.2.2 Rigid-body motion: Screw Theory

Rotations matrices

A rotation matrix $\mathbf{R}$ is a matrix used to represent the orientation of an object in space. Additionally, it can function as an operator, allowing for the transformation of the reference frame with respect to which a vector is defined, or enabling the rotation of a vector or frame.

When a rotation matrix $\mathbf{R}_a = \mathbf{R}_{sa}$ or $\mathbf{R}_{ab}$ is intended to represent orientation, the subscript a denotes the orientation of the global space frame $\{s\}$ relative to $\{a\}$, and the subscript ab denotes the orientation of frame $\{b\}$ relative to $\{a\}$. From Figure 3.8, we can see how $\mathbf{R}_a$ and $\mathbf{R}_{ab}$ are expressed in 3.10. The property $\mathbf{R}_{ij} = \mathbf{R}_{ji}^T$ always holds true for any pair of frames i and j.

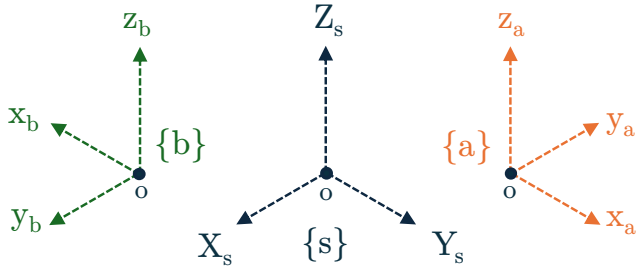

Figure 3.8: Representation of $\{s\}$, $\{a\}$, and $\{b\}$ frames with the same origin in o.

$$\mathbf{R}_a = \mathbf{R}_{sa} = \begin{bmatrix} 0 & -1 & 0 \\ 1 & 0 & 0 \\ 0 & 0 & 1 \end{bmatrix} \qquad \mathbf{R}_{ab} = \begin{bmatrix} -1 & 0 & 0 \\ 0 & -1 & 0 \\ 0 & 0 & 1 \end{bmatrix} \tag{3.10}$$

When using a rotation matrix to change reference frames, $\mathbf{R}_{as}$ represents the orientation of frame $\{a\}$ relative to frame $\{s\}$, and $\mathbf{R}_{sb}$ represents the orientation of frame $\{s\}$ relative to the fixed frame $\{a\}$. Therefore, the orientation of frame $\{a\}$ relative to frame $\{b\}$, $\mathbf{R}_{ab}$ can be calculated as shown in 3.11.

$$\mathbf{R}_{as} \cdot \mathbf{R}_{sb} = \mathbf{R}_{ab} \qquad \begin{bmatrix} 0 & 1 & 0 \\ -1 & 0 & 0 \\ 0 & 0 & 1 \end{bmatrix} \cdot \begin{bmatrix} 0 & 1 & 0 \\ -1 & 0 & 0 \\ 0 & 0 & 1 \end{bmatrix} = \begin{bmatrix} -1 & 0 & 0 \\ 0 & -1 & 0 \\ 0 & 0 & 1 \end{bmatrix} \tag{3.11}$$

The ultimate purpose of a rotation matrix is to rotate a vector or a frame around an axis $\hat{\omega} = (\omega_1, \omega_2, \omega_3)$ an angle θ. If we understand $\mathbf{R}$ as a rotation operator, $\mathbf{Rot}(\hat{\omega}, \theta)$, we can express a generic rotation as shown in 3.12. This rotation matrix simplifies when rotating a body or set of points, with respect to one of the coordinate axes of the frame to which they are referenced, as shown in 3.13. The positive rotation goes on the direction of the right-hand convention.

Starting with a rotation matrix as a form of relative orientation $\mathbf{R}_{sa}$, multiplication by the rotation operator $\mathbf{Rot}(\hat{x}, 90)$ can result in two possible rotations. If the operator is pre-multiplied, the rotation is understood to occur around the x-axis of the fixed frame $\{s\}$.

$$\mathbf{Rot}(\hat{\omega},\theta) = \begin{bmatrix} c_\theta + \omega_1^2(1-c_\theta) & \omega_1\omega_2(1-c_\theta) - \omega_3 s_\theta & \omega_1\omega_3(1-c_\theta) + \omega_2 s_\theta \\ \omega_1\omega_2(1-c_\theta) + \omega_3 s_\theta & c_\theta + \omega_2^2(1-c_\theta) & \omega_2\omega_3(1-c_\theta) - \omega_1 s_\theta \\ \omega_1\omega_3(1-c_\theta) - \omega_2 s_\theta & \omega_2\omega_3(1-c_\theta) + \omega_1 s_\theta & c_\theta + \omega_3^2(1-c_\theta) \end{bmatrix} \tag{3.12}$$

Equation 3.12: The expression c_θ refers to $cos(\theta)$ and the expression s_θ refers to $sin(\theta)$.

$$\mathbf{Rot}(\hat{x}_i,\theta) = \begin{bmatrix} 1 & 0 & 0 \\ 0 & cos(\theta) & -sin(\theta) \\ 0 & sin(\theta) & cos(\theta) \end{bmatrix} \quad \mathbf{Rot}(\hat{y}_i,\theta) = \begin{bmatrix} cos(\theta) & 0 & sin(\theta) \\ 0 & 1 & 0 \\ -sin(\theta) & 0 & cos(\theta) \end{bmatrix}$$
$$\mathbf{Rot}(\hat{z}_i,\theta) = \begin{bmatrix} cos(\theta) & -sin(\theta) & 0 \\ sin(\theta) & cos(\theta) & 0 \\ 0 & 0 & 1 \end{bmatrix} \tag{3.13}$$

Equation 3.13: The torarion axes $(\hat{x}_i, \hat{y}_i, \hat{z}_i)$ represent the coordinate axes of the generic frame $\{i\}$ where the rotation is referred.

If the operator is post-multiplied, the rotation is understood to occur around the x-axis of the referenced frame$\{a\}$. Figure 3.9 shows both results.

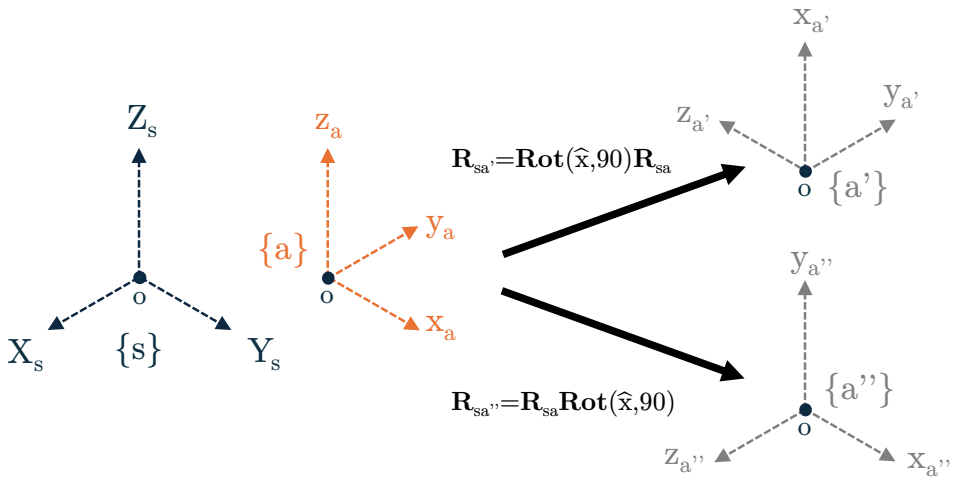

Figure 3.9: Representation of $\{a'\}$, and $\{a''\}$ as the result of pre-multiplying and post-multiplying the rotation operation $\mathbf{Rot}(\hat{x}, 90)$ with $\mathbf{R}_{sa}$.

Homogeneous transformation matrices

After defining a rotation matrix as a method for orienting frames and as an operator, we will represent the position and orientation of a rigid body as a combination of a rotation matrix $\mathbf{R} = \mathbf{R}_{sb} \in SO(3)$, which orients the body's frame $\{b\}$ relative to the fixed frame $\{s\}$, and a displacement defined by a column vector $\mathbf{p} \in \mathbb{R}^3$, representing the origin of $\{b\}$ relative to $\{s\}$.

The Special Euclidean group $SE(3)$ is defined as the group of homogeneous transformation matrices, or rigid body motions, in $\mathbb{R}^3$. It consists of a $\mathbf{T}$ form set of 4×4 matrices described in 3.14.

$$\mathbf{T} = \begin{bmatrix} \mathbf{R} & \mathbf{p} \\ 0 & 1 \end{bmatrix} = \begin{bmatrix} r_{11} & r_{12} & r_{13} & p_1 \\ r_{21} & r_{22} & r_{23} & p_2 \\ r_{31} & r_{32} & r_{33} & p_3 \\ 0 & 0 & 0 & 1 \end{bmatrix} \tag{3.14}$$

For any $\mathbf{T} \in SO(3)$, the following properties hold: the inverse of a homogeneous transformation matrix is also a homogeneous transformation matrix, the product of two homogeneous transformation matrices is another homogeneous transformation matrix, and the product of homogeneous transformation matrices is associative but not commutative.

Homogeneous transformation matrices can be used in the same cases as rotation matrices, but they implicitly include both the position and orientation of a reference frame attached to body $\{b\}$ relative to the fixed frame $\{s\}$.

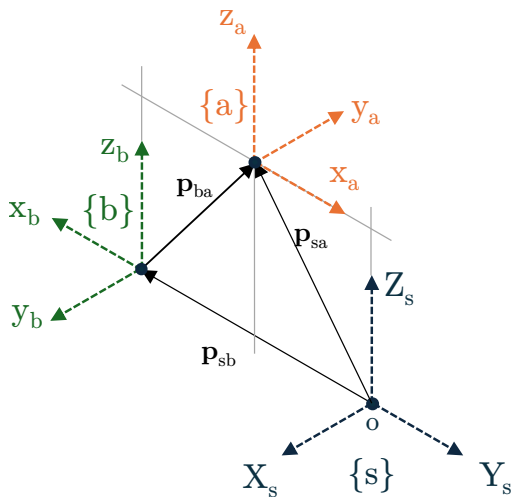

Figure 3.10: Relative position and orientation of frames $\{s\}$, $\{a\}$, and $\{b\}$

When $\mathbf{T} \in SE(3)$ is used to represent position and orientation of a frame, the same guidelines as with $\mathbf{R} \in SO(3)$ are followed. For the frames represented in Figure 3.10, their relative orientation matrices are shown in 3.23 as well as their relative origin location in 3.16. Their Homogeneous Transformation matrices are constructed as shown in 3.17.

$$\mathbf{R}_{sa} = \begin{bmatrix} 0 & -1 & 0 \\ 1 & 0 & 0 \\ 0 & 0 & 1 \end{bmatrix} \qquad \mathbf{R}_{sb} = \begin{bmatrix} 0 & 1 & 0 \\ -1 & 0 & 0 \\ 0 & 0 & 1 \end{bmatrix} \qquad \mathbf{R}_{ba} = \begin{bmatrix} -1 & 0 & 0 \\ 0 & -1 & 0 \\ 0 & 0 & 1 \end{bmatrix} \tag{3.15}$$

$$\mathbf{p}_{sa} = \begin{bmatrix} 0 \\ -1 \\ 1 \end{bmatrix} \qquad \mathbf{p}_{sb} = \begin{bmatrix} 0 \\ -2 \\ 0 \end{bmatrix} \qquad \mathbf{p}_{ba} = \begin{bmatrix} -1 \\ 0 \\ 1 \end{bmatrix} \tag{3.16}$$

$$\mathbf{T}_{sa} = \begin{bmatrix} 0 & -1 & 0 & 0 \\ 1 & 0 & 0 & -1 \\ 0 & 0 & 1 & 1 \\ 0 & 0 & 0 & 1 \end{bmatrix} \qquad \mathbf{T}_{sb} = \begin{bmatrix} 0 & 1 & 0 & 0 \\ -1 & 0 & 0 & -2 \\ 0 & 0 & 1 & 0 \\ 0 & 0 & 0 & 1 \end{bmatrix} \qquad \mathbf{T}_{ba} = \begin{bmatrix} -1 & 0 & 0 & -1 \\ 0 & -1 & 0 & 0 \\ 0 & 0 & 1 & 1 \\ 0 & 0 & 0 & 1 \end{bmatrix} \tag{3.17}$$

When using Transformation matrices $\mathbf{T}$ to change the reference frame, the process is analogous to that used for rotation matrices $\mathbf{R}$. Continuing with the previous example: $\mathbf{T}_{sa} = \mathbf{T}_{sb}\mathbf{T}_{ba}$

Finally, when using a Homogeneous Transformation matrix to displace a body (rotation + translation), $\mathbf{T}$ is constructed from a rotation operator $\mathbf{Rot}(\hat{\omega}, \theta)$ and a translation column vector $\mathbf{p} = (p_x, p_y, p_z)^T$. An example of $\mathbf{T}(\mathbf{Rot}(\hat{y}, \theta), (1, 0, 0)^T)$ is shown in 3.18.

$$\mathbf{T}(\mathbf{Rot}(\hat{y}, \theta), (1, 0, 0)^T) = \begin{bmatrix} \mathbf{Rot}(\hat{y}, \theta) & \mathbf{p} \\ 0 & 1 \end{bmatrix} = \begin{bmatrix} cos(\theta) & -sin(\theta) & 0 & 1 \\ sin(\theta) & cos(\theta) & 0 & 0 \\ 0 & 0 & 1 & 0 \\ 0 & 0 & 0 & 1 \end{bmatrix} \tag{3.18}$$

As in the previous case, pre-multiplying by the displacement operator $\mathbf{T}(\mathbf{Rot}(\hat{y}, \theta), (1, 0, 0)^T)$ refers the transformation to the fixed frame $\{s\}$, while post-multiplying refers it to the body frame $\{b\}$. This is illustrated in Figure 3.11 for the case $\theta = 90°$. Pre-multiplication first performs the rotation and then the translation, whereas post-multiplication first performs the translation and then the rotation.

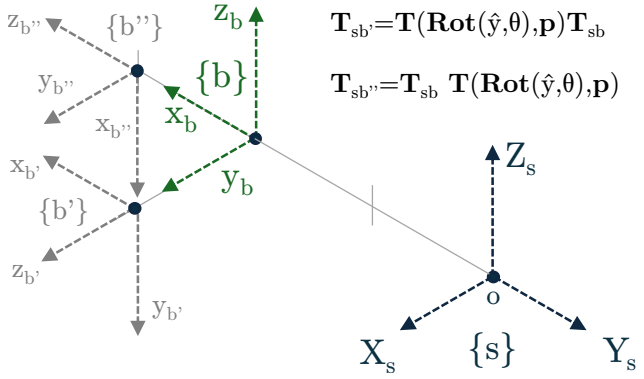

Figure 3.11: Graphical result of pre-multiplying and post-multiplying the displacement operator $\mathbf{T}(\mathbf{Rot}(\hat{y}, 90°), (1, 0, 0)^T)$ and the relative position matrix $\mathbf{T}_{sb}$.

Screw axis definition

A normalized Screw axis $\mathcal{S}$ for a given reference frame defines its combined movement consisting of rotation around the axis and translation along the axis. A screw axis is characterized by a point q, a unit direction vector $\vec{s}$ and a pith $h = v/\omega$ being v the linear speed along the axis and ω the angular speed around it. See Figure 3.12. For a screw axis to be normalized, it must satisfy that one of $||\vec{\omega}||$ or $||\vec{v}||$ must be unity.

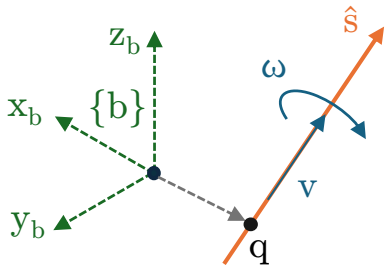

Figure 3.12: Graphical representation of a Screw axis.

When $||\vec{\omega}|| = 0$, the Screw axis represents pure translational motion, as h becomes infinite. However, if $||\vec{\omega}|| = 1$, $\vec{v}$ is calculated according to $\vec{v} = -\vec{\omega} \times \vec{q} + h \cdot \vec{\omega}$. For pure rotation in this case h must be zero.

A Screw axis $\mathcal{S}(\omega, v)$ can be written as a 4×4 matrix $[\mathcal{S}]$ as shown in 2.2. The matrix formula of $\mathcal{S}$ is expressed in $se(3)$ which is the adjoint representation of $SE(3)$.

$$[\mathcal{S}] = \begin{bmatrix} [\omega] & v \\ 0 & 0 \end{bmatrix} = \begin{bmatrix} 0 & -\omega_3 & \omega_2 & v_x \\ \omega_3 & 0 & -\omega_1 & v_y \\ -\omega_2 & \omega_1 & 0 & v_z \\ 0 & 0 & 0 & 0 \end{bmatrix} \in se(3) \tag{3.19}$$

3.2.3 Robot kinematics

Forward kinematics

Forward kinematics refers to the calculation of the relationship between the position and orientation of the end-effector frame $\{b\}$ respect to the fixed frame $\{s\}$ for a given joint configuration $\mathbf{\Theta} = (\theta_1, \theta_2, \theta_3)$.

Using the $3R$ planar robot in Figure 3.13 as an example, and applying the Homogeneous Transformation matrices described above, we can refer the position and orientation of $\{b\}$ to $\{s\}$. To model de multy-body system, its interesting to refer $\{b\}$ to $\{s\}$ by using the intermediate frames $\{1\}$ and $\{2\}$ as shown in 3.20. Each $\mathbf{T}$ matrix is described in 3.21. This expression allows for the calculation of the position and orientation of the end-effector for any value of $\mathbf{\Theta}$.

$$\mathbf{T}_{sb} = \mathbf{T}_{s1}\mathbf{T}_{12}\mathbf{T}_{2b} \tag{3.20}$$

$$\mathbf{T}_{s1} = \begin{bmatrix} cos(\theta_1) & -sin(\theta_1) & 0 & 0 \\ sin(\theta_1) & cos(\theta_1) & 0 & 0 \\ 0 & 0 & 1 & 0 \\ 0 & 0 & 0 & 1 \end{bmatrix} \quad \mathbf{T}_{12} = \begin{bmatrix} cos(\theta_2) & -sin(\theta_2) & 0 & L_1 \\ sin(\theta_2) & cos(\theta_2) & 0 & 0 \\ 0 & 0 & 1 & 0 \\ 0 & 0 & 0 & 1 \end{bmatrix}$$
$$\mathbf{T}_{2b} = \begin{bmatrix} cos(\theta_3) & -sin(\theta_3) & 0 & L_2 \\ sin(\theta_3) & cos(\theta_3) & 0 & 0 \\ 0 & 0 & 1 & 0 \\ 0 & 0 & 0 & 1 \end{bmatrix} \tag{3.21}$$

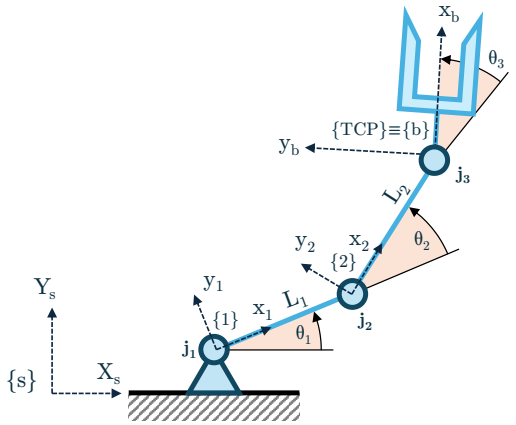

Figure 3.13: Reference frames for $3R$ plane robot. The lengths of links 1 and 2 are respectively L_1, and L_2. Frames $\{s\}$ and $\{1\}$ have the same origin but are shown separately for clarity.

An alternative is the use of Screw axes to simplify the computation of the robot's kinematics. For this purpose, each joint, in this case of type R, is defined as a screw axis, and the position of frame $\{b\}$ relative to frame $\{s\}$ is modeled as a Product of Exponentials (PoE). For any robot manipulator, the PoE formula can be defined as in 3.22.

$$\mathbf{T}_{sb}(\mathbf{\Theta}) = e^{[\mathcal{S}_1]\theta_1} e^{[\mathcal{S}_2]\theta_2} \ \cdots \ e^{[\mathcal{S}_n]\theta_n} \mathbf{M} \tag{3.22}$$

The matrix $\mathbf{M}$ is defined as as the position and orientation of $\{b\}$ referred to $\{b\}$ at the robot's home position $\mathbf{\Theta}_H$. $\mathbf{M} = \mathbf{T}_{sb}(\mathbf{\Theta}_H)$. Following the example of Figure 3.13, $\mathbf{M}$ is defined in

$$\mathbf{M} = \begin{bmatrix} 1 & 0 & 0 & L_1 + L_2 \\ 0 & 1 & 0 & 0 \\ 0 & 0 & 1 & 0 \\ 0 & 0 & 0 & 0 \end{bmatrix} \tag{3.23}$$

$\mathcal{S}$ represents the screw axis with zero pitch associated with each joint. Since they have zero pitch, $h = 0$ and $||\vec{\omega}|| = 1$. For example, the screw axis $\mathcal{S}_3$ for joint j_3 can be expressed as shown in 3.24. $\mathcal{S}_3$ is constructed from: $\vec{\omega}_3$, which is the unit vector along the rotation axis of

j_3, $(0,0,1)$ and $\vec{v_3}$ which is calculated as in 3.25, where $h=0$ and $\vec{q_3}$ is the position vector of any point in the joint axis referred to $\{s\}$ at $\mathbf{\Theta}_H$.

$$[\mathcal{S}]_3 = \begin{bmatrix} 0 & -1 & 0 & 0 \\ 1 & 0 & 0 & -(L_1+L_2) \\ 0 & 0 & 0 & 0 \\ 0 & 0 & 0 & 0 \end{bmatrix} \tag{3.24}$$

$$\vec{v_3} = -\vec{\omega_3} \times \vec{q_3} + h \cdot \vec{\omega_3} = -[(0,0,1) \times (L_1+L_2,0,0)] = -(0, L_1+L_2, 0) \tag{3.25}$$

The same procedure is followed with $\mathcal{S}_2$ and $\mathcal{S}_1$ and the result is shown in 3.26. By using the PoE formula (3.22), the position and orientation of $\{b\}$ referred to $\{s\}$ can be obtained for any value of $\mathbf{\Theta}$.

$$[\mathcal{S}]_2 = \begin{bmatrix} 0 & -1 & 0 & 0 \\ 1 & 0 & 0 & -L_1 \\ 0 & 0 & 0 & 0 \\ 0 & 0 & 0 & 0 \end{bmatrix} \qquad [\mathcal{S}]_1 = \begin{bmatrix} 0 & -1 & 0 & 0 \\ 1 & 0 & 0 & 0 \\ 0 & 0 & 0 & 0 \\ 0 & 0 & 0 & 0 \end{bmatrix} \tag{3.26}$$

The main advantages of this methodology over others, such as Denavit-Hartenberg parameters (D-H parameters), are that it does not require the definition of any link frames, avoids local singularities, and allows for closed-form calculations of inverse kinematics, which will be explained later in the document. A robot singularity is a condition where a robotic manipulator loses its ability to move in certain directions.

In some situations, it is easier to define the trajectory's target points in frame $\{b\}$. In such cases, the PoE formula can be modeled as if $\{b\}$ were the fixed frame and $\{s\}$ the body frame, resulting in $\mathbf{T}_{bs}(\mathbf{\Theta}$. See equation 3.27. The Screw axis in this configuration, $\mathcal{B}_i$ should be calculated as if $\{b\}$ was the fixed frame. The matrix $\mathbf{M}$ remains unchanged because, by substituting post-multiplication with pre-multiplication, its reference frame is automatically adjusted, as explained in the Homogeneous Transformation Matrices section.

$$\mathbf{T}_{bs}(\mathbf{\Theta}) = \mathbf{M} e^{[\mathcal{B}_1]\theta_1} e^{[\mathcal{B}_2]\theta_2} \ \cdots \ e^{[\mathcal{B}_n]\theta_n} \tag{3.27}$$

The accuracy of the robot's kinematic calculations will largely depend on the precision with which the robot's geometric parameters are obtained, and this constitutes a limiting factor in high-precision processes.

Inverse kinematics

The inverse kinematics problem involves determining the values of the components of the vector $\mathbf{\Theta}$ that satisfy a given relative position between frames $\{b\}$ and $\{s\}$, meaning that they result in a known displacement matrix matrix $\mathbf{T}_{sb}$. The problem is likely to have multiple solutions, which adds to its complexity.

The first consideration when solving an inverse kinematics problem is that the target points must always be within the robot's workspace. If they are not, the problem has no solution. Furthermore, if the points need to be reached with a specific orientation, they must be within the robot's task space.

There are two approaches to solving the problem: finding closed-form analytical solutions to the nonlinear equations, or finding solutions numerically.

The first approach relies on leveraging the geometry of the robot to find solutions, while the second requires an initial estimate and an iterative calculation process. In our case, since we are dealing with robotic manipulators that have a high number of DoF, we will opt for numerical solutions.

To tackle the resolution of the problem, it is necessary to first define the Jacobian matrix $\mathbf{J}$ of the robotic manipulator.

Establishing $\mathbf{X}(t)$ as the vector that represents the position and orientation of $\{b\}$ as a function of time, and based on the definition of the forward kinematics problem, we can state that expression 3.28 is satisfied over time.

$$\mathbf{X}(t) = f(\mathbf{\Theta}(t)) \quad \Rightarrow \quad \begin{bmatrix} x_1 \\ \vdots \\ x_m \end{bmatrix} = \begin{bmatrix} f_1(\mathbf{\Theta}) \\ \vdots \\ f_m(\mathbf{\Theta}) \end{bmatrix} \in \mathbb{R}^m \tag{3.28}$$

Therefore, the Jacobian matrix of the manipulator $\mathbf{J}$ can be defined as an $m \times n$ matrix, where each column J_j represents the unit variation of position and orientation of frame with respect to the variation in the degree of freedom θ_j. See equation 3.29. Here, n is the total number of DoF in the system. In our study, since the robot manipulator used is a 6R robot and the World space frames are defined with a six coordinates system, $J(\mathbf{\Theta}) \in \mathbb{R}^{6\times 6}$.

$$\mathbf{J}(\mathbf{\Theta}) = \frac{\partial f}{\partial \mathbf{\Theta}} = \begin{bmatrix} \frac{\partial f_1}{\partial \theta_1} & \cdots & \frac{\partial f_1}{\partial \theta_n} \\ \vdots & \ddots & \vdots \\ \frac{\partial f_m}{\partial \theta_1} & \cdots & \frac{\partial f_m}{\partial \theta_n} \end{bmatrix} \in \mathbb{R}^{m\times n} \tag{3.29}$$

To better understand the problem, it is important to note that the Jacobian matrix is invertible as long as there is no singularity at the point of calculation. To avoid computational difficulties, it is common practice in these algorithms to use the pseudoinverse of the Jacobian matrix, $\mathbf{J}^\dagger$, to solve the systems of equations.

The inverse kinematics problem is defined in equation 2.24. In this equation, $\mathbf{x}_d$ represents the target position and orientation of frame $\{b\}$, and $\mathbf{\Theta}_d$ represents the corresponding target in the Joint space. Since $\mathbf{\Theta}_d$ is an unknown, a first estimated solution $\mathbf{\Theta}^i$ close to the objective should be proposed. This estimated solution can be expressed as in 3.30 to 3.33.

$$\mathbf{X}_d = f(\mathbf{\Theta}_d) = f(\mathbf{\Theta}^i) + \left.\frac{\partial f}{\partial \mathbf{\Theta}}\right|_{\mathbf{\Theta}^i} (\mathbf{\Theta}_d - \mathbf{\Theta}^i) + \cancelto{0}{o(x^2)} \tag{3.30}$$

$$\left.\frac{\partial f}{\partial \mathbf{\Theta}}\right|_{\mathbf{\Theta}^i} = \mathbf{J}(\mathbf{\Theta}^i) \tag{3.31}$$

$$(\mathbf{\Theta}_d - \mathbf{\Theta}^i) = \Delta\mathbf{\Theta} \tag{3.32}$$

$$\mathbf{X}_d - f(\mathbf{\Theta}^i) = \mathbf{J}(\mathbf{\Theta}^i)\Delta\mathbf{\Theta} \tag{3.33}$$

$\Delta\mathbf{\Theta}^*$ can be finally expressed as 3.34 using the pseudoinverse Jacobian $\mathbf{J}^\dagger$ to avoid singularities. At a singularity $det(\mathbf{J}) = 0$ and thus $\mathbf{J}$ is not invertible.

$$\mathbf{J}^{-1}(\mathbf{\Theta}^i)(\mathbf{X}_d - f(\mathbf{\Theta}^i)) = \Delta\mathbf{\Theta} \quad \Rightarrow \quad \mathbf{J}^\dagger(\mathbf{\Theta}^i)(\mathbf{X}_d - f(\mathbf{\Theta}^i)) = \Delta\mathbf{\Theta}^* \tag{3.34}$$

The final Newton-Raphson algorithm in matrix form, starting from a maximum allowable error ϵ in the solution to be obtained, would be:

- **Inicialization:** given $\mathbf{X}_d \in \mathbb{R}^m$ and an initial estimation $\mathbf{\Theta}^0 \in \mathbb{R}^n$, for $i = 0$:
- **Let us define:** $e = \mathbf{X}_d - f(\mathbf{\Theta}^i)$.
- **While** $||e|| > \epsilon \ \rightarrow \ \mathbf{\Theta}^{i+1} = \mathbf{\Theta}^i + J^\dagger(\mathbf{\Theta}^i)e \ \rightarrow \ i = i + 1$

This method allows for a numerical solution to the inverse kinematics problem while minimizing computational issues caused by the singularities of the manipulator as it moves through its workspace. At a singularity, small changes in joint parameters can lead to large and unpredictable changes in the end-effector's position and orientation.

3.2.4 Trajectories and paths

The trajectory of a robotic manipulator is defined as the position to be taken by the robot's joints as a function of time $\mathbf{\Theta}(t)$. For a trajectory to be feasible, its time dependence must satisfy the velocity and acceleration limits associated with each joint of the robot. In other words, the kinematic constraints in Joint space define the kinematic constraints in World space.

To isolate the limiting effects of velocities and accelerations, it is sometimes necessary to separate a path from its time dependence by explicitly defining a path. A path, $\mathbf{\Theta}(s)$ maps the robot joint position to be followed for each value of $s \in [0, 1]$. As s increases the robot follows the defined path. With this approach, the geometric parameter s decouples the position definition from the time parameter t.

A path can be defined in the two workspaces of the robotic manipulator: Joint space and World space, and referred to any of its frames: $\{j\}$, $\{s\}$ or $\{b\}$, since their relations are defined by the forward or inverse robot kinematics.

A waypoint is defined as each commanded point with a known position that is provided to the manipulator along its movement. Around these points, the manipulator will interpolate a

path that needs to be defined. The waypoints represent locations on the overall trajectory where minimal positioning error is ensured. The more waypoints included in the path, the more precise the movement will be. However, an excessive number of waypoints can lead to issues if the minimum angle movement limit of any joint is surpassed.

Any type of curve can be used to interpolate the trajectory between two points, although the most common choices are straight-line or polynomial paths. In this work we will focus on straight-line interpolations.

A straight-line path between a start configuration $\boldsymbol{\Theta}_{start}$ and an end configuration $\boldsymbol{\Theta}_{end}$ can be defined in either Joint space or Task space. The benefit of defining this path as a straight line in Joint space is its straightforwardness. Joint limits are usually defined as $\theta_{i,min} \leq \theta_i \leq \theta_{i,max}$ for each joint i, which creates a convex free space in Joint space. As a result, a straight line connecting any two points in the Joint space will also lie within it. This straight-line path can be formulated as in 3.35. See Figure 3.14.

$$\boldsymbol{\Theta}(s) = \boldsymbol{\Theta}_{start} + s(\boldsymbol{\Theta}_{end} - \boldsymbol{\Theta}_{start}), \qquad s \in [0, 1] \tag{3.35}$$

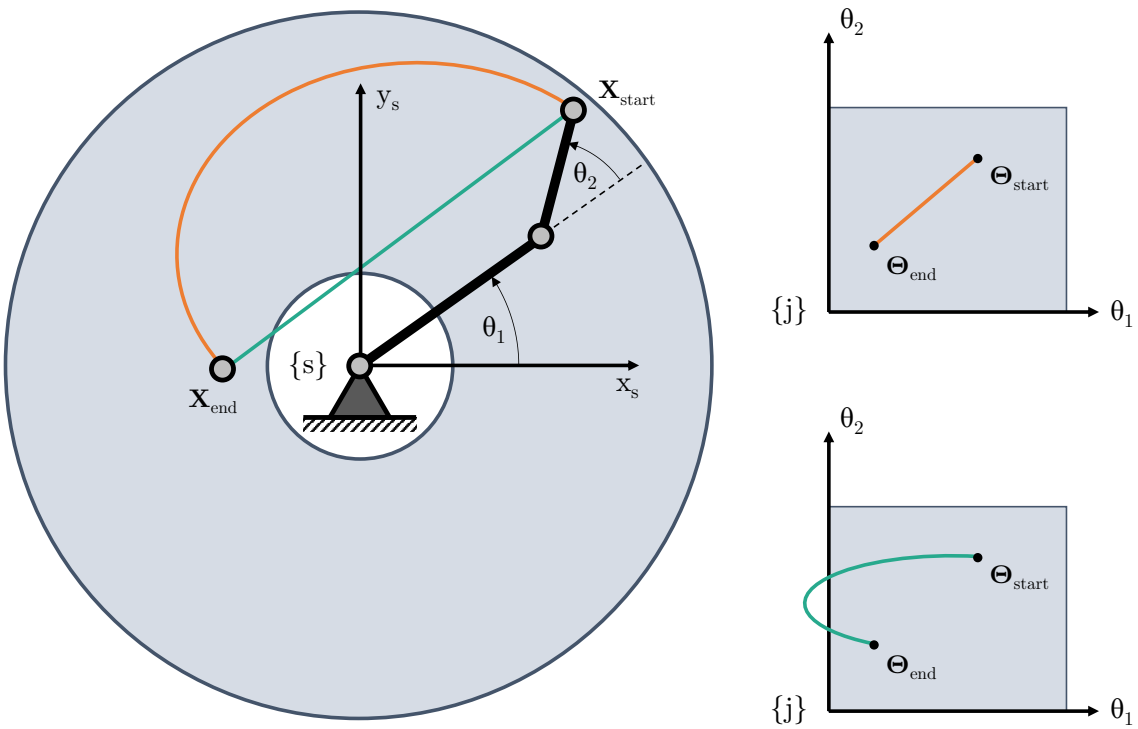

Figure 3.14: Comparison between a straight-line path defined in Joint space $\{j\}$ and World space $\{s\}$.

If the straight-line path is defined in World space, $\mathbf{X}(s)$, caution must be taken to ensure that the trajectory does not exceed the robot's workspace limits. If it does, the inverse kinematics solution will not exist, resulting in a lockup of the robotic manipulator as seen in Figure 3.14. The World space is not always convex.

In both definitions of the straight-line path, potential collisions between the physical components of the robot, the attached end-effector, or the surrounding environment must be considered.

Therefore, throughout this work, a trajectory for a robotic arm will be defined using a series of waypoints referenced to the World space $\mathbf{X}(s)$, as shown in Figure 3.15. Once the waypoints are defined, straight-line paths will be interpolated between them, and the inverse kinematics problem will be solved to obtain the vector $\mathbf{\Theta}(s)$. Subsequently, it will be verified that all paths remain within the robot's workspace. Finally, s will be replaced by t, ensuring that the velocity and acceleration values of each joint do not exceed their respective limits. The velocities and accelerations along the interpolated path are calculated as shown in equations 3.36-3.38.

$$\mathbf{\Theta}(t) = \mathbf{\Theta}_{start} + t(\mathbf{\Theta}_{end} - \mathbf{\Theta}_{start}), \qquad t \in [0, T] \tag{3.36}$$

$$\frac{d\mathbf{\Theta}}{dt} = \mathbf{\Theta}_{end} - \mathbf{\Theta}_{start} \tag{3.37}$$

$$\frac{d^2\mathbf{\Theta}}{dt^2} = 0 \tag{3.38}$$

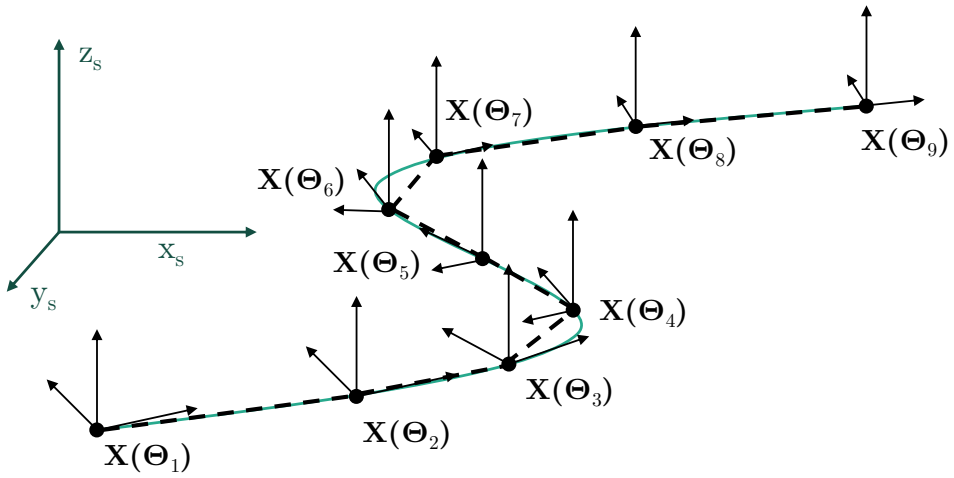

Figure 3.15: Example of straight-line path interpolation from nine given waypoints. The green line shows the objective path while the dash black straight-lines its interpolation from the given waypoints. Note that waypoints in $\{s\}$ are defined in both position and orientation.

Chapter 4

Materials

Throughout this chapter, the materials used in the execution of the thesis are summarized. These materials are categorized into three sections: the first focuses on the laboratory equipment utilized, the second on the software employed, and the third on the additive manufacturing materials for which the design methodology is developed based on their properties.

4.1 Laboratory equipment

The laboratory equipment encompasses all the materials used for the design, manufacturing, and validation of the non-planar robotic additive manufacturing cell:

- **UR10 CB3 collaborative robot:** developed by Universal Robots, is utilized in this study for its robust capabilities in industrial automation tasks. As part of the $CB3$ series, the $UR10$ offers a maximum payload of $10[kg]$ and an operational reach of $1300[mm]$, providing an optimal balance between flexibility and performance. Its intuitive programming interface and seamless integration with various end-effectors and sensors make it ideal for applications in non-planar robotic additive manufacturing. Additionally, its collaborative design ensures safe interaction within shared workspaces, adhering to the highest safety standards. Table 4.1 sumarizes the main specifications of the UR10 CB3 collaborative robot shown in Figure 4.1.
- **SICK laser distance sensor OD5 - 30W05, and SICK signal conditioner AOD5 - P1:** The OD5-30W05 is a high-precision laser distance sensor designed for industrial measurement applications. It operates using a laser triangulation principle to achieve accurate distance measurements over a specified range. The sensor is equipped with an integrated light source and optics, enabling precise detection and measurement of surfaces regardless of material or reflectivity. Measurement Range: $25 - 35[mm]$. Resolution: $0.1[\mu m]$. Output Type: Analog or digital signal, configurable for integration with control systems [198]. Figure 4.2 shows the equipment.

  The AOD5-P1 signal conditioner is designed to complement the OD5-30W05 laser sensor by converting, amplifying, and stabilizing the output signals for enhanced

Figure 4.1: UR10 CB3 collaborative robot.

compatibility with downstream systems. It ensures reliable data transmission and integration into monitoring or control processes. Input Compatibility: Supports signals from the OD5-30W05 sensor. Output Type: Standardized outputs (e.g., $4-20[mA]$, $0-10[V]$) for easy interface with programmable logic controllers (PLCs) or other systems. Signal Conditioning: Provides noise reduction and linearization for accurate signal interpretation. Power Supply: $12[V]$.

- **Mitutoyo Crysta-Plus M544:** high-precision Coordinate Measuring Machine designed for dimensional measurement applications in a variety of industrial and research settings. This machine is utilized for measuring the physical geometrical characteristics of an object by sensing discrete points on the object's surface. The Crysta-Plus M544 is capable of providing highly accurate three-dimensional measurements, making it essential for quality control, product development, and metrology applications [199]. Figure 4.3 shows the equipment.

  The machine has a measuring range that includes a $500[mm]$ range along the X-axis, $400[mm]$ along the Y-axis, and $300[mm]$ along the Z-axis. In terms of accuracy, the Crysta-Plus M544 boasts a maximum measuring accuracy of $2.5[\mu m]$, although this can vary depending on the specific model and environmental conditions. Additionally, its repeatability is typically within $\pm 1.5[\mu m]$, guaranteeing consistent and reliable results

Specification	Description
Manufacturer	Universal Robots
Model	UR10 CB3
Payload Capacity	Up to 10 kg
Reach	1300 mm
Degrees of Freedom	6 (rotational joints)
Repeatability	±0.1 mm
Weight	28.9 kg
Power Supply	110-240 VAC
Communication Interfaces	Ethernet, Modbus TCP, USB
Programming Interface	Graphical user interface (PolyScope) and script programming
Safety Features	Force sensing, collision detection, configurable safety planes
Applications	Non-planar additive manufacturing, assembly, pick-and-place, machine tending, welding
Specification	**Magnitude**
Base Diameter	190 mm
Height (to shoulder axis)	175 mm
Elbow Joint to Wrist Joint Length	612 mm
Wrist Joint to Tool Mounting Plate Length	136 mm
Tool Flange Standard	ISO 9409-1-50-4-M6
Joint Range	Base: ±360°, Shoulder: ±360°, Elbow: ±360°, Wrist 1: ±360°, Wrist 2: ±360°, Wrist 3: ±360°
Maximum Linear Speed	1 m/s
Maximum Joint Speeds	Base: 120°/s, Shoulder: 120°/s, Elbow: 180°/s, Wrist 1-3: 360°/s

Table 4.1: Specifications of the UR10 CB3 collaborative robot, including geometrical parameters [197].

for repeated measurements of the same object.

The machine's frame is designed to offer high stability and resistance to vibration, which is essential for ensuring accurate measurements in environments that may introduce mechanical noise. The granite base contributes to thermal stability, while air bearings on the moving parts reduce friction and enhance precision during movement along the axes, contributing to overall measurement accuracy.

Figure 4.2: SICK laser distance sensor OD5 - 30W05.

Lastly, the Mitutoyo Crysta-Plus M544 is compatible with Mitutoyo's MCOSMOS software. This software provides advanced measurement capabilities, data analysis tools, and comprehensive reporting functions. It supports complex measurement routines such as form analysis, geometric dimensioning, and tolerance checks, which are crucial for quality control in manufacturing processes and ensure that components meet precise design specifications.

- **BIQU H2V2S extruder:** is an Additive Manufacturing precise filament extrusor. Designed to be compact, lightweight, and versatile. Direct drive extruder, which offers advantages such as improved retraction control and better handling of flexible filaments. The extruder is equipped with a dual-gear mechanism that enhances its grip on the filament, reducing slipping and providing better control over the extrusion process. This dual-gear design also facilitates the use of a wider range of filaments, from standard PLA and ABS to more challenging materials like TPU and PETG. The table 4.2 summarizes the main specifications of the extruder. Figure 4.4 shows the extruder.

Specification	**Magnitude**
Motor Type	NEMA 17 stepper motor
Filament Compatibility	1.75 mm
Drive Mechanism	dual-drive gear system
Extrusion Rate	extrusion speed of 10 mm^3/s
Temperature Range	$200°C$ to $300°C$
Cooling System	cooling fan
Build Compatibility	Bowden tube or direct drive
Weight	$0.3kg$

Table 4.2: Specifications of the BIQU H2V2S Extruder [200].

In addition to the primary materials listed, other laboratory materials used in the construction of the non-planar additive manufacturing cell are mentioned throughout the text. Due to

Figure 4.3: Mitutoyo Crysta-Plus M544.

their lesser significance to the project in relation to the main equipment, their selection and technical characteristics are detailed in the methodology chapters.

4.2 Software

At the software level, two programming languages have been used: URScript, embedded within the Polyscope graphical interface of UR robots, and MATLAB, which has been used as the primary calculation language. Finally, Ansys and Comsol Multiphysics have been used to perform structural and heat transfer simulations respectively.

- **Polyscope** is the graphical user interface (GUI) and programming environment developed by Universal Robots for controlling their robotic arms. It is designed to facilitate programming and operation of robotic manipulators with a focus on ease of use and versatility. Polyscope supports two primary modes of programming: graphical programming through an intuitive flowchart-based interface, and script-based programming using **URScript**, a specialized programming language. The graphical interface allows users to construct robot programs by arranging function blocks that represent different commands, providing a straightforward way to design workflows for common tasks, such as pick-and-place, assembly, or machine tending. This visual approach to programming simplifies the process, even for those with limited coding experience.

  For more advanced applications, Polyscope integrates URScript, which is the native scripting language for Universal Robots. URScript provides users with the ability to write custom code for tasks that require specific control or logic that the graphical interface may not support. It enables users to create more complex behaviors by

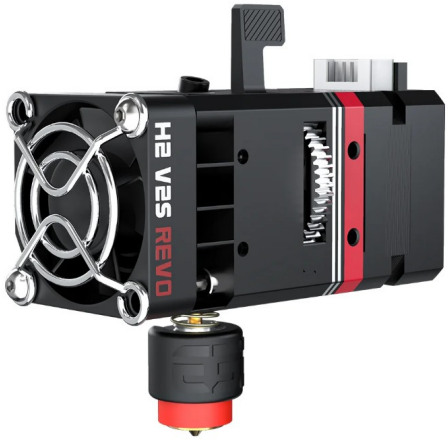

Figure 4.4: BIQU H2V2S extruder.

allowing detailed manipulation of the robot's movements, advanced data processing, mathematical operations, and the integration of external sensors or systems. The flexibility of URScript makes it suitable for applications that go beyond basic robot movement, such as tasks that require conditional control, real-time feedback, or custom interactions with other automation equipment.

Polyscope provides real-time feedback and visualization, allowing users to see a simulation of the robot's movements before executing the program on the physical robot. This feature helps to minimize errors by giving users the opportunity to verify the program's operation and make adjustments if necessary, before the robot performs the task. In addition to the visual programming interface, Polyscope allows for detailed control over the robot's motion parameters. Users can define the robot's speed, acceleration, and the type of motion path (e.g., linear or joint-based), which is critical for achieving precise control during complex tasks.

The system also includes tools for configuring the robot's interaction with its environment. Polyscope allows users to define tool and workpiece frames, ensuring that the robot can manipulate objects accurately according to the defined frames of reference. Calibration of the robot's tools and workspace is a crucial feature for ensuring precision during task execution, especially when dealing with objects that require exact positioning.

Polyscope supports integration with external devices through its input/output (I/O) system, which allows the robot to communicate with other machinery, sensors, or systems in the environment. It provides both digital and analog I/O ports, making it suitable for automation tasks where the robot must interact with external equipment, such as conveyors, cameras, or safety systems. The system also includes several built-in safety features, such as the ability to define safety zones and implement emergency stop protocols. These features are important for ensuring that the robot operates safely in environments where human workers may be present, and they comply with industrial safety standards.

- **MATLAB:** is a high-level programming language and environment primarily used for numerical computing, data analysis, and algorithm development. It is widely utilized in engineering, scientific research, and industrial applications due to its powerful matrix-based computing capabilities, ease of use, and extensive built-in libraries. The language is designed to facilitate mathematical operations, data visualization, and algorithm design, making it an ideal tool for applications that require complex computations and data processing.

  One of the key features of MATLAB is its App Designer, a tool for creating interactive applications with graphical user interfaces. **App Designer** allows users to design custom user interfaces by dragging and dropping components such as buttons, sliders, and axes, which can be linked to MATLAB code to interact with the underlying data and algorithms. The tool provides a simple, visual approach to creating applications, making it easier for users to develop professional-quality interfaces without needing extensive experience in GUI programming. The integration between App Designer and MATLAB code allows for seamless communication between the graphical interface and the computational backend, making it particularly useful for developing interactive control systems, simulations, or monitoring tools.

  MATLAB also includes a robust set of robotics libraries, specifically designed to facilitate the development of robotic applications. These libraries provide a comprehensive collection of functions for modeling, simulating, and controlling robotic systems. Key components of MATLAB's **robotics toolbox** include tools for forward and inverse kinematics, path planning, trajectory generation, and control system design. The robotics toolbox allows users to simulate robot motions in a virtual environment, test control algorithms, and optimize robotic trajectories. Additionally, MATLAB supports integration with hardware platforms and simulation environments, enabling the development of real-world robotic applications.

  The **Robotics System Toolbox** is a key MATLAB library that enhances its capabilities for robotic applications. It provides functions for robot motion planning, kinematic analysis, and multi-robot coordination. The toolbox includes models for common types of robots (e.g., manipulators, mobile robots) and integrates with tools like Simulink, enabling users to design and test control algorithms in a simulation environment before deploying them on real hardware. Additionally, MATLAB's ability to interface with various robotic hardware platforms, such as **ROS** (Robot Operating System), allows users to develop and test software for robots in real-time, with direct communication between the software and the physical robot.

- **ANSYS:** is a comprehensive engineering simulation software widely used in various industries for simulating and analyzing the behavior of products under real-world conditions. The software provides an extensive range of tools for simulating structural, fluid, thermal, and electromagnetic phenomena, utilizing finite element analysis (FEA), computational fluid dynamics (CFD), and other advanced numerical methods. ANSYS is highly regarded for its accuracy, robustness, and versatility, enabling engineers to optimize designs, predict performance, and solve complex engineering problems.

The **Mechanics Module** in ANSYS focuses on the simulation of structural mechanics, providing tools for analyzing the strength, deformation, and failure of materials under various loading conditions. It supports both linear and nonlinear static and dynamic analyses, allowing users to simulate complex behaviors such as large deformations, plasticity, and contact between parts. The module also includes capabilities for simulating vibrational modes, fatigue, and fracture mechanics, making it suitable for a wide range of mechanical design and testing scenarios. With its advanced meshing capabilities and support for various material models, including composites and advanced alloys, the Mechanics Module is essential for understanding how structures will perform under real-world conditions and ensuring the reliability and durability of products.

- **COMSOL Multiphysics:** is a powerful simulation software platform used for modeling and solving complex engineering problems involving multiple physical phenomena. It provides an integrated environment that allows users to simulate systems where different physics interact. COMSOL utilizes a finite element analysis (FEA) approach, making it ideal for handling multiphysics problems in diverse fields. The software is highly versatile, offering specialized modules that extend its capabilities to address specific application areas, and it is widely used in research and industry for designing, analyzing, and optimizing engineering systems.

  The **Heat Transfer Module** in COMSOL Multiphysics is designed for simulating heat transfer in solids, fluids, and multiphase systems. It covers a wide range of heat transfer phenomena, including conduction, convection, radiation, and phase change processes. This module allows users to model both steady-state and transient thermal behavior in complex geometries, making it suitable for applications such as thermal management, heat exchangers, and material processing. It also supports the coupling of thermal simulations with other physical models, such as fluid dynamics or structural mechanics, to handle problems where heat transfer interacts with other physical effects. The module's advanced capabilities, including thermal contact resistance, optimization, and multiphysics coupling, make it a powerful tool for engineers and researchers working on thermal simulations.

4.3 Materials

Throughout the development of the thesis, various types of materials for additive manufacturing are discussed. This section aims to define the main properties of each material and, therefore, their intended use within the additive manufacturing designs generated. Based on these criteria, the materials for extrusion are divided into three groups: rigid materials, flexible materials, and soluble materials.

- **Rigid Materials:** these are materials that, once printed, do not exhibit significant deformations under small loads. This group includes extrusion materials such as PLA, ABS, PETG, among others.

  PLA (Polylactic Acid) is one of the most commonly used materials in additive manufacturing due to its ease of use and environmentally friendly characteristics. PLA is

a biodegradable thermoplastic made from renewable resources, such as cornstarch or sugarcane. It has a low melting point, typically around $180 - 220°C$, making it suitable for use with most desktop 3D printers. PLA is known for its excellent printability, producing smooth and detailed prints with minimal warping or shrinkage. It also emits fewer fumes compared to other materials, making it safer to use in indoor environments. However, PLA is relatively brittle and lacks the impact resistance and heat resistance required for some functional applications.

ABS (Acrylonitrile Butadiene Styrene) is a strong and durable thermoplastic widely used in industrial applications due to its toughness and resistance to impact and heat. In additive manufacturing, ABS is favored for producing parts that require higher strength, durability, and thermal stability than PLA. It has a higher melting temperature, typically between $210 - 250°C$, which helps ensure better mechanical properties under stress and elevated temperatures. ABS is also known for its ability to be easily post-processed, allowing for sanding, painting, and gluing. However, ABS is more prone to warping during the printing process and emits fumes, requiring good ventilation when printed. It is often used for producing functional prototypes, automotive parts, and household items.

PETG (Polyethylene Terephthalate Glycol-modified) is a versatile material known for combining the strengths of both PLA and ABS. PETG offers excellent impact resistance and flexibility, making it less brittle than PLA and more durable under stress. It has a lower melting point than ABS, typically around $230 - 250°C$, and is less prone to warping during printing, which makes it easier to handle in 3D printing applications. PETG is also known for its clarity, which is desirable for applications where transparency or aesthetic appeal is important. It is resistant to moisture absorption, making it suitable for parts exposed to humidity or outdoor environments. While PETG prints with ease and has better strength properties than PLA, it can be more prone to stringing during the printing process, requiring careful tuning of print settings for optimal results.

- **Flexible Materials:** are those that, once printed, exhibit significant deformation under small applied loads. A prominent material in this category is Thermoplastic Polyurethane, whose elasticity is characterized using the Shore hardness scale. The most flexible TPU variants typically have a Shore hardness around 70A, while those with medium flexibility are in the range of 80A. TPU materials that remain flexible yet exhibit greater rigidity usually have a Shore hardness of approximately 95A.

  TPU (Thermoplastic Polyurethane) is a highly flexible, durable, and elastic thermoplastic material commonly used in additive manufacturing. It is known for its excellent abrasion resistance, impact strength, and flexibility, making it ideal for applications that require both elasticity and toughness, such as custom gaskets, seals, and flexible enclosures. It offers good chemical resistance, including resistance to oils, greases, and solvents, and has the ability to return to its original shape after deformation. TPU is also resistant to UV radiation and weathering, making it suitable for both indoor and outdoor applications. However, it requires precise printing conditions, such as proper temperature control, to achieve optimal results in 3D printing.

- **Soluble Materials:** are materials designed to dissolve in a specific solvent after printing, leaving behind intricate and complex structures or parts with delicate features that cannot be easily removed by traditional mechanical methods. These materials are particularly useful in applications where support structures are required for overhangs, complex geometries, or internal cavities. Once the printing process is completed, these soluble materials can be washed away with the appropriate solvent, leaving only the primary printed part. This property enables the creation of intricate designs, especially in multi-material printing where the support structure can be easily removed without affecting the main print.

  One of the most commonly used soluble materials in 3D printing is **PVA** (Polyvinyl Alcohol), which is highly water-soluble and widely employed as a support material in dual extrusion 3D printers. PVA is compatible with a variety of other thermoplastic materials like PLA, PETG, and ABS, making it ideal for use in multi-material 3D printing applications. It has excellent adhesion to a wide range of materials, ensuring stable support for complex prints, while being easily removed by soaking in water or running water through the printed part. PVA also exhibits good printability, with low warping and minimal shrinkage, and can be printed at relatively low temperatures, typically between $190 - 220°C$. However, it is sensitive to moisture and should be stored in dry conditions to maintain its printing performance.

Chapter 5

Axisymmetric non-planar slicing and path planning strategies for robot-based additive manufacturing

Chapter 5 presents the methodology developed for the lamination of solids on curved surfaces. This methodology was published on an open access article where this chapter has been condensed, [201].

The proposed methodology operates between two spaces: World space, and Slicing space; which are defined throughout the chapter highlighting the advantages of their interaction as well as the challenges arising from their definition. Additionally, once this interaction is established, the complete implementation of the methodology is carried out within a non-planar robotic additive manufacturing cell.

The implementation of the methodology in a real manufacturing cell involves the development of the non-planar lamination slicer as well as the physical components of the manufacturing station, which are presented as results in the chapter. The functionality is validated through two case studies.

Other essential elements for the station's proper operation, such as the calibration methodology and the architecture for synchronizing the robotic arm with external systems, are utilized in this thesis but are developed in previous works. Figure 5.1 shows the methodology workflow.

The methodology presented will be divided into four subsections. Subsection 4.1 will provide brief insights into part design and the selection of optimal layer shapes, along with the definition of space transformations. Once these foundational concepts are established, Subsection 4.2 will focus on strategies for non-planar layer slicing and infill. To demonstrate the versatility of the methodology, Subsections 4.3 and 4.4 will present the results of its implementation in a custom-developed robotic station, utilizing a personalized slicer that streamlines the process.

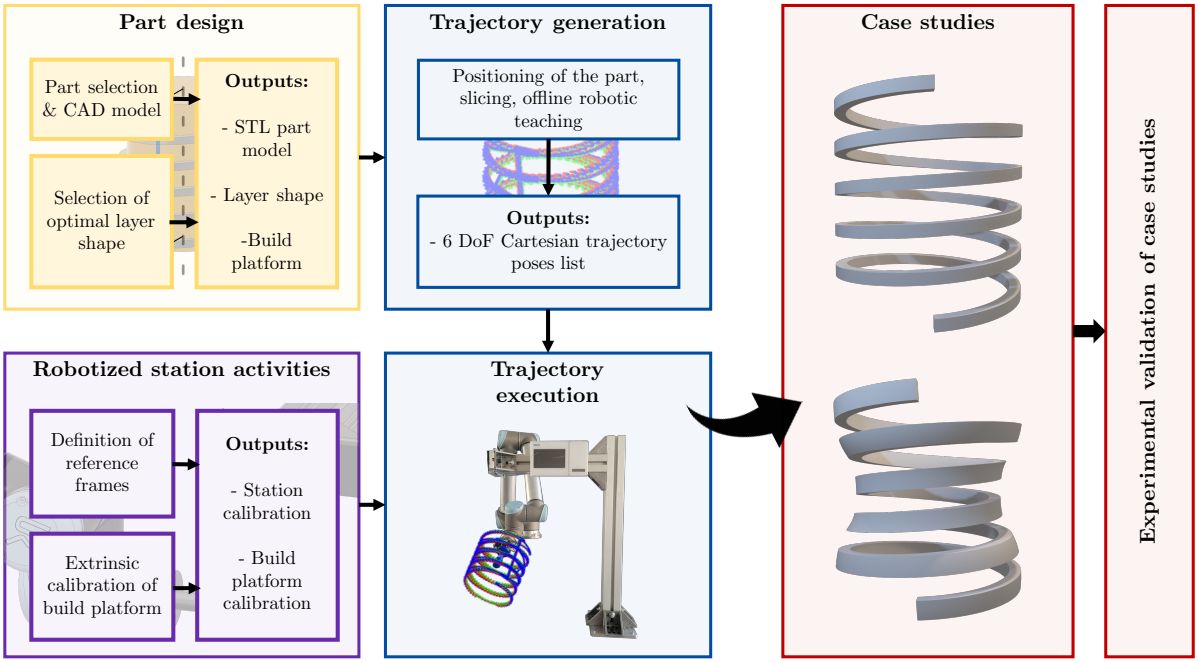

Figure 5.1: Schematic diagram of the methodology presented.

5.1 Methodology for Slicing Solids using Parametric Non-Planar Axisymmetric Layers

5.1.1 Part design and optimal layer shape selection

The case studies chosen to demonstrate the operation of the non-planar slicing methodology are helical springs with a square cross-section. When these springs are axially loaded, the spring cross-section is subjected to torsional stresses. In order to prevent delamination, the layers should be deposited parallel to the neutral axis along the spring helix, irrespective of the shape of the spring, either cylindrical or hourglass-shaped in the case studies considered here.

Additional outcomes of the use of non-planar layers parallel to the spring helix are that the staircase effect on the lateral surface of the spring helix would disappear, and that supports would be no further needed. Figures 5.2.a through 5.2.d show the intended results.

These insights will be applied in this paper in the definition of the curved layers for each case study. The chosen case studies are thoughtfully selected to provide a comprehensive exploration of the capabilities and versatility of the presented methodology. The first case study (Figure 5.2.e) focuses on a conventional helical spring modeled through cylindrical layers, serving as a starting point for methodology comprehension and calibration validation. The second case study (Figure 5.2.f) introduces an hourglass-shaped helical spring modeled through hourglass-shaped layers and was selected to highlight the algorithm's adaptability and creative potential on variable curvature surfaces. Although the hourglass design may initially appear challenging for traditional manufacturing methods, the extraction of the part

is thought to be possible through the utilization of a soluble build platform, among other methods.

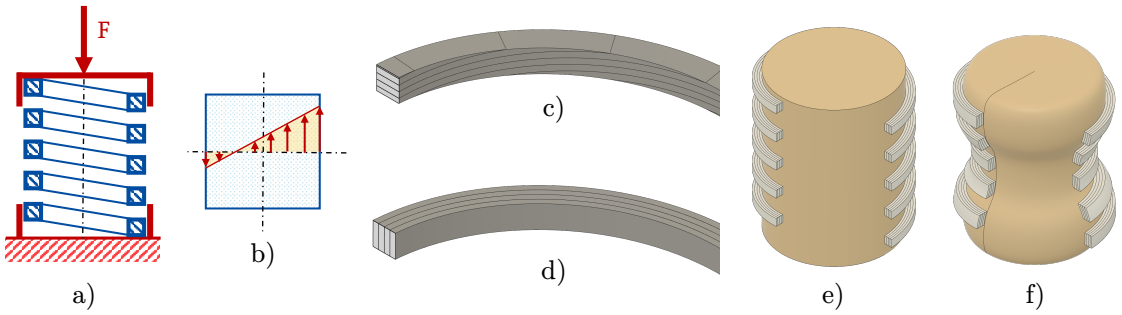

Figure 5.2: a) Diagram of a helical spring under a compression load, b) typical cross-section stress diagram of a compressed helical spring, c) conventional 3 axis AM slicing of a helical spring, d) optimal NPAM slicing for a helical spring, e) a cylindrical helical spring sliced following cylindrical layers and f) an hourglass-shaped helical spring sliced following hourglass-shaped layers. Figures e) and f) depict the springs in cross-section to appreciate the deposition of the layers.

5.1.2 Definition of the isomorphism

This subsection aims at describing how to create the surface of revolution build surfaces based on parametric curves given a layer shape and how to define the isomorphism based on the curve. Once the isomorphism has been established, the trajectory generation workflow will be presented. A detailed diagram is shown in Figure 5.3.

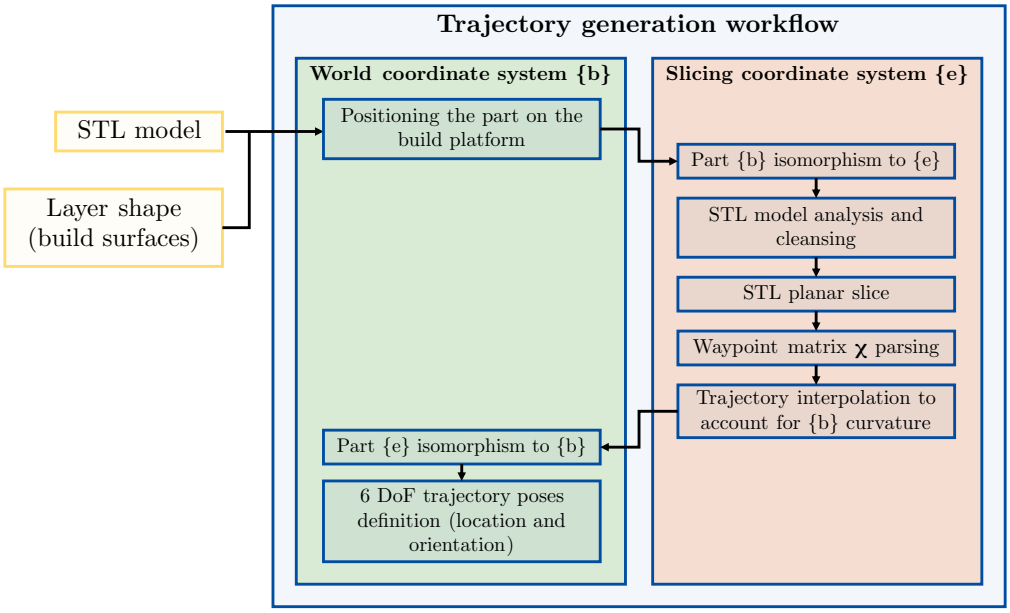

Figure 5.3: Schematic representation of the trajectory generation workflow. Of note, the STL model and the build platform shape are required as inputs for the algorithm, resulting in the 6 DoF pose list trajectory to be executed by the robotized station.

Build platform geometry definition through parametric curves

Composite Bézier splines have been selected as the parametric base curve to create the surface of revolution build platform; however, any parametric curve can be used as a base curve for the methods proposed in this paper. A composite Bézier spline consists of a series of Bézier curves as a function of a parameter $t \in [0, 1]$, a basis matrix $\mathbf{B}$, and a control polygon matrix $\mathbf{C}$ composed of control points $\mathbf{P}_i$, as shown in 5.1.

$$\mathbf{\Gamma}(t) = \begin{pmatrix} t^3 & t^2 & t & 1 \end{pmatrix} \begin{pmatrix} -1 & 3 & -3 & 1 \\ 3 & -6 & 3 & 0 \\ -3 & 3 & 0 & 0 \\ 1 & 0 & 0 & 0 \end{pmatrix} \begin{pmatrix} \mathbf{P}_0 \\ \mathbf{P}_1 \\ \mathbf{P}_2 \\ \mathbf{P}_3 \end{pmatrix} = \mathbf{t} \cdot \mathbf{B} \cdot \mathbf{C} \tag{5.1}$$

The composition of Bézier curves into a composite Bézier spline is based on the expansion of the parameter t to a parameter $u \in [0, n]$, where n is the number of curves composing the spline, and an expanded control polygon $\mathbf{C}$ which must ensure C^0 continuity. The extreme values of the parameter u interval shall correspond to the intersection points of $\mathbf{\Gamma}(u)$ with the z-axis. If the selected curve has points at infinity, then $\mathbf{\Gamma}(u)$ is defined $\forall u \in [0, +\infty)$ or $\forall u \in \mathbb{R}$ and it will have less than two intersection points with the z-axis across the domain.

Necessary conditions for a curve to be used as build platform

For the isomorphism to exist, the generatrix curves, defined in the Cartesian zx-plane, must fulfil a series of conditions on parametric and geometric continuity, complexity, convexity, and tangency at the extreme values of the parameter domain. In terms of continuity, the generatrix curve must be at least G^1 continuous across the entire parameter domain. In addition to that, the base curves must not have cusps or nodes, must be convex throughout the domain, and their tangents must be orthogonal with respect to the axis of revolution when intersecting it. These conditions result in a globally bijective homomorphism (isomorphism) and are easily verifiable for piecewise-defined curves. However, any curve can be used if the region where the part is located is locally isomorphic. Examples are provided in Figure 5.4. Regarding the right-hand side diagrams in Figure 5.4, it is of note that base curves that do not fulfil all said requirements will instead define several isomorphable regions where the homomorphism is locally bijective and, therefore, printable regions. For a part to be manufacturable through this methodology, all points composing the part model must be located within the same isomorphable region.

Isomorphism definition

The methodology followed to slice 3D models using surfaces of revolution is based on the transformation of the points defined in the part STL model between two coordinate systems. The first coordinate system is the reference Task coordinate system $\{b\}$. The second coordinate system is defined by a trihedron $\{e\}$, whose direction vectors are defined according to the base curve which defines the generatrix of the non-planar layers and the stacking direction, as depicted in Figure 5.5. It is considered that the z-axis of the Task coordinate system $\{b\}$ works as axis of revolution of the slicing surfaces.

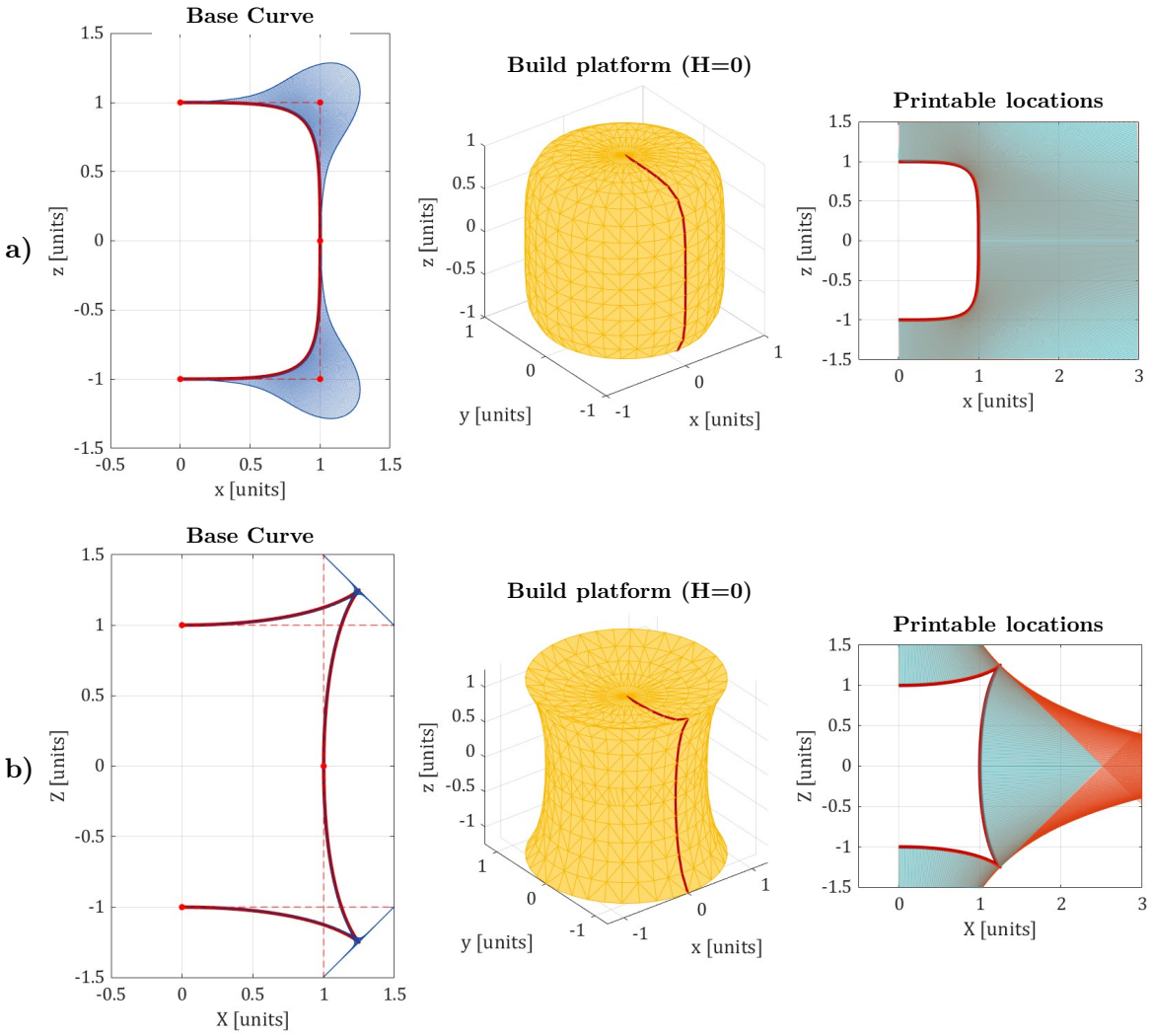

Figure 5.4: a) Example of a base piecewise-defined parametric curve fulfilling all mathematical conditions. b) Example of a G^2 base piecewise-defined parametric curve with cusps. For both examples, left-hand side diagrams represent the base curve in solid red line, its control polygon in dashed red line and its curvature comb in blue. The center diagrams represent the build platform (yellow) when the based curve is used as the generatrix for the surface of revolution. Lastly, the right-hand side diagrams represent in cyan shade the areas of printable locations for a cross section of the build platform.

Given the equation of the generatrix curve, contained in the zx-plane of $\{b\}$, as $\mathbf{\Gamma}(u)_{\{b\}}$in parametric form 5.2.

$$\mathbf{\Gamma}(u)_{\{b\}} = x(u)\mathbf{e}_x + z(u)\mathbf{e}_z, \quad \forall u \in [0, n] \tag{5.2}$$

The orthonormal basis of the slicing coordinate system $\{e\}$ shall be defined from its three director vectors $\{e_L, e_\theta, e_H\}$. For each point in $\mathbf{\Gamma}(u)$, e_L is defined as the unit tangent vector to $\mathbf{\Gamma}(u)$ along the path of the curve in ascending u value, e_H is defined as the outward unit

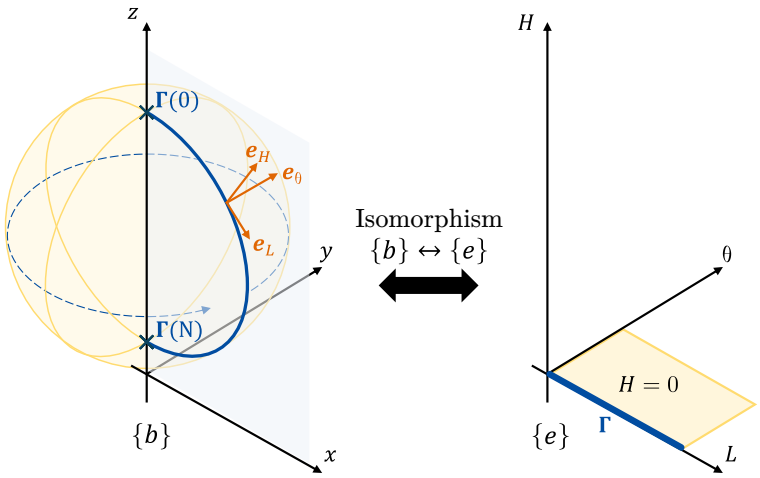

Figure 5.5: Schematic representation of an isomorphism between Task space $\{b\}$ and slicing $\{e\}$ coordinate systems given an arbitrary revolved curve $\mathbf{\Gamma}(u)$ (solid blue) as a build platform (yellow).

normal vector to $\mathbf{\Gamma}(u)$, and e_θ is defined as in 5.5. Mathematically, the tangent and normal unit vectors to the curve $\mathbf{\Gamma}(u)$ can be written as in 5.3 and 5.4 respectively. Hence, the coordinates (L, θ, H) associated with the orthonormal basis in $\{e\}$ respectively represent the arc length along the base curve, angle of revolution from the $y_{\{b\}} = 0$ plane, and distance from the base curve.

$$\mathbf{e}_L = \frac{\nabla \mathbf{\Gamma}(t)}{||\nabla \mathbf{\Gamma}(t)||} \tag{5.3}$$

$$\mathbf{e}_H = \mathbf{e}_y \times \mathbf{e}_L \tag{5.4}$$

$$\mathbf{e}_\theta = \mathbf{e}_H \times \mathbf{e}_L \tag{5.5}$$

Subsequently, the forward and inverse transformation in between the spaces $\{b\}$ and $\{e\}$ must be defined.

Inverse transformation: $(L, \theta, H)_{\{e\}} \rightarrow (x, y, z)_{\{b\}}$

Any point $\mathbf{P}_{\{e\}} = (L, \theta, H)$ can be defined in $\{b\}$ in two steps. Firstly, let π be a vertical plane in $\{b\}$ which contains the $z_{\{b\}}$-axis and the point $\mathbf{P}_{\{b\}}$. In that plane, the Cartesian components of the point $\mathbf{P}_{\{\pi\}} = (x^*, z^*)_{\{\pi\}}$ shall be defined as in 5.6.

$$\begin{pmatrix} x^* \\ z^* \end{pmatrix}_{\{\pi\}} = H_p \cdot \begin{pmatrix} \boldsymbol{e}_H(u^*)_x \\ \boldsymbol{e}_H(u^*)_z \end{pmatrix}_{\{\pi\}} + \begin{pmatrix} \mathbf{\Gamma}(u^*)_x \\ \mathbf{\Gamma}(u^*)_z \end{pmatrix}_{\{\pi\}} \tag{5.6}$$

In 5.6, $\mathbf{\Gamma}(u^*)$ represents the point along $\mathbf{\Gamma}$ whose normal vector $H_p \mathring{\mathbf{u}} \mathbf{e}_H(u^*)_{\{pi\}}$ passes through point $\mathbf{P}_{\{pi\}}$. Therefore, H_p represents the distance between $\mathbf{\Gamma}_{\{pi\}}$ and $\mathbf{P}_{\{pi\}}$. The formula for

calculating the arc length of $\mathbf{\Gamma}$ is used to define the u^* value 5.7. With this relationship it is possible to define f so that $u^* = f(L)$.

$$L = \int_0^{u^*} ||\nabla \mathbf{\Gamma}(u)||\, du \tag{5.7}$$

Integrating 5.7 numerically and substituting in 5.6 yields a system, 5.8, of 2 equations where x^* and z^* are the unknowns.

$$\begin{pmatrix} x^* \\ z^* \end{pmatrix}_{\{\pi\}} = H_p \cdot \begin{pmatrix} \boldsymbol{e}_H(f(L))_x \\ \boldsymbol{e}_H(f(L))_z \end{pmatrix}_{\{\pi\}} + \begin{pmatrix} \mathbf{\Gamma}(f(L))_x \\ \mathbf{\Gamma}(f(L))_z \end{pmatrix}_{\{\pi\}} \tag{5.8}$$

Lastly, to implement θ, a rotation along the z-axis is applied (5.9).

$$\begin{pmatrix} x_p \\ y_p \\ z_p \end{pmatrix} = \mathbf{R}_z(\theta) \begin{pmatrix} x^* \\ 0 \\ z^* \end{pmatrix}_{\{\pi\}} \tag{5.9}$$

This allows for the conversion of coordinates and orientations between the slicing map $\{e\}$ and the Cartesian map $\{b\}$. This transformation is schematically presented in Figure 5.6.

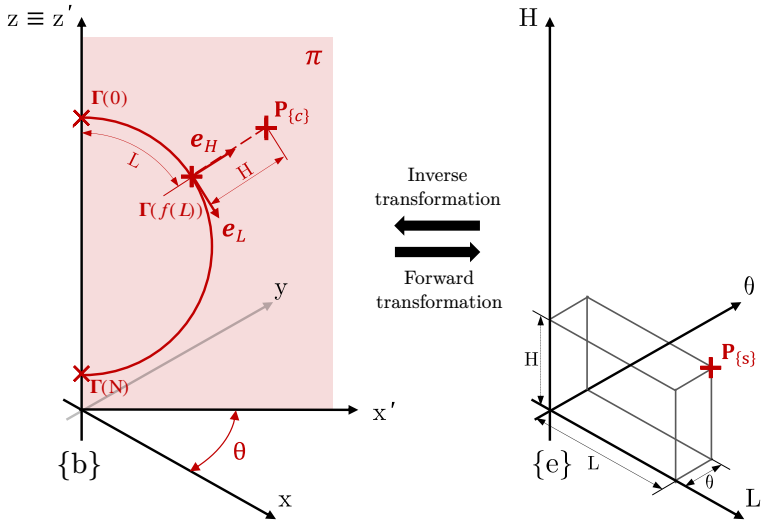

Figure 5.6: Schematic representation of the isomorphism, depicting the transformation of coordinates between the Task coordinate system $\{b\}$ (left-hand diagram) and the slicing coordinate system $\{e\}$ (right-hand diagram).

Direct transformation: $(x, y, z)_{\{b\}} \rightarrow (L, \theta, H)_{\{e\}}$

The inverse transformation $\{b\}$ to $\{e\}$, using 5.8, requires solving a non-linear equation system, which can be solved numerically for points located in areas where the transformation is locally bijective. In this transformation, $\mathbf{P}_{\{\pi\}}$ is defined as in 5.10 where $\theta = atan(y/x)$. The non-linear system to solve is defined in 5.11.

$$\begin{pmatrix} x^* \\ 0 \\ z^* \end{pmatrix}_{\{\pi\}} = \mathbf{R}_z^T(\theta) \begin{pmatrix} \mathbf{P}_x \\ \mathbf{P}_y \\ \mathbf{P}_z \end{pmatrix}_{\{b\}} \tag{5.10}$$

$$\begin{pmatrix} x^* \\ z^* \end{pmatrix}_{\{c\}} = H_p \cdot \begin{pmatrix} \boldsymbol{e}_H(u^*)_x \\ \boldsymbol{e}_H(u^*)_z \end{pmatrix}_{\{\pi\}} + \begin{pmatrix} \boldsymbol{\Gamma}(u^*)_x \\ \boldsymbol{\Gamma}(u^*)_z \end{pmatrix}_{\{\pi\}} \tag{5.11}$$

Solving for u^* and H allows for the calculation of L through 5.7, establishing the mapping of points from the slicing coordinate system $\{e\}$ to the Task coordinate system $\{b\}$. Figure 5.7 represents two examples of the complete transformation of a set of points. Case A transforms two planes in $\{b\}$ within the ranges $L \in [0, L(u = 4)]$, $\theta \in [0, 2\pi]$ and $H = [0, 1]$, given a base curve $\boldsymbol{\Gamma}_{\{b\}}$ in the shape of a straight line. Case B transforms four planes in $\{b\}$ within the ranges $L \in [0, L(u = 2)]$, $\theta \in [0, 2\pi]$ and $H = [0, 3]$, given a barrel-shaped base curve $\boldsymbol{\Gamma}_{\{b\}}$.

5.2 Slicing and infill strategies on non-planar surfaces

Based on the bijective transformations defined in the previous section, it can be concluded that any curved surface meeting the specifications of these transformations can be converted into a space $\{e\}$ where slicing with planes parallel to the $L\theta$-plane, after reverting the transformation, results in stacked lamination surfaces in the H direction. Initially, validations were performed using a commercial slicer, but its limitations made the development of a custom slicer necessary. This custom slicer was designed to incorporate the standard functionalities of a planar slicer, adapted to non-planar layers as well as to the reference systems of the robotic manipulator. Additionally, new features were incorporated to allow for fully customized orientation of non-planar layers, while also addressing the challenges posed by infill gaps that arise when curving the layers.

The objective of this section is, therefore, to explain the methodology for slicing and filling non-planar layers in space $\{e\}$, as well as the constructive logic of the slicer developed for this purpose. The section is divided into three parts: the first part addresses the slicing of solids, the second part covers infill functionalities and specific features, and the third part defines the output trajectories to be followed by the robot based on the generated layers and infills. The outcome of this process is a non-planar, uniform, multiaxial slicing of solids in a tessellated format with a customized infill strategy.

5.2.1 Slicing algorithm in $\{e\}$

The starting point of this work is an STL solid. An STL file is composed of two data matrices: a point matrix and a connectivity matrix. In the Task space, each row of the point matrix contains the (x_b, y_b, z_b) coordinates of one of the solid's points, referenced to $\{b\}$. Each row of the connectivity matrix contains the three vertices of each triangle that makes up the tessellated surface of the solid. The order of the points in the connectivity matrix defines the exterior face of the solid using the cross product rule.

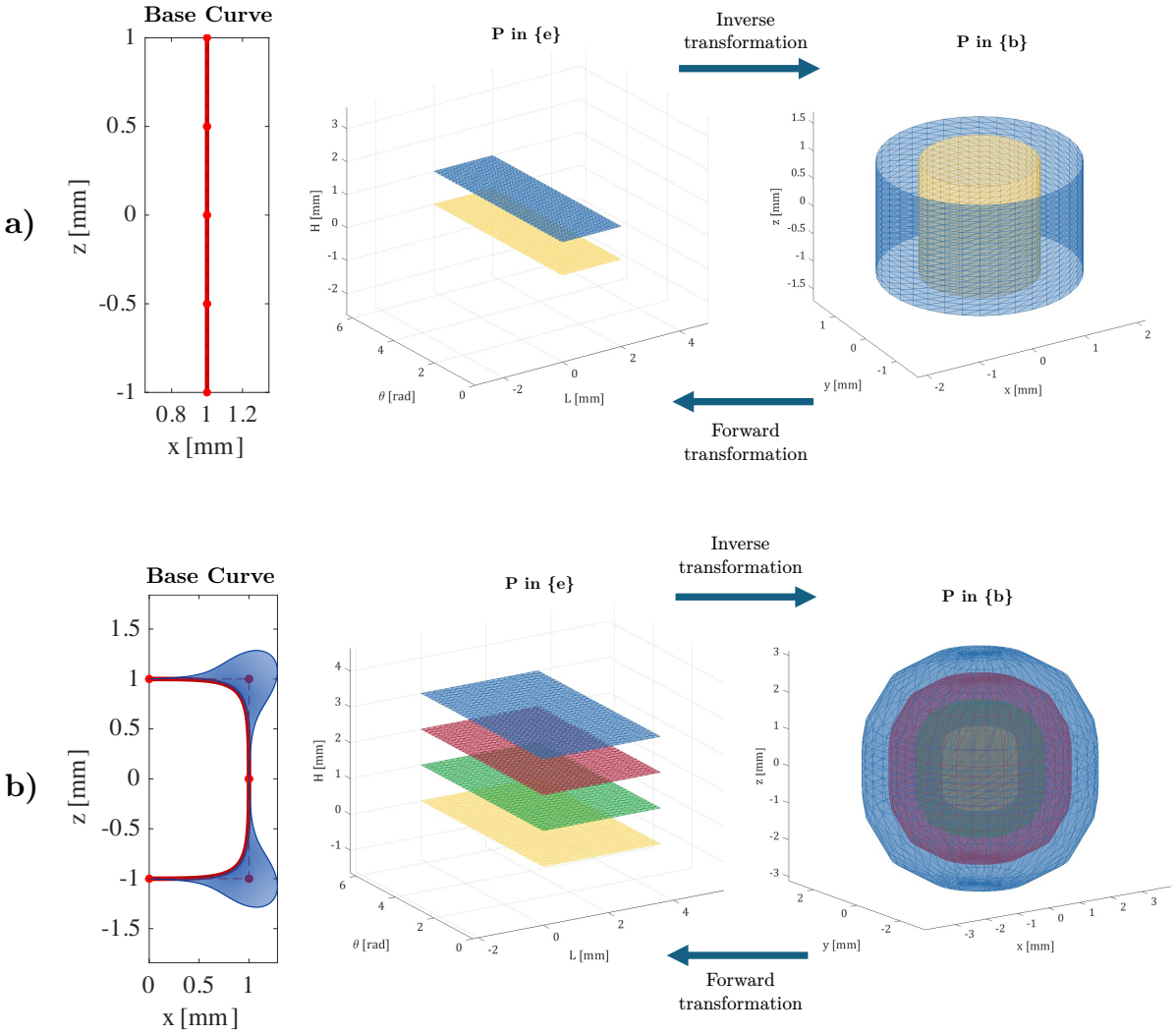

Figure 5.7: Examples of a complete transformation of a set of points in $\{e\}$ given a base curve $\mathbf{\Gamma}$. a) Straight line base curve $\mathbf{\Gamma}$, b) Barrel-shaped base curve $\mathbf{\Gamma}$.

The first step in generating the NPAM trajectories the isomorphism of all STL vertices onto the slicing space $\{e\}$. Once the STL vertices of the part have been isomorphed, a bijection check should be performed to ensure the manufacturability of the part, in case the base curve selected as a build platform does not fulfil the aforementioned conditions. Should the bijection check be satisfactory, the isomorphed STL connectivity matrix may be filtered in case the robot joints are not able to provide an unlimited angular range of motion and are limited to a range, for instance, from 0 to $2\pi[rad]$.

The original STL connectivity matrix associates vertices in the Task coordinate system. However, in the slicing coordinate system, the connection between Cartesian neighbouring points surrounding $\theta = 0[rad]$ implies the existence of faces connecting extreme points of θ (close to 0 and $2\pi[rad]$) wrapping around throughout the θ axis, as seen in Figure 5.8a, leading to slicing errors (Figure 5.8b). An algorithm has been developed to avoid this θ wrapping, detecting faces which contain points around the extreme limits of θ, and removing these faces.

An application of this algorithm is shown in Figures 5.8c and 5.8d.

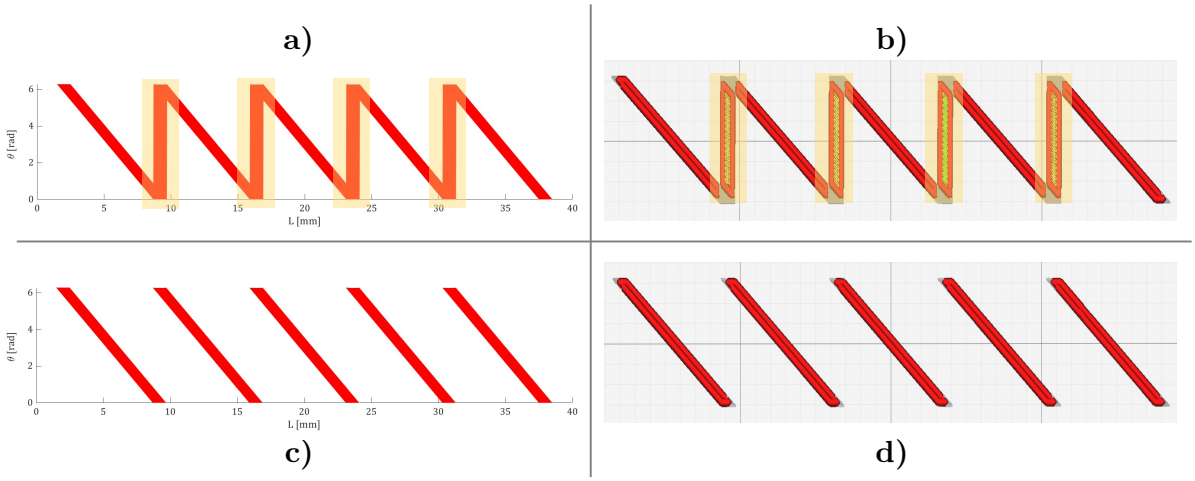

Figure 5.8: a) Non-filtered STL part model after the isomorphism onto $\{e\}$. b) Slicing of non-filtered STL part model. c) Filtered STL part model after the isomorphism. d) Slicing of filtered STL part model. The yellow shaded rectangles indicate the regions where the inherited Cartesian STL connectivity matrix creates faces wrapping around the θ axis and slicing errors.

Once the solid is referenced in the slicing space, the lamination is performed in a conventional planar manner. Figure 5.9 illustrates the procedure. Since the lamination methodology is uniform and follows the direction of the H coordinate, the solid is sliced using λ-planes that are parallel to the $L\theta$-plane. The height of each λ plane, its H coordinate, defines the layer height.

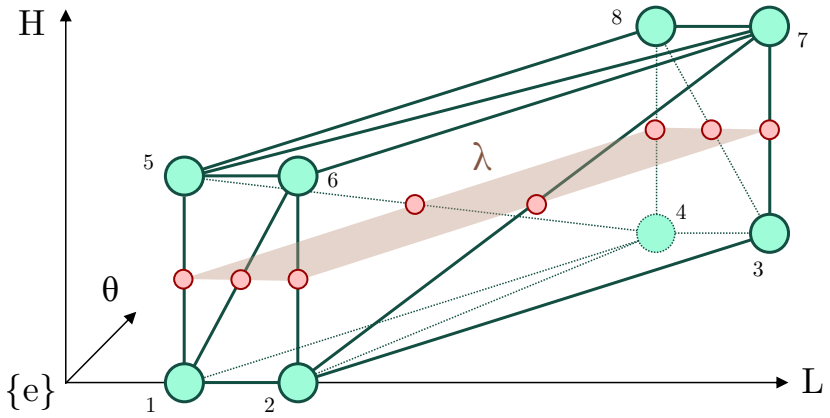

Figure 5.9: Helical spring coil converted to $\{e\}$ sliced by a plane λ built parallel to $L\theta$-plane.

To obtain the intersection between the λ-plane and the laminated solid, a series of operations is performed starting from the solid in $\{e\}$. First, points in the STL point matrix that lie below the plane are identified by checking their H coordinate. Once these points are located, the connectivity matrix is used to determine which points they are connected to. This involves searching the connectivity matrix for occurrences of points below the plane. Next, connections between points below the plane are ignored, and connections with points above the plane

are analyzed. Finally, the intersection of the plane with the edges connecting these points is computed to obtain the contour polygon vertices.

The algorithm has been optimized for execution with more complex solids. Since lamination is performed sequentially from planes with lower to higher H coordinates, all connections between points below the λ-plane are eliminated in each iteration. Additionally, points that no longer have connections with points above the plane are removed from the point and connectivity matrices. Finally, segment equations defining triangle sides are stored to avoid recalculating them during the slicing plane operations. Segments that are below the λ-plane are then removed. These improvements substantially reduce execution time.

The result of these operations is, for each λ-plane, a dataset of contour polygon points that outline the layer to be manufactured.

5.2.2 Infill procedure: functionalities and specific NPAM features

From the contour polygon points dataset the slicer aims to fulfil the NPAM printing requirements. These requirements will be further explained into the following sections: layer walls, infill density, infill direction, and Travels.

Layer wall generation

In additive manufacturing, a contour wall is defined as the boundary of each layer's contour. Generally, walls are constructed by depositing material tangentially to the surface at all times. The number of walls generated along the contour will determine the rigidity of the part. In the case of the algorithm designed for NPAM in this work, we will categorize the walls into two types: seam walls and standard walls.

Seam walls are defined as those formed by points with a coordinate $\theta = 0$ or $\theta = 2\pi$. On these walls the points on both sides of the θ wrapping coincide in the Task space. Therefore, the goal for these walls is to create a seam that connects both parts of the piece ensuring its integrity.

To start the wall generation process, it is necessary to organize the contour points. From this 2D dataset, an initial algorithm was developed based on convex hulls, which was later reprogrammed to use alpha-shapes. This algorithm defines the dataset's contour and organizes the boundary points sequentially. This data is stored in a polyshape variable in MatLab.

Once the points are organized, the trajectory should follow them sequentially. If additional walls are required, the polybuffer function is used to offset the contour inward by a specified value, typically corresponding to the nozzle diameter. This operation can be repeated as many times as needed to generate the desired number of walls for the manufacturing process. Figure 5.10 represents how plane layer walls are seen in a single coil helical spring.

The next step involves identifying the seam walls. This is done by searching for contour regions where $\theta = 0$ and $\theta = 2\pi$, and determining which segments coincide in L-coordinate values. In these regions, both sides of the part will overlap. To address the seam problem, a zigzag trajectory is implemented. This approach "stitches" both sides of the part together,

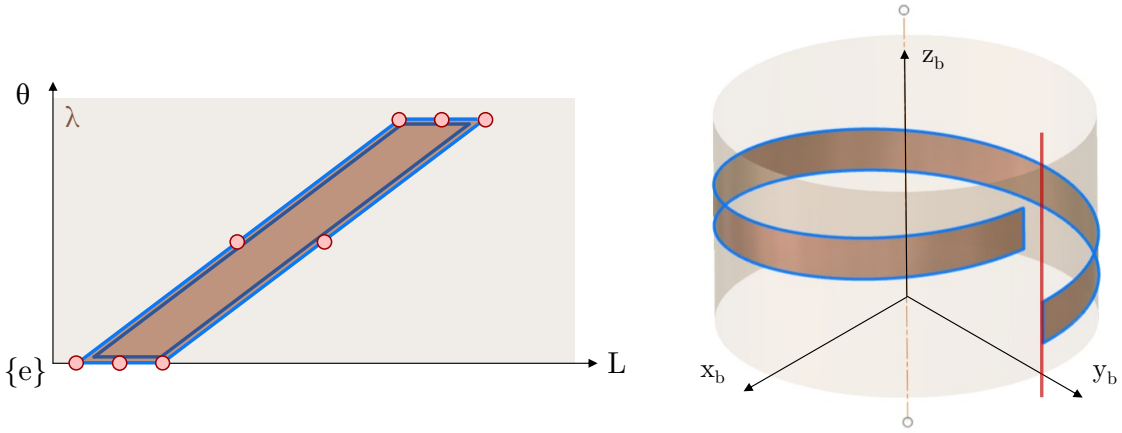

Figure 5.10: Helical spring coil layer in $\{e\}$ standard double wall along its entire perimeter.

avoiding mobility issues for the robot that could arise from generating a continuous trajectory.

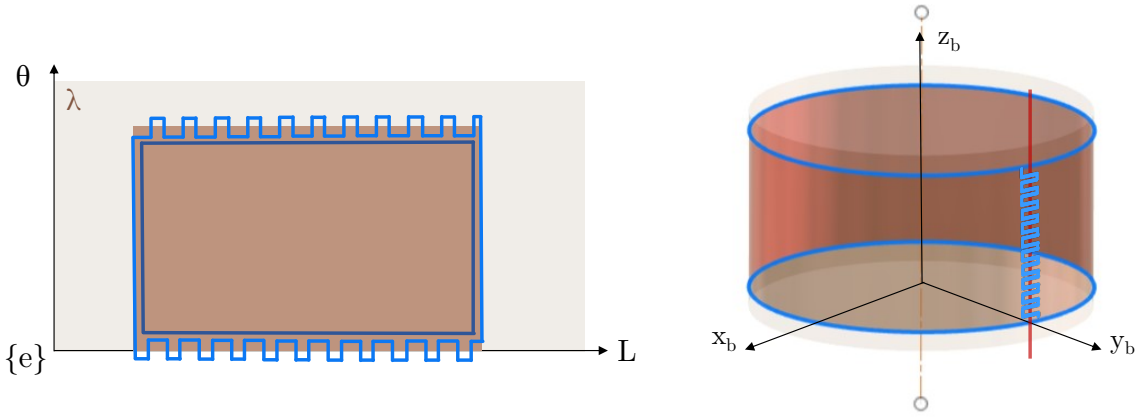

Figure 5.11: Axysimmetric cylinder layer in $\{e\}$ seam wall on $\theta = 0$ and $\theta = 2\pi$.

Figure 5.12 illustrates how both parts of the lamination are connected in the case of a cylinder constructed from cylindrical layers. They are formed so that each "tooth" of the zigzag pattern has an external width twice the diameter of the nozzle, and each gap has the same internal width. It is important to overlap the zigzag patterns between layers to enhance their adhesion.

The same zigzag effect can be applied across multiple layers instead of a single one. This offers advantages in surface finish for the part. Figure XXX shows the result of applying this methodology in consecutive layers.

Infill density

This section aims to equip the slicer with the ability to adapt the layer infill density according to the user's needs. To achieve this, it must be noted that, of the three coordinates in the slicing space $\{e\}$, only H is in true scale relative to its final conversion to the Task space.

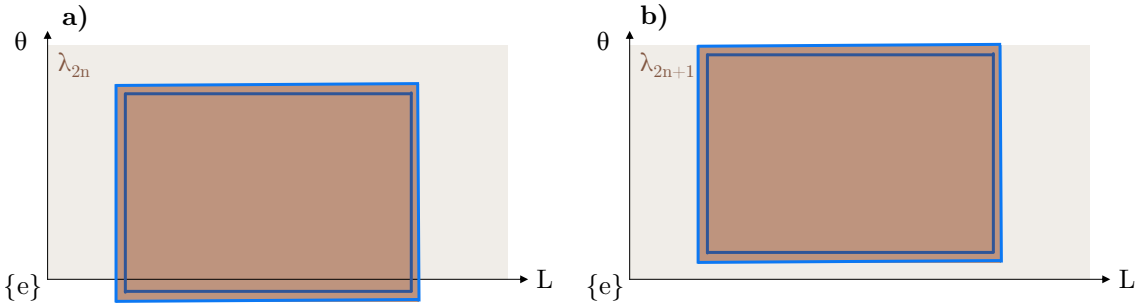

Figure 5.12: Axysimmetric cylinder layer in $\{e\}$ seam wall based on layer superposition in the vicinity of $\theta = 0$. a) shows the even layers layout, $n \in \mathbb{Z}^+$. b) shows the odd layers layout, $n \in \mathbb{Z}_{\geq 0}$.

Based on this premise, we begin to interpret a method for quantifying the spatial deformation generated by the bijective transformation. In this way, we can assess the need for points in each region of the slicing space $\{e\}$, ensuring appropriate infill density based on local deformation.

The spatial deformation using this methodology can exhibit double curvature, meaning curvature in both the L and θ coordinates. To approach the problem in the simplest way possible, we will start with the lamination generated by a surface with a single constant curvature. Specifically, this refers to a cylindrical bed slicing a cylindrical ring as shown in Figure 5.13a.

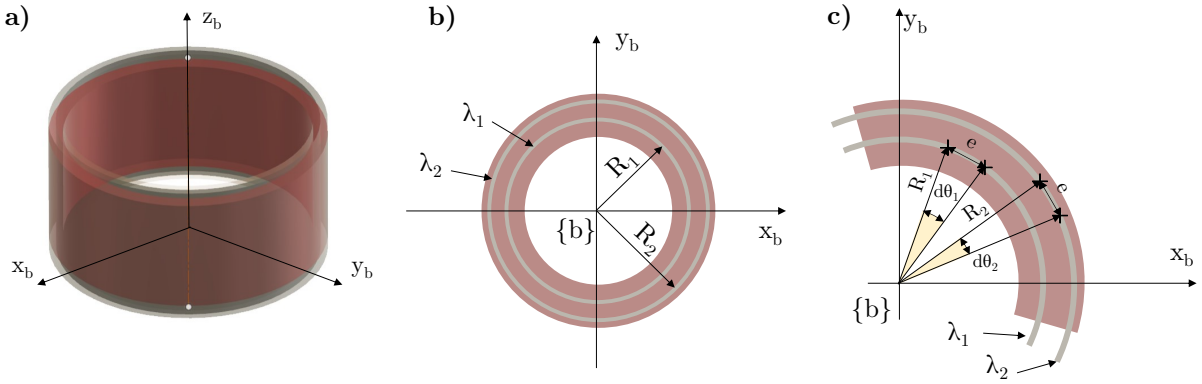

Figure 5.13: a) Cylinder laminated by cylindrical layers. b) Parameter definition of the layers viewed from the $x_b y_b$-plane. c) $d\theta$ definition for two pairs of equidistant points in each layer λ_1 and λ_2.

The relation between θ coordinate magnitude in both spaces, $\{e\}$ and $\{b\}$ is: $\theta_{\{e\}} \in [0, 2\pi]_{\{e\}}$ and $\theta_{\{b\}} \in [0, 2\pi R]_{\{b\}}$, where $R = \sqrt{x_b^2 + y_b^2}$. For each layer, R increases and therefore, $\theta_{\{b\}}$ increases in size. To maintain a constant distance between points along $\theta_{\{b\}}$, it will be necessary to increase the point density in each successive layer.

In other words, as shown in Figures 5.13b and 5.13c, to maintain a constant distance e between points in two layers with different radii R, it will be necessary to decrease the angular distance $d\theta$ in the slicing space $\{e\}$ between the points.

Given a desired distance between points (e.g., the nozzle diameter or a desired 50% infill), The relationship between the original distance (cord) and the actual arc length: (L/e) can be calculated as shown in 5.12 with respect to the radius of $\mathbf{\Gamma}$ at that specific point and direction. This ensures that the point spacing remains consistent across cylindrical layers.

$$\frac{A}{e} = \frac{2 \cdot R \cdot sin^{-1}(\frac{e}{2R})}{e} \tag{5.12}$$

It is convenient to reference the equation to curvature instead of radius to simplify future calculations. Curvature, κ_θ, being the inverse of the radius, allows for a more general approach to handling different geometries as shown in 5.13.

$$\frac{A}{e} = \frac{2 \cdot sin^{-1}(\frac{\kappa_\theta \cdot e}{2})}{\kappa_\theta \cdot e} \tag{5.13}$$

This methodology works when the lamination surface has curvature in only one direction, as the L and H coordinates maintain constant their metrix in both spaces. However, for surfaces with double curvature, L undergoes a spatial deformation similar to the previous case with θ.

Assuming a generatrix curve on its parametric form on the xz-plane, $\mathbf{\Gamma}(u) = (x(u), z(u))$, it is straightforward to calculate the curvature profile along the L coordinate as shown in 5.14 and 5.15. In turn, the parameter R, as previously defined, specifies the curvature in the θ direction for along z coordinate.

$$\mathbf{\Gamma}'(u) = \left(\frac{dx(u)}{du}, \frac{dz(u)}{du}\right) \qquad \mathbf{\Gamma}''(u) = \left(\frac{d^2x(u)}{du^2}, \frac{d^2z(u)}{du^2}\right) \tag{5.14}$$

$$\kappa_L(u) = \frac{||\mathbf{\Gamma}'(u) \times \mathbf{\Gamma}''(u)||}{||\mathbf{\Gamma}'(u)||^3} \tag{5.15}$$

The final result is a combination of curvatures in both directions, L and θ. This results in areas of high and low point density depending on the deformation experienced by the space. In other words, a surface differential $d\sigma$ in $(L_\sigma, \theta_\sigma)_{\{e\}}$ will be deformed in the L coordinate according to the curvature κ_L and in the θ direction according to the curvature κ_θ.

Areas with greater deformation will require a higher point density in the direction of the deformed coordinate in order to cover the space with evenly spaced points. Figure 5.14.a shows the result of this curvature analysis along the generatrix curve with both positive and negative curvature. As seen in Figure 5.14.c, the curvature in θ direction tends to invinite when the curve intersects the z-axis. This occurs because the radius R is zero, meaning a single point would cover the entire space. Along the θ direction, the curvature κ_θ is always positive due to its condition of revolution. The relation A/e needed for each L =constant line to be equidistant along the entire surface in $\{e\}$ will be calculated as expressed in 5.13.

Similarly, Figure 5.14.b shows the deformation in the L direction along the print bed, what could be seen as how the distance between points along a θ =constant line varies as a function

of the curvature κ_L. Mathematically shown in 5.16. In this case, both positive and negative curvatures appear. Positive curvatures tend to shrink the surfaces in the L direction, while negative curvatures tend to enlarge them.

Figure 5.14.d shows the deformation in the L direction along the print bed, what could be seen as how the distance between points along a L =constant line varies as a function of the curvature κ_θ.

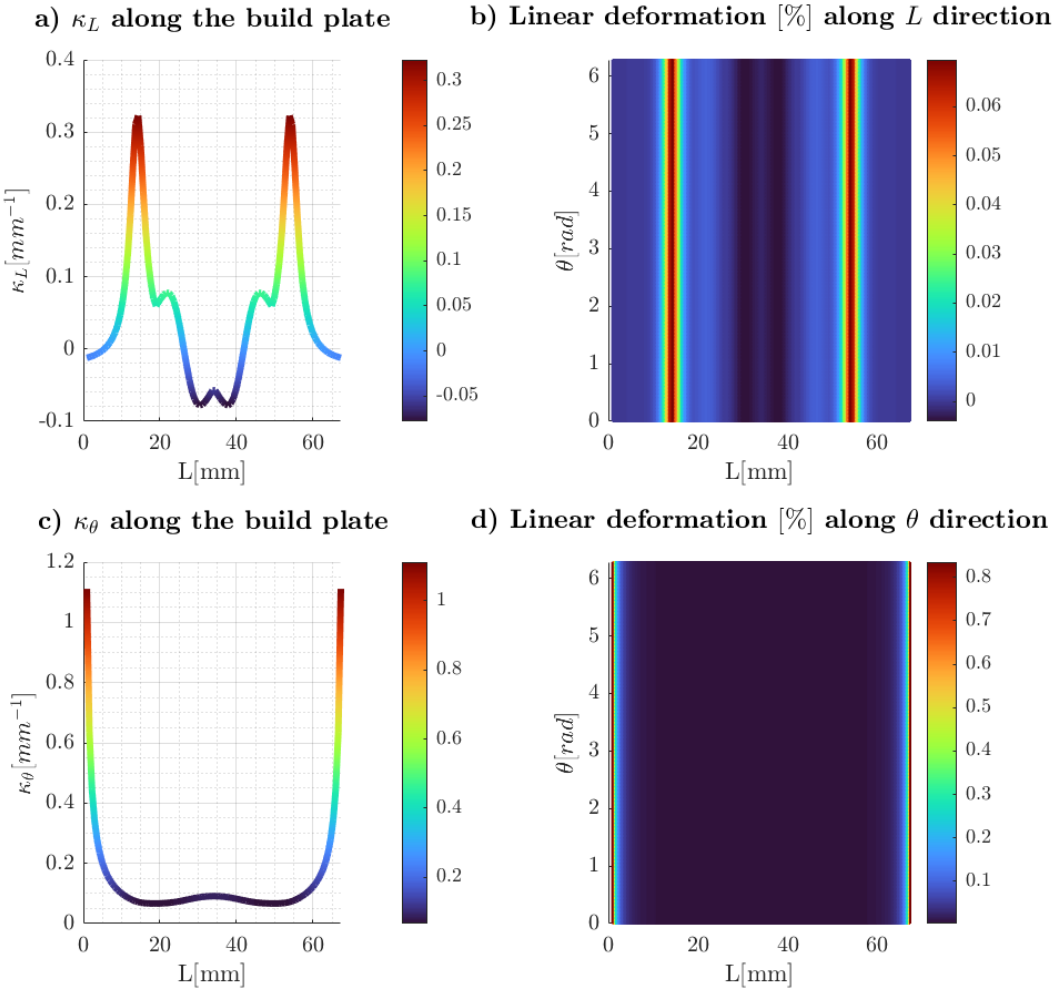

Figure 5.14: Surface curvature and deformation along the L and θ directions. a) Curvature κ_L along the build plate. b) Curvature κ_θ along the build plate. c) Linear deformation [%] along the L-direction. d) Linear deformation [%] along the θ-direction.

$$\frac{A}{e} = \frac{2 \cdot sin^{-1}(\frac{\kappa_L \cdot e}{2})}{\kappa_L \cdot e} \tag{5.16}$$

For the correct functioning of the developed methodology, the order of magnitude of e must be much smaller than $1/\kappa_L$ and $1/\kappa_\theta$. Otherwise, its application would not be meaningful. In

subsequent tests and validations, it has been established that a characteristic radius of the build platform of at least 10 mm works as a minimum limit for a 0.4 mm nozzle if there are no further constraints.

One final way to understand the deformation generated in the slicing space $\{e\}$ is by considering lines of the type L =constant in the $L\theta$-plane. The curvature κ_θ defines how much length of that line is covered by a surface differential, while the curvature κ_L indicates the width covered by that surface differential.

To generalize the deformation of $d\sigma$ along any direction in the $L\theta-$plane, the normal curvature κ_n in the direction defined by vector $\mathbf{n}$, which forms an angle α with the L direction, can be defined using an extension of Euler's formula for curvatures in arbitrary directions as shown in 5.17.

$$\kappa_n = \kappa_L \cdot cos^2(\alpha) + \kappa_\theta \cdot sin^2(\alpha) \tag{5.17}$$

Infill direction

The direction of filling is crucial for enhancing the mechanical properties of manufactured parts. Therefore, the algorithm has been designed to enable the filling of contours oriented in any direction within the $L\theta$-plane.

It is important to note that for this slicer functionality to enhance the mechanical properties of the manufactured part, a stress analysis must be performed to align the layers as parallel as possible to the first two principal stresses at each point. In other words, the normal vector to the surface should be as parallel as possible to the third principal stress at each point within the solid volume.

Once this alignment is achieved, the filling will be oriented within the $L\theta$-plane, associated with the surface, in the direction closest to the principal stress in one layer and perpendicular to it in the next layer. Chapters 5 and 6 provide a comprehensive overview of the process for enhancing mechanical properties by utilizing curve-based layers designed according to this methodology.

To develop the filling algorithm in any direction, an additional contour is created by applying an offset inward from the contour polygon. Straight lines are then defined aligned with the specified orientation.

The distance between the fill lines is determined based on the required density, as explained in the previous section. Once the lines are defined, the algorithm computes the intersection between the outermost contour polygon and each line. The path begins at the farthest end of the polygon's longest side and proceeds in a zigzag pattern until it reaches the opposite end. In some cases, not all lines are fully completed. When this happens, a travel path is generated, and the process restarts at the intersection of the next line with the outer polygon.

In cases where the generated polygon is non-convex, either due to its inherent nature or the presence of internal holes, some fill lines may be interrupted by the contour but need to be traversed again in other areas. Therefore, it is crucial to account for all the line segments

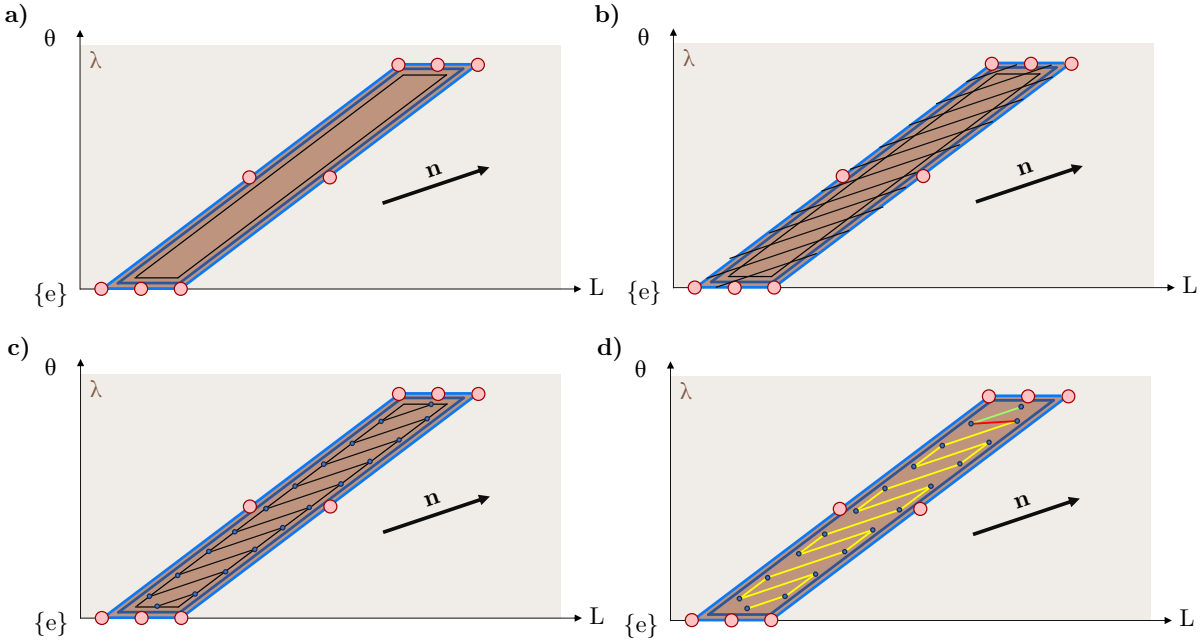

Figure 5.15: Methodology for filling layer contours in a specified direction **n** on a helical coil layer: a) inward offset of the contour; b) definition of lines with an assigned density along the specified direction **n**; c) identification of intersections between the inner contour and the generated lines; d) trajectory definition. The yellow line represents the first iteration of contour filling, the green line indicates the second iteration, and the red line denotes a travel displacement between the two trajectories.

within the polygon and ensure the algorithm continues until every segment has been fully covered.

Finally, once the fill trajectories are generated, it is necessary to incorporate additional waypoints in them according to the required density in each area and direction. This directional density is determined by the local curvatures κ_L and κ_θ.

Figure 5.15 illustrates the complete process described for generating trajectories based on a direction defined by vector **n**. In successive layers, this process is repeated, rotating the direction of the segments by 90° degrees for each layer.

Traveling trajectory design

In additive manufacturing, "travel paths" refer to movements that occur outside the material deposition trajectory. During these displacements, particularly in flat additive manufacturing, the nozzle retracts material, moves upward on the z-axis, and then travels to another area where printing is required. In the case of NPAM, this travel must occur above the curved printing surface to avoid any collisions with the previously printed surface.

This is where one of the main advantages of this slicing method lies. By defining the Slicing space $\{e\}$ through the coordinates (L, θ, H), the displacements in H-coordinate are always normal to slicing surface at each point. Furthermore, the displacements at constant H planes

in $\{e\}$ are always parallel to the slicing surface.

Therefore, for any travel trajectory between two points in $\{e\}$, collisions can be avoided by increasing the H-coordinate of the nozzle along the previously generated travel path contained in any the $L\theta$-plane.

After executing the algorithm, the entire trajectory, consisting of waypoints defining the walls, infill, and travel paths for each layer, is sequentially stored in the variable $\mathcal{X}$, which corresponds to the target positions of the robot represented in the Slicing space. This variable holds, for each point, its $(L, \theta, H))$ coordinates concatenated with the unit normal vector to the $L\theta$-plane: $(0, 0, 1))$. The number of rows in the variable corresponds to the total number of waypoints in the trajectory.

A seventh column is filled with a variable τ indicates the type of trajectory being executed, as each type has specific properties depending on its condition: travels do not involve extrusion, infill is performed at higher speeds, and walls are carried out at slower speeds for greater precision among other differences. Equation 5.18 illustrates the output variable.

$$\mathcal{X} = \begin{pmatrix} L_1 & \theta_1 & H_1 & 0 & 0 & 1 & \tau_1 \\ L_2 & \theta_2 & H_2 & 0 & 0 & 1 & \tau_2 \\ \vdots & \vdots & \vdots & \vdots & \vdots & \vdots & \vdots \\ L_n & \theta_n & H_n & 0 & 0 & 1 & \tau_n \end{pmatrix} \tag{5.18}$$

Once the variable is obtained, the forward transformation is applied to convert the waypoints into the world space. The transformed variable is $\mathbf{X}$ described in 5.19. Where the first three coordinates indicate the required position of the nozzle, the next three represent the orientation in Euler angles, and the seventh coordinate indicates the type of trajectory, which remains the same as in the previous case.

$$\mathbf{X} = \begin{pmatrix} x_1 & y_1 & z_1 & \alpha_1 & \beta_1 & \gamma_1 & \tau_1 \\ x_2 & y_2 & z_2 & \alpha_2 & \beta_2 & \gamma_2 & \tau_2 \\ \vdots & \vdots & \vdots & \vdots & \vdots & \vdots & \vdots \\ x_n & y_n & z_n & \alpha_n & \beta_n & \gamma_n & \tau_n \end{pmatrix} \tag{5.19}$$

5.2.3 Output trajectories: robot implementation

This section explains the process used to reference the generated slicer trajectories and transform them into the world space relative to the $\{s\}$ frame. To properly situate the printing locations under the fixed extrinsic extruder head reference frame in $\{b\}$, a workflow of homogeneous transforms has been developed. This workflow is schematically represented in Figure 5.16, where each reference frame is expressed with respect to another reference frame, denoted as a subscript.

This workflow is subdivided in three steps. In the first step, $\mathcal{X} = \mathcal{X}_{\{e\}}$ is isomorphed back to the World space referred to its model frame $\{model\}_{\{bp\}}$, including in this transformation the isomorphed $\{e\}_{\{s\}}$ trihedron inherent to each point through the inverse transformation

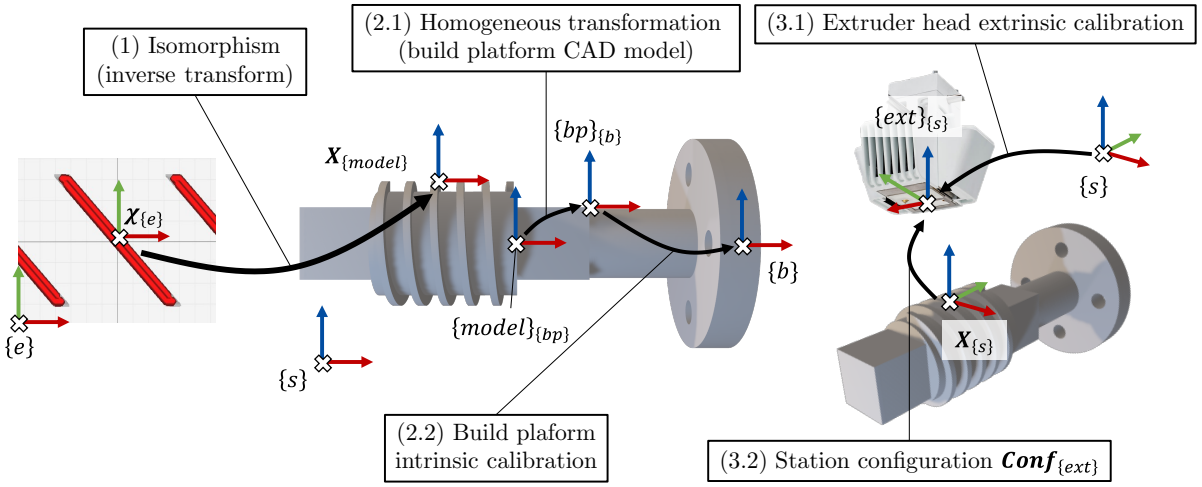

Figure 5.16: Schematic representation of the transformation operations to locate the part under the extrusion nozzle.

method (Equation 5.20, with reference frames expressed as homogeneous transformation matrices). The transformed printing locations $\mathbf{X}_{model}$ are initially referenced to the model origin $\{model\}_{\{bp\}}$ on the build platform $\{bp\}_{\{b\}}$. Thus, the second step involves referencing these locations with respect to the robot's reference frame $\{b\}$. This is done through a pair of homogeneous transformations. Firstly, the printing locations are expressed in $\{bp\}_{\{b\}}$. This transformation is obtained from the CAD model when locating and orienting the part for slicing. These printing locations, expressed as $\mathbf{X}_{\{bp\}}$, shall be expressed as $\mathbf{X}_{\{b\}}$ by means of an intrinsic calibration method. The final step involves aligning the printing locations with the extrinsic extruder head reference frame $\{ext\}_{\{s\}}$ using the robotic manipulator. This extrinsic reference frame is to be calibrated before the trajectory is executed. The condition for the extrusion direction to be perpendicular to the build platform leaves one unrestricted DoF The configuration homogeneous transform $\{\mathbf{Conf}\}_{\{ext\}}$ is then applied to constrain this final DoF as shown in 5.21.

$$\mathcal{X}_{\{e\}} = \begin{pmatrix} & \mathbf{I}_{3\times3} & & L \\ & & & \theta \\ & & & H \\ 0 & 0 & 0 & 1 \end{pmatrix} \longrightarrow X_{model} = \begin{pmatrix} \mathbf{e}_{L_{\{s\}}} & \mathbf{e}_{\theta_{\{s\}}} & \mathbf{e}_{H_{\{s\}}} & x \\ & & & y \\ & & & z \\ 0 & 0 & 0 & 1 \end{pmatrix} \tag{5.20}$$

$$\mathbf{X}_{\{s\}} = \{ext\}_{\{s\}} \cdot \{\mathbf{Conf}\}_{\{ext\}} \tag{5.21}$$

5.3 Construction of an industrial robot-based NPAM cell prototype

This section aims to provide a detailed explanation on the implementation of the theoretical basis explained on a robotized AM machine. A brief graphical summary is presented in Figure 5.17. This implementation resembles architectures defined by other authors [58].

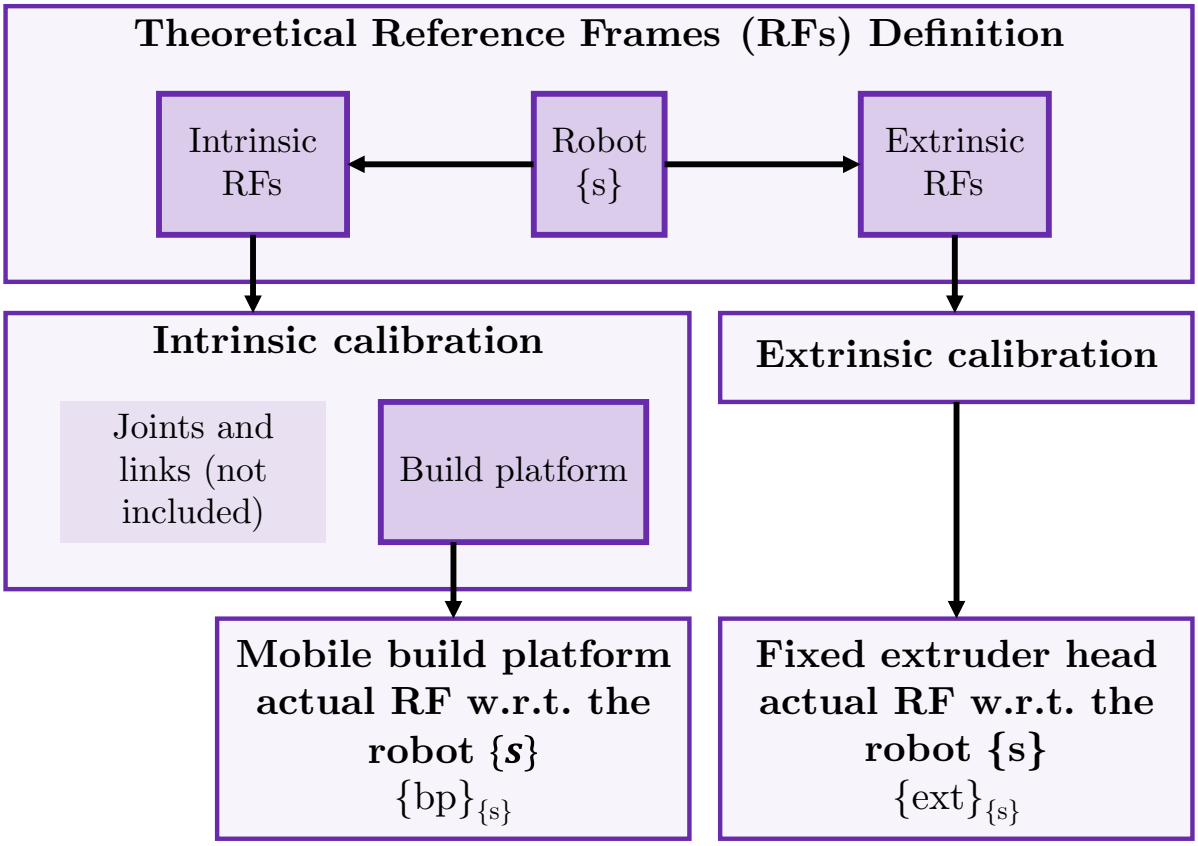

Figure 5.17: Steps for the implementation of the theoretical basis in a robotized station. With respect to (w.r.t.).

The first step in establishing the robotized station workflow is the definition of several reference frames (RFs), both intrinsic (associated to the robot arm kinematic configuration, dependent on joint coordinates), and extrinsic (associated to a global RF $\{s\}$ irrespective of joint coordinates). A full graphical description of these frames is shown in Figure 5.18.

The first RF to be defined, $\{ext\}_{\{s\}}$, is the extrinsic reference frame linked to the point of material deposition in the extruder. The second RF $\{TCP\}_{\{b\}}$ is the one linked to the end effector Tool Center Point, which are the printing locations expressed with respect to the robot flange $\mathbf{X}_{\{b\}}$. The relationship between these two coordinate systems consists of a homogeneous transformation between the robot base base (which is set as the global reference frame $\{s\}$), and $\{ext\}$; as well as a variable transformation between $\{s\}$ and $\{TCP\}$ calculated through the inverse kinematics of the robotic manipulator. Figure 5.18 spatially locates the three frames in a digital model of the station.

To ensure the robotized station achieves precise printing locations, a calibration workflow has been implemented, although it is important to note that the primary focus of this paper is not on the calibration process itself. The $\{ext\}$ extrinsic calibration method implemented in this paper has been extracted from a procedure outlined in a prior work by the authors [59], whereas the $\{TCP\}$ intrinsic calibration method was adapted from the same work. This adaptation involves transitioning from a mobile laser-fixed part configuration to a mobile part-

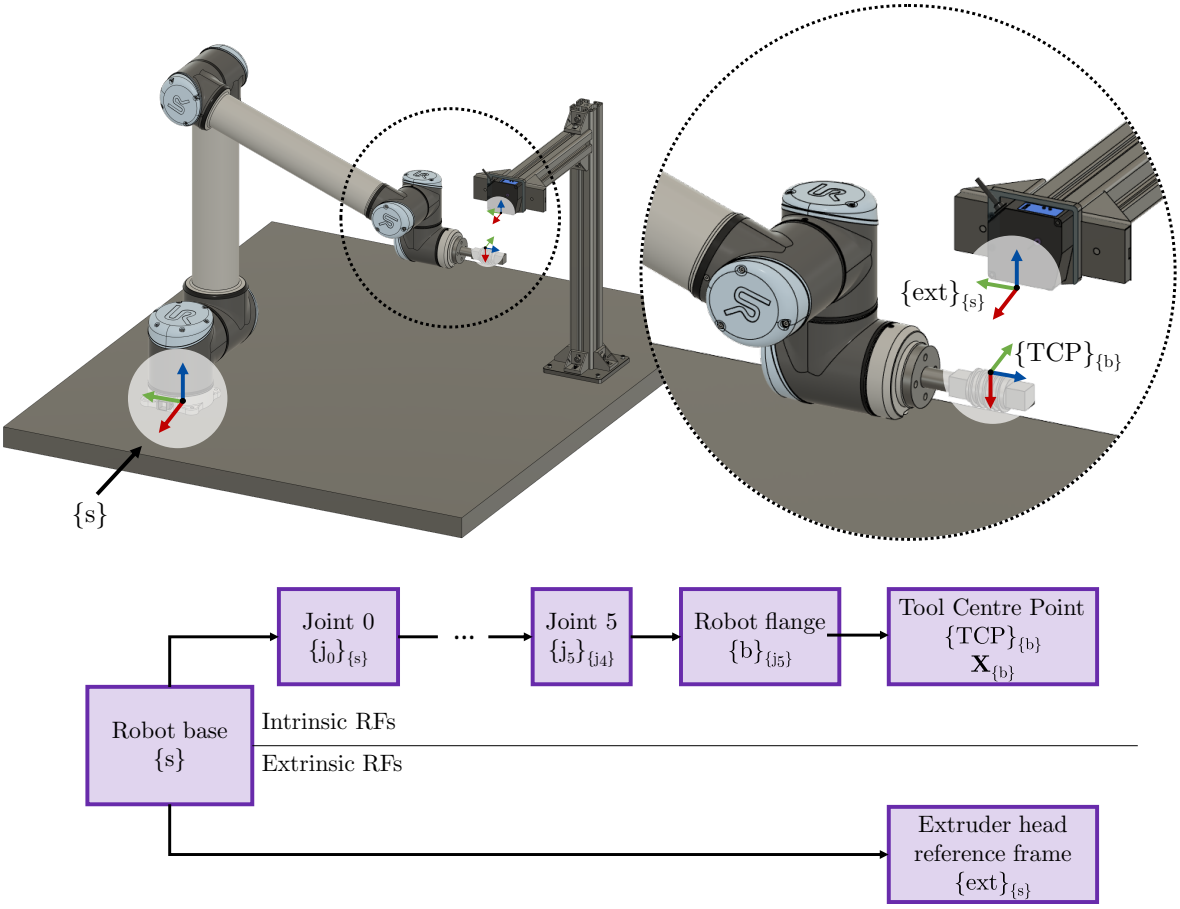

Figure 5.18: Representation of RFs defined in the robotized station.

fixed laser configuration. The adapted method still consists of extracting seven characteristic points associated to a calibration feature on the mobile part, in this case, two calibration cubes at each end of the build platform (Figure 5.16). The result of this extrinsic calibration is the location of the $\{ext\}_{\{s\}}$ reference frame, while the result of the build platform calibration is the location of the $\{bp\}_{\{b\}}$ reference frame.

To validate the methodology, a trajectory tracking test was carried out on the robotized station. In this test, a laser distance sensor measures the distance between the $\{TCP\}$ and $\{ext\}$ reference systems while the robot executes the calculated printing trajectories. If the robot keeps the distance between the two frames $\{ext\}$ and $\{TCP\}$ constant along the entire trajectory, it would validate that an extruder can accurately deposit material on the predefined trajectory. The test not only validates the execution of a trajectory on the pre-printed case studies but also gauges the performance of the calibration methods that locate in space, in position and orientation, the extruder head extrinsic reference frame $\{ext\}_{\{s\}}$ and the build platform intrinsic reference frame $\{bp\}_{\{b\}}$.

The test was conducted on the two geometries proposed as case studies. The build platforms studied in this paper are defined through the control polygons shown as tables in Figure 5.19. Two composite Bézier curves were selected, having the cylindrical case composed of

a)

Cylindrical spring case control points	
x [mm]	z [mm]
15	40
15	35
15	30
15	25
15	20
15	10
15	0

b)

Hourglass spring case control points	
x [mm]	z [mm]
0	40
10	40
15	42
15	35
15	28
11	27
11	20
11	13
15	12
15	5
15	-2
10	0
0	0

Figure 5.19: Planarly printed case studies. a) Cylindrical spring case, build platform control polygon and resulting test artifact, b) Hourglass shaped spring, build platform control polygon and resulting test artifact. The case studies were manufactured using poly(lactic acid) (PLA), specifically, Ultrafuse PLA from BASF.

two splines, and the hourglass case composed of four splines. The springs were designed by conformally coiling a $2mm$ wide strip around the build platform and extruding it $2mm$ in the radial direction. The build platforms have been manufactured using planar additive manufacturing in an Ultimaker $S5$ AM machine. As depicted in Figure 5.19, the geometries forming the proposed robotic NPAM trajectories were also planarly manufactured along with the build platform. By constructing both the spring and the build platform within the same component, it becomes possible to measure the accuracy of maintaining a constant distance between the nozzle and the surface throughout the trajectory execution.

The trajectory generation algorithm was implemented in Matlab 2023*b*. In addition, the trajectories were executed on an instrumented station by a Universal Robots robotic manipulator model $UR10$. The distance between the $\{TCP\}$ and $\{ext\}$ systems was measured using a SICK laser distance sensor model $OD5-30W05$, connected to a SICK signal conditioner $AOD5-P1$. To read the data, the analog signal from the conditioner was connected to the PLC managing the robot and extracted via TCP/IP through the UR Log Viewer software (version 1.2.1.0), enabling the synchronization of distance measurement with the robot pose. This test environment is shown in Figure 5.20.

5.4 Results and discussion

5.4.1 Robot-based NPAM slicer

The main outcome of the non-planar layer slicing and infill methodology is the development of a slicer with the necessary functionalities to generate the required printing trajectories.

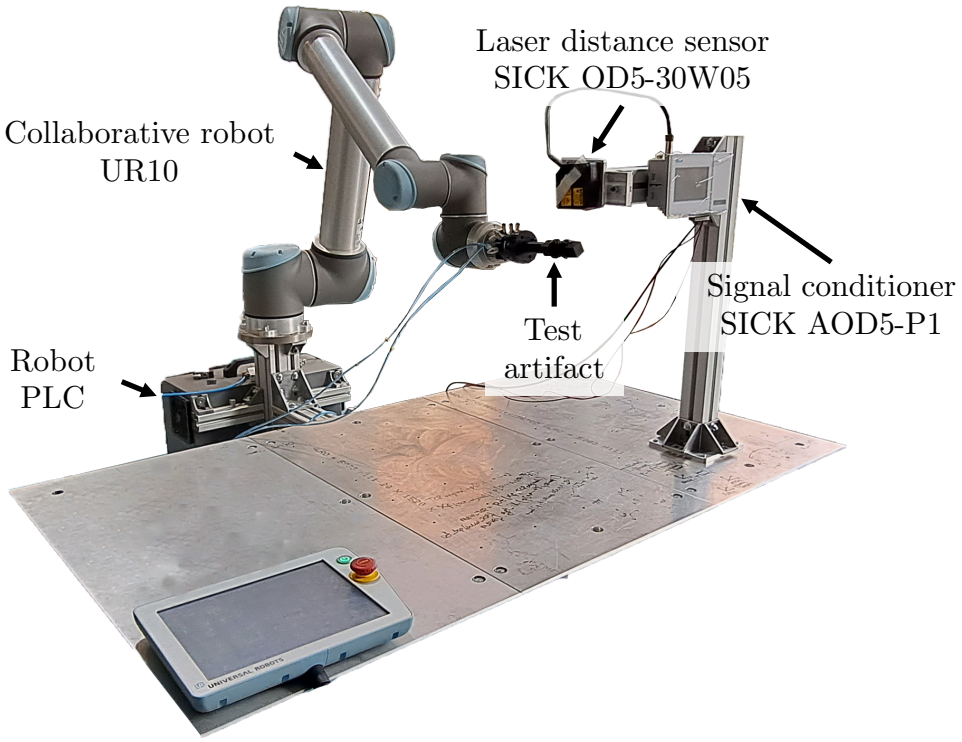

Figure 5.20: Instrumented robotized station utilized for testing.

From 3D solid and the user's desired print bed, the software is able to generate, visualize and modify the trajectories to be implemented in the robotic additive manufacturing station.

The slicer workflow is summarized in the diagram of Figure 5.21. The software operates between two defined spaces in the methodology: World space, represented in blue, and the Slicing space, in red.

Starting with a 3D solid in STL format and a print bed defined by a cubic spline, the slicer displays their relative positioning in the world space referred to $\{b\}$. Once verified as correct, the inverse transformation function is executed, converting the STL into the Slicing space generated by the print bed referred to $\{e\}$.

After inputting slicer parameters and pressing *slice*, the software sections the solid based on the input parameters and fills the layers. This process can be performed using two slicers: a commercial slicer, Ultimaker Cura, which operates at higher speeds and handles more complex parts but is not optimized for NPAM, or a custom slicer developed in this thesis. The custom slicer allows for optimization and addresses all issues arising from work in a deformed subspace, but it is not optimized for speed and requires substantial time when processing complex geometries. The slice section then compiles the trajectory data into the variable $\mathcal{X}_{\{e\}}$, which is shown layer by layer. Finally, once the slicing is validated, the software applies the direct transformation, returning the trajectories to world space, captured in the variable $\mathbf{X}_{\{b\}}$.

The software has been developed using Matlab 2023b AppDesigner. A window layout similar to commercial planar slicers was chosen. In these slicers, the lamination process is divided into two stages: Prepare, where the part is placed on the build platform and its orientation is

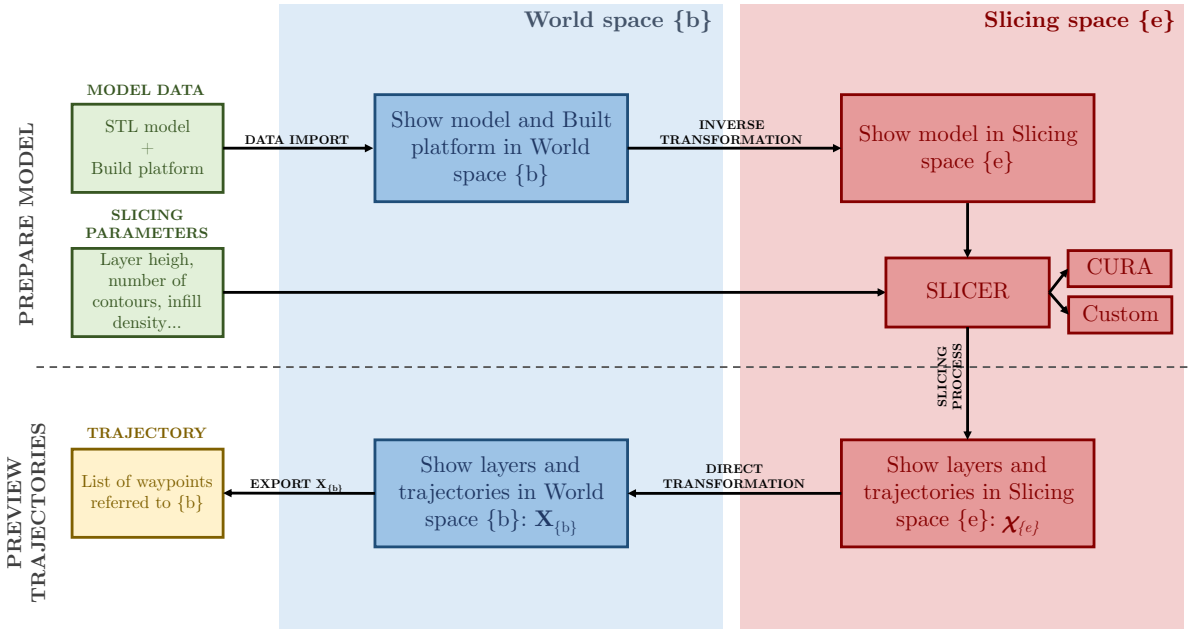

Figure 5.21: Slicer workflow.

visualized, and Preview, where, after the lamination is complete, the toolpaths are previewed. Additionally, a third dedicated window is included for inputting lamination and layer infill parameters.

To validate the software's functionality, a total of seven case studies have been conducted, aimed at ensuring its proper performance:

- **Half cylinder on a cylindrical built platform:** This case aims to validate the functionality of the wall generation during the slicing of figures that do not encompass a full 360°.
- **Cylinder on a cylindrical built platform:** This case aims to validate the functionality of seam walls.
- **Truncated cone on a conical built platform:** This case is used to validate the construction of overhanging surfaces in the slicing space.
- **Hourglass shape on an hourglass build platform:** This case is used to validate functionality on beds with highly variable curvature.
- **Cylindrical coil and hourglass coil constructed on cylindrical and hourglass-shaped platforms:** These two cases are utilized throughout the entire methodology and will later be implemented in the robotic station.

The results pertaining to the last two case studies will be presented next, as they follow the narrative of the text. The remaining simple geometries case studies used for validation are included in Annex A of the document.

Figure 8 shows the slicing process of a cylindrical spring coil using the custom slicer that works between $\{b\}$ and $\{e\}$. In addition to validating the necessary steps, it confirms that

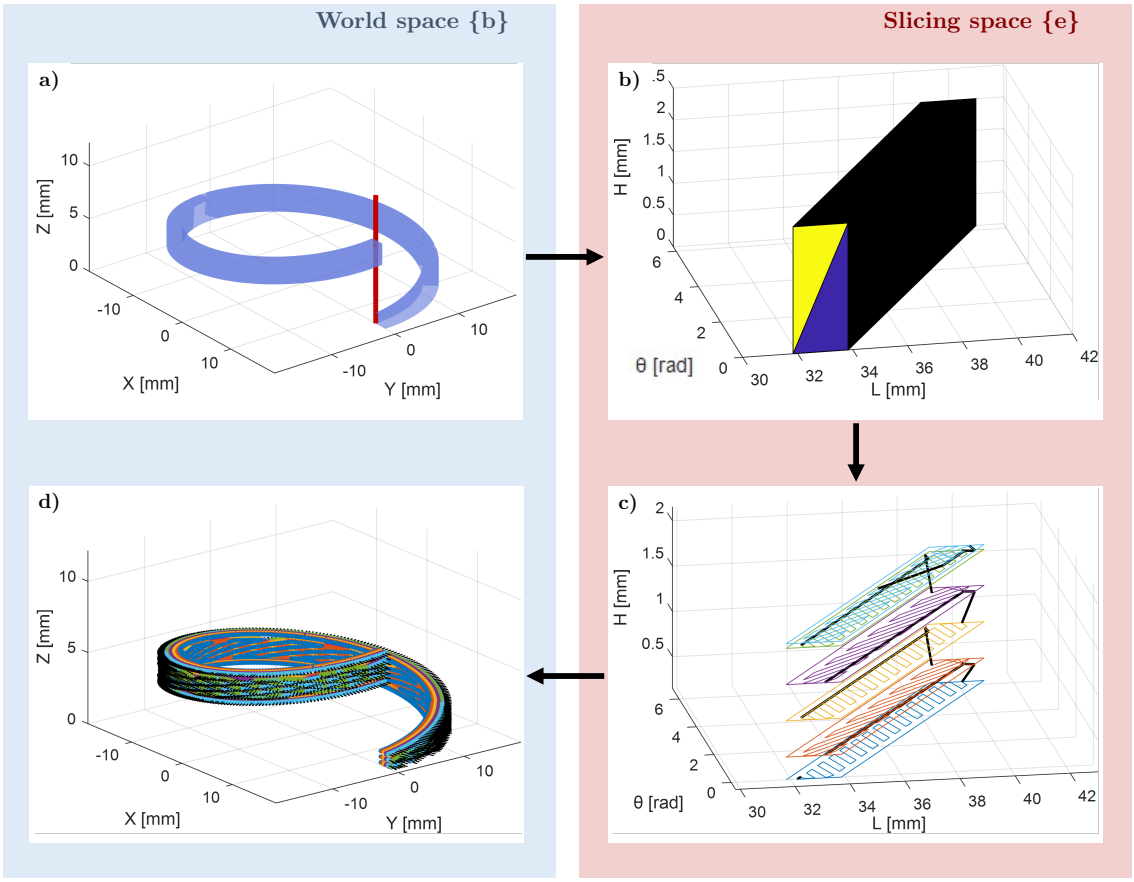

Figure 5.22: Trajectory generation for a cylindrical spring coil. a) STL file and print bed in World space referred to $\{b\}$. b) STL file converted to Slicing space referred to $\{e\}$. c) laminated solid in $\{e\}$ with its defined trajectories: $\mathcal{X}_{\{e\}}$. d) laminated solid in $\{b\}$ with its defined trajectories: $\mathbf{X}_{\{b\}}$. Normal vectors in black represents the extruder orientation.

the direction of layer infill can be selected, and the travel movements are correctly generated. Figure 8.d visualizes the black vectors, normal to the surface at all times, guiding the orientation of the extruder at each point. A similar observation can be made in Figure 5.23, where an hourglass-shaped spring coil demonstrates the slicer's functionality for more complex curvatures.

5.4.2 Robotic Non-Planar Additive Manufacturing cell prototype

This section details the generated trajectories for each case study (sliced uniformly and conformally to the build platforms) and validation of the entire workflow on the robotized station outlined in the test setup. The discussion is mainly focused on the precision challenges of implementation of robot-based NPAM processes, emphasizing the precision of the generated trajectories in the context of robotized high-precision manufacturing operations.

Firstly, the trajectories generated following the methodology for both case studies are represented in Figure 5.24. For the sake of simplicity, only the outer shells of the models were

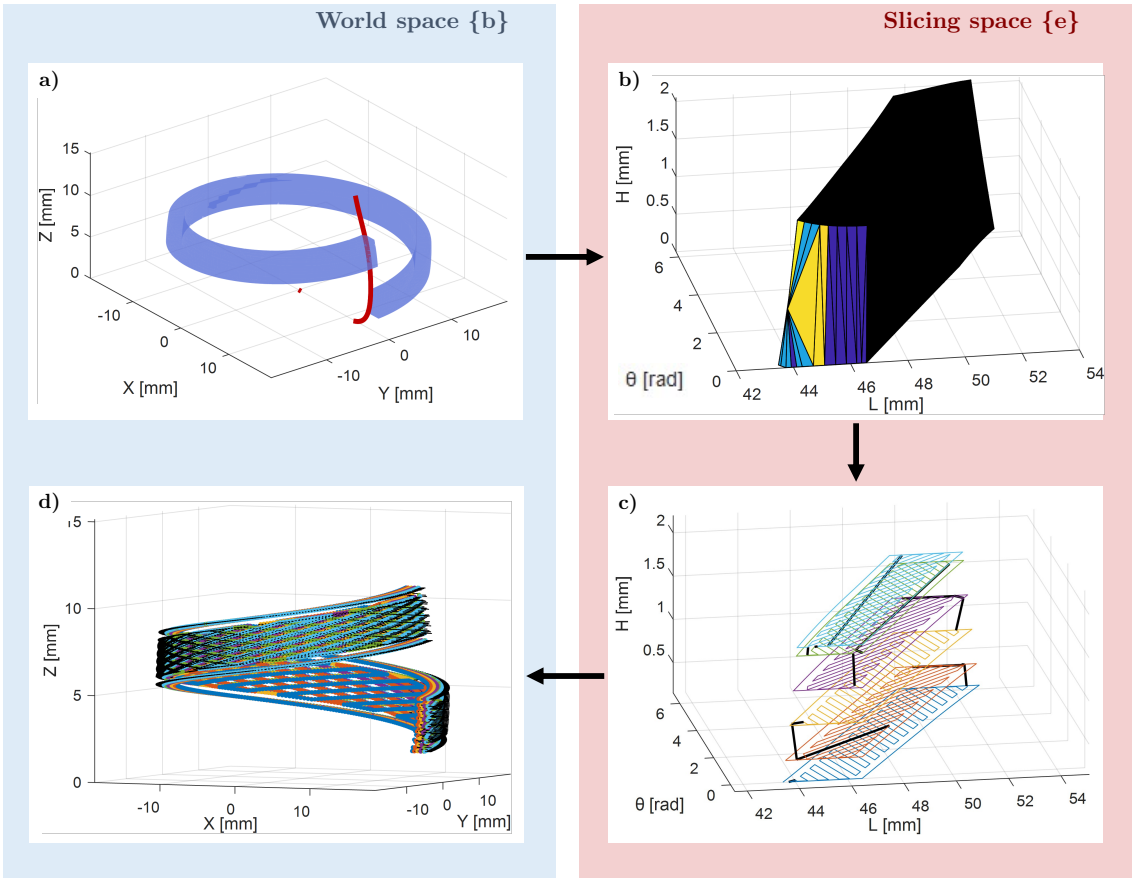

Figure 5.23: Trajectory generation for an Hourglass-shapped spring coil. a) STL file and print bed in World space referred to $\{b\}$. b) STL file converted to Slicing space referred to $\{e\}$. c) laminated solid in $\{e\}$ with its defined trajectories: $\mathcal{X}_{\{e\}}$. d) laminated solid in $\{b\}$ with its defined trajectories: $\mathbf{X}_{\{b\}}$. Normal vectors in black represents the extruder orientation.

generated. Of note, regarding the right-hand side diagrams in Figure 5.24, the travel moves (represented in solid black line) generated by the software are not interpolated by the present algorithm, which in turn may result in deviations when implementing the trajectories in the robotized station.

For the cylindrical case, an operation time in the range of $7200s$ (at a commanded linear speed of $20[mm/s]$) would be required, whereas for the hourglass-shaped case, an operation time in the range of $7500s$ would be required at the same commanded linear speed. The difference between both cases is explained by the slight difference in volume between the two parts, as well as different travel paths defined by the algorithm, which are to be performed at the same linear speed. In addition to this trajectory time, a preparation time of $600s$ would be required before the operation to set the heated components and calibrate the build platform, as well as a post-operation time of $300s$ to cool the heated components and extract the part.

Regarding the implementation validation of the generated trajectories and their precision, only one and a half coils of each spring were executed in the robotized station as these datasets

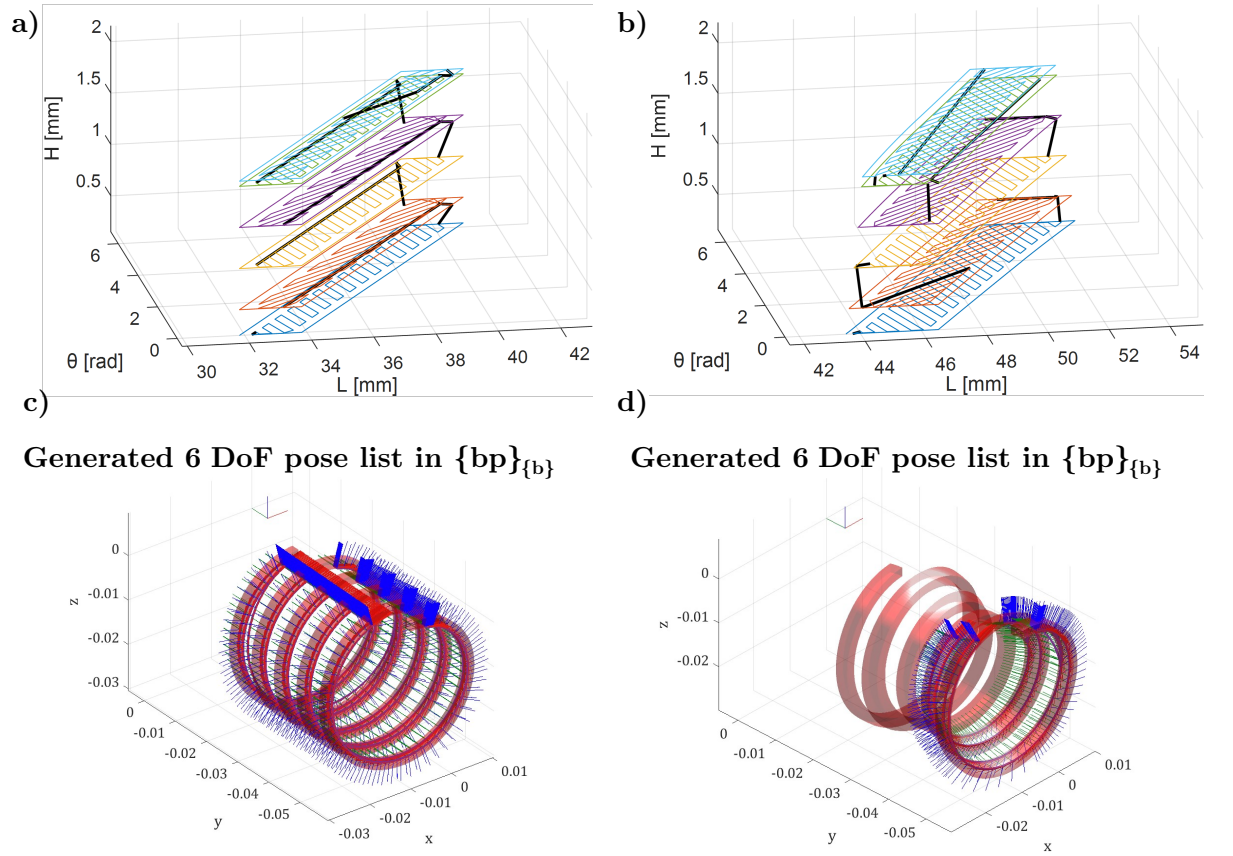

Figure 5.24: a) Planarly generated trajectories of the cylindrical case study in the slicing coordinate system $\{e\}$, first layer. b) Planarly generated trajectories of the hourglass-shaped case study in the slicing coordinate system $\{e\}$, first layer. c) Parametric 6 DoF pose list in $\{bp\}$, first layer. d) Parametric 6 DoF pose list in Cartesian coordinate system $\{bp\}$, first layer. For this case study, only the first 3000 points were represented for diagram clarity.

were considered sufficiently representative of the setup precision. Figure 5.25 represents the measurements obtained from the laser tracker along the trajectories generated for the printing of the case studies. Additionally, Figure 5.26 represents a comparison between 5 test repetitions carried out for each case, proving the repeatability in the execution of the trajectories.

The results of Figure 5.25.a show that the error in the execution of the trajectory with respect to the predicted value is $\pm 250 \mu m$. This error corresponds to the sum of the calibration error and the calculation error derived from the inverse kinematics of the robot. In addition, the difference between the peak and valley values of the measurements and the moving average corresponds to the positioning uncertainty associated with the robot axes controllers. This error of around $\pm 100 \mu m$ corresponds to the error provided by the robot manufacturer [197].

On the second case study, Figure 5.25.b, it can be seen how the error increases to $\pm 350 \mu m$. This error is explained by the fact that, while in the case of the cylinder, the calibration error of the axis parallel to the axis of revolution of the bed does not affect the measurement, in

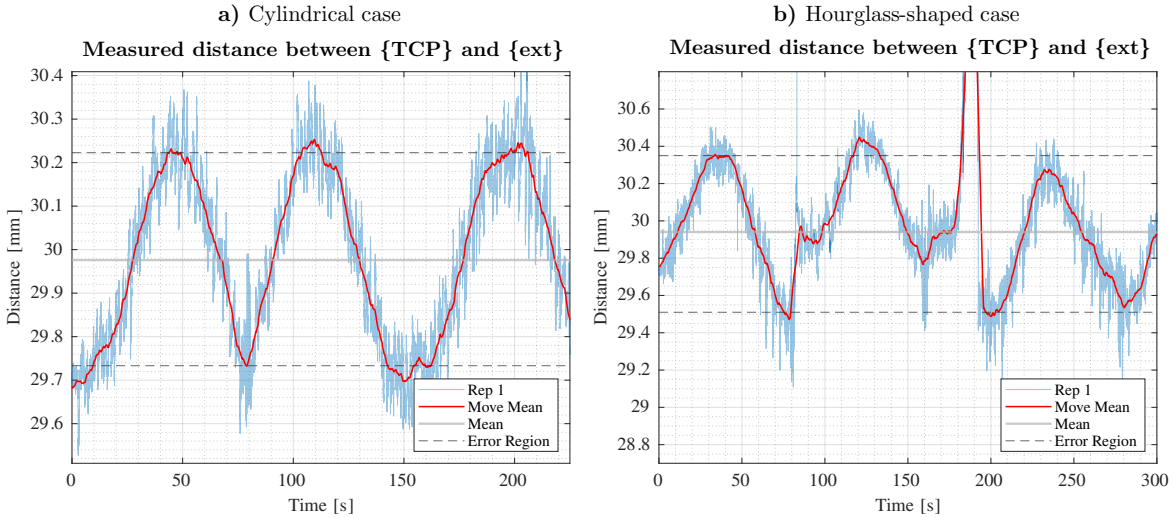

Figure 5.25: Measured distance between $\{TCP\}$ and $\{ext\}$ along trajectory execution. a) cylindrical spring case, b) hourglass-shaped case.

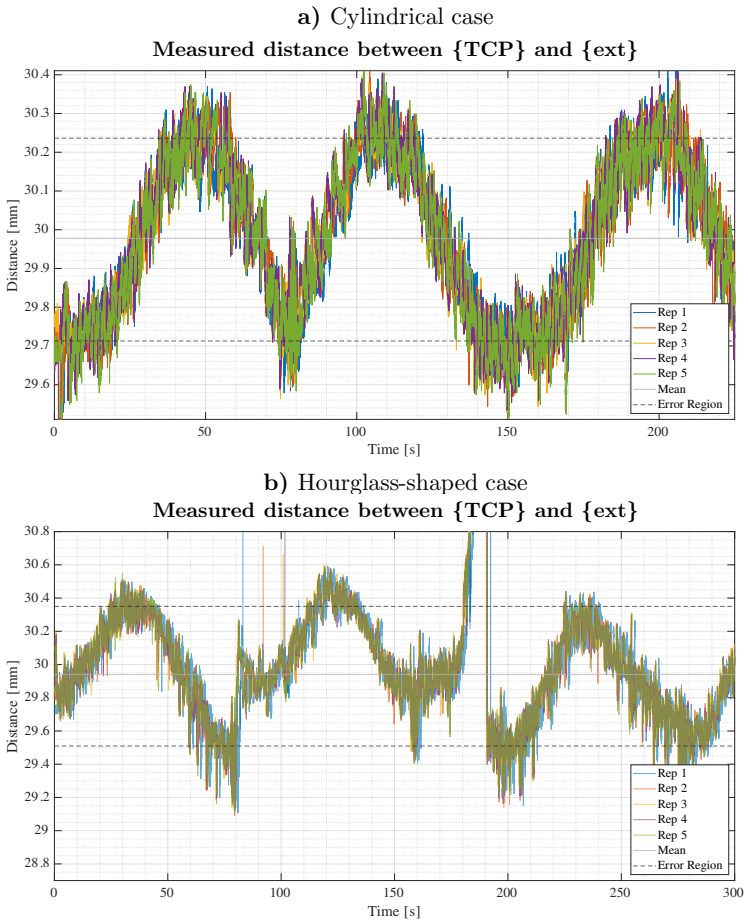

Figure 5.26: Repeatability in the trajectory execution: a) Cylindrical spring case. b) Hourglass-shaped case.

more complex geometries it does.

When the test is repeated (Figure 5.26), the calibration and kinematic calculation error is systematic, while the error associated with the axes controllers is random. Even so, the repetitions correspond to the experimental results and show the feasibility of the trajectory execution as well as a noticeable improvement with respect to the calibration and execution errors presented by other authors in the literature [31, 29, 30].

It should also be noted that in Figures 5.25.b and 5.26.b the central peak is the one associated with the implementation of travel movements established by the algorithm and converted to the World space, as explained previously. It is therefore repeated in all the trajectories. This does not occur in the case of a cylindrical spring because the robot will adopt positions conformal to the build surfaces through regular planar travel movements.

Build platform prototype construction

After validating the methodology, focus shifted to constructing a functional aluminum cylindrical build platform for operating the robotized non-planar additive manufacturing cell. This platform is engineered to meet multiple requirements, including calibration, printing surface, thermal control, and robot connection, as outlined below:

- **Callibration:** Two calibration cubes needed to be integrated into the design to perform the previously mentioned calibration operations. Additionally, they had to be placed as far apart as possible from each other, with tight tolerances for flatness and face perpendicularity to avoid distorting the laser measurements.
- **Printing surface:** A cylindrical surface was chosen for the first prototype due to its versatility in removing the printed parts. Therefore, a cylindrical build surface with a $30mm$ diameter and $40mm$ height was implemented. This surface features a tight tolerance for cylindricity and relative positioning with respect to the calibration cubes, which will be crucial for improving accuracy.
- **Thermal control:** It was decided that the prototype's level of detail must be sufficient for its future operational use; thus, a heating element and a thermocouple were incorporated along with all necessary wiring for heating and future control. The goal is to achieve a bed operating temperature between $40 - 80°C$.
- **Robot connection:** The connection to the robotic arm was designed to be as monolithic as possible, minimizing deviations between reference frames $\{b\}$ and $\{bp\}$. To achieve this, conical joints and angular locking systems were utilized. Additionally, the interface between the robot and the bed features a nylon barrier that prevents overheating of the robotic manipulator's tip during operation.

Figure 5.27 shows the final design and construction of the printing bed prototype. The platform was modeled in CATIA V5, allowing for accurate geometric construction and iterative refinement throughout the design process. A key aspect was ensuring the proper fit and alignment of components, especially given the complex interactions within the robotic cell. A cylindrical heater was strategically placed to ensure uniform heat distribution, and the overall assembly was designed to avoid interference with the robot's movements. Standardized

components, such as Allen-head screws and easily accessible fasteners, were incorporated to streamline assembly and maintenance processes.conducted on it.

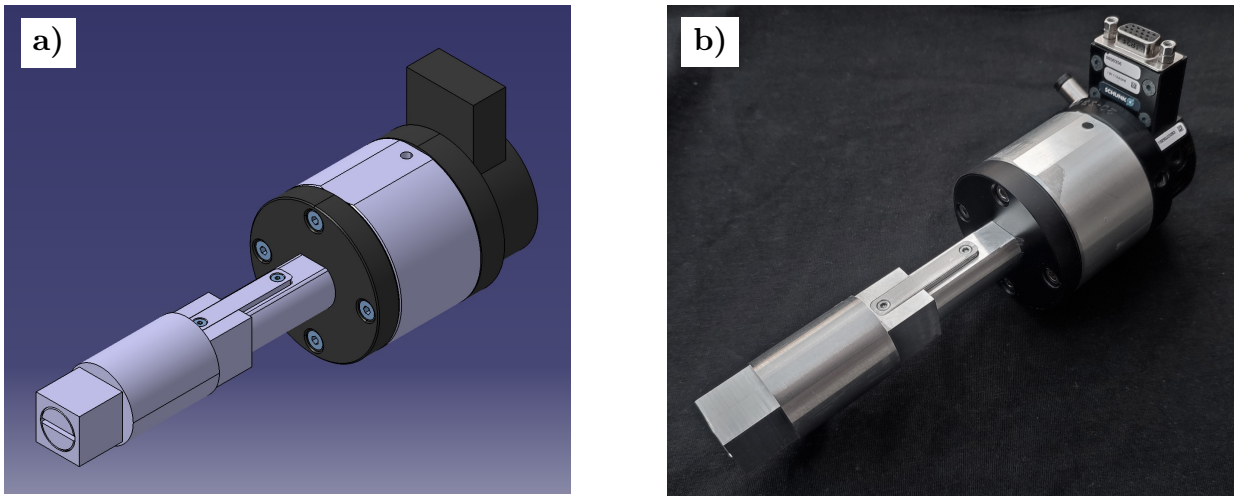

Figure 5.27: Robot-based NPAM built platform final design. a) Model. b) Manufactured prototype.

A finite element analysis was conducted using COMSOL Multiphysics to evaluate the platform's thermal performance, particularly focusing on the heater's placement and the insulating materials. See Figure 5.29. The analysis confirmed that centering the heater provided uniform temperature distribution, with less than 0.5°C variation across the surface. Nylon was selected as the insulation material for its thermal resistance and availability. A supplemental thermal regulation system was proposed to prevent overheating, which could compromise the thermally sensitive paste used in the manufacturing process and impact the longevity of the platform components. The model has been validated with a heating test carried out with the set up described in Figure 5.28.a with satisfactory results that validate the model shown in Figure 5.28.b.

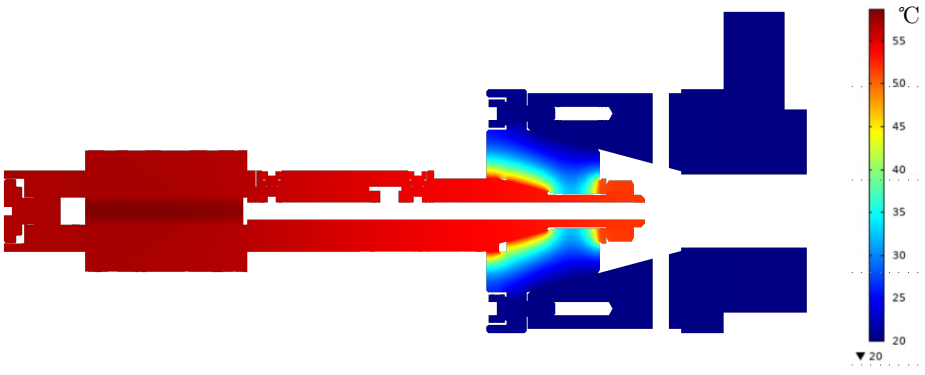

Figure 5.28: COMSOL Multiphysics thermal analysis under working condition. Axial cross section.

The platform's precision directly impacted the quality of the parts produced. Critical surfaces were evaluated for flatness, perpendicularity, and parallelism, with tolerances set to as low as $10\mu m$ for flatness and perpendicularity, and $0.1mm$ for parallelism. These tight tolerances

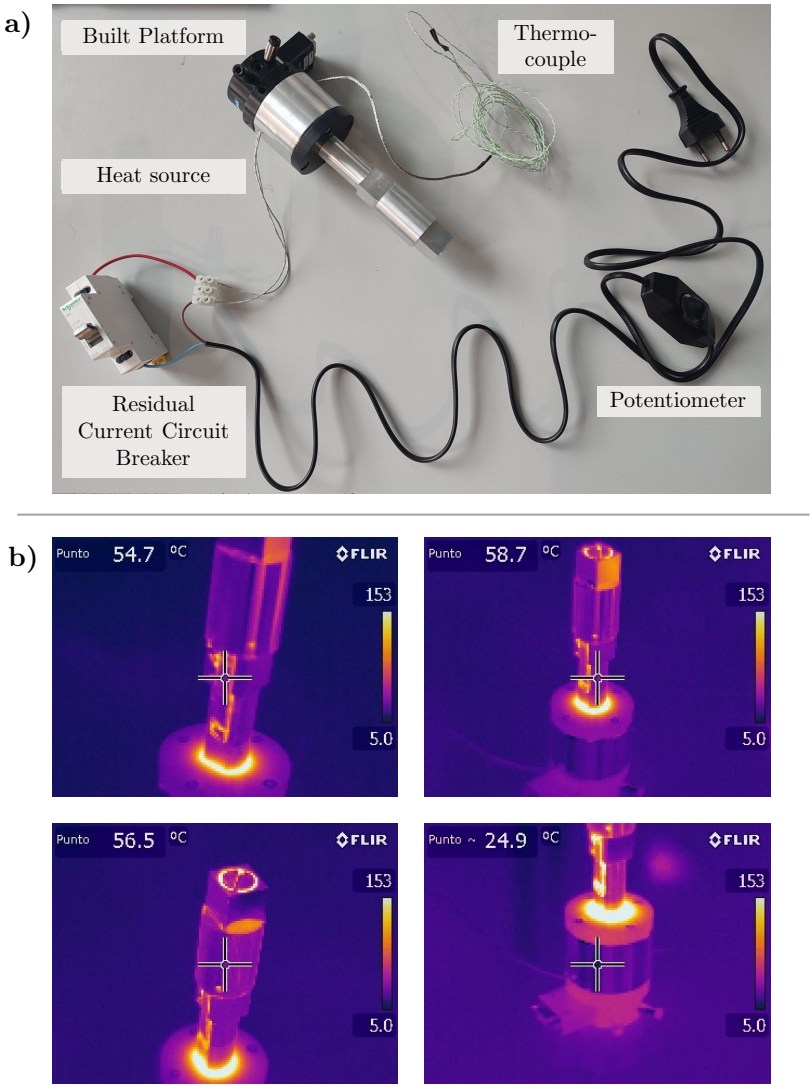

Figure 5.29: a) Built platform thermal operation conditions test setup. b) Temperature results under operating conditions in different build platform areas.

were necessary to ensure proper alignment with the robotic system and to maintain the platform's structural integrity under repeated use, thereby contributing to the overall quality of the printed parts.

Tolerance measurements were conducted using the Mitutoyo Crysta-Plus M544 coordinate measuring machine, and the overall results are presented in Tables 5.1, 5.2, and 5.3.

During the assembly phase, minor mechanical adjustments were required to compensate for manufacturing variations. While precise CAD modeling provided a solid foundation, real-world deviations highlighted the need for iterative adjustments. This underscored the importance of integrating manufacturing feedback early in the design process to ensure component compatibility and prevent assembly issues that could affect platform stability or performance.

Table 5.1: Flatness tolerance results for the manufactured part faces referred as shown in Figure 5.27.Values of 12 points dataset and 4 repetitions on each plane.

Flatness μm	Interior cube			Exterior cube		
	90	180	270	90	180	270
Mean $\overline{x}$	5.5	5.8	5.3	9.5	5.0	4.3
Std. deviation $\overline{\sigma}$	0.7	1.0	1.3	1.2	1.0	0.8

Table 5.2: Perpendicularity tolerance between contiguous faces. Results for the manufactured part faces referred as shown in Figure 5.27.Values of 12 points dataset and 4 repetitions on each plane.

Perpendicularity μm	Interior cube		Exterior cube	
	90 - 180	180 - 270	90 - 180	180 - 270
Mean $\overline{x}$	5.6	5.5	0.8	6.5
Std. deviation $\overline{\sigma}$	2.0	3.0	4.2	3.0

Table 5.3: Paralelism between faces of the external and internal cubes. Results for the manufactured part faces referred as shown in Figure 5.27.Values of 12 points dataset and 4 repetitions on each plane.

Face paralelism μm	90	180	270
Mean $\overline{x}$	13.9	12.0	10.5
Std. deviation $\overline{\sigma}$	1.2	0.6	0.6

The trajectory tracking tests were conducted using the new machined aluminum print bed. In this case, few improvements in process accuracy were observed. This is because the majority of the positioning error between the laser and the bed is due to the robotic arm's joint positioning errors, with only a minor contribution from the surface finish and relative tolerances of the calibration cubes. In other words, a more precise robotic arm is required to achieve further improvements in accuracy. The precision limit of this manipulator has been reached. This hypothesis is further validated with the manufacturer's data.

However, the efforts made in the manufacturing of the print bed will be utilized for the final implementation of the additive manufacturing station.

Extrusion-callibration head prototype construction

The design of the robot-based Non-Planar Additive Manufacturing cell has been finalized with the development of a custom extruder head that will replace the existing laser holder. This newly designed head integrates both the extrusion system and calibration mechanism within a single mount. The extrusion and calibration systems are assembled in a monolithic block due to the critical influence that precise knowledge of the relative position between the calibration element (calibration cubes) and the extruder has on calibration accuracy.

As outlined previously, this mount will be secured to a support structure, with the robot positioning the build platform beneath it for the extrusion process. During the design phase,

the following key aspects were carefully considered:

- **Thermal performance and management:** The extrusion system integrates an active cooling mechanism ensuring stable operating temperatures. The addition of insulation around heat-sensitive components further optimized thermal stability, preventing overheating of critical electronics and prolonging the system's operational life.
- **Precision and calibration:** To ensure high accuracy in non-planar printing, a laser-based calibration system was implemented, allowing for precise control of the nozzle's position relative to the printing surface. This calibration system, combined with the robotic arm's six degrees of freedom, ensured that the nozzle remained perpendicular to the surface at all times, minimizing layer misalignment.
- **Tolerances and mechanical stability:** The mechanical components of the extrusion head were designed with tight tolerances to enhance system rigidity and precision. The aluminum frame and other structural elements were machined to ensure that the extrusion head maintained consistent alignment throughout the printing process. These tolerances were particularly critical in preventing mechanical drift, which could compromise the system's ability to deposit material with time.
- **Material deposition and multimaterial capability:** The extrusion system was design for multimaterial printing, allowing for alternating deposition of different materials without manual intervention. The use of a selector mechanism to switch between materials ensured seamless transitions during the printing process.

Taking all these factors into account, the extruder shown in Figure 5.30 has been successfully designed. This head allows for the integration of two extruders into a monolithic block along with the calibration laser. The entire assembly is mounted on a structure oriented in such a way that the robot can access it from multiple directions. This configuration minimizes the issues of singularities that may arise during the execution of printing trajectories. A protective external cover has been added to shield the laser from potential impacts.

All components have been assembled and their kinematic functionality has been successfully validated. This functionality has been tested by executing material deposition trajectories on the cylindrical build platform, as shown in Figure 5.31. During this phase of the project, synchronized extrusion with movement was not performed, which will be carried out in future work. The assembly and functional validation of the complete system have been successfully completed. Figures 5.20 and 5.32 present the final design and the manufactured system.

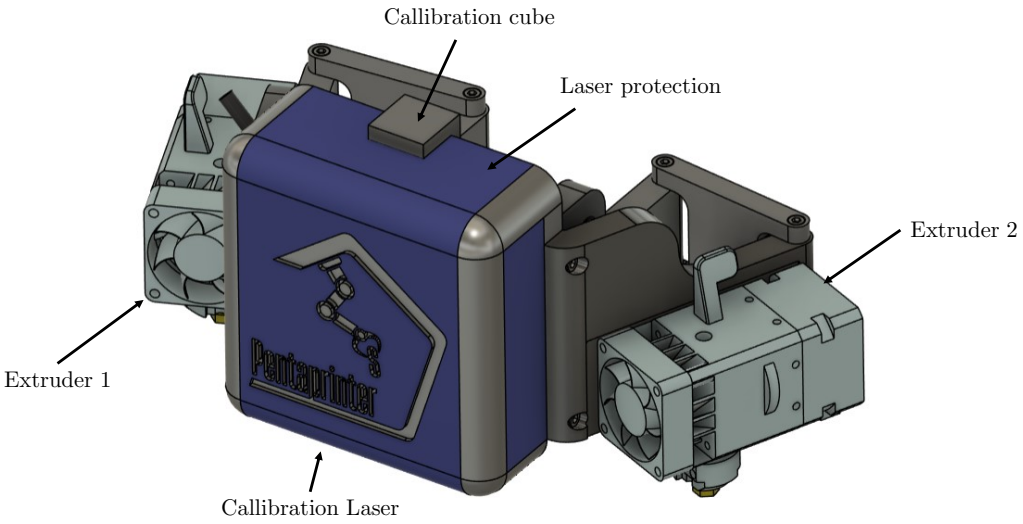

Figure 5.30: CAD model of the extrusion head designed with two extruders, calibration laser, and protective structure.

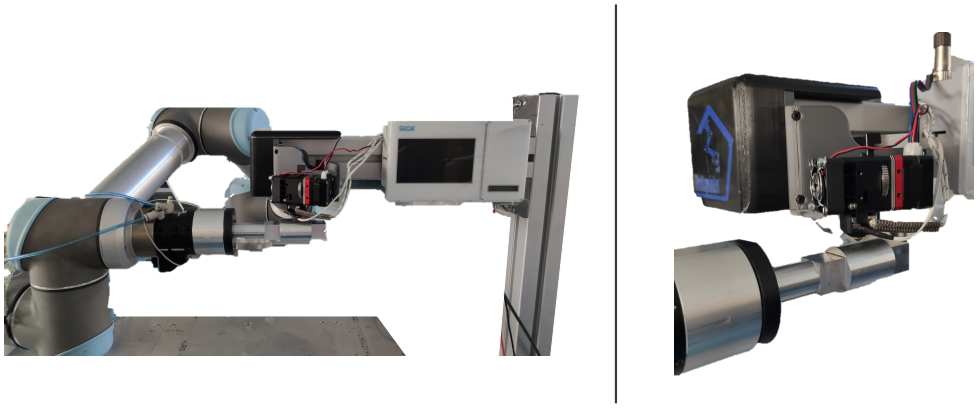

Figure 5.31: Final design of the robot-based non-planar additive manufacturing cell.

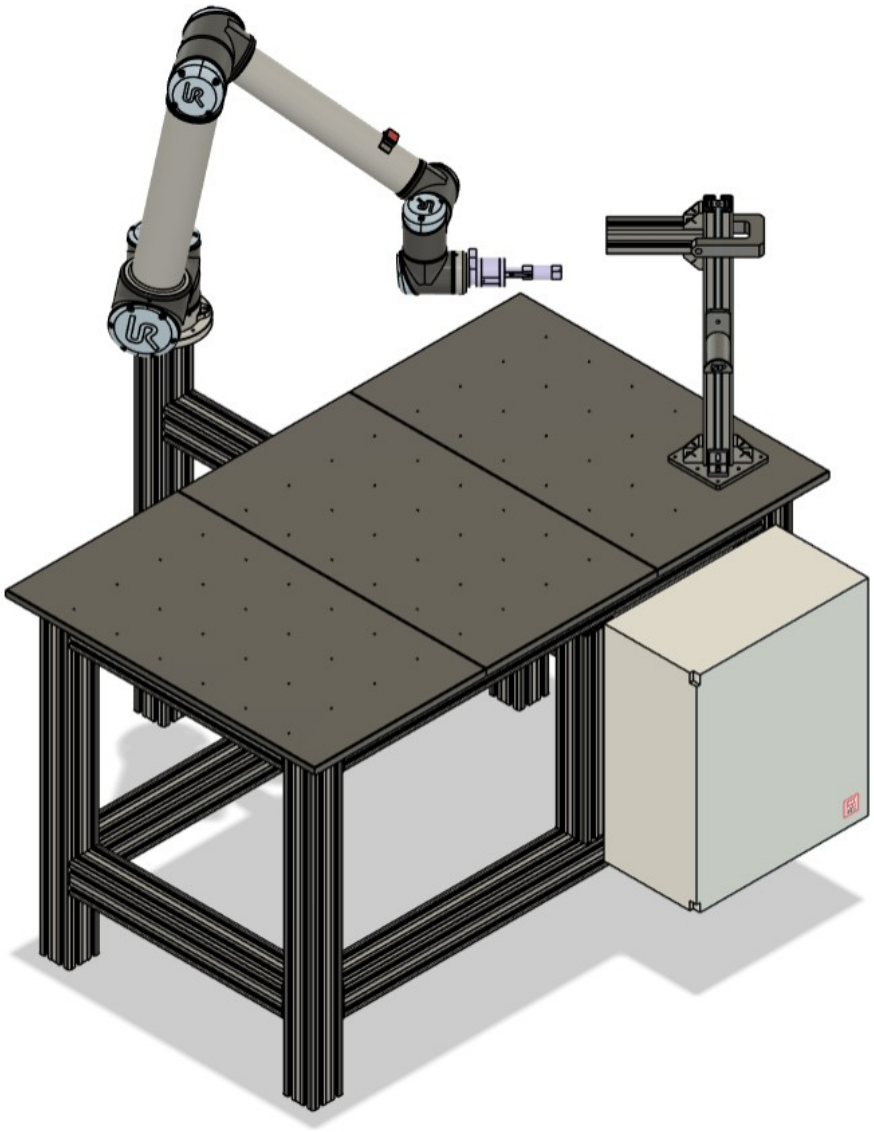

Figure 5.32: Final assembly of the robot-based non-planar additive manufacturing cell consisting of: robot manipulator from Universal Robots UR10, movable build platform mounted on the robot's TCP, and fixed extrusion head anchored to the workbench.

Chapter 6

Slicing space: key enabler for improved Design for Non-Planar Additive Manufacturing

Within the motivation outlined in the introduction of the thesis, the application of the additive manufacturing methodology implemented in the robotic cell is discussed in relation to various industrial uses through different case studies. All of these case studies fall under the scope of design for additive manufacturing (DfAM).

Chapter 5 presents a new methodology of DfAM, built upon the results of Chapter 4. Specifically, the design methodologies introduced are framed within the concept of Design for Non-planar Additive Manufacturing (DfNPAM). These methodologies aim to streamline the design process, engineering calculations, and the fabrication of parts by employing unconventional additive manufacturing techniques.

The improvement of the DfNPAM process focuses on two main strategies. The first is the use of the Slicing space, referenced to $\{e\}$, for design purposes instead of the conventional Carthesian space. The second strategy leverages the Slicing space to determine the axisymmetric build platform that optimizes the mechanical performance of a part under a specific load condition.

Under this new DfNPAM methodology, the case study presented in this chapter has been developed: *Origami Structures for Skin Expansion.* The case study chosen for the development and validation of this design methodology was selected due to the technical complexity of the design, which requires mechanical optimization and surface finish refinement, as well as the curved printing geometry enabled by the methodology.

Furthermore, the geometries designed for this case study have been integrated as a result of the BIOMET4D project: Smart 4D Biodegradable Metallic Shape-Shifting Implants for Dynamic Tissue Restoration.

6.1 Methodology

6.1.1 Using the Slicing space as design space overview

The use of the Slicing space, referenced to $\{e\}$, as the design space provides DfNPAM with great versatility in generating complex geometries in a highly simplified manner. To fully leverage this advantage, it is essential to have a comprehensive understanding of how the Slicing space operates and its limitations.

In general, the topological space, Slicing space, is defined as an infinite point space with the following constraints: $L \in (0, L(t_{max}); \theta \in [0, 2\pi)]$; and $H \in [0, \infty)$. This holds for any parametric curve $\mathbf{\Gamma}(t)$ used as generatrix with positive curvature throughout its entire range of definition and that satisfies the C^2continuity condition. However, when dealing with other types of curves, it is important to be mindful of potential regions within the slicing space where bijectivity may not hold.

Bijectivity may fail for two reasons: The first reason is the presence of negative curvature in the generatrix. In regions of negative curvature, the maximum value that H can assume at each point in the negative curvature area will be its radius of curvature at that point. The slicing space $H-$coordinate in negative curvature areas of $\mathbf{\Gamma}(t)$ is defined as: $H \in [0, -\rho(\mathbf{\Gamma}))$.

The second reason is the discontinuity of the $L-$coordinate at points where only a C^1 continuity condition is achieved. At each C^1 curvature point, the $L-$coordinate exhibits a discontinuity that interrupts the slicing space. Consequently, the definition of the $L-$coordinate is as follows: $L \in (0, L(t_{C^1})) \cup (L(t_{C^1}), L(t_{max}))$.

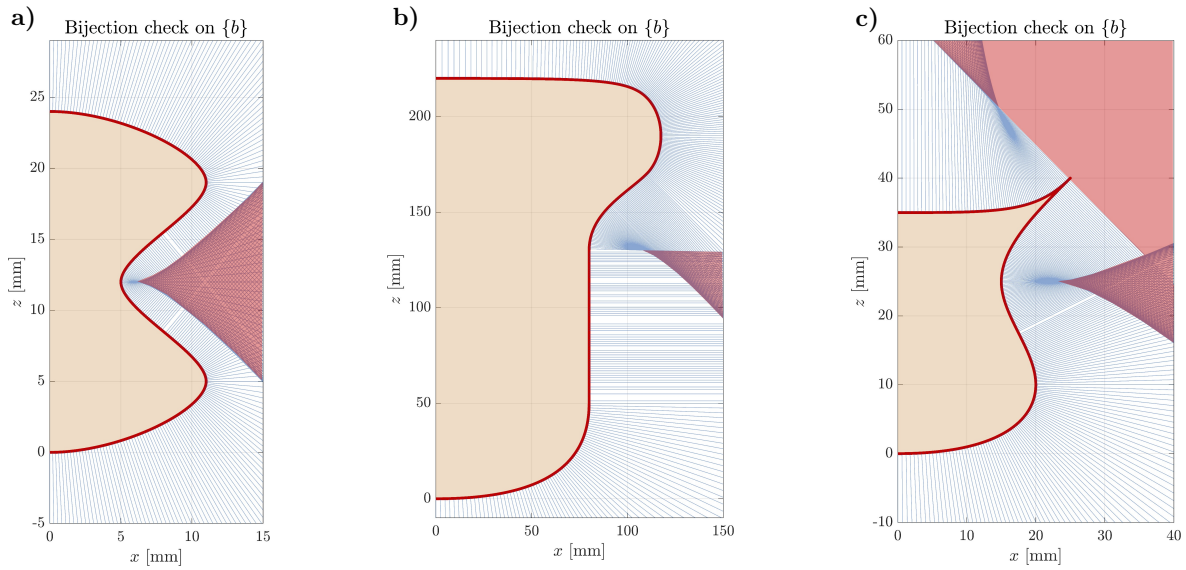

Figure 6.1: Verification of bijective areas for three curve cases with both positive and negative curvature. a) C^2 continuity. b) C^1 continuity. c) C^0 Continuity

Figure 6.1 illustrates the bijective areas of different curves under three conditions: C^2 continuity with both positive and negative curvature, C^1 continuity with both positive and negative curvature, and C^0 continuity with both positive and negative curvatures. These

bijective areas, the ones shaded in blue lines, will constitute the design space for NPAM. The rest of the space in red does not meet the requirements to be considered a bijective zone and be part of the Design space.

Once the limitations of the slicing space associated with the build platform are understood, the space referenced in e functions as a flat canvas, allowing for the planar design of any geometry. After applying the direct transformation described in 5.11, this design is converted into the target geometry expressed in $\{b\}$ where the robot manipulator can build it. To complete the methodology the part is sliced and the trajectories are generated as presented in chapter 4.

6.1.2 Origami structures for skin expansion

Origami, traditionally known as the art of paper folding, has evolved far beyond its recreational roots, becoming a critical area of study in engineering. This transformation gained momentum in the late 20th century, as researchers began to explore the mathematical foundations of folding. Origami's unique characteristics offer significant advantages in engineering, particularly in converting two-dimensional designs into durable, three-dimensional structures. This capability allows for high foldability, enabling substantial volume reduction, which is invaluable across various practical applications.

Historically, origami-based designs have relied on external mechanical or electrical actuators to achieve folding and unfolding. However, this reliance introduced limitations, primarily because the actuators themselves were not foldable, thus undermining the inherent benefits of origami's flexibility. In recent years, advancements in materials science have enabled the integration of smart materials into origami-based engineering. This breakthrough has eliminated the need for bulky external actuators, enhancing the functionality and versatility of origami structures.

The primary goal of this case study is to address the design challenges involved in creating shape-shifting, non-planar origami joints. By focusing on innovative design and manufacturing techniques, the study aims to improve the performance of these systems. Specifically, the research explores the integration of origami principles with advanced materials through non-planar additive manufacturing techniques, leading to adaptive structures capable of transforming their shape and function in response to various stimuli. The results of this research are expected to advance non-planar additive manufacturing and broaden the applicability of origami-based systems across multiple industries.

To meet the objectives of this case study, a comprehensive methodology was developed, encompassing design, simulation, and manufacturing planning. A library of non-planar designs utilizing smart materials was created, focusing on structures that enable a wide range of movements during the manufacturing process. The study evaluates patterns featuring advanced geometric configurations, leveraging the unique capabilities of non-planar fabrication methods.

Key design considerations include both the structural features and the integration of smart materials. These features are engineered to ensure stability while incorporating materials that

promote adaptive behavior. The study will define essential design criteria to evaluate the performance of these non-planar structures in real-world scenarios, contributing significantly to the advancement of non-planar additive manufacturing techniques and expanding the practical use of origami-based systems in various sectors.

6.1.3 Design of the origami pattern library

The case study focuses on the development of origami actuators designed to be used as skin expanders. To achieve full functionality, these actuators have been developed using conventional additive manufacturing (AM) techniques and then subjected to the DfNPAM methodology described earlier. This approach is necessary because, if the origami patterns are printed flat, they tend to flatten out again after deformation. This is the opposite of the desired effect in these types of interventions, where the device is forced to flatten when inserted under the skin and, through its natural tendency to return to its original printed shape, curves and expands the skin.

The selection process began by identifying origami patterns of particular interest. The main criterion was to choose patterns that would result in a variety of movements after folding/unfolding, aiming to create a useful library for future applications of these patterns. The standardized patterns selected include:

- Yoshimura claw (a variant of the traditional Yoshimura resembling a pincer movement)
- Kresling
- Fan
- Miura-ori
- Square twist

After selecting the patterns, the design process focused on the two main zones of origami structures: folds and facets. This design also considered the added difficulty of thickness when using polymeric materials instead of paper. Incorporating materials other than traditional paper requires a specific approach to address thickness, leading to a complex design ensuring that folds function properly as key elements to allow movement between facets. Additionally, the design took into account the activation mechanism of the smart material. Five different fold zone variants were designed, each adapted to three different lengths.

Next, the tool used for the design was described, including the specific configurations applied to implement each origami pattern with the proposed fold zones. Each origami pattern selected was then detailed, including the movements generated during unfolding, the morphology of the folds, their dimensions, and specific considerations for adapting their morphology to materials other than traditional paper.

Design criteria for patterns

Before starting the pattern design itself, it was necessary to define the morphology to be implemented in the folds and facets. Both parts require distinct behaviors. The facets provide stability and resistance to the folded origami form and should not activate when in contact

with the stimulus (water), meaning they must not be made of water-sensitive material. Facets must be as small and optimized as possible while remaining compatible with the folds.

On the other hand, folds are responsible for providing movement to the origami structures, acting as a kind of hinge between two facets. Therefore, folds should be made of flexible materials with high resistance to fatigue and must activate when in contact with the water stimulus. However, the folds should not consist solely of the water-sensitive material, as they must maintain the connection between facets even after the smart material has been activated.

As a general rule in origami applications in engineering, including thick origami, folds and facets often have different thicknesses. Typically, folds are one-third the thickness of the facets. This thickness relationship helps facilitate folding and ensures the structure's integrity.

Fold design

Three main design alternatives were derived for the fold zones, each considering the use of both water-sensitive and non-sensitive materials. Each of these alternatives stems from different folding principles, with the goal of determining the most suitable fold zone for origami application in later studies. Figure 6.2 shows the different designs.

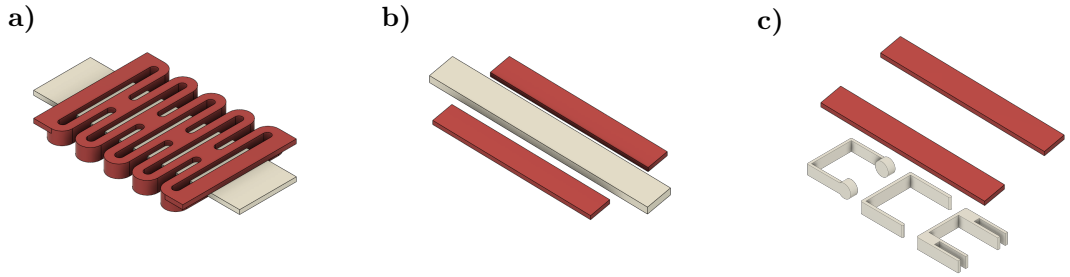

Figure 6.2: Proposed fold design for the origami patterns. a) Fold zone 1. b) Fold zone 2. c) Fold zone 3.

- **Fold Zone 1:** This design is based on a flat, wavy spring morphology. It features symmetrical undulating curves across a longitudinal axis, enhancing the design's stability and uniformity. The structure is 1 mm thick and includes rounded transitions to eliminate stress concentration points, improving both aesthetics and durability. The folds are composed of interconnected curves and straight lines in a zigzag pattern, creating a structure capable of traction, compression, torsion, and flexion movements. A central rectangular void is added to house the water-sensitive material, which activates the fold when exposed to water.
- **Fold Zone 2:** This alternative features a beam system combining lateral support elements with a central damping element. The central beam, made from the water-sensitive material, absorbs deformation caused by folding. The lateral beams provide rigidity, preventing breakage during folding. Three variants of this design were considered, differing in the thickness of the central beam ($1mm$, $0.4mm$, and $0.6mm$).
- **Fold Zone 3:** This option is similar to Fold Zone 2 but without the central beam. Instead, an external auxiliary piece, made entirely from water-sensitive material, is

introduced. This auxiliary piece helps hold the facets in place during folding and releases the fold upon activation by water, allowing the structure to expand. Three different auxiliary designs were considered, each featuring a hook-shaped geometry to secure the facets.

Facet design

The facet design, unlike the folds, depends entirely on the specific origami pattern being represented. However, three general criteria were defined:

Facets will have through-holes to reduce material usage, allow for hook integration during folding, and help characterize and distinguish the patterns. The facet thickness will be $1.8mm$, matching the fold zone thickness, to ensure compatibility and structural integrity. Facets will include a rectangular recess on their thickness face to accommodate the protruding section of the fold, ensuring a secure connection between flexible and rigid parts.

Pattern design

Once the design of the facets and joints is completed, the development of the full origami patterns begins, including a summary of their morphology and folding structure, key parameters, actuation movement, and the selected values for their parameters.

Based on the characterization of parameters for each origami design, it is possible to define the folding pattern and thus construct the entire origami structure. However, the folding patterns described below correspond to origami with zero thickness, meaning they are designed as if they were made from flat paper. To incorporate real thickness into the origami design, additional adjustments must be made in the folding zones. The procedure for this adjustment is as follows, illustrated in Figure 6.3. In this figure, the peaks are shown in red, the valleys in blue, and the facets in black throughout the initial design process.

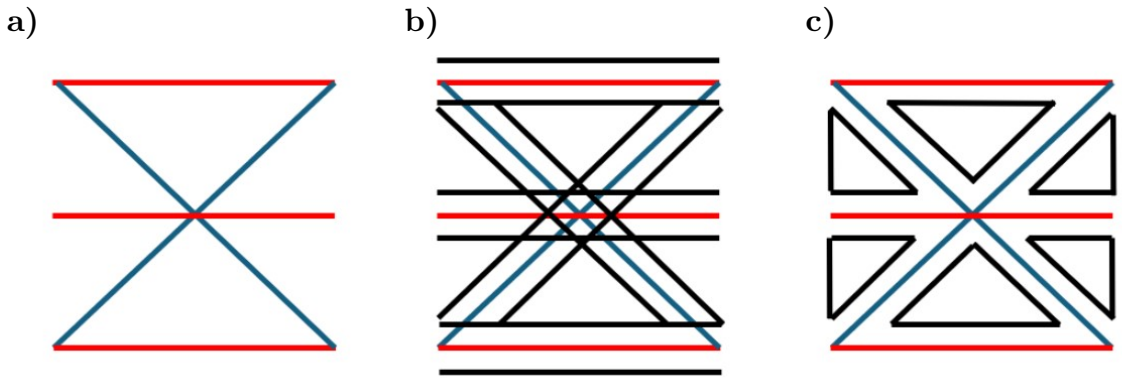

Figure 6.3: Proposed methodology for transitioning from origami patterns to basic design geometry. a) Base origami pattern. b) Folding zone definition. c) Facet adjustment.

The folding pattern is first sketched as though it were a flat origami design, without considering the material's thickness. For each fold, which is represented as a straight line in the design, two additional lines are added, parallel to the original fold and spaced $10.5mm$ on each side of the central line. This adjustment is based on the requirement that the fold zone must have

a total length of $21mm$. Therefore, the fold expands symmetrically by $10.5mm$ on each side, generating a new fold zone with a length of $21mm$, compatible with the original design. Facet Trimming: Based on the two newly added lines, the facets are trimmed. This ensures that there is a $21mm$ distance between two facets forming a fold, without altering the morphology or parameters previously defined for the pattern.

- **Yoshimura**

  The Yoshimura origami pattern is a predefined and tessellated design, formed through the repetition of a base pattern. This base pattern typically consists of a quadrilateral, usually a square, featuring valley folds along its main diagonals and mountain folds on its top and bottom edges. Additionally, the quadrilateral is divided by a horizontal line in its midsection, which also serves as a mountain fold. The tessellation is created by organizing this base pattern into rows and columns. The symmetrical properties of the base pattern significantly simplify the design process, reducing the number of parameters required to define it to only an angle α and a length L. These parameters can be determined using simple trigonometric relationships. Figure 6.4 shows the basic yoshimura pattern and its tesselation.

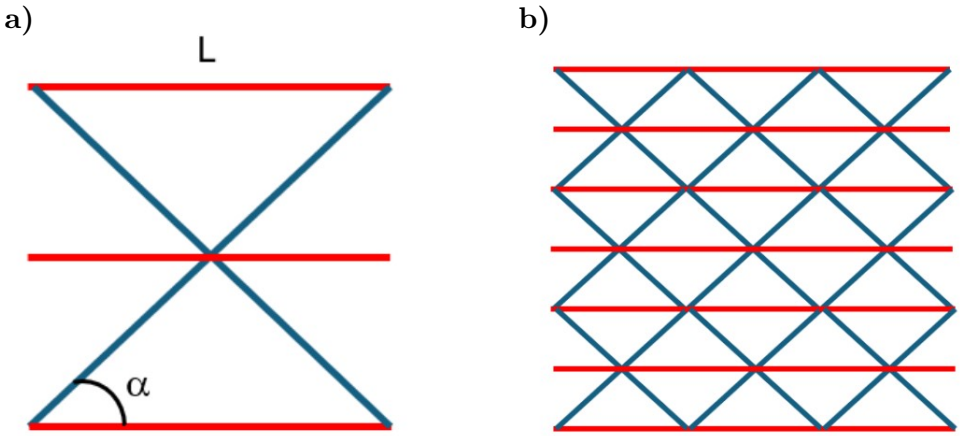

Figure 6.4: a) Yoshimura pattern definition. b) Yoshimura tesselation.

This pattern is commonly utilized to construct cylindrical structures, where the tessellation forms the cylinder's walls. In such a configuration, all valley folds align perpendicular to the cylinder's axis, with the cylinder's radius depending on the parameters of the base pattern. Once this cylindrical structure is established, the primary mode of actuation is axial compression. The origami folding is achieved by compressing the top and bottom edges axially, while deployment occurs through axial tension on the same edges.

The shape of the selected quadrilateral plays a crucial role in the compression movement. For example, when the quadrilateral is an elongated rectangle in a vertical orientation, fewer base pattern blocks are necessary to achieve the same level of compression, although this design requires greater force to compress. Conversely, a horizontally elongated rectangle requires more base pattern blocks to attain the same compression, yet applies less force. Observing the structure from a top view reveals a polygonal shape rather

than a perfect cylinder, with the number of columns in the tessellation dictating the polygon's form. Each successive row appears as an identical, but offset, polygon, with the offset angle calculated by dividing 180° by the number of columns in the cylinder. For this specific design, a square morphology with a side length of $82mm$ has been chosen, using only a single base pattern to minimize complexities associated with folding origami with non-zero thickness.

- **Kresling**

  The Kresling origami pattern is a predefined and tessellated design based on a parallelogram base, where the shorter side is oriented horizontally. The folding pattern of the Kresling features mountain folds along all four edges of the parallelogram, with a valley fold along the longer diagonal, which is inclined in the same direction as the edges. This pattern enables the creation of two types of Kresling structures, depending on how the tessellation is arranged: the Helicoidal Kresling, where the base pattern is organized into rows and columns without altering the orientation of the parallelogram; and the Inverted Kresling, which alternates the inclination of the diagonals in each consecutive row. Despite this change in orientation, the types of folds remain consistent, maintaining mountain folds on the edges and valley folds along the diagonal.

  The morphology of the Kresling pattern is asymmetrical, unlike previous patterns, and it exhibits horizontal symmetry only in the Inverted Kresling when the number of rows in the tessellation is even. The parameters that fully define the base block include the larger angle β, the smaller angle α, and the horizontal length L. Additionally, to consider its tessellation, it is necessary to define the number of rows and columns that will form the structure. Figure 6.5 illustrates the basic kresling pattern and its both tesselation alternatives.

  The Kresling pattern, in either configuration, is primarily used in cylindrical structures, with the left edge of the tessellation joined to the right to close the cylinder. The method of actuation varies significantly based on the configuration of the pattern. In the Helicoidal Kresling, activation is achieved through torsional movements along the cylinder's axis. To fold the pattern, the twist must be applied in a specific direction aligned with the inclination of the longer diagonal, while deployment requires twisting in the opposite direction. Conversely, the Inverted Kresling is activated through compression or tension movements along the cylinder's axis, but it is critical for this configuration to have an even number of rows in the tessellation to ensure proper functionality, stability, and symmetry during folding and unfolding.

  For the specific design to be realized, the following parameter values have been selected: $\beta = 70°$, $\alpha = 34°$, $L = 89mm$, with one row and three columns. A single row of the pattern has been chosen to limit the complexity associated with folding the top and bottom edges. By selecting the larger angle close to 90^{circ}, the design aims to achieve a morphology that facilitates a greater degree of compression when integrated into a cylindrical structure.

- **Accordion fan**

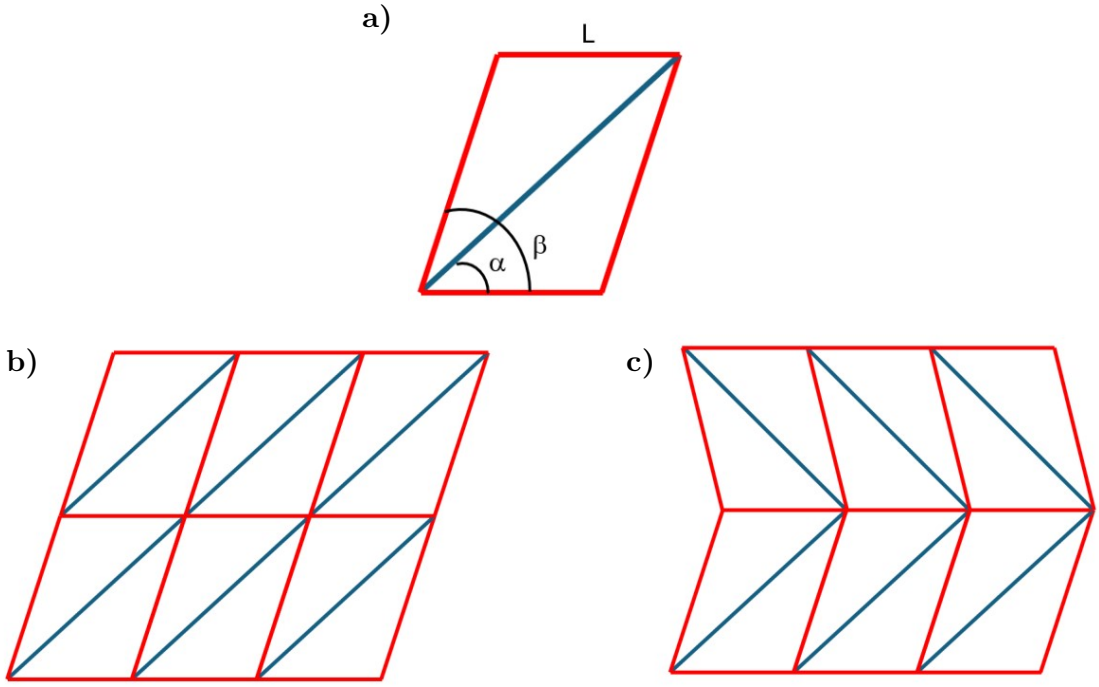

Figure 6.5: a) Kresling pattern definition. b) Helicoidal Kresling tesselation. c) Inverted Kresling tesselation.

The origami pattern known as the *accordion fan* is a widely recognized and standardized design, although it does not have a specific name like Yoshimura, Kresling, or Miura. This tessellated pattern features a base block shaped like a circular trapezoid (a portion of a circular ring), where the lateral edges consist of valley folds, while a radial mountain fold is located at its center. The tessellation of this pattern is created by repeating the base block in a single row, resulting in a series of circular trapezoids that alternate between valley and mountain folds.

The parameters that fully define the base block include the angle between the valley and mountain folds (α), the diameter of the larger circumference (ϕ_1), and the diameter of the smaller circumference (ϕ_2). For the tessellation, it is also necessary to define the number of base blocks that comprise the fan row. The base block, tessellation, and mentioned parameters can be observed in Figure 6.6.

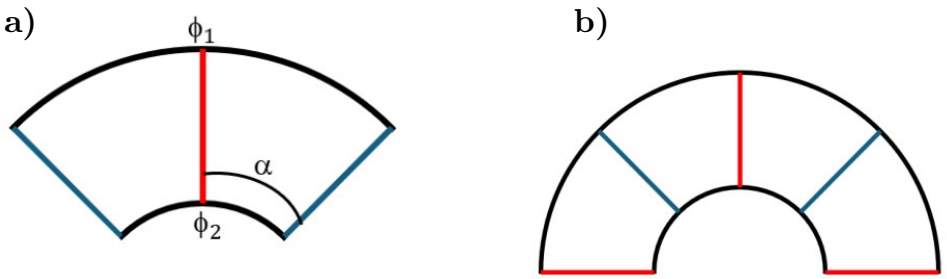

Figure 6.6: a) Accordion fan pattern definition. b) Accordion fan tesselation.

The actuation of this pattern is achieved through the application of a compressive force (folding) or a tensile force (unfolding) between the left and right edges of the tessellation. This process generates an accordion-like folding motion, allowing the origami to change shape from a portion of a circular ring to a completely flat structure.

For the design to be implemented, the following parameter values have been selected: $\alpha = 40°$, $\phi_1 = 120mm$, $\phi_2 = 40mm$, and the number of blocks is four. Consequently, a fan consisting of four blocks is generated, which includes two valley folds and one mountain fold, or vice versa. The thickness of the formed circular ring is $40mm$.

- **Miura-ori**

  The Miura origami pattern is one of the most well-known designs, characterized by its tessellation based on the repetition of rhomboid parallelograms. Its base unit consists of four parallelograms arranged in two vertical columns, with a negative slope on the lateral edges of the first two parallelograms and a corresponding reflection in the next two, thus creating a vertical axis of symmetry along the right lateral edge. Specifically, the parallelograms numbered 1 and 3 have vertical lateral edges and negatively sloped upper and lower edges, while parallelograms 2 and 4 exhibit positive slopes for their upper and lower edges. In this structure, the upper and lower edges are valley folds, while the lateral edges represent mountain folds for parallelograms 1 and 2 and valley folds for parallelograms 3 and 4. The internal inclined edges are mountain folds, and the internal vertical edges consist of valley folds between parallelograms 1 and 2 and mountain folds between parallelograms 3 and 4.

  This complex pattern lacks immediately obvious fold definitions and exhibits vertical symmetry but not horizontal symmetry. To configure the tessellation, it is essential to define the number of rows and columns of the base unit. The key parameters that define the pattern include the vertical edge length L_1, the sloped edge length L_2, and the angle α formed between these two edges. The structure of the base unit, its tessellation, and relevant parameters are illustrated in Figure 6.7.

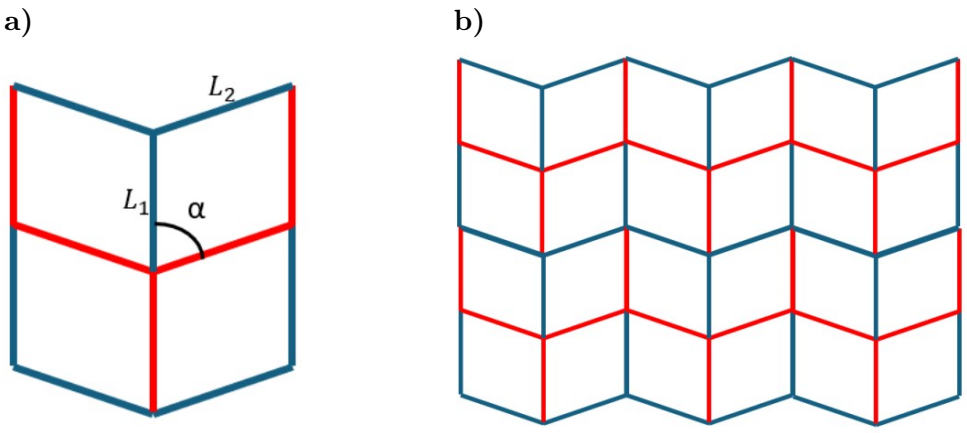

Figure 6.7: a) Miura-ori pattern definition. b) Miura-ori tesselation.

The actuation of the Miura pattern is typically executed in the plane, similar to the fan

pattern. This is achieved by applying compressive or tensile forces to the lateral edges of the tessellation. The resulting motion resembles an accordion folding mechanism, yet unlike the fan pattern, it does not produce a circumferential effect; the internal vertical edges maintain their original orientation throughout the process. This characteristic allows for a high compression ratio, as the morphology of the pattern can change dramatically from a fully deployed state in the plane to a completely folded state, thus categorizing it as a flat-folding pattern.

For the intended design, the following values have been selected for each parameter: $L_1 = 43mm$, $L_2 = 53mm$, and $\alpha = 64°$, with one row and two columns. These chosen values allow for the creation of facets of minimal size, optimizing the printing area. Additionally, a configuration of only one row and two columns has been selected to limit the complexity of the folding process.

- **Square-twist**

  This pattern belongs to traditional origami designs and features a central square from which four pairs of parallel folds radiate from each side. The structure consists of a twisted square rotated 45 degrees, along with four pairs of rectangles and trapezoids arranged alternately. From each side of the central square, a trapezoid extends, with its parallel edges oriented perpendicular to the corresponding side. Adjacent to each trapezoid is a rectangle with matching dimensions, forming an overall square outline. The sides of the central square are folded according to a mountain fold pattern. The shorter edge of the trapezoid produces a mountain fold, while the longer edge creates a valley fold. The key parameters defining this pattern are the side length of the square L_1, the angle of the trapezoid α, and the length of the longer edge of the trapezoid L_2. These elements are illustrated in Figure 6.8.

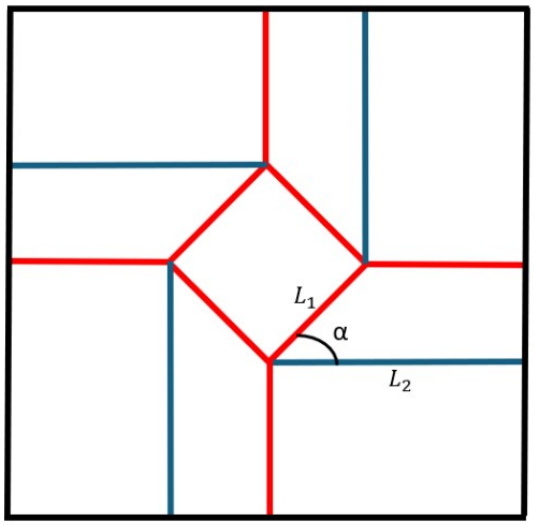

Figure 6.8: Square twist pattern definition.

The actuation of this pattern, as its name suggests, is based on the twisting of the central square. This twisting can only occur in the direction indicated by the inclined

edge of the trapezoid. The resulting movement enables the square formed by the outer edges of the pattern to decrease in section after folding. This characteristic allows for a compact configuration, which can be useful in various applications where space optimization is crucial.

For the design to be executed, the following values have been selected for each parameter: $L_1 = 41mm$, $L_2 = 74mm$ and $\alpha = 45°$. These dimensions are chosen to optimize the size of the facets, minimizing them as much as possible while maintaining a folding length of $21mm$. In this configuration, the resulting outer square has a side length of $150mm$. The careful selection of these parameters ensures that the origami structure is both functional and efficient in terms of material usage.

4D Origami fabrication

The fabrication of 4D origami patterns begins with finalizing the designs, followed by selecting and defining the materials, printer, and its configurations. Key material properties are emphasized, particularly their responsiveness to stimuli and deformation capacity. The main focus is on the interaction of the materials with water as the applied stimulus, which is crucial for achieving the desired transformations in the origami patterns.

In 4D origami fabrication, the choice of materials is vital for realizing specific transformations in response to stimuli. Two types of polymers are utilized: one that is sensitive to water and another that is insensitive. The sensitive polymer responds to moisture or immersion in water, while the insensitive polymer retains its shape regardless of humidity. Both materials are required in filament form, as the 3D printing technique employed is fused deposition modeling (FDM). The first polymer, Polyvinyl Alcohol (PVA), is a synthetic semicrystalline polymer known for its excellent formability, high tensile strength, flexibility, and biodegradable nature. Its properties vary with the degree of hydrolysis, which influences solubility and crystallinity, making partially hydrolyzed PVA more suitable for 4D applications due to its greater flexibility and response to moisture.

The second polymer, Glycol-Modified Polyethylene Terephthalate (PETG), is an amorphous copolymer that offers enhanced properties compared to traditional PET. It is characterized by improved flexibility, impact resistance, and lower moisture absorption. PETG is used as a non-responsive material in the 4D printing process, ensuring that structures maintain their integrity and original properties over time. Despite its recyclability, improper disposal of PETG can contribute to microplastic pollution, highlighting the importance of responsible material management.

For the production of the pieces, a dual-extruder printer is required to simultaneously incorporate both materials. The Bambu Lab X1 Carbon printer, utilized at the Polytechnic University of Madrid, is an advanced 3D printer that supports multi-material and multi-color printing with high precision and speed. Key features include a high-resolution lidar for detailed prints, CoreXY architecture for rapid movement, automatic bed leveling for reliability, and AI-driven enhancements for vibration compensation and error detection. This printer enables the effective fabrication of complex 4D origami structures while ensuring optimal print quality and efficiency.

Dynamic simulation of the origami fold zones

The methodology for simulating origami joint patterns involves finite element simulations to enhance understanding of the movements and folding angles achievable in origami structures. Following kinematic simulations, dynamic analyses are incorporated to investigate the structural behavior under applied forces. Given the complexity of simulating complete patterns, the study focuses on a simplified structure consisting of two facets and a single fold. The primary aim is to ascertain the force required to fold this simplified structure, ensuring that the smart material (PVA) achieves plastic deformation while the non-sensitive material (PETG) remains elastic. This approach not only elucidates the mechanical loads involved in folding but also anticipates design limitations under specific loading conditions.

The objectives of these dynamic simulations are threefold: firstly, to accurately identify the compression force needed for folding while ensuring the PVA reaches its plasticity threshold without exceeding the elastic limit of PETG; secondly, to confirm that maximum stress is localized within the designed plastic material; and thirdly, to evaluate the efficiency of different folding zones in terms of stress distribution and load-bearing capabilities. The simulation also analyzes how variations in folding zone length influence the required folding force and stress levels, aiming to optimize stress distribution and minimize the necessary compression force.

The simulations utilize ANSYS software, specifically the Static Structural module, where various stages such as engineering data input, geometry creation, and boundary condition setups are performed. The simulations incorporate the principles of deformation, focusing on elastic and plastic behaviors of materials. Key design considerations involve ensuring that the sensitive material can plastically deform while the other material remains within its elastic range, crucial for maintaining functional folds without structural failure.

To achieve this, figure 6.9 illustrates the procedure followed. Starting from a test geometry that includes the folding zone, the meshing is performed, differentiating between both materials involved in the joint fabrication. Once this is done, the boundary conditions are applied, fixing the upper right vertex of the piece while allowing its rotation and displacing the lower left vertex in the direction of the represented $x-$axis.

Overall, this simplified experimental setup involving only one fold aims to reduce complexity and enhance simulation accuracy, allowing for a detailed understanding of origami patterns' dynamic behavior under mechanical stress. By importing geometries designed in Autodesk Fusion and assigning materials accordingly, the study leverages advanced simulation tools to inform future designs and applications of origami mechanisms in practical scenarios.

Experimental degradation test under water

The methodology for the experimental tests focuses on validating the material's behavior and the functionality of different folding zones under conditions of plastic deformation and subsequent activation in water. Following the simulations and 3D printing of the components, initial tests were conducted using simplified specimens designed for finite element simulations. These specimens consist of two facets and a folding zone, representing a fold within origami. The goal was to demonstrate that after undergoing plastic deformation, the structures could return to their original configuration when the PVA material is activated by contact with

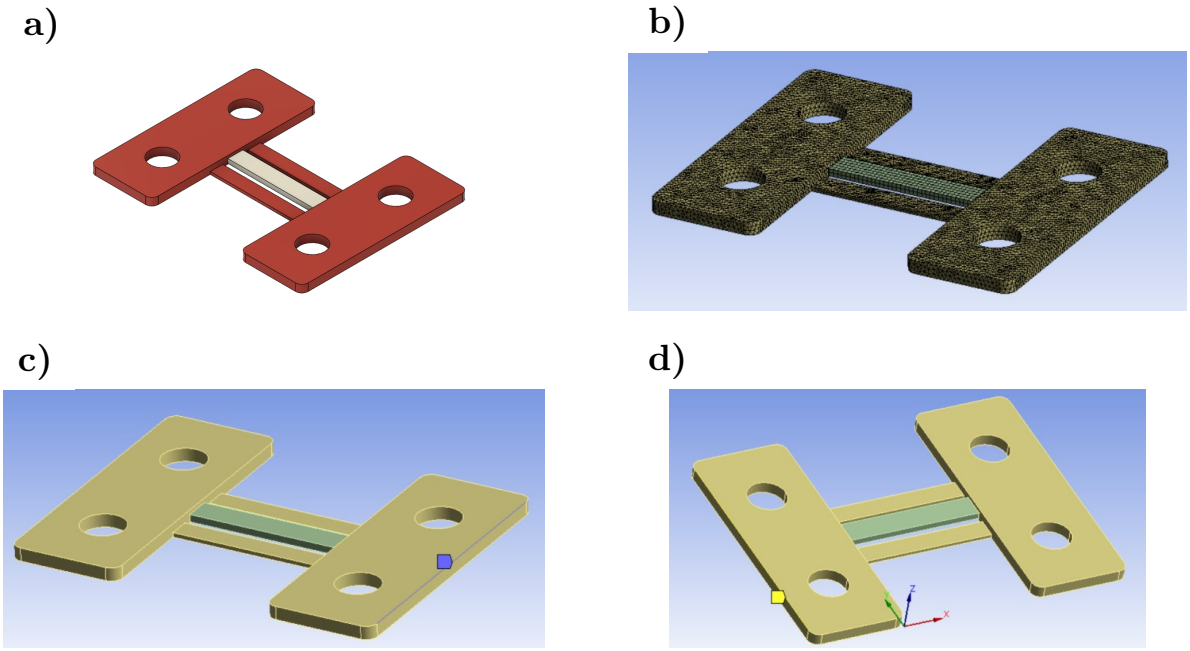

Figure 6.9: Simulation process followed to understand the behavior under stresses in each of the designed folding zones. Folding zone 2. a) Test specimen design. b) Test specimen meshing and material properties assignation. c) Fixed support with free rotation on the upper right vertex. d) Forced displacement on the $x-$axis direction on the lower left vertex.

water.

In addition to the preliminary tests, more complex experiments were carried out using the Yoshimura pattern, which features six folding zones. These additional tests aimed to assess the behavior of a more intricate structure and validate the applicability of origami patterns. The figure 6.10 shows all the specimens tested for activation through degradation in an aquatic environment.

The experimental assembly involved several components, including simplified specimens, a Yoshimura pattern model, a glass water container, and a recording system. The Yoshimura pattern was constructed with a folding zone and a length of 21 mm, designed to facilitate the more complex test. The glass container was used for its transparency, allowing for real-time observation and documentation of the tests. The water was heated to approximately $30°C$, which is suitable for activating PVA without significantly accelerating material degradation.

The testing procedure comprised four main steps. Initially, each specimen was plastically deformed by applying a force until the facets formed a 45-degree angle. This deformation was maintained for 10 minutes to ensure structural stabilization. Next, the specimen was affixed to the bottom of the glass container using silicone, and water at the prepared temperature was poured in to initiate the test. During the immersion, simultaneous recording captured the activation of the PVA material, with images taken every 0.5 seconds over a period of 25 minutes, totaling 3.000 frames.

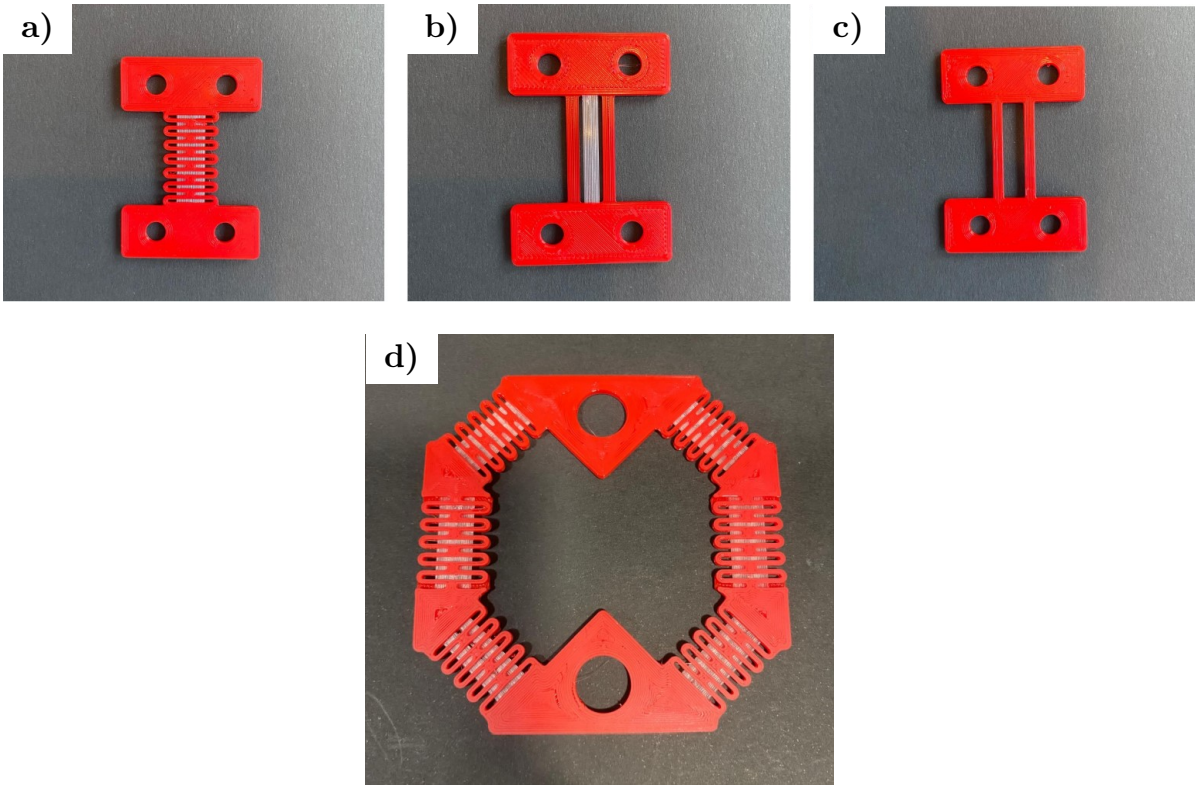

Figure 6.10: Specimens tested for activation through degradation in an aquatic environment. a) Folding zone 1. b) Folding zone 2. c) Folding zone 3. d) Origami pattern built up using folding zone 1 joints.

Finally, after the 25−minute immersion, the recording was halted, and the specimen was extracted from the water. This method allowed for thorough documentation of the process, including the specimen's return to its initial configuration and any additional deformations that might have occurred during the test. This comprehensive approach provided valuable insights into the material properties and behavior of the origami structures under study.

6.1.4 Design for non planar additive manufacturing

Once the functionality of the origami actuators arranged in a flat plane has been verified, their design for printing in non-planar layers becomes necessary. This is because the goal is for the actuators to reach their resting state in a non-planar form, remaining preloaded when flattened.

To achieve this, based on the dynamic tests conducted, the curve that best fits the stress tensors generated after deformation is defined. Once the base curve is selected, the geometry is mapped into the Slicing space referred to $\{e\}$ and placed on the build platform. Finally, the assembly is returned to the world space referred to $\{b\}$ where the lamination process begins.

To select the curved workspace, the curvature resulting from the dynamic simulation after applying the maximum force, which ensures the physical integrity of the devices in the case of folding zones 1, 2, and 3, has been considered. The curvature has been reduced to always

work on the side of safety. Additionally, to prevent excessive curvature in the $\theta-$direction, the part needs to be positioned sufficiently far from the $z-$axis of revolution. For this purpose, the bed shown in Figure 6.11 has been shaped and transformed to a b-spline defined by its control polygon in Table 6.1.

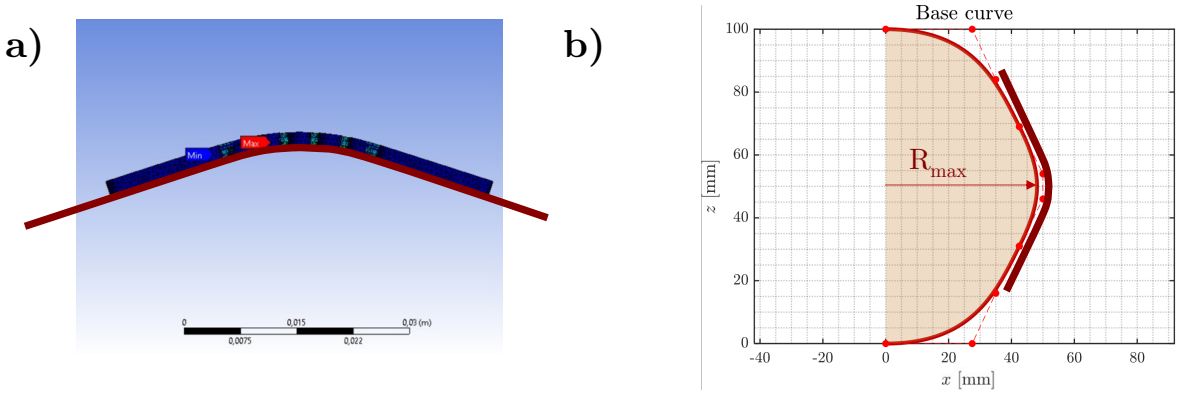

Figure 6.11: Generation of workspace from deformation modeled by simulation. a) deformation curvature. b) build platform and design space in $\{e\}$.

Table 6.1: Design space definition in $\{e\}$ for curved fold zones design.

Design Space Control Polygon	
xmm	**zmm**
0	0
27.5	0
35	16
42.5	31
50	46
50	54
42.5	69
35	84
27.5	100
0	100

Once the design space has been defined, the previously created flat design must be placed in the optimal area to align with the required curvature. In our case, we are interested in centering the designed folding zone at the $L-$coordinate. To achieve this, we evaluate the length of the spline and center the object on it. Once centered, we need to determine the angle θ of the design space that we want the part to cover. To avoid unnecessary deformations, we calculate the arc of a circumference with a maximum radius R_{max} of the bed. With this radius, we compute the angle θ such that the arc length A is equal to the original length of the part. Finally, the part is scaled in the $\theta-$direction so that its width in this direction spans the arc of the circumference without deforming its central zone.